

# Generation of monoenergetic ion beams with a laser accelerator

DISSERTATION

zur Erlangung des akademischen Grades

DOCTOR RERUM NATURALIUM (DR. RER. NAT.)



vorgelegt dem Rat der

PHYSIKALISCH-ASTRONOMISCHEN FAKULTÄT  
FRIEDRICH-SCHILLER-UNIVERSITÄT JENA

von Dipl.-Phys. Sebastian M. Pfothhauer

geboren am 03.02.1980 in Jena

## **Gutachter**

1. *Prof. Dr. Malte C. Kaluza*  
Institut für Optik und Quantenelektronik  
Friedrich-Schiller-Universität Jena, Germany
2. *Prof. Dr. Roland Sauerbrey*  
Forschungszentrum Dresden-Rossendorf  
Technische Universität Dresden, Germany
3. *Prof. Dr. Wolfgang Sandner*  
Max-Born-Institut für Nichtlineare Optik und Kurzzeitspektroskopie  
Technische Universität Berlin, Germany

Tag der letzten Rigorosumsprüfung: 26.1.2009

Tag der öffentlichen Verteidigung: 29.1.2009





# Zusammenfassung

Die vorliegende Arbeit beschäftigt sich mit der Erzeugung monoenergetischer Protonen- und Ionenstrahlen mittels laserbasierter Teilchenbeschleuniger. Eine Methode wurde entwickelt, welche es erlaubt, die bei relativistischen Laser-Plasma-Wechselwirkungen auf Festkörpertargets auftretenden Raumladungseffekte gezielt mit einer punktförmigen Teilchenquelle zu kombinieren. Durch diese einzigartige Interaktionsgeometrie konnten zum ersten Mal Protonenstrahlen mit einem intrinsisch schmalen Energiespektrum mit einem wenige Mikrometer großen Laserbeschleuniger generiert werden. Der experimentelle Aufbau wurde im Verlauf der vergangenen drei Jahre konsequent im Hinblick auf Reproduzierbarkeit und die maximal erzielten Teilchenenergien verbessert. Der daraus resultierende Grad an Verlässlichkeit erlaubte die Bestimmung der ersten Energie-Skalierungsgesetze speziell für monoenergetische Protonenstrahlen. Darüber hinaus konnte die Interaktionsgeometrie auf verschiedene Targetmaterialien übertragen werden, was die Erzeugung monoenergetischer Kohlenstoffstrahlen ermöglichte. Die experimentelle Arbeit wurde von der parallelen Entwicklung eines komplexen theoretischen Modells unterstützt, welches die Beobachtungen vollständig erklärt und in hervorragender Übereinstimmung mit zahlreichen numerischen Simulationen ist. Die hier vorgestellten Ergebnisse weisen weit über die Grenzen der vorliegenden Arbeit hinaus: Die Möglichkeit, zuverlässig monoenergetische Ionenstrahlen mittels kompakter, laserbasierter Teilchenbeschleuniger zu erzeugen ist—in Verbindung mit den einzigartigen Eigenschaften laserproduzierter Teilchenstrahlen—von fundamentaler Bedeutung für die Grundlagenforschung, für die Materialwissenschaften und potenzielle medizinische Anwendungen und wird maßgeblich zur Entwicklung einer neuen Generation von Beschleunigern beitragen.



# Abstract

A method for the generation of monoenergetic proton and ion beams from a laser-based particle accelerator is presented. This method utilizes the unique space-charge effects occurring during relativistic laser-plasma interactions on solid targets in combination with a dot-like particle source. Due to this unique interaction geometry, MeV proton beams with an intrinsically narrow energy spectrum were obtained, for the first time, from a micrometer-scale laser accelerator. Over the past three years, the acceleration scheme has been consistently improved to enhance both the maximum particle energy and the reliability of the setup. The achieved degree of reliability allowed to derive the first scaling laws specifically for monoenergetic proton beams. Furthermore, the acceleration scheme was expanded on other target materials, enabling the generation of monoenergetic carbon beams. The experimental work was strongly supported by the parallel development of a complex theoretical model, which fully accounts for the observations and is in excellent agreement with numerical simulations. The presented results have an extraordinarily broad scope way beyond the current thesis: The availability of monoenergetic ion beams from a compact laser-plasma beam source—in conjunction with the unique properties of laser-produced particle beams—addresses a number of outstanding applications in fundamental research, material science and medical physics, and will help to shape a new generation of accelerators.





# Contents

<b>Zusammenfassung</b>	<b>v</b>
<b>Abstract</b>	<b>vii</b>
<b>Table of contents</b>	<b>viii</b>
<b>Figures</b>	<b>x</b>
<b>1 Introduction</b>	<b>1</b>
1.1 The experiment . . . . .	2
1.2 Thesis outline . . . . .	4
<b>2 Relativistic laser-plasma interactions</b>	<b>7</b>
2.1 Fundamentals of relativistic laser-plasma physics . . . . .	7
2.1.1 Ionization and plasma formation at solid targets . . . . .	7
2.1.2 Single electron acceleration and the ponderomotive force . . . . .	12
2.1.3 Optical properties of plasmas . . . . .	14
2.1.4 A multitude of absorption mechanisms . . . . .	16
2.2 Target Normal Sheath Acceleration (TNSA) . . . . .	22
2.2.1 The physical picture . . . . .	22
2.2.2 Theoretical models and scaling laws for thermal proton spectra . . . . .	23
2.2.3 Dependencies on target and laser pre-pulse conditions . . . . .	29
2.3 Concerning the spectral shaping of laser-generated proton beams (Confined TNSA) . . . . .	30
2.3.1 Thermal spectra . . . . .	30
2.3.2 Confinement of the proton source - the Esirkepov/Bulanov model . . . . .	31
2.3.3 Charge separation effects . . . . .	34
<b>3 Experimental considerations</b>	<b>41</b>
3.1 Proton emission source size and source layer manipulation . . . . .	41
3.2 Microstructured targets . . . . .	43
3.3 The Jena 10 TW Titanium:Sapphire laser system (JETI) . . . . .	45
3.4 Experimental setup for Confined TNSA . . . . .	47
<b>4 Narrow-band proton and ion beams</b>	<b>49</b>
4.1 Monoenergetic proton beams . . . . .	49
4.1.1 Exemplary proton spectra . . . . .	49
4.1.2 Beam properties . . . . .	51
4.1.3 PIC simulations . . . . .	53
4.2 Reproducibility studies and the inevitability of target cleaning . . . . .	56

4.3	Scaling laws for monoenergetic proton beams . . . . .	58
4.3.1	Peak position scaling . . . . .	58
4.3.2	Peak width scaling . . . . .	60
4.4	Target composition and the “Proton Density Reduction” scheme (PDR) . . . . .	63
4.4.1	Impact of the heavy ion background on the proton spectrum . . . . .	63
4.4.2	PDR theory & simulation studies . . . . .	64
4.4.3	PDR experiments . . . . .	70
4.5	Monoenergetic ion beams . . . . .	73
4.6	Multiple peak structures . . . . .	75
4.7	Alternative approaches to narrow-band ion beams . . . . .	76
<b>5</b>	<b>Future prospects for laser-generated narrow-band proton beams</b>	<b>81</b>
5.1	POLARIS Petawatt scaling . . . . .	81
5.2	Contrast improvements . . . . .	84
5.3	Radiation oncology based on laser accelerators - an estimation . . . . .	85
5.3.1	Ion beam therapy vs. other radiation treatments - a physical overview . . . . .	86
5.3.2	Laser-based ion beam therapy . . . . .	89
	<b>Appendix A: Laser ablation</b>	<b>95</b>
	<b>Appendix B: The Jena 10 TW Titanium:Sapphire laser system (JETI)</b>	<b>99</b>
	<b>Bibliography</b>	<b>101</b>
	<b>Curriculum Vitae</b>	<b>121</b>
	<b>Publication list</b>	<b>123</b>
	<b>Eidesstattliche Erklärung</b>	<b>125</b>
	<b>Danksagung</b>	<b>127</b>

# List of Figures

1.1	TNSA from a thin foil target and “Confined TNSA” from a microdot source . . . . .	3
2.1	Multi-photon ionization processes . . . . .	9
2.2	Laser reflection in a plasma at oblique incidence and resonance absorption . . . . .	18
2.3	The Mora 1D fluid model . . . . .	25
2.4	Proton acceleration from a geometrically confined dot source (Esirkepov model). . . . .	32
2.5	Charge separation effects . . . . .	35
2.6	Proton phase-space during peak formation . . . . .	38
2.7	Convergence of the peak position during the acceleration process . . . . .	39
3.1	Proton source size and emission within energy cones . . . . .	42
3.2	Microstructured targets . . . . .	44
3.3	The Jena 10 TW Titanium:Sapphire laser system (JETI) . . . . .	46
3.4	Experimental set up . . . . .	48
4.1	Monoenergetic proton beams . . . . .	50
4.2	Monoenergetic proton spectrum from 2D-PIC simulation (OSIRIS code) . . . . .	54
4.3	Angular emission properties of protons from a dot source . . . . .	55
4.4	Reproducibility studies with controlled laser ablation . . . . .	57
4.5	Scaling law for monoenergetic proton beams . . . . .	59
4.6	Scaling of the spectral peak width . . . . .	62
4.7	Impact of the heavy ion background on the generation of monoenergetic spectra . . . . .	64
4.8	PDR simulation studies (1D-PIC) . . . . .	66
4.9	PDR peak energy scaling as a function of the initial proton density (1D-PIC) . . . . .	67
4.10	PDR peak energy scaling as a function of the laser intensity (1D-PIC) . . . . .	67
4.11	PDR simulation studies (2D-PIC) . . . . .	69
4.12	PDR peak energy scaling as a function of the initial proton density (1D-PIC) . . . . .	69
4.13	PDR peak energy scaling as a function of the initial proton density (experiment) . . . . .	72
4.14	PDR peak energy scaling with proton density and laser energy (experiment) . . . . .	72
4.15	Monoenergetic carbon beams . . . . .	74
4.16	Multiple peak structures . . . . .	75
4.17	Energy modulation from multi-stage acceleration . . . . .	78
5.1	2D-PIC simulation for 15 J pulse energy (OSIRIS code) . . . . .	82
5.2	Petawatt scaling for the POLARIS laser (2D-PIC) . . . . .	83
5.3	Comparison of the stopping power of electrons, protons and $\alpha$ -particles in biological tissue . . . . .	87
5.4	Dose deposition patterns for photons, electrons, protons and carbon ions . . . . .	88
5.5	Bragg peak calculated for the POLARIS proton spectrum . . . . .	92
5.6	PMMA absorption spectra . . . . .	95
5.7	Etch rate and incubation effects for UV laser ablation . . . . .	96
5.8	JETI THG-autocorrelation trace . . . . .	99

## List of Figures

---

# List of Tables

4.1	Beam properties of exemplary proton spectra . . . . .	53
4.2	Simulation parameters of the 1D-PIC simulations for the PDR scheme . . . . .	65
4.3	Simulation parameters of the 2D-PIC simulations for the PDR scheme . . . . .	70
4.4	Composition of the deuterated polymer microdots for the PDR study . . . . .	71
5.1	Kinetic ion energy required for the penetration of 30 cm water . . . . .	90



# 1 Introduction

Throughout the past decade, high intensity lasers have ventured widely into the domain of particle acceleration. Relativistic laser-plasmas [1, 2] generated by the interaction of multi-Terawatt (TW) laser pulses with matter have been identified as a brilliant source of GeV electrons [3, 4], MeV ions [5–8], and versatile photon beams [9–16]. Laser-produced particle beams possess a number of unique properties, including ultra-short pulse duration of the order of the laser pulse duration (femto- to picoseconds) [7], excellent emittance values [17], and ultra-high peak currents leading to gigantic magnetic fields of the order of Megagauss [18–21]. Most importantly, the acceleration process takes place on a micrometer to centimeter scale, which has excited wide speculations about a new generation of compact laser-driven particle sources and their potential applications.

In fact, compact accelerators of ultra-short particle pulses would be pivotal for a multitude of outstanding applications [2, 22], such as the definition of novel radiation sources for the structural analysis of matter [9, 11, 13], as pre-accelerators for conventional acceleration devices [23], for fast ignition of inertial confinement fusion [24–26], for medical isotope production [27, 28], or for oncological radiation therapy [29–33].

However, most of these promising applications depend crucially on the availability of particle beams with narrow energy distribution, whereas for a long time laser-produced particle beams commonly displayed a broad, quasi-thermal energy spectrum (see e.g. [34–40] for electrons, and [5, 6, 27, 41–44] for ions). For example, the proposed fast ignition schemes presuppose the availability of an intense, monoenergetic proton beam for the localized heating of a pellet target [24, 25]. The use of laser plasma sources as injectors for conventional accelerators requires particle beams with small bandwidth and emittance in order to match the injected bunch to the subsequent accelerator [23]. And especially for oncological radiation therapy, spectral control is an inevitable key criterion [29, 30, 33].

In 2004, a milestone for laser particle acceleration was accomplished by the *first production of monoenergetic electron beams* [45–48]. Since then, laser electron acceleration has matured greatly, both by increasing the maximum achievable kinetic energy for monoenergetic bunches to the GeV level [3, 4] as well as significantly lowering the experimental restrictions for such beams [49, 50], so that by now, laser-driven electron sources have already passed the threshold to application [9].

The aim of the present thesis is to provide a similar *laser-based particle source for monoenergetic ion beams*. In particular, this source should not involve additional beam shaping devices (e.g. magnets) in order to maintain the advantages of compact laser accelerators with respect to conventional ones, but enable *intrinsic control over the produced ion spectra*. A suitable acceleration scheme for protons was experimentally realized in 2005 at the Institute of Optics and Quantum Electronics Jena (IOQ) using a special laser-target interaction geometry, which demonstrated, for the first time, that relativistic laser-plasma interactions can in fact be utilized to produce narrow-band proton beams [51]. Together with a simultaneous work on laser-generated monoenergetic carbon ion beams by Hegelich et al. [52], this represented the starting point for many fruitful investigations concerning the spectral shaping of

laser-produced ion beams, resulting in a large number of publications until the present day.

Having established this proof-of-principle, follow-up research at IOQ mainly addressed the optimization of the proton beams in terms of achievable peak energy and bandwidth control. Particular emphasis was thereby put on the reliability of the laser acceleration scheme, which is a crucial prerequisite when aiming at the applications mentioned above. As of today, monoenergetic proton spectra with approximately 8% bandwidth at up to 3 MeV peak energy containing about  $10^9$  protons can be produced. The reproducibility for the generation of monoenergetic beams can be as high as  $\approx 80\%$ . Moreover, in the course of this thesis, an advanced theoretical model for laser ion acceleration with multiple ion species was developed that accounts for the observed spectra and dependencies in a satisfactory manner [53–55]. Supported by multidimensional particle-in-cell (PIC) simulations performed by Alex Robinson and Paul Gibbon, the theoretical model suggested several improvements of the setup, including an alteration of the target composition and the transferability of the monoenergetic acceleration scheme to other ion species. The predicted improvements could be verified in dedicated experiments.

From extensive statistical analysis, an empirical scaling law between the narrow-band peak energy and the laser energy was derived, which allows to extrapolate the current results to future laser systems. At present, laser-accelerated ion beams are not yet a competitor for conventional accelerators. The scaling, however, illustrates that within the next decade, laser-based proton accelerators will be part of a new generation of particle sources with unique applications. The monoenergetic beams presented in this thesis have established a firm fundament for this development and may serve for a number of initial application studies already, e.g. in first biophysical irradiation experiments with ultra-short pulsed protons. 10 MeV protons - a value easily obtained by many of today's lasers - can penetrate up to 1.2 mm into biological tissue, which in conjunction with the narrow bandwidth would allow for a concise dose application and first radiological test series with ultra-short, laser-generated proton beams.

In the prospect of such promising experiments, the capacity of reliably generating bunches of  $10^9$  monoenergetic protons with less than 10% bandwidth by means of a scalable technique marks an important step towards application and will contribute significantly to the future of laser particle acceleration.

## 1.1 The experiment

In the second part of this prelude chapter, the central experiment of the thesis shall be briefly introduced, describing the generation of monoenergetic ion beams from laser-plasmas on an intuitive level. Here, as well as for the most part of the thesis, the Jena 10 TW Titanium:Sapphire laser (JETI) shall be treated simply as a “black box” light source at the free disposal of the experimentalist.<sup>1</sup>

When a high intensity laser pulse hits a thin metal foil, a plasma is formed at the target front side. In this plasma, electrons are accelerated by the laser field to relativistic energies and

---

<sup>1</sup>The simplifying assumption should not be mistaken to diminish the 'laser part' of laser plasma experiments. In fact, laser development, optimization and maintenance constitutes a central element laser plasma physics, and a major chunk of experimental time is dedicated to this purpose. The JETI laser will be introduced to the reader in some detail in chapter 3.3. Certain properties of the laser pulse and their variation may be discussed earlier in the thesis when relevant to the ion acceleration experiments. For more exhaustive treatment, refer to [56, 57].



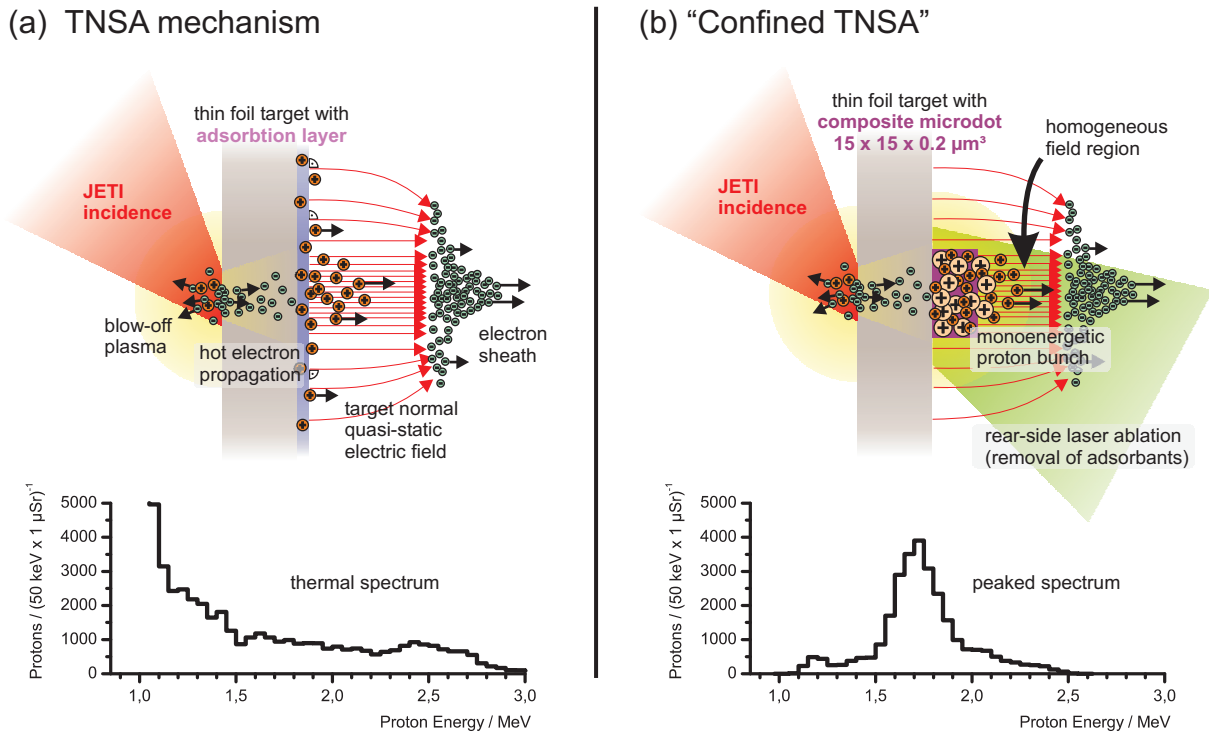


Figure 1.1: Target Normal Sheath Acceleration (TNSA) from a thin foil target and “Confined TNSA” from a microdot source. (a) The TNSA process. A TW-laser pulse hits a thin foil target at the front side and creates a hot electron plasma. The plasma electrons are accelerated by the laser field through the target, and form a symmetric electron sheath at the back side. In the resulting electric fields, surface atoms are ionized and accelerated up to MeV energies. The bottom graph shows a typical proton spectrum obtained from TNSA, displaying a broad quasi-thermal energy distribution. (b) “Confined TNSA” from a microdot source. The extended TNSA proton source layer is replaced by a confined dot source. The TW-laser pulse hits the titanium foil exactly opposite to dot position, so that the dot is located in the central homogeneous part of the TNSA field. In addition, charge separation effects between protons and carbon ions from the dot lead to a charge discontinuity at the slower carbon front, resulting in a shock acceleration of protons across this carbon front and their subsequent accumulation as a monoenergetic bunch in the zero-field region behind it. This monoenergetic acceleration process works well for dots of up to micrometer thickness. Surface contaminants outside the confined dot source experience a weaker accelerating field and act parasitically on the monoenergetic acceleration process, but may be removed by controlled laser ablation of the target back side. A typical monoenergetic spectrum obtained from Confined TNSA is shown in the bottom right graph.

pushed into the target [1, 2, 58, 59]. If the target is sufficiently thin, the electrons are expelled at the back side, where the restoring Coulomb force counteracts the charge separation. Thus, the main part of the hot electron population is trapped and constitutes an electron sheath at the target rear (Fig. 1.1a), which is retained until the laser pulse stops driving electrons through the target and the electron population starts to cool down. The resulting electric fields between the sheath and the positively charged target are of the order of several  $10^{12}$  V/m and suffice to field-ionize the foil material as well as adsorbates present on the target surface

(mostly hydrocarbons and water). The generated ions are accelerated immediately in the sheath field, whereas the light protons are favoured for acceleration due to the highest charge to mass ( $q/m$ ) ratio. This process is known as Target Normal Sheath Acceleration (TNSA) [42, 60].

The proton beams produced via TNSA typically show an exponential energy spectrum with a distinct cutoff energy  $E_{\text{cutoff}}$  of typically a few MeV, which depends strongly on the laser and target parameters [44]. This broad distribution can be explained mainly by two contributions: First, the accelerating sheath field possesses a bell-shaped symmetry and is inhomogeneous in the transverse direction, which means that the maximum energy a proton can reach is determined by its radial position. Protons located in the center of the field are accelerated the most, up to the maximum energy  $E_{\text{cutoff}}$ , whereas protons outside the center experience a lower electric field strength and consequently are accelerated to lower energies. Secondly, the accelerating electric field decays when reaching into regions of higher charge density. Deeper sited protons in the source layer will thus be (partially) screened from the electric field by their faster predecessors. Both the screening effects as well as the transverse inhomogeneity effectuate that the resulting spectrum has a strong correlation to the initial distribution of the protons to be accelerated from the target.

Following this understanding, Esirkepov and Bulanov [61] proposed an acceleration scheme for the generation of monoenergetic beams, where all protons are radially confined to a "dot" source within the central homogeneous region of the TNSA field. If the proton source is furthermore sufficiently thin so that screening effects are negligible, all protons experience the same potential and are accelerated to a monoenergetic distribution. However, recent theoretical studies by Robinson and Gibbon [54] showed that the limitation of the dot thickness is actually not a critical criterion: For thick dots, the formation of monoenergetic spectra is supported by charge separation effects between the light protons and more inert ions (e.g. carbon), which leads to a region of uniform proton shock acceleration at the heavy ion front, where protons are trapped and form a stable monoenergetic bunch [55, 62]. Note that radial source confinement nonetheless essential, as the transverse inhomogeneity of the TNSA field would inevitably lead to a broad energy distribution.

This acceleration scheme—a radially confined ion source located centrally in the TNSA field, and consisting of at least two ion species such as to enable charge separation—is at the heart of this thesis's research and shall henceforth be referred to as "*Confined TNSA*" (Fig. 1.1b). In the course of this work, it will be shown that Confined TNSA represents a reliable, potent and versatile technique for the generation of proton and ion beams with narrow energy distribution.

## 1.2 Thesis outline

The thesis will be structured as follows. Chapter 2 will provide an introduction to the physics of laser-plasma interaction, with particular emphasis on laser-based ion acceleration. The chapter will start out from a discussion of several ionization mechanisms applicable to high power laser-matter interaction leading to the formation of a plasma. An estimation of the specific plasma conditions encountered at JETI will be provided. The chapter will continue with a description of the interaction between an intense laser field and an ensemble of free electrons, including fundamental optical properties of plasmas and their connection to the free electron density. With this background, the chapter will then discuss the different absorption

mechanisms found in laser plasmas.

The second half of chapter 2 will be concerned with laser-driven ion acceleration. “Target Normal Sheath Acceleration” (TNSA) as the central mechanism at stake will be introduced in detail using several theoretical models. This section will include a discussion of the dependency of TNSA-produced proton beams on different parameters such as target thickness and pre-pulse characteristics. Finally, a special acceleration scheme for the utilization of TNSA for the generation of monoenergetic proton and ion beams will be presented. This “Confined TNSA” scheme will be bound to two conditions—a radial confinement of the proton source to a “micro-dot”, and charge separation effects between multiple ion species—both of which will be discussed in great detail. Particle-In-Cell (PIC) simulations will help to understand the key mechanisms involved.

Chapter 3 deals with the experimental realization of Confined TNSA. From the two conditions and general TNSA properties, a special target design will be derived and translated into a fabrication routine for microstructured double layer targets. The JETI laser system itself and the implementation of the targets at JETI will be discussed.

In chapter 4, the major experimental results of the thesis as well as supporting numerical studies will be presented. First, the properties of the produced monoenergetic proton beams will be discussed. Secondly, the reproducibility of the Confined TNSA mechanism will be examined, highlighting particularly the importance of controlled target cleaning using laser ablation. In a third step, scaling laws for the peak energy and width as a function of the laser energy will be derived. This analysis will be greatly supported by numerical simulations. The chapter will then move on to a discussion of the effects of different target compositions. It will turn out that both the specific concentration of the leading ion species (in this case protons) as well as the heavy ion contributions in the beam have a significant impact on the spectrum. Furthermore, the transferability of the Confined TNSA scheme will be demonstrated by the providing evidence for the generation of monoenergetic carbon beams from a heavy ion dot source. Finally, a number of alternative techniques for the generation of narrow-band proton and ion beams shall be briefly discussed.

In chapter 5, the potential of laser-produced ion beams for applications will be evaluated. In particular, the current results for monoenergetic spectra obtained from microstructured targets will be extrapolated to higher laser energies using 2D-PIC simulations, which allows to estimate the proton beam parameters expected from the POLARIS laser currently under construction in Jena. The simulations indicate that the POLARIS beams will be suitable for a number of outstanding applications, which will be discussed in detail for the example of medical ion beam therapy.

Appendix A will present, in a nutshell, the physics of laser ablation, paying particular attention to the types of ablation encountered during the course of the thesis. Finally, Appendix B will provide an exemplary THG autocorrelation trace recorded at JETI.

Let us, however, begin with an introduction to the physics of relativistic laser plasma interaction and laser-based particle acceleration, providing the theoretical background for the experiments to be discussed below.



## 2 Relativistic laser-plasma interactions

If one intends to build a particle accelerator by means of a strong laser, it is imperative to know about the mechanisms of energy transfer from laser energy into particle kinetic energy. More precisely, the central task is to convert the energy of the rapidly oscillating laser field into directed particle momentum. At least for ions, this energy transfer cannot be obtained directly, as the large ion inertia prohibits an efficient direct acceleration in the laser field at currently available intensities. Although this restriction may be challenged by future laser systems with intensities  $I > 10^{24}$  W/cm<sup>2</sup>, the energy transfer to ions with today's laser accelerators must rely on mediation processes based on laser-electron interaction. The required free electron population is created by the laser itself in a so-called laser plasma. Over the past years, laser plasma science has been increasingly successful in disentangling the consecutive events of plasma generation and heating, directed electron acceleration, and ion emission. In the following sections, the individual processes at stake shall be introduced in detail, providing the physical basis of laser accelerators as a robust and versatile means to produce MeV ion beams in an entirely new fashion.

### 2.1 Fundamentals of relativistic laser-plasma physics

#### 2.1.1 Ionization and plasma formation at solid targets

*High intensity laser-solid interactions are dominated by rapid ionization dynamics and the formation of a hot electron plasma. The plasma temperature determines the ion sound speed and hence the plasma expansion velocity. At JETI, a plasma with a scale length of  $L_p \approx \lambda$  is formed prior to the arrival of the main pulse. The electron density and temperature determine the screening of electric fields in the plasma, expressed by the Debye length  $\lambda_D$ .*

In classical optics, the interaction of light with matter is described by electromagnetic (em) theory and a linear material response to the incident em-waves. For high intensities, the interaction enters the perturbative regime of nonlinear optics, where the material response is described by higher order terms of the dielectric tensor. *Ultra-intense laser-matter interactions*, on the contrary, are typically governed by ionization dynamics and plasma formation, leading to a large reservoir of free electrons and a fundamentally different interaction behaviour. The free electrons are immediately exposed to the laser field and may gain substantial kinetic energy from it. If the laser field is strong enough, the electron energies can become relativistic, which gives rise to the regime of “relativistic optics” or “relativistic laser-plasma interactions” [1, 63].

Most laser systems used in relativistic interactions work in the infrared (IR) range and may therefore not conduct ionization directly. For Titanium:Sapphire (Ti:Sapphire) lasers ( $\lambda_{\text{Ti:Sapph}} \approx 795$  nm), the energy of a single photon is  $E_{\text{photon}} = 1.6$  eV. In comparison, ionization energies are typically of the order of tens of eV, e.g.  $E_{\text{ion}}(\text{H}^+) = 13.6$  eV for hydrogen and  $E_{\text{ion}}(\text{C}^+) = 11.2$  eV for carbon. However, at intensities  $> 10^{10}$  W/cm<sup>2</sup>, multiphoton processes become sufficiently probable to excite electrons from bound states to the

ionization threshold (“multi-photon ionization”) or even beyond (“above-threshold-ionization”) [58]. These processes are illustrated in Fig. 2.1.

Note that for the calculation of multi-photon ionization cross sections, the impact of the laser field on the Coulomb potential of the atom is typically neglected. This approximation does obviously not hold true anymore if the laser field strength<sup>1</sup> becomes comparable to the atomic field strength,

$$\mathbb{E}_{\text{at}} = \frac{e}{4\pi\epsilon_0 a_{\text{B}}^2} \approx 5.1 \times 10^{11} \text{ V/m} \quad (2.1)$$

which is reached at a laser intensity (“atomic intensity”) of

$$I_{\text{at}} = \frac{1}{2}\epsilon_0 c \mathbb{E}^2 \approx 3.5 \times 10^{16} \text{ W/cm}^2. \quad (2.2)$$

Here,  $e$  is the electron charge,  $\epsilon_0$  the vacuum permittivity,  $a_{\text{B}} = \hbar^2/m_e e^2$  the radius of the Bohr atom, and  $c$  the speed of light. Note that multi-photon ionization sets in well below this intensity [58]. However, when the atomic intensity is approached, the static Coulomb potential will be periodically superimposed by the rapidly oscillating laser field  $\mathbb{E}(t)$ , yielding a total electric potential of

$$U(x, t) = -\frac{Ze^2}{4\pi\epsilon_0 x} - ex\mathbb{E}(t), \quad (2.3)$$

where  $x$  is the direction of the laser polarization. In case of ultra-strong laser fields, the atomic potential can thus be deformed to a degree that electrons may tunnel from the bound state through the remaining barrier into the continuum (“tunnelling ionization”). The so-called Keldysh parameter  $\gamma_{\text{K}} = \sqrt{E_{\text{ion}}/2\Phi_{\text{p}}^{\text{class}}}$  allows to distinguish between these two regimes, yielding  $\gamma_{\text{K}} > 1$  for multi-photon ionization,  $\gamma_{\text{K}} \leq 1$  for tunnelling ionization, where  $E_{\text{ion}}$  is the ionization energy for the specific electron state under consideration,  $\Phi_{\text{p}}^{\text{class}} = e^2 \mathbb{E}^2/m_e \omega$  is the classical ponderomotive potential as discussed in the next section (cf. Eq. 2.29), and  $\omega$  is the laser angular frequency. If the field suffices to lower the Coulomb wall *below* an atomic state or even to the ground state, electrons will be stripped off the nucleus instantly and the atom gets (fully) ionized. This “barrier suppression ionization” can be expressed by the “appearance intensity” of a certain ion state,

$$I_{\text{app}} = \left(\frac{4\pi\epsilon_0}{Ze^2}\right)^2 \cdot \frac{\epsilon_0 c}{32e^2} \cdot E_{\text{ion}}^4 \quad (2.4)$$

$$\approx \frac{(E_{\text{ion}}/\text{eV})^4}{Z^2} \cdot 4 \times 10^9 \text{ W/cm}^2, \quad (2.5)$$

for which the maximum of the reduced Coulomb wall at a certain laser intensity has been identified with the ionization energy of the electron state [58]. For hydrogen, the appearance intensity amounts to  $I_{\text{app}} = 1.4 \times 10^{14} \text{ W/cm}^2$  with  $\gamma_{\text{K}} = 0.9$ , which is still well below the atomic intensity [Eq. 2.2].

<sup>1</sup>In this thesis, the electric field will be denoted by  $\vec{\mathbb{E}}$  or  $\mathbb{E}$  for vector and scalar expressions, respectively. In order to avoid confusion, energies will always be denoted by a capital Italic  $E$ .

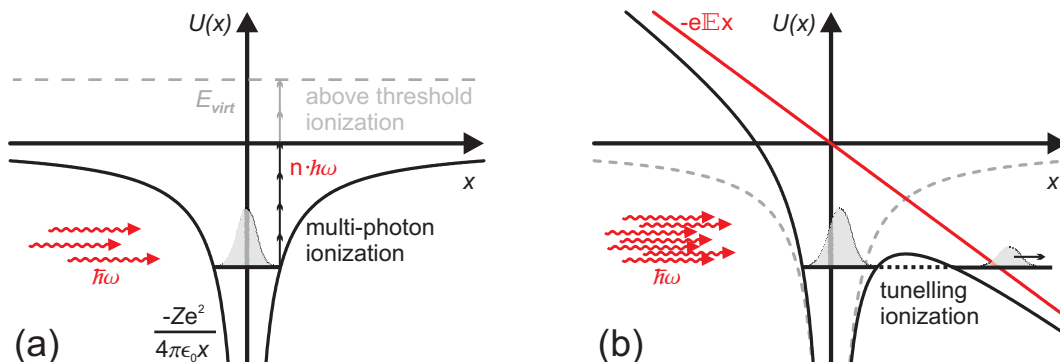


Figure 2.1: (a) Multi-photon ionization and above-threshold ionization. For a large number of incident photons (i.e. at high intensities), the probability for multi-photon absorption processes is no longer negligible. Multi-Photon absorption arises due to the fact that electrons also “tentatively” absorb non-resonant photon energies and remain on the corresponding virtual energy state for a time  $\Delta t$  associated with the energy uncertainty of this state,  $\Delta t \approx \hbar/2\Delta E$ . If the photon flux is sufficiently high, the electron may absorb more photons during that time and eventually enter the continuum. By the same mechanism, electron may absorb more photons than necessary for ionization, and thus enter the continuum with a well-defined kinetic energy given by multiples of the photon energy minus the ionization energy (“above-threshold ionization” - ATI). (b) Tunnelling ionization. For ultra-intense laser fields, the field strength becomes comparable to the atomic field and the mutual impact can no longer be neglected. Electrons may thus tunnel through the remaining Coulomb barrier of the deformed field (“tunnelling ionization”), or even leave the atom instantly if the atomic potential is suppressed below the bound states (“barrier suppression ionization”).

The ionization processes discussed above effectuate that any solid target—no matter whether initially reflective (e.g. a metal), transparent (e.g. a glass substrate), or opaque (e.g. plastic)—will rapidly form a plasma slab on the surface when irradiated with a sufficiently intense laser pulse. Especially in the case of ultra-short laser pulses impinging on solid targets, the free electron population will increase very rapidly [64], and avalanche ionization and collisional ionization will support the plasma formation [15, 65–69]. In order to characterize the actual *laser-plasma interaction*, it is important to know about the plasma density profile and the relevant scale lengths. A number of fundamental properties can be derived using the *fluid model of a freely expanding plasma*. This model will reappear later in this work when sheath acceleration at the target back is described (cf. section 2.2). The fluid model assumes that the plasma is collisionless, and no further ionization and recombination occur during the expansion (i.e. the particle number is preserved) [70]. The phase-space density  $f_j(\vec{x}, \vec{v}, t)$  of  $j$ -th particle species in the plasma is then conserved, which is expressed by the *Vlasov equation*,

$$\frac{\partial f_j}{\partial t} + \vec{v} \cdot \frac{\partial f_j}{\partial \vec{x}} + \frac{q_j}{m_j} \left( \vec{\mathbb{E}} + \frac{1}{c} \vec{v} \times \vec{\mathbb{B}} \right) \cdot \frac{\partial f_j}{\partial \vec{v}} = 0. \quad (2.6)$$

Here,  $q_j$  &  $m_j$  are the particle charge and mass, respectively, and  $\vec{\mathbb{E}}$  &  $\vec{\mathbb{B}}$  are the electric and magnetic fields associated with the charged fluid. From integration of the Vlasov equation, one can obtain the continuity and the force equation for the fluid particle density

$n_j = \int f_j(\vec{x}, \vec{v}, t) d\vec{v}$  and mean velocity  $\vec{v}_j = 1/n_j \cdot \int \vec{v} f_j(\vec{x}, \vec{v}, t) d\vec{v}$ ,

$$\frac{\partial n_j}{\partial t} + \frac{\partial}{\partial \vec{x}_j} (n_j \vec{v}_j) = 0 \quad (2.7)$$

$$n_j \left( \frac{\partial \vec{v}_j}{\partial t} + \vec{v}_j \frac{\partial \vec{v}_j}{\partial \vec{x}_j} \right) = n_j \frac{q_j}{m_j} \left( \vec{E} + \frac{1}{c} \vec{v}_j \times \vec{B} \right) - \frac{1}{m_j} \nabla p_j, \quad (2.8)$$

$p_j$  being the fluid pressure determined by the equation of state [70]. For an isothermal expansion, this equation of state is simply  $p_j = n_j k_B T_j$ , where  $k_B$  is the Boltzmann constant and  $T_j$  the temperature of the isothermal particle distribution. Limiting the discussion to two particle species here (i.e. electrons and one ion species), and neglecting the magnetic field contributions as well as the electron inertia, one obtains the following continuity and force equation for the ion population

$$\frac{\partial n_i}{\partial t} + \frac{\partial}{\partial x_i} (n_i v_i) = 0 \quad (2.9)$$

$$\frac{\partial v_i}{\partial t} + v_i \frac{\partial v_i}{\partial x_i} = -\frac{1}{m_i} \left( \frac{\bar{Z} \nabla p_e}{n_e} - \frac{\nabla p_i}{n_i} \right) = -c_s^2 \frac{1}{n_i} \frac{\partial n_i}{\partial x}, \quad (2.10)$$

where the electron and ion density are connected by the average ion charge state  $\bar{Z}$ ,  $n_e = \bar{Z} n_i$ . The ion sound speed  $c_s$  is given by

$$c_s = \sqrt{\frac{\bar{Z} \cdot k_B T_e}{m_i} + \frac{k_B T_i}{m_i}} \approx \sqrt{\frac{\bar{Z} \cdot k_B T_e}{m_i}} \approx 0.31 \times 10^6 \frac{\text{m}}{\text{s}} \cdot \sqrt{\frac{k_B T_e}{\text{keV}} \cdot \frac{\bar{Z}}{A}}, \quad (2.11)$$

$A$  being the mass number of the ion. The differential equations 2.9 and 2.10 are solved by

$$v_i = c_s + \frac{x_i}{t} \quad (2.12)$$

$$n_i = n_{i,0} \exp \left\{ -\frac{x_i}{c_s t} \right\}, \quad (2.13)$$

$$n_e = \bar{Z} n_i \quad (2.14)$$

which means that an isothermal, freely expanding plasma will obey an exponential density profile. Furthermore, it can be seen that the plasma density scale length  $L_P$  increases over time with the ion sound speed,  $L_P = n_i / \nabla n_i = c_s t$ .

Let us now attempt to estimate some of the plasma parameters. At high intensity laser systems such as JETI, the laser pulse is typically anteceded by pre-pulses and a pico- to nanosecond pedestal of Amplified Spontaneous Emission (ASE), which may evoke pre-plasma formation on the target front side prior to the arrival of the main pulse. Consequently, the plasma expansion and the interaction conditions depend strongly on the contrast ratio between the ASE/pre-pulse and the main pulse. At JETI, a contrast of  $I_{\text{ASE}}/I_{\text{main}} < 10^{-8}$  can be warranted 40 ps before the main pulse, where plasma formation can be neglected. 30 ps before the main pulse, however, a pre-pulse with  $I_{\text{pp}}/I_{\text{main}} \approx 10^{-5}$  is ejected (cf. Appendix B), which suffices to create a pre-plasma on the target. Assuming that this pre-plasma is heated to about  $k_B T_e = 150 \text{ eV}$  and that the foil material is ionized to  $\text{Ti}^{3+}$ , one obtains a plasma expansion velocity of  $c_s = 3.1 \times 10^5 \text{ m/s}$ , resulting in a plasma scale length of  $L_P = 0.94 \mu\text{m} \approx 1.18 \lambda$  for



the interaction of the main pulse (cf. [58]).

For the sake of illustration, let us briefly consider a second, more idealized interaction scenario, where ionization is initiated only by the main pulse. At relativistic intensities, titanium is rather easily ionized to  $\text{Ti}^{12+}$  ( $E_{\text{ion}}(\text{Ti}^{12+}) = 291.5 \text{ eV}$ ), with an appearance intensity of approximately  $I_{\text{app}}(\text{Ti}^{12+}) = 2 \times 10^{17} \text{ W/cm}^2$  (cf. Eq. 2.5). A typical JETI pulse ( $\tau_{\text{FWHM}} = 80 \text{ fs}$ ,  $I = 3.7 \times 10^{19} \text{ W/cm}^2$ ) reaches this intensity roughly 290 fs before the pulse maximum. Assuming that the plasma is initially heated to a temperature of 1 keV by rising edge of the main pulse (cf. [58], page 128), the plasma expansion velocity amounts to  $c_s = 6.3 \times 10^4 \text{ m/s}$ , which in turn yields a plasma scale length of  $L_p = 0.02 \mu\text{m} \approx 0.03 \lambda$  prior to the pulse maximum. This value is significantly smaller than the one derived above, implying that for very clean ultra-short laser pulses, the plasma has hardly time to expand, and the arriving pulse would interact with an almost-solid density target. Note that in all subsequent estimations, the larger value (i.e. the one resulting from the pre-pulse) will be used, which will be of particular importance when talking about absorption processes in section 2.1.4.

Before moving on to the behaviour of a plasma under the impact of electromagnetic waves, some electrostatic properties of plasmas shall be discussed briefly. For a given charge  $q$  located at a fixed position  $\vec{x}$  within a plasma (e.g. a single inert ion), the free electrons will immediately form an equilibrium distribution around it. For a Maxwellian electron spectrum with initial (unperturbed) electron density  $n_{e,0}$ , the density is modified by the electrostatic potential  $\Phi_{\text{el}}$  introduced by the positive charge to

$$\begin{aligned} n_e &= \int f(\vec{x}, \vec{v}) d\vec{v} = \left( \frac{m_e}{2\pi k_B T_e} \right)^{\frac{3}{2}} \exp \left\{ -\frac{\frac{m_e}{2} (v_x^2 + v_y^2 + v_z^2) - e\Phi_{\text{el}}}{k_B T_e} \right\} \\ &= n_{e,0} \exp \left\{ \frac{e\Phi_{\text{el}}}{k_B T_e} \right\}, \end{aligned} \quad (2.15)$$

Assuming that electron and ion density are initially the same,  $n_{e,0} \equiv n_{i,0}$ , the Poisson equation reads

$$\begin{aligned} \nabla^2 \Phi_{\text{el}} &= -\frac{1}{\varepsilon_0} [q\delta(\vec{x}) + e(n_e - n_{i,0})], \\ &= -\frac{1}{\varepsilon_0} \left[ q\delta(\vec{x}) + en_{e,0} \left( \exp \left\{ \frac{e\Phi_{\text{el}}}{k_B T_e} \right\} - 1 \right) \right] \\ &\approx -\frac{1}{\varepsilon_0} \left[ q\delta(\vec{x}) + en_{e,0} \left( 1 + \frac{e\Phi_{\text{el}}}{k_B T_e} - 1 \right) \right], \end{aligned} \quad (2.16)$$

where the RHS has been expanded to first order, supposing that the electric potential  $\Phi_{\text{el}}$  drops very quickly. Acknowledging the spherical symmetry of the problem, one can re-write the Laplacian as

$$\nabla^2 \Phi_{\text{el}} = \frac{1}{r^2} \frac{\partial}{\partial r} \left( r^2 \frac{\partial \Phi_{\text{el}}}{\partial r} \right) \equiv \frac{1}{r} \frac{\partial^2}{\partial r^2} (r\Phi_{\text{el}}) \stackrel{!}{=} -\frac{1}{\varepsilon_0} q\delta(r) - \frac{e^2 n_{e,0} \Phi_{\text{el}}}{\varepsilon_0 k_B T_e}. \quad (2.17)$$

This differential equation is solved by the function

$$\Phi_{\text{el}} = \frac{q}{4\pi\varepsilon_0} \frac{e^{-r/\lambda_D}}{r}, \quad (2.18)$$

where the *Debye length*

$$\lambda_D = \sqrt{\frac{\varepsilon_0 k_B T_e}{e^2 n_{e,0}}} \approx 0.24 \mu\text{m} \times \sqrt{\frac{k_B T_e / \text{MeV}}{n_{e,0} / 10^{21} \text{cm}^{-3}}} \quad (2.19)$$

was introduced. Eq. 2.18 holds that any individual charge in a plasma is effectively shielded over the distance  $\lambda_D$ .

### 2.1.2 Single electron acceleration and the ponderomotive force

*The motion of electrons in an intense laser field is described by the relativistic Lorentz force. Due to the magnetic fields, electrons start to oscillate in laser direction, resulting in a characteristic figure-8 motion. The ponderomotive force  $F_p$  leads to a net acceleration along the intensity gradient, whereas the ponderomotive potential  $\Phi_p$  determines the temperature of the electron ensemble.*

The following section shall serve to illustrate how electrons can gain directed momentum from the oscillating transverse electromagnetic laser field. The microscopic interaction of an electron with an em-wave is described by the Lorentz force,

$$\vec{F}_L = e \left( \vec{\mathbb{E}} + \vec{v} \times \vec{\mathbb{B}} \right) = \frac{d\vec{p}}{dt} = \frac{d}{dt} (\gamma m_e \vec{v}), \quad (2.20)$$

where  $\gamma = (1 - \vec{v}^2/c^2)^{-1/2} = \left(1 + \vec{p}^2/(m_e c)^2\right)^{1/2}$  is the relativistic factor and  $\vec{p}$  the electron momentum. For laser intensities exceeding  $I = 10^{18} \text{W/cm}^2$ , the oscillation velocity of the electrons approaches the speed of light, and the  $\vec{\mathbb{B}}$ - term in Eq. 2.20 cannot be neglected anymore. The coupled set of equations of motion 2.20 can be solved using the energy equation

$$\frac{dE_{\text{kin}}}{dt} = m_e c^2 \frac{d\gamma}{dt} = -e \left( \vec{v} \cdot \vec{E} \right). \quad (2.21)$$

With a little calculus [58], and limiting the analysis to one transverse dimension here, one finds for the electron momentum and orbit in the laboratory frame

$$p_x = a_0 (1 - \delta^2)^{\frac{1}{2}} \sin \Phi \quad (2.22)$$

$$x = -a_0 \frac{c}{\omega} (1 - \delta^2)^{\frac{1}{2}} (1 - \cos \phi) = f(a_0) \quad (2.23)$$

$$p_z = \frac{a_0^2}{4} [1 + (2\delta^2 - 1) \cos 2\Phi] \quad (2.24)$$

$$z = \frac{a_0^2 c}{4 \omega} \left( \phi + \frac{2\delta^2 - 1}{2} \sin 2\phi \right) = f(a_0^2), \quad (2.25)$$

where  $x$  is the  $\vec{\mathbb{E}}$ -field axis,  $z$  the propagation axis of the wave, and  $\phi = (\omega t - kz)$  the phase of the wave.  $\delta$  represents the polarization of the laser beam, with  $\delta = 0$  for linear polarization and  $\delta = \pm 1/\sqrt{2}$  for circular polarization. The factor  $a_0$  denotes the *relativistic amplitude*

$$a_0 = \frac{\mathbb{E}e}{\omega m_0 c} \approx \sqrt{\frac{I \lambda^2}{1.37 \times 10^{18} \frac{\text{W}}{\text{cm}^2} \cdot \mu\text{m}^2}}. \quad (2.26)$$

Acknowledging that  $\mathbb{E}e/\omega m_0 = v_{\text{osc}}^{\text{class}}$ , the classical oscillation velocity in the E-field, one can equally write  $a_0 = v_{\text{osc}}^{\text{class}}/c$  to see that  $a_0$  represents a measure for the “relativisticness” of the interaction. The ion acceleration experiments at JETI were typically carried out at  $a_0 \approx 2-5$ .

Note that the  $z$ -term of the electron motion shows two distinct contributions: a *net drift in laser propagation direction*, and a superimposed *2 $\Phi$ -oscillation* (i.e. with twice the laser frequency). The latter gives rise to the well-known relativistic figure-8 motion of the electron in a time-averaged co-moving frame of reference. One also notices that the  $z$ -motion becomes dominant in the ultra-relativistic limit due to the  $a_0^2$ -dependency, which means that for strong laser pulses electrons will be *accelerated mainly in forward direction*, representing a feasible mechanism for the generation of directed electron currents into the target (cf. section 2.1.4).

In a more rigorous treatment of the electron motion, both spatial and temporal dependencies of the laser pulse envelope must be included; the above equations would, strictly speaking, put the electron to rest again once the laser pulse has passed, and will hence be left with a net kinetic energy of zero.

A useful model of the electron acceleration is obtained by introducing the *ponderomotive force*  $F_p$ , which describes the time-averaged net force transferred onto an electron by an inhomogeneous laser field. Assuming for the sake of simplicity a transverse inhomogeneity only, an expression for the (nonrelativistic) ponderomotive force can be obtained by expanding the electric field around the initial electron position  $x_0$  to second order,  $\mathbb{E}(\vec{r}, t) \approx \mathbb{E}_0(x_0) \cos \Phi + \nabla_x \mathbb{E}_0(x)|_{x=x_0} \cdot (x - x_0) \cos \Phi$ . Solving for the first order term and plugging the obtained results back into the expansion, one may average  $\vec{F} = e\mathbb{E}(\vec{r}, t)$  over the rapid oscillations to find [58, 71]

$$\overrightarrow{F_p^{\text{class}}} = -\frac{e^2 \cdot \vec{e}_x}{4m_e \omega^2} \nabla_x (\mathbb{E}_0^2(x)), \quad (2.27)$$

which can be easily generalized to a 3D field amplitude,

$$\overrightarrow{F_p^{\text{class}}} = -\langle e \vec{\mathbb{E}}(\vec{r}, t) \rangle = -\frac{e^2}{4m_e \omega^2} \nabla (\overrightarrow{\mathbb{E}_0^2}(\vec{r})). \quad (2.28)$$

A corresponding *ponderomotive potential* can be introduced,

$$\begin{aligned} \Phi_p^{\text{class}} &= -\int \overrightarrow{F_p^{\text{class}}} d\vec{r} = \frac{e^2}{4m_e \omega^2} \overrightarrow{\mathbb{E}_0^2}(\vec{r}) \\ &= \frac{a_0^2}{4} m_e c^2, \end{aligned} \quad (2.29)$$

as an expression of how much energy an electron can gain due to the ponderomotive force.

The derivation of a relativistic version of the ponderomotive force requires a more sophisticated mathematical treatment [72–74], but eventually arrives at a very similar expression,

$$\overrightarrow{F_p^{\text{rel}}} = -m_e c^2 \nabla \bar{\gamma} = -\frac{e^2}{4m_e \omega^2 \bar{\gamma}} \nabla (\mathbb{E}^2(x)), \quad (2.30)$$

where the time-averaged relativistic factor  $\bar{\gamma} = (1 + p_{\text{slow}}^2/m_e^2 c^2 + a_0^2/2)^{1/2} \approx (1 + a_0^2/2)^{1/2}$  has been inserted, with  $p_{\text{slow}}^2/m_e^2 c^2$  representing the slowly varying envelope component and  $a_0^2/2$  the oscillatory component of the electron momentum, respectively [58]. The correspond-

ing ponderomotive potential now derives as

$$\Phi_{\text{p}}^{\text{rel}} = (\gamma - 1) m_e c^2 = \left( \sqrt{1 + a_0^2} - 1 \right) \times 0.51 \text{ MeV}, \quad (2.31)$$

which corresponds to the relativistic kinetic energy acquired by an electron from the laser field.

The ponderomotive force reveals a characteristic  $\nabla \mathbb{E}^2$ -dependency, implying that *electrons are pushed away from the region of highest intensity*, i.e. the center of the laser pulse. Taking into account the finite diameter of a Gaussian pulse, the restoring forces of the transverse oscillations are less strong outside the pulse center, and the electrons will hence be ejected at a certain angle with respect to the laser propagation axis. This angular emission is known as “ponderomotive scattering.” The ejection angle can be determined according to the simple relation [58]

$$\cos \Theta_{\text{eject}} = \sqrt{\frac{\gamma - 1}{\gamma + 1}}. \quad (2.32)$$

Thus, a Gaussian shaped laser pulse can be imagined as “ploughing” through the plasma, which gives an intuitive account for the conversion from the oscillatory energy of the laser field to directed kinetic energy of the electrons.

It has been argued [75] that for the relativistic regime, the hot electron temperature can be approximated by the ponderomotive potential,

$$k_{\text{B}} T_e \approx \Phi_{\text{p}}^{\text{rel}}, \quad (2.33)$$

which proves to be in excellent agreement with many experiments [14, 57, 76–82]. This identity will become intelligible when discussing ponderomotive heating among the absorption mechanisms in section 2.1.4. At JETI, a laser pulse energy 0.8 J on target (1.3 J before compression) leads to  $a_0 = 4.2$ , which results in a hot electron temperature of  $k_{\text{B}} T_e \approx \Phi_{\text{p}}^{\text{rel}} = 1.7 \text{ MeV}$ . These values will be repeatedly used for subsequent approximations.

### 2.1.3 Optical properties of plasmas

*For light of frequency  $\omega$ , the optical properties of a plasma are solely determined by the plasma frequency  $\omega_{\text{p}}$ , which is a function of the free electron density  $n_e$ . Light may penetrate the plasma only up to the critical density  $n_c$  before being reflected, thus demarcating a region of overdense plasma from an underdense plasma.*

Most fundamental optical properties of plasmas can be obtained from the theory of metals as known for example from the Drude model of conductivity, and standard electromagnetic theory. In the Drude model, the plasma is considered as an electron cloud in front of uniform, positive background of immobile ions, and collisions are neglected. In absence of electron resonances (i.e. for free electrons), the dielectric function of the electron ensemble is given by [83, 84]

$$\varepsilon(\omega) = 1 - \frac{n_e e^2}{\varepsilon_0 m_e \omega^2} = 1 - \frac{\omega_{\text{p}}^2}{\omega^2}, \quad (2.34)$$

where  $\omega_p$  denotes the *plasma frequency*

$$\omega_p^2 = \frac{n_e e^2}{\varepsilon_0 m_e}. \quad (2.35)$$

The corresponding refractive index  $n_r$  of the plasma thus assumes the form

$$n_r(\omega) = \sqrt{\varepsilon(\omega)} = \sqrt{1 - \frac{\omega_p^2}{\omega^2}}. \quad (2.36)$$

Note that for a given laser frequency  $\omega$ , the right hand side of Eq. 2.36 depends on the plasma frequency only, which in turn is but an expression of  $n_e$ . The optical properties of the plasma are hence completely determined by the free electron density. Furthermore, it can be seen that  $\omega_p$  designates threshold where the refractive index changes from a real to an imaginary expression. For  $\omega > \omega_p$ , the refractive index is fully real and em-waves may propagate through the plasma. In this case, one finds the *plasma dispersion relation*

$$\omega^2 = \omega_p^2 + c^2 k^2, \quad (2.37)$$

which is a direct result of the wave equation and  $\varepsilon(\omega) = c^2 k^2 / \omega^2$ . On the other hand, for  $\omega < \omega_p$  the refractive index becomes fully imaginary and plasma does not support the penetration by an em-wave. Note also that the reflectivity of an ideal plasma is 1 at the boundary  $\omega = \omega_p$ , which follows immediately from the Fresnel equations.<sup>2</sup>

Recalling the exponential density profile of an freely expanding isothermal plasma (cf. section 2.1.1), it is instructive to rewrite the index of refraction 2.36 in slightly different manner:

$$n_r = \sqrt{1 - \frac{n_e}{n_c}}. \quad (2.38)$$

Here,  $n_c = \omega^2 \varepsilon_0 m_e / e^2$  is the *critical electron density*, which for a given laser frequency  $\omega$  denotes the point up to which light may penetrate a plasma profile with increasing density before being reflected, thereby distinguishing a region of overdense ( $n_e > n_c$ ) from an underdense ( $n_e < n_c$ ) plasma. For oblique laser incidence at an angle  $\Theta_{\text{in}}$  into an inhomogeneous plasma (like for the JETI ion acceleration experiments), the situation is slightly different: From the conservation of the  $k$ -vector [70] and the Helmholtz equation one obtains

$$\frac{d^2 \mathbb{E}(z)}{dz^2} + \frac{\omega^2}{c^2} (\varepsilon(z) - \sin^2 \Theta_{\text{in}}) \mathbb{E} = 0, \quad (2.39)$$

where reflection can be seen to occur when  $\varepsilon(z) = \sin^2 \Theta_{\text{in}}$ , i.e. at  $n_{e,\text{refl}} = n_c \cos^2 \Theta_{\text{in}} < n_c$  (cf. Eq. 2.38). At oblique incidence, the pulse is therefore reflected *before* reaching the critical density.

By way of example, consider again the above scenario with a pre-plasma consisting of triple ionized titanium and a hot electron population of temperature  $k_B T_e = 150 \text{ eV}$  at a time 30 ps before the main pulse. At the arrival of main pulse, the plasma profile will be of the form  $n_e = 3 \cdot n_{i,0}^{\text{Ti}} \exp\{-x/c_s t\} = 1.70 \times 10^{22} \text{ cm} \cdot \exp\{-x_i/0.94 \mu\text{m}\}$ . The critical density for a

<sup>2</sup>This effect is utilized by so-called plasma mirrors, which play an important role in current ultra-short-pulse laser science [85–88]. See comments in section 5.2.

Ti:Sapphire wavelength of 795 nm is  $n_c = 1.77 \times 10^{21} \text{ cm}^{-3}$ , which means that at normal incidence the pulse will be reflected at a distance  $x(90^\circ) = 2.13 \mu\text{m}$  in front of the target. On the contrary, for laser incidence at an angle of  $45^\circ$ , this distance changes to  $x(45^\circ) = 2.78 \mu\text{m}$ . The distance between the density of reflection and the critical density therefore amounts to  $\Delta s = 0.65 \mu\text{m} \approx 0.8\lambda$ , which will be important when discussing absorption mechanisms in the following. Note that for the current estimation the simplifying assumption of a 1D plasma profile has been made.

#### 2.1.4 A multitude of absorption mechanisms

*Numerous theoretical models have been suggested to account for the high absorption rates observed in laser-plasma interaction. For ultra-short pulses, the predominant mechanisms are collisionless and include resonance absorption, Brunel absorption and  $\vec{j} \times \vec{B}$  heating.*

From the previous sections it is evident that the physics of laser plasma interaction can vary greatly depending on the prior plasma formation and expansion. The main part of the laser pulse may either encounter a very steep density gradient leading to a direct interaction with an almost undisturbed solid target, or an extended region of underdense plasma corona, where the pulse can interact ponderomotively with the free electrons over a long distance, and excite strong plasma waves and instabilities. The difficulties encountered by both theorist and experimentalists when considering this wide range of possible interaction scenarios is nicely captured by P. Gibbon in the following quotation:

“... to make matters worse, the last fifteen years have seen femtosecond-solid experiments escalate across an intensity range of *seven* orders of magnitude. Unsurprisingly then, it is not easy to decide what physics to include and what to omit when constructing theoretical models of such interactions. Coupling the laser energy to the target material posed the first such dilemma, and still remains one of the more hotly disputed issues in the field. This is because more than one physical picture is possible depending on whether the material is treated as a dense conductor, or a ‘sandwich’ of cold solid plus a hot, thin or extended layer of plasma in the region of the laser’s focal spot. To date, there is no single model which can adequately describe all the main pieces of absorption physics, not to mention the numerous other effects - mass and energy transport, nonlinear propagation, fast particle generation, and so on - which can also take place.” [58]

The current section shall review a few major absorption mechanisms that apply to the intensity and pre-plasma conditions at JETI, not claiming to provide an exhaustive treatment of the subject. Contrary to the motion of single electrons in the laser field described above, here the emphasis shall be put on a more macroscopic description of the energy transfer, aiming at the derivation of specific absorption rates for the applied laser energy.

##### (a) Resonance absorption and the anharmonic oscillator model

At intensities above  $10^{16} \text{ W/cm}^2$ , high absorption rates of 50–70% are consistently observed in experiments [58, 78, 79]. Contrary to the early long-pulse (nanosecond) experiments, however, for ultra-short pulses this substantial energy transfer cannot be explained by electron-ion collisions. This is true mainly for two reasons: First, the collision frequency scales as  $k_B T_e^{-3/2}$ , and collisions there become increasingly ineffective for the fast rising electron temperature in short-pulse interactions (eq. 2.46). Secondly, at high intensities, the electron quiver velocity

$v_{\text{osc}}$  may exceed the thermal velocity  $v_{\text{th}}$ , and hence the collective motion outweighs the collisions [58]. Therefore, models for *collisionless absorption processes* had to be developed in order to account for the high absorption rates, most of which make explicit use of the steep plasma gradients applicable to short pulse interaction.

Consider a p-polarized laser pulse entering a steep plasma profile ( $L_p \leq \lambda$ ) at oblique incidence with respect to the density gradient. The electric field vector still has a component in the direction of the gradient, which typically coincides with the target-normal direction. In fact, since a considerable fraction of the incident light is reflected at the critical density, a target-normal standing wave pattern will form at the target front side.

The  $\mathbb{E}$ -field thus causes the electrons to oscillate in target normal direction, which leads to periodic charge density modulations and hence the excitation of an electron plasma wave. The excitation works best when the laser frequency is in resonance with the eigenfrequency of the plasma, i.e. at the critical density  $n_c$  where  $\omega = \omega_p$ , which has coined the name *resonance absorption*. It was noted in section 2.1.3 that under oblique incidence in an inhomogeneous plasma, the pulse is already reflected before it reaches the resonance condition, i.e. at  $n_{e,\text{refl}} < n_c$  (cf. Fig. 2.2); however, for a steep gradient, the electric field may tunnel into the critical density region and excite the plasma resonantly [70, 89–91]. This is well in agreement with the estimation of section 2.1.3, where the distance between  $n_{e,\text{refl}}$  and  $n_c$  was found to be  $< \lambda$ .

Plasma waves are able to transport large amounts of energy, which can be released into the plasma either by collisions or, more importantly for short pulses, by wave-breaking and subsequent electron acceleration along the charge density gradient [70]. In fact, resonance absorption works best when collisions are ineffective, i.e. for high electron temperatures and short plasma scale lengths. Both conditions are fulfilled at JETI. An electron temperature  $k_B T_e \approx \Phi_p^{\text{rel}} = 1.7 \text{ MeV}$  was derived in section 2.1.2, and the distance between  $n_{e,\text{refl}}$  and  $n_c$  estimated to  $0.65 \mu\text{m}$ , i.e. less the laser wavelength.

An expression for the absorbed intensity fraction can be found by determining the size of the decaying electric field at the critical density. Under the simplifying assumption of a linear density profile  $n_e = n_{\text{crit}} z / L_p$ , this yields [70]

$$\eta_{\text{abs}}^{\text{ra}} = \frac{1}{2} \left( 2.3\tau \cdot \exp \left\{ -\frac{2\tau^3}{3} \right\} \right)^2, \quad (2.40)$$

where  $\tau = (kL_p)^{1/3} \sin \Theta_{\text{in}}$ . The term in parentheses is the so-called Ginzberg function. Using again the JETI values, the expected fraction of resonance absorption amounts to  $\eta_{\text{abs}}^{\text{ra}} \approx 15\%$ . Generally, resonance absorption can account for absorption rates well above 50% [89–92]. The lower value at JETI is mostly owed to the comparably large plasma scale length, which does not strictly fulfill  $L_p \ll \lambda$ .

A recent theoretical model by Mulser et al. [93] expanded the scope of resonance absorption to a much broader parameter range. As elaborated above, resonant excitation of a plasma takes place at the critical density  $n_c$  where  $\omega = \omega_p$ . This region is typically reached only by some evanescent fraction of the laser light. Thus, there has been a long-lived debate concerning how efficient this type of energy transfer actually is under real conditions. In a detailed study, Mulser et al. showed that the conditions for resonance absorption are not as rigid as previously assumed, because the for the definition of the resonance frequency as  $\omega_p = (n_e e^2 / \epsilon_0 m_e)^{1/2}$  strictly holds for a harmonic plasma oscillation regime only, i.e. for low

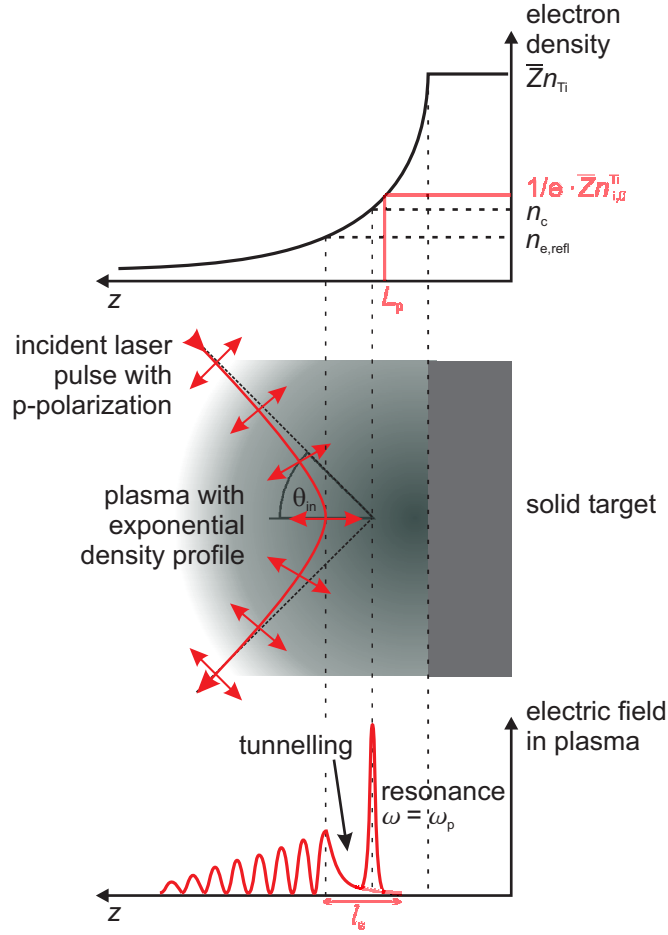


Figure 2.2: Laser reflection in a plasma at oblique incidence and resonance absorption. The optical properties of a plasma are solely determined by the frequency  $\omega$  of the incident em-wave and the free electron density  $n_e$ . In particular, light of frequency  $\omega$  may not propagate into regions “overdense plasma”, where the electron density is larger than the “critical electron density”  $n_c = \omega^2 \epsilon_0 m_e / e^2$ . The critical density thus represents a boundary at which the incident laser pulse is reflected. However, this criterion holds strictly true only for incidence along the plasma density gradient. At oblique incidence, the pulse is reflected already at  $n_{e,\text{refl}} = n_c \cos^2 \Theta_{\text{in}} < n_c$  due to the conservation of the  $\vec{k}$ -vector, and may undergo additional deflection in direction of the plasma gradient according to Fermat’s principle. Together, the incident and reflected pulse contributions form a standing wave pattern in front of the target. For p-polarized laser light at oblique incidence, the electric field possesses a target-normal component, which creates periodic charge density modulations in target-normal direction in the plasma ( $n_e < n_c$ ), leading to the formation of plasma waves. The excitation of such a plasma wave works best if the laser field is in resonance with the eigenfrequency of the electron distribution, i.e. the plasma frequency  $\omega_p = \sqrt{n_e e^2 / \epsilon_0 m_e}$ , which happens exactly at exactly the critical density  $n_c$ . For this “resonant absorption” case, the wave is excited so strongly that it breaks, releasing a large large population of hot electrons into the target. Note that even though an obliquely incident pulse does actually not reach the critical density, resonant excitation may still be aroused because the strong excitation may cause the plasma oscillation to become anharmonic, and photons may also tunnel through the remaining gap.



intensities. For ultra-strong driving fields, however, i.e. for  $I \geq 10^{18} \text{ W/cm}^2$ , the restoring Coulomb force ceases to be a linear function of the electron displacement with respect to the ionic background, and the potential deviates significantly from a harmonic one, leading to lower plasma resonance frequencies  $\omega_p^{\text{anharm}} < \omega_p$ . Therefore, in this *anharmonic oscillator* model, the plasma excitation may jump into resonance well below  $n_c$  and might in fact lie within the region of laser penetration.

### (b) The Brunel mechanism and relativistic $\vec{j} \times \vec{\mathbb{B}}$ heating (ponderomotive heating)

Another absorption mechanism occurring at very steep plasma gradients is the Brunel effect [92, 94–96]. This effect becomes effective when the longitudinal electron oscillation caused by the target-normal electric field component exceeds the plasma density scale length,  $z_{\text{osc}} = e\mathbb{E}/m_e\omega^2 = v_{\text{osc}}^{\text{class}}/\omega \geq L_p$ , which is only roughly fulfilled at JETI ( $z_{\text{osc}} \approx 1.2 L_p$ ). However, it is still worth looking at the Brunel effect, since a very similar argumentation applies to the  $\vec{j} \times \vec{\mathbb{B}}$  mechanism described below. For  $z_{\text{osc}} \geq L_p$ , then, the plasma will be unable to support plasma waves and resonance absorption; however, some electrons may follow the oscillation of the electric field out of the plasma slab into the vacuum, and be efficiently re-accelerated into the slab and beyond the critical density by the second half cycle of the field. Since the laser can only penetrate the overdense region up to the characteristic skin depth  $l_s \approx c/\omega_p \ll z_{\text{osc}}$ , the electrons will be immediately screened from the electric field and thus deposit all of their kinetic energy in the solid via collisions.

An estimation concerning the absorption rate can be made using the standing wave assumption and a simple capacitor model, where the Brunel-accelerated electrons are basically treated as a sheet with a certain surface charge density [97], yielding the implicit expression

$$\eta_{\text{abs}}^{\text{Brunel}} = \frac{f \tan \Theta_{\text{in}}}{\pi a_0} \left[ (1 + f^2 a_0^2 \sin^2 \Theta_{\text{in}})^{\frac{1}{2}} - 1 \right]. \quad (2.41)$$

Here,  $f = 1 + (1 - \eta_0)^{1/2}$  is a correction term accounting for the asymmetry of the standing wave due to the loss of laser energy to the plasma caused by other absorption mechanisms and imperfect reflection, and still depends on  $\eta_0 = (4a_0/\pi) \sin^3 \Theta_{\text{in}} / \cos \Theta_{\text{in}}$ , the Brunel absorption fraction in the uncorrected, non-relativistic case [94]. In the approximation  $a_0 \gg 1$ , one can simplify equation 2.41 to an explicit expression depending on  $\Theta_{\text{in}}$  only,

$$\eta_{\text{abs}}^{\text{Brunel}} = \frac{4\pi \sin \Theta_{\text{in}} \tan \Theta_{\text{in}}}{(\pi + \sin \Theta_{\text{in}} \tan \Theta_{\text{in}})^2}, \quad (2.42)$$

which for  $45^\circ$  gives  $\eta_{\text{abs}}^{\text{Brunel}} \approx 60\%$ . This large value is to be taken with a big grain of salt: As mentioned above, the density gradient is not sufficiently steep to enable efficient Brunel absorption. Furthermore, the Brunel model does actually not take into account *any* finiteness of the density gradient, and also neglects other effects like lateral surface currents [98]. Numerical studies by Gibbon and Bell [97] showed that although the Brunel mechanism may account for up to 70% absorption at intermediate intensities and very short scale lengths,  $\eta_{\text{abs}}^{\text{Brunel}}$  can be assumed to approach a saturation value of rather 10 – 15% for the conditions relevant at JETI.

A process very similar to the Brunel mechanism is the relativistic  $\vec{j} \times \vec{\mathbb{B}}$  heating. Analogously, it relies on the acceleration of displaced electrons from the vacuum into a steep plasma

gradient, whereas in this case the target-normal momentum comes from the magnetic contributions of the Lorentz force 2.20 and the related longitudinal  $2\omega$ -oscillation in  $z$ -direction as discussed in Eq. 2.25, rather than the target-normal  $\mathbb{E}$ -component at oblique laser incidence. Consequently and contrary to the Brunel effect,  $\vec{j} \times \vec{\mathbb{B}}$  heating works best at normal incidence. The impact of this absorption type is negligible compared to Brunel and resonance absorption in the sub-relativistic case  $\vec{\mathbb{E}} = \vec{\mathbb{B}}/c$ , but it becomes comparable to the latter at modestly relativistic intensities, and dominant in the ultra-relativistic limit due to the  $a_0^2$ -dependency of the  $z$ -momentum (cf. Eq. 2.25) [71]. The relativistic amplitudes of  $a_0 = 2 - 5$  at JETI suggest that  $\vec{j} \times \vec{\mathbb{B}}$  heating will occur at the same order of magnitude as Brunel heating. Since the mechanism of energy transfer is basically the same as for the Brunel effect, similar absorption rates can be expected.

Besides the rapidly oscillating field components ( $\mathbb{E}$ -component for Brunel heating,  $\mathbb{B}$ -component for  $\vec{j} \times \vec{\mathbb{B}}$  heating), also the inhomogeneous envelope field of the Gaussian pulse contributes to the acceleration of electrons into the target via the ponderomotive force. This *ponderomotive heating* can be intuitively by the notion of ponderomotive scattering of section 2.1.2, where electrons are ponderomotively pushed into the overdense region. The ponderomotive heating is related to the linear term of the  $z$ -motion of the electron (eq. 2.25), from which the expedient ponderomotive scaling at relativistic intensities [75] discussed in section 2.1.2 can be understood in terms of the increasing relative weight of the  $\vec{j} \times \vec{\mathbb{B}}$  term for  $a_0 \gg 1$ . At ultra-high intensities, ponderomotive heating becomes the sole determinant of the acceleration process, and the hot electron temperature of the electron population can be identified with the ponderomotive potential,  $k_B T_e \approx \Phi_p^{\text{rel}}$ , resulting in the characteristic  $\sqrt{I\lambda^2}$ -dependency for most central acceleration parameters.

### (c) Collisional absorption and the skin effect

The absence of collisions assumed by the previous models is, strictly speaking, not true for any laser-plasma interactions. Generally, collisional absorption processes such as *inverse bremsstrahlung* (i.e. the absorption of a photon by an electron during its collision with an ion or another electron) or *stimulated Raman* and *Brillouin scattering* (i.e. the scattering of photons from plasma waves) can lead to a significant transfer of energy, to plasma heating and eventually damping of the incident em-wave. Although collisional absorption processes play a minor role for ultra-short laser pulses, it is instructive to modify the Drude model to account for collisions, which shall be done in the following.

Collisions are typically introduced to the force equation 2.8 as a damping term  $-\gamma_c n_e v_e$ , containing the collision frequency  $\gamma_c$  related to a damping time constant  $\tau_{\text{damp}}$  as  $\gamma_c = 1/\tau_{\text{damp}}$ . With collisions, the dielectric function 2.34 then acquires the form [83, 84]

$$\varepsilon(\omega) = n^2(\omega) = 1 - \frac{\omega_p^2}{\omega(\omega + 2i\gamma_c)} = \left\{ 1 - \frac{\omega_p^2}{\omega^2 + 4\gamma_c^2} \right\} + i \left\{ \frac{2\gamma_c \omega_p^2/\omega}{\omega^2 + 4\gamma_c^2} \right\} \quad (2.43)$$

with the dispersion relation

$$\omega^2 = \omega_p^2 \left( 1 - i \frac{\gamma_c}{\omega} \right) + c^2 k^2, \quad (2.44)$$

$i$  being the imaginary unit. It can be seen that in case of a small collision rate  $\gamma_c \ll \omega$ ,

equations 2.43 & 2.44 reduce to 2.37 & 2.37. On the other hand, if the number of collisions per wave cycle is large,  $\gamma_c \gg \omega$ , the dielectric function will be increasingly dominated by its imaginary part. The complex refractive index  $n = \sqrt{\varepsilon(\omega)} \equiv n_{\text{Re}} + in_{\text{Im}}$  gives rise to the so-called collisional *skin effect*, where an em-wave can only enter an outer “skin” layer of the plasma up to the depth

$$l_s \approx \frac{c}{\omega_p} \sqrt{1 + i \frac{\gamma_c}{\omega}} \approx \frac{c}{\omega_p} \approx 0.16\lambda \quad (2.45)$$

before it is damped (Fig 2.2). An expression for the collision frequency can be found using sophisticated mathematical analysis based on the Fokker-Planck equation, which for a Maxwellian energy distribution yields [70, 99]

$$\gamma_c \approx [2.91 \times 10^6 \text{ s}^{-1}] \cdot \bar{Z} \ln \Lambda \cdot \frac{n_e/10^{21} \text{ cm}^{-3}}{(\text{k}_B T_e/\text{MeV})^{\frac{3}{2}}}, \quad (2.46)$$

where  $\ln \Lambda = \ln(9N_D/Z)$  is the Coulomb logarithm with  $N_D = 4/3 \cdot \pi \lambda_D^3 n_e$ , the particle number in the Debye sphere. Assuming again a cold pre-plasma with  $\text{k}_B T_e = 150 \text{ eV}$  and  $\bar{Z} = 3$  (cf. section 2.1.1), and taking the electron density to be the critical density  $n_{\text{crit}}$ ,<sup>3</sup> the collision frequency amounts to  $\gamma_c \approx 0.02 \omega$ , which gives a small but non-negligible contribution in the imaginary part of  $n$ . The fraction of absorbed laser energy due to collisions  $\eta_{\text{abs}}^{\text{coll}}$  can be calculated using the Fresnel equations, which for p-polarized light give

$$\eta_{\text{abs}}^{\text{coll}} = 1 - R_p = 1 - \left| \frac{\tan(\Theta_{\text{in}} - \Theta_{\text{trans}})}{\tan(\Theta_{\text{in}} + \Theta_{\text{trans}})} \right|^2. \quad (2.47)$$

Here,  $\Theta_{\text{in}} = 45^\circ$  is the angle of incidence,  $\Theta_{\text{trans}} = \arcsin(\sin \Theta_{\text{in}}/n)$  the generalized complex angle of transmission with  $n$ , the complex index of refraction, following from Eq. 2.43. Plugging in the above values, the absorption rate amounts to  $\eta_{\text{abs}}^{\text{coll}} \approx 14\%$ .

The assumption of Fresnel-like absorption actually presupposes that the density gradient is a step-function and that the surface electron density is large compared to the critical density,  $n_e \gg n_{\text{crit}}$ . The first condition is again only roughly fulfilled at JETI; the second condition holds true, since  $n_e$  decays from three times the titanium ion density  $n_{\text{i},0}^{\text{Ti}} = 0.57 \times 10^{22} \text{ cm}^{-3}$  for triple ionization (cf. section 2.1.1).

A more sophisticated treatment of collisional absorption in inhomogeneous plasmas with finite slope is possible, for example, by solving the Helmholtz equations for the dielectric function 2.43 (see e.g. [58, 71, 100, 101]). An analytic solution can be found for the limit  $L_p \gg \lambda$  using the WKB-approximation. Assuming an exponential density profile with scale length  $L_p$  and laser incidence at  $45^\circ$ , Kruer [70] derives the fraction of collisionally absorbed laser energy to be

$$\eta_{\text{abs}}^{\text{coll}} = 1 - \exp \left\{ -\frac{8\gamma_c L_p}{3c} \cos^3 \Theta_{\text{inc}} \right\}. \quad (2.48)$$

Despite the initial requirement  $L_p \gg \lambda$  for this solution, Gibbon [58] notes that the WKB treatment actually delivers reasonable results down to a scale length of  $L_p \approx 0.1\lambda$ , which holds

<sup>3</sup>According to Kruer [70], this is a reasonable approximation because both the collision rate maximizes and the group velocity minimizes at the critical density.

true for JETI where  $L_p \approx \lambda$ . In comparison to the Fresnel approximation, the Helmholtz-like absorption yields  $\eta_{\text{abs}}^{\text{coll}} \approx 13\%$ , which is in good agreement with the previous result. It shall be mentioned that depending on the scale length and angle of incidence, the absorption can in principle be as high as 60%, which underlines the overall relevance of collisional damping for laser-plasma interactions [58, 100–103]. However, as noted above, collisions become increasingly ineffective for ultra-short pulses, which is why even the derived 14% in this section must be taken as an upper limit, as they most likely overestimate the impact.

Another absorption mechanism describing a situation very much alike like the normal (collisional) skin effect has been identified in [58, 104–106]—the only difference being that the heated electrons in the skin layer do not necessarily dissipate their kinetic energy locally, but may propagate beyond the skin depth. In this *anomalous skin effect* regime, the mean free path between collisions exceeds the skin depth,  $v_{\text{th}}/\gamma_c > l_c$ , where  $v_{\text{th}} = \sqrt{3k_B T_e/m_e}$  is the thermal electron velocity. For a pre-plasma temperature  $k_B T_e = 150$  eV, the thermal electron velocity amounts to  $8.89 \times 10^6$  m/s, so that  $v_{\text{th}}/\gamma_c = 0.19 \mu\text{m} > l_c = 0.13 \mu\text{m}$  is fulfilled at JETI. In this case, the collision frequency  $\gamma_c$  needs to be replaced by an effective frequency  $\nu_{\text{eff}} = v_{\text{th}}/l_a$ , where  $l_a$  is the thickness of the extended skin layer given by  $l_a = (v_{\text{th}} c^2 / \omega \omega_p^2)^{1/3}$  [58]. The corresponding absorption rate of the anomalous skin effect derives as [105, 106]

$$\eta_{\text{ase}} = \frac{8\omega l_a}{3\sqrt{3}c} \approx \left( \frac{k_B T_e}{511 \text{ keV}} \right)^{1/6} \left( \frac{n_c}{n_e} \right)^{1/3}, \quad (2.49)$$

where  $l_a$  is the effective extended skin depth, defined as  $l_a = (2/\pi)^{1/6} (c^2 v_{\text{th}} / \omega_p^2 \omega)^{1/3}$ . Plugging in the above values, and assuming again triple ionization and a step-like solid surface ( $n_e \approx 3 \cdot n_{i,0}^{\text{Ti}} = 3 \cdot 0.57 \times 10^{22} \text{ cm}^{-3} \approx 9.6 n_c$ ), the conversion efficiency amounts to 12%.

In summary, it is a virtually impossible undertaking to identify a singular mechanism responsible for the heating of the plasma. The conditions at JETI ( $L_p \approx \lambda$ ) represent a kind of intermediate regime, for which many approximations do not strictly hold true, but cannot be conclusively rejected, either. This fact is witnessed by the magnitude of the derived absorption rates, most of which lie in the 10 – 15% range, indicating that laser-driven plasma heating at JETI is really an blurred overlap of many simultaneous and partly related physical processes (arguably with a slight bias towards ponderomotive heating). The following section shall go on to present how such a heated electron population can be used to pursue ion acceleration from a thin foil target.

## 2.2 Target Normal Sheath Acceleration (TNSA)

### 2.2.1 The physical picture

*TNSA is a potent ion acceleration mechanism based on charge separation effects between a sheath of hot plasma electrons expelled at the target rear side, and the positively charged foil target.*

In the previous sections it was shown how laser acceleration of electrons can be achieved at solid targets. This electron acceleration essentially relied on strong-field ionization, the relativistic Lorentz force and damping of the laser field in overdense plasmas. The task is now to re-convert the laser energy deposited in the hot electron population into kinetic energy of ions in order provide the means for a feasible laser ion accelerator.

This re-conversion can be realized best with the help of thin foil targets. Consider a strong laser pulse impinging on the front surface of a thin metal foil such that plasma formation

and electron acceleration into the foil occur in the above-described manner. Now, if the foil is sufficiently thin, the electrons will traverse it and be expelled at the rear side, leaving behind a positively charged target. The restoring Coulomb force will counteract the charge separation, and the main part of the hot electron population gets trapped in a plasma sheath at the target rear side. In this sheath, the free electrons distribute around the positive surface similar to a screened Coulomb potential (cf. section 2.1.1), which has given rise to the name “Debye sheath”.<sup>4</sup>

The resulting electric fields between the Debye sheath and the target surface are of the order of several  $10^{12}$  V/m, which suffices to field-ionize the foil material as well as contaminants present on the target surface.<sup>5</sup> The thus generated ions are immediately accelerated in the sheath field, whereas the ions with the highest charge to mass  $q/m$ -ratio (typically protons) are favoured for acceleration. Driven by the self-similar fields between the ions and the electrons, the electron-ion plasma starts to expand into the vacuum. Since the electric field vectors at the initially solid target surface, this process has become widely known as *Target Normal Sheath Acceleration (TNSA)* [42, 60]. TNSA has proven to be a potent scheme for the production multi-MeV proton and ion beams from laser plasmas at a large number of laser systems [5, 7, 27, 44, 108].

## 2.2.2 Theoretical models and scaling laws for thermal proton spectra

*Several central properties of laser proton acceleration, including the proton cutoff energy and spectrum, can be derived from the Mora 1D fluid model. A critical parameter is the initial electron density  $n_{e,0}$  obtained from assumptions about laser-electron conversion efficiency. The model by Schreiber highlights the interrelation between proton energy and laser pulse duration. For Petawatt lasers, the acceleration mechanisms are expected to change, giving way to the “piston” or “radiation pressure dominated” regime. All models fall short of incorporating multi-dimensional effects or multiple ion species.*

### The Mora model

The most simple analytical approach for TNSA acceleration is a 1D self-similar model proposed by Gurevich et al. [109], which has been widely modified and extended over time, most notably by Mora [110]. For the sake of simplicity, this model shall be henceforth be referred to as the “Mora model.” The Mora model starts out from a collisionless plasma consisting of electrons and a single ion species, whereas the ions occupy the half-space  $z < 0$  with a constant density  $n_{i,0}$  at the time  $t = 0$  (Fig. 2.3). The hot electrons follow a Boltzmann distribution 2.15. The electric potential generated by the charge separation is given by Poisson’s equation

$$\nabla^2 \Phi_{\text{el}} = \frac{1}{\varepsilon_0} e (n_e - Z n_i), \quad (2.50)$$

where  $Z$  is the ion charge state, and  $n_e$  and  $n_i$  are the local electron and ion densities, respectively. The ion density  $n_i$  initially follows a step function with  $n_i = n_{i,0}$  for  $z \leq 0$ , and  $n_i = 0$  for  $z > 0$ , implying charge neutrality for  $z \rightarrow -\infty$ . An expression for the initial electric

<sup>4</sup>This intuitive picture neglects, among other things, the effect of electron re-circulation, i.e. the fact that Coulomb-trapped electrons may turn around and traverse the foil in opposite direction [107]. The notion of a sheath should therefore be rather understood as a quasi-static approximation.

<sup>5</sup>In comparison, the threshold for field ionization of hydrogen is  $\mathbb{E}_{\text{ion}}(H) = 3 \times 10^{10}$  V/m.

field can be obtained by integrating Eq. 2.50 over the half-space  $z \geq 0$ , which gives

$$\mathbb{E}_{x=0} = \sqrt{\frac{2}{\tilde{e}}}\mathbb{E}_0, \quad (2.51)$$

where  $\tilde{e}$  is Euler's number and  $\mathbb{E}_0 = \sqrt{n_{e,0}k_B T_e/\varepsilon_0}$ . For a hot electron temperature of  $k_B T_e = 1.7 \text{ MeV}$  and an electron density of  $n_e = 2.0 \times 10^{20} \text{ cm}^{-3}$  (cf. below for an estimation) one finds an initial field of  $\mathbb{E}_{x=0} = 6.7 \times 10^{12} \text{ V/m}$ .

The expansion of the ions is described by the fluid dynamic equations as introduced in section 2.7, obeying the same continuity and force equations 2.7 & 2.8

$$\frac{\partial n_i}{\partial t} + \frac{\partial}{\partial z}(n_i v_i) = 0 \quad (2.52)$$

$$\left(\frac{\partial v_i}{\partial t} + v_i \frac{\partial v_i}{\partial z}\right) = \frac{Ze}{m_i} \nabla \Phi_{\text{el}}. \quad (2.53)$$

Analogously, the equations are solved by the self-similar solutions

$$n_e(z, t) = Zn_i = n_{e,0} \exp\left\{-\frac{z}{c_s t} - 1\right\}, \quad (2.54)$$

$$v_i(z, t) = c_s + \frac{z}{t}, \quad (2.55)$$

$$\mathbb{E}_{\text{ss}}(z, t) = \frac{k_B T_e}{ec_s t} = \frac{\mathbb{E}_0}{\omega_{p,i} t}, \quad (2.56)$$

where  $\mathbb{E}_{\text{ss}}$  represents the self-similar field solution,  $c_s = (Zk_B T_e/m_i)^{1/2}$  is the well-known ion sound speed, and  $\omega_{p,i} = (Zn_{e,0}e^2/\varepsilon_0 m_i)^{1/2}$  is the ion plasma frequency. It can be seen that for  $\omega_{p,i} t \rightarrow 0$  the electric field exceeds the initial field, which means that the self-similar solutions are invalid for times  $t < 1/\omega_{p,i}$ . In order to account for a finite expansion of the ion front and a finite ion energy, the plasma density scale length  $L_p = c_s t$  is identified with the local Debye length of co-expanding electron distribution  $\tilde{\lambda}_D = (\varepsilon_0 k_B T_e / e^2 n_e)^{1/2} = \lambda_D \sqrt{n_{e,0}/n_e}$  (cf. Fig. 2.3), which proves to be an experimentally sustainable assumption. Integration of Eq. 2.56 then gives the electric field at the ion front for large  $\omega_{p,i} t$ ,  $\mathbb{E}_{\text{front}} = 2\mathbb{E}_{\text{ss}} = 2\mathbb{E}_0/\omega_{p,i} t$ . Finally, a physically adequate interpolation between the two limits  $\sqrt{2/\tilde{e}}\mathbb{E}_0$  and  $2\mathbb{E}_0/\omega_{p,i} t$  can be found by

$$\mathbb{E}_{\text{front}} = \frac{2\mathbb{E}_0}{\sqrt{2\tilde{e} + \omega_{p,i}^2 t^2}}, \quad (2.57)$$

which proves to be in good agreement with numerical simulations for all times.

With this knowledge about the accelerating field at the ion front, one can derive an expression for the kinetic ion energy in the asymptotic limit by integrating the ion acceleration in this field over time,

$$E_{\text{max}} = \frac{m_i}{2} \left[ \int_0^\infty dt \frac{Ze\mathbb{E}_{\text{front}}}{m_i} \right]^2 = 2Zk_B T_e \ln^2 \left\{ \tau + \sqrt{\tau^2 + 1} \right\}. \quad (2.58)$$

Here,  $\tau = \omega_{p,i} t / \sqrt{2\tilde{e}}$  represents a normalized acceleration time of ions in the Debye sheath.

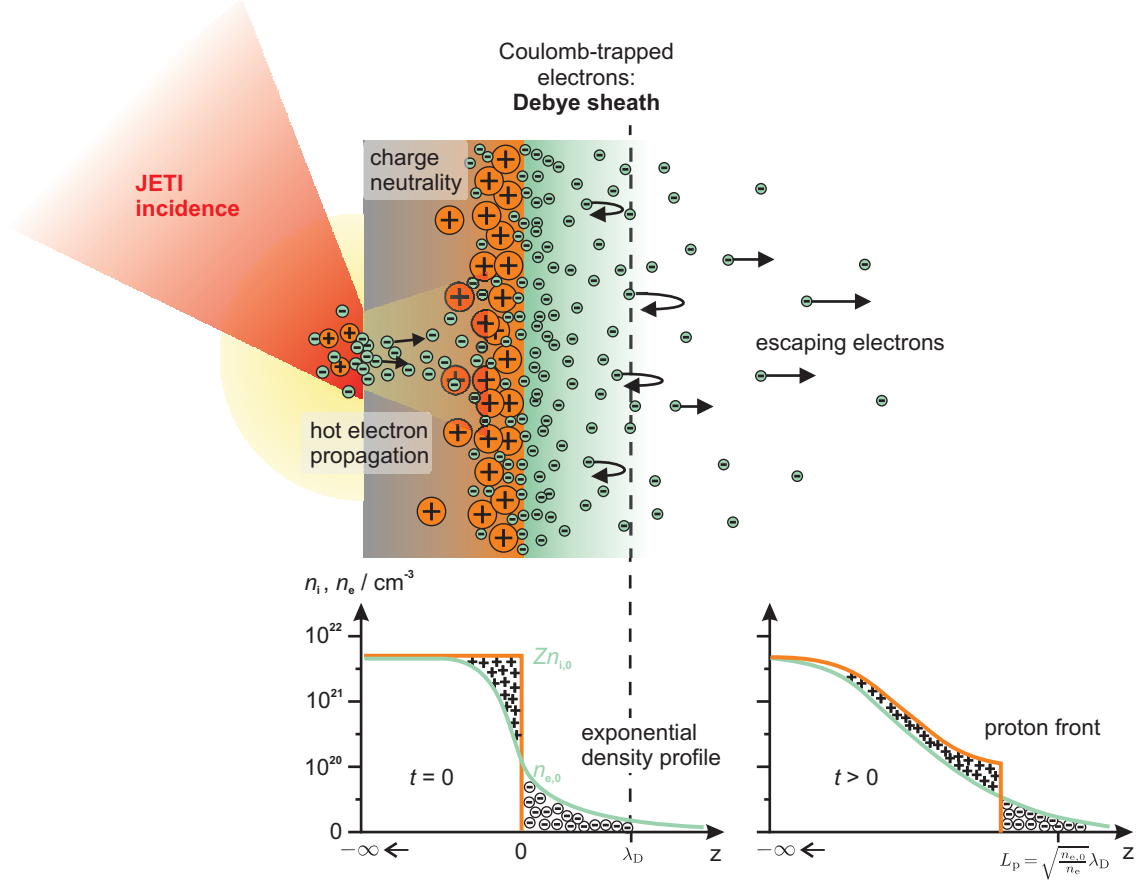


Figure 2.3: The Mora 1D fluid model. The model by Mora [110] describes the plasma expansion into vacuum using standard fluid dynamic methods as for example presented in [71]. From a number of simplifying assumptions, various properties of the accelerated proton population can be derived, including the position and velocity of the proton front, as well as the (thermal) proton spectrum. The two bottom graphs show how for two times the hot like electron distribution extends beyond the proton front and into the vacuum with a scale length related to the Debye length  $\lambda_D$ , where the electrons are trapped by the restoring Coulomb force and create an electron sheath. The proton front can be seen to expand from the initially occupied half-space  $z < 0$  in positive  $z$ -direction to a smoother distribution, but is still assumed to terminate at a sharp proton front. Note that although the laser incidence is displayed in a 2D fashion for the sake of visualization, the Mora model describes a 1D expansion only.

Extensive studies by Fuchs et al. [7, 111] showed that best accordance with experimental data is obtained if  $t = \alpha(\tau_{\text{laser}} + \tau_{\text{min}})$  is assumed for the duration of the acceleration process. Here,  $\alpha$  is an intensity-dependent factor obtaining the value 1.3 in the present case, and  $\tau_{\text{min}} = 60$  fs, resulting in  $t = 182$  fs  $\approx 2.3 \cdot \tau_{\text{laser}}$  and  $\tau = 1.44$ . The Mora model also provides an expression for the expected ion spectrum,

$$\frac{dN(E)}{dE} = \frac{n_{i,0}t}{\sqrt{m_i}} \cdot \frac{\exp\left\{-\sqrt{\frac{2E}{Zk_B T_e}}\right\}}{\sqrt{2E}}. \quad (2.59)$$

In order to make use of Eqs. 2.58 & 2.59, an estimation of the initial electron density  $n_{e,0}$  of the Debye sheath is required. Note that  $n_{e,0}$  is implicitly contained in the ion plasma frequency  $\omega_{p,i}$  via  $n_i = Zn_e$ . In accordance with the absorption laws discussed above, it is generally assumed that one can determine a certain conversion efficiency  $\eta_e$  between laser energy  $E_{\text{laser}}$  and the number of hot electrons  $N_e$  with the average temperature  $k_B T_e$ ,

$$\eta_e E_{\text{laser}} = N_e k_B T_e. \quad (2.60)$$

The electron density then corresponds to the number of electrons per sheath volume,  $n_{e,0} = N_e/V_{\text{sheath}}$ , which is taken to be roughly  $V_{\text{sheath}} = c\tau_{\text{laser}} \cdot A_{\text{emission}}$ , where  $A_{\text{emission}}$  is the area of electron emission on the target rear surface. This area can be estimated by assuming that the electrons propagate through the foil with a certain opening angle  $\theta_{\text{prop}}$ , so that

$$A_{\text{emission}} = \pi R_{\perp}^2 = \pi (\omega_0 + d \tan \theta_{\text{prop}})^2, \quad (2.61)$$

where  $R_{\perp}$  is the radius of the electron emission spot,  $\omega_0$  the beam waist of the laser focus, and  $d$  the target thickness. Thus, the initial electron density becomes [44]

$$n_{e,0} = \frac{\eta_e E_{\text{laser}}}{k_B T_e c \tau_{\text{laser}} \cdot \pi R_{\perp}^2}. \quad (2.62)$$

It can be seen that the predicted cutoff energies depend critically on the somewhat phenomenological parameters  $\eta_e$  and  $\theta_{\text{prop}}$ , i.e. the conversion efficiency and the propagation angle through the foil. Concerning the conversion efficiency, references are rare and vary greatly in their conclusions, from 14% for 0.25 J/130 fs pulses [112], to 20..30% for 15..20 J/450 fs pulses [113] and 40..50% for 200..500 J/500 fs pulses [42]. An intensity scaling  $\eta_e = 1.2 \times 10^{-15} I^{0.74} / \text{Wcm}^{-2}$  has been proposed in [7, 114], which seems, however, to overestimate the situation at JETI with a resulting 36%—a value more likely to be found at multi-10 J laser systems. A similar uncertainty applies to the electron angle of propagation. While good agreement with experiments has previously been found for  $\theta_{\text{prop}} = (8 \pm 2)^\circ$  at a laser system comparable to JETI [44], a number of measurements [115–117] and PIC simulations [118, 119] suggest that the transverse extent of the electron sheath should be rather of the order of 10–20  $\mu\text{m}$  and follow an opening angle of  $\theta_{\text{prop}} \geq 30^\circ$  for a 5  $\mu\text{m}$  target. In addition, electron recirculation may increase the transverse extent of the sheath even further [107]. This large degree of uncertainty is due to the rather crude estimation of the hot electron density via the sheath volume  $c\tau_{\text{laser}} \cdot A_{\text{emission}}$ . In absence of a better definition, this work will stick to it for the time being, emphasizing, however, the limitations of this approximation. Assuming thus a moderate  $\eta_e = 20\%$  and  $\theta_{\text{prop}} = 45^\circ$  at JETI, one arrives at a rear side density of  $n_{e,0} = 2.0 \times 10^{20} \text{ cm}^{-3}$ , which in turn yields (Eq. 2.58) a theoretical cutoff energy of 3.6 MeV. This value is in good agreement with the maximum energies observed at JETI.

The 1D self-similar fluid model has proven fairly accurate in the prediction of particle energies observed in many laser ion acceleration experiments, including the maximum proton energy achieved at JETI. However, a few critical remarks concerning the predictive and explanatory power of the model shall be added. First of all, one may notice that both the cutoff energy  $E_{\text{max}}$  and the spectrum  $dN(E)/dE$  diverge for large acceleration times  $t$ , which is usually been taken care of by introducing a finite acceleration time (as done by Fuchs et al. [7]). Although this is not an implausible assumption, the acceleration time obviously entails an additional degree of freedom in the fitting of the experimental data.



Secondly, several underlying assumptions of the Mora model can be challenged. For example, although the solutions 2.54-2.56 are thought to be good representations of the late states  $\omega_{p,i}t \gg 1$ , PIC simulations indicate that at least at very early times the assumption of global charge neutrality must be given up for an adequate description. Also, the assertion of a constant electron temperature over the whole acceleration process is unrealistic, given the temporal profile of the laser pulse and the intrinsic dynamics of the expanding front side plasma. Several attempts for a more better approximation have been made, including a two-phase temperature model of a linear rise followed by an adiabatic cooling [120]. Even then, however, the model does not seem to account for the ultra-high intensity regime [8], and further amendments concerning possible 3D effects have been suggested. A more accurate description can also be expected from the inclusion of two electron populations with different temperatures, which has been extensively treated in [118, 121, 122]. Finally, real TNSA scenarios typically include more than one ion species to be accelerated from the target back side. This will be of particular importance when talking about the generation of monoenergetic proton beams in the next chapter.

### The Schreiber model

An alternative analytic model for the prediction of the maximum ion energies has been proposed by Schreiber et al. [123], which circumvents both the dependency on the electron temperature and the divergence problems. Similarly, the model starts out from an electron bunch of dimension  $c\tau_{\text{laser}} \cdot A_{\text{source}}$  at the target rear side with exponential energy distribution, which induces a surface charge with the potential

$$\Phi_{\text{el}}(\xi) = \frac{1}{e} E_{\infty} s(\xi), \quad (2.63)$$

where  $\xi = z/R_{\perp}$ ,  $E_{\infty} = Qe/(2\pi\epsilon_0 R_{\perp})$  is the minimum escape energy for electrons to leave the rear surface potential, and  $s(\xi) = 1 + \xi - (1 + \xi^2)^{1/2}$ . For electrons with the mean kinetic energy  $k_{\text{B}}T_e$ , the return point  $z_{\text{ret}} = \xi_{\text{ret}} \cdot R_{\perp}$  is naturally given by the Debye length  $\lambda_{\text{D}}$ , which brings about that  $Q = 2N_e \cdot \lambda_{\text{D}}/c\tau_{\text{laser}}$  electrons are permanently outside the foil.  $N_e$  is again the total number of accelerated electrons given by 2.60, where similar difficulties concerning the determination of the conversion efficiency  $\eta_e$  are encountered. From these assumptions, Schreiber et al. [123] derive expressions for the electric field,

$$\mathbb{E}(\xi) = \frac{k_{\text{B}}T_e}{e\lambda_{\text{D}}} \left( 1 - \frac{\xi}{\sqrt{1 + \xi^2}} \right) \quad (2.64)$$

and the energy gain of surface ions within this field assuming an infinite acceleration time,

$$E_{i,\infty} = 2Zm_e c^2 \sqrt{\frac{\eta_e P_{\text{laser}}}{0.87 \times 10^{10} \text{ W}}}, \quad (2.65)$$

$P_{\text{laser}}$  being the laser power. Note that Eq. 2.65 does not depend on the hot electron temperature anymore, and also shows a characteristic  $\sqrt{P_{\text{laser}}}$ -dependency. However, the assumption of an infinite acceleration time seems to overestimate the expected particle energies; for example, using the JETI values from above ( $\eta_e = 20\%$ ,  $P_{\text{laser}} \approx 10 \text{ TW}$ ), one obtains an energy of  $E_{i,\infty} = 15.2 \text{ MeV}$ , which suggests to include a finite acceleration bound to the laser pulse

duration  $\tau_{\text{laser}}$ . The authors proceed by integrating the equation of motion over time [123] and finally arrive at an implicit expression for the interrelation between the (normalized) laser pulse duration and the (normalized) maximum ion energy

$$\frac{\tau_{\text{laser}}}{\tau_0} = \sqrt{\frac{E_{\text{max}}}{E_{i,\infty}}} \left( 1 + \frac{1}{2} \frac{1}{1 - \frac{E_{\text{max}}}{E_{i,\infty}}} \right) + \frac{1}{4} \ln \left\{ \frac{1 + \sqrt{\frac{E_{\text{max}}}{E_{i,\infty}}}}{1 - \sqrt{\frac{E_{\text{max}}}{E_{i,\infty}}}} \right\}, \quad (2.66)$$

where  $\tau_0 = R_{\perp} / \sqrt{2E_{i,\infty}s(\infty)/m_i}$ . Importantly, this expression emphasizes the interplay between the laser energy and pulse duration, holding that for laser ion acceleration it is generally not desirable to use the shortest possible pulses, since the power increase is eventually outweighed by the loss in acceleration time. According to the model, it would thus be unreasonable to build, for example, an ion accelerator-based of a Petawatt laser with less than 100 fs pulse duration. The prediction of an optimum pulse duration for a given laser power is a strong advantage of this model, and is in good agreement with numerous experiments carried out at different laser systems. For the JETI pulse duration of 80 fs, the Eq. 2.66 projects a cutoff energy of  $E_{\text{max}} \approx 1.8$  MeV, which amounts to about 50% of the actually observed energies.

### Petawatt scalings

Besides the high-energy amendments to the Mora model discussed above [8], a number of PIC simulation studies exist to explore proton energy scalings for future laser generations. It is commonly agreed on that for intensities exceeding  $\approx 5 \times 10^{21}$  W/cm<sup>2</sup>, other acceleration mechanisms than TNSA will play an important role. D’Humieres et al. [124] point out that in the Petawatt regime the quasi-static field acceleration is supported by a shock wave from the target bulk, which may outmatch the conventional TNSA mechanism. Prominent works by Esirkepov et al. [125, 126] discuss ion acceleration in the “radiation pressure dominated” or “laser piston” regime as a very efficient way to accelerate ions at high intensities. In this regime, the acceleration process has been shown to depend on the so-called “electron areal density” parameter  $\sigma = n_e d$ , which attains an optimum for  $\sigma^{\text{opt}} \approx \left( 3 + 0.4 \sqrt{0.73 \cdot I \lambda^2 / 10^{18} \text{ W cm}^{-2} \cdot \mu\text{m}^2} \right) n_c \lambda$ . If the interaction takes place at this optimum, PIC simulations predict the maximum proton energy to scale as

$$E_{\text{max}} = 228 \text{ MeV} \times \eta_e Z \sqrt{\frac{P_{\text{laser}}}{\text{PW}}}, \quad (2.67)$$

which has been the outset for fruitful debates about the potential of Petawatt lasers for sophisticated accelerator applications. Note that this result displays the same characteristic  $P_{\text{laser}}^{1/2}$ -dependency as the theoretical model by Schreiber et al. [123] and the empirical scaling laws for high intensities found by Robson et al. [8].

Recently, a few theoretical works also discussed the use of circularly polarized laser light for ion acceleration [127–130]. Especially in combination with the radiation pressure regime, circular polarization is thought to enable direct acceleration of whole bunches of ions from the foil bulk. In this case, the ponderomotive pressure is not dominated by the longitudinal  $2\omega$ -oscillation anymore, such that hot electron production and sheath field acceleration are largely suppressed. The ponderomotive pressure thus varies only slowly (with the envelope function of the pulse) and allows for a quasi-static, “cold” uniform acceleration of the bulk

ions, promising GeV ion beams with an intrinsically narrow energy distribution. A detailed discussion of the matter is, however, beyond the scope of this work.

### 2.2.3 Dependencies on target and laser pre-pulse conditions

*TNSA-produced ion beams show a strong dependency on several laser and target parameters, resulting for example in an optimum target thickness for every target material, and an optimum ASE duration for every target thickness.*

As of today, TNSA has been employed at many lasers around the world to produce energetic ion beams from wide range of target materials, for example metals [41, 42, 131–133], insulators and plastics [41, 42, 134, 135], low density foams [136, 137], droplets [138, 139], clusters [140] and gaseous target [141]. This overall robustness of the TNSA mechanism should, however, not obscure the fact that the properties of the TNSA-produced ion beams show a strong dependency on experimental boundary conditions.

The choice of the target material has a significant impact on several aspects of the acceleration process. In a first and trivial sense, the foil material represents the ion reservoir for the particles to be accelerated. At the same time, the foil also represents the reservoir of electrons required for the acceleration process, which varies according to the ionization properties of the material and determines plasma formation and heating. The electron number and temperature dictates the current density through the target, which is limited by the finite resistivity of the material and return currents, efficiently inhibiting the electron flux due to the induction of strong electric fields [58, 142–145]. The remaining electron current density gives rise to the widely-acclaimed, gigantic azimuthal magnetic fields, which have a significant impact on the collimation of the electron beam [20, 21, 119, 136, 146]. This becomes particularly important when considering the issue of filamentation: Depending on the target material, the relativistic electron beam may split up into several filaments (e.g. via the Weibel instability) [147, 148], which may, however, reunite due to mutual magnetic attraction [119, 149, 150].

High- $Z$  materials also provide a higher cross section for Coulomb interaction and hence facilitate electron stopping and the creation of bremsstrahlung [14, 76, 151]. Finally, one must take into account mechanical properties such as the expansion of laser-induced shock waves, which may deform the target surface and thus affect the ion emission [152, 153]. Mechanical properties also play a practical role when considering target handling. These very different processes result in the existence of an *optimum target thickness for ion acceleration* at any given material, which has been the subject of many experimental studies [6, 44, 107, 154].<sup>6</sup>

In sections 2.1.1 and 2.1.4 it has been elaborated that the plasma formation and coupling of the laser field into the plasma depends strongly on ASE pedestals and pre-pulses, which may, in the worst case, lead to a complete evaporation of the target before the arrival of the main pulse [156]. Studies by Kaluza et al. [44, 157] demonstrated that the length of the ASE pedestal (varied on a nanosecond scale) has a direct impact on the observed ion spectra. It was concluded that ASE may initiate shock waves and radiative heating in the target, which can inhibit rear side acceleration altogether. Furthermore, it was found that for every target thickness there exists an optimum ASE duration, which does typically not coincide with the shortest possible value. Other studies have investigated the effect of pre-formed plasmas on the target front and rear side with the help of additional laser pulses, which can enhance

<sup>6</sup>It shall be mentioned that the choice of the target material and thickness has a necessary impact on the observation of proton contributions from the target front side [133, 155].

or suppress ion emission, and even give rise to strong modulations in the spectra [158–160]. In particular for advanced acceleration schemes (including the “piston” and the “radiation pressure dominated” regime mentioned above, as well as the use of ultra-thin targets), a steep plasma gradient at the front side is of crucial importance.

## 2.3 Concerning the spectral shaping of laser-generated proton beams (Confined TNSA)

### 2.3.1 Thermal spectra

*TNSA produces ion beams with quasi-thermal energy distribution. The broad spectra can be explained by the transverse inhomogeneity of the accelerating field across the proton source in combination with screening effects.*

In the previous section, TNSA has been established as a robust means to generate MeV ion beams from relativistic laser-plasma interactions. However, the TNSA mechanism as discussed above is capable of producing broad, quasi-thermal ion spectra only, which are not suitable for most applications. The broad energy distribution of TNSA beams is mostly due to two distinct effects, a radial field inhomogeneity in the electron sheath and a longitudinal field inhomogeneity due to screening effects.

First, since the accelerating TNSA field is inhomogeneous in the radial direction, the maximum energy an ion can reach is determined by its radial transverse position  $\rho$  with respect to the laser incidence [30]. Protons located in the center of the TNSA field are accelerated the most, up to the maximum energy  $E_{\text{cutoff}}$ , whereas protons outside the center experience a lower electric field strength and are consequently accelerated to lower energies  $E_{\text{max}}(\rho)$ . The inhomogeneous shape of the TNSA field has been measured with different probing techniques, including proton deflectometry [161] and all-optical transverse probing [117]. These measurements revealed a bell-shaped symmetry of the sheath fields, which is well supported by PIC simulations, and is also in agreement with measurements of the beam divergence demonstrating that the ion emission takes place within symmetrical cones of energy-dependent radius [5, 17, 44] (see also section 3.1).

The second major contribution to the broad spectrum are screening effects: As the electric field decays when reaching into regions of higher particle density, deeper sited protons in the source layer will be partially screened from the field by their faster predecessors. This implies that for every radial position  $\rho$ , all particle energies up to a maximum of  $E_{\text{max}}(\rho)$  are emitted. In particular, the full spectral range up to  $E_{\text{cutoff}}$  can be observed from the sheath center.

The transverse inhomogeneity and the screening effects bring about that the resulting spectrum has a strong correlation to the initial distribution of the leading ion species on the target.<sup>7</sup>

In this chapter, a modified version of TNSA shall be presented which allows to utilize the TNSA principle for the generation of monoenergetic ion beams. This “Confined TNSA” scheme is based on an advanced understanding of the acceleration processes at the target rear side,

---

<sup>7</sup>Strictly speaking, a third mechanism responsible for the broad ion spectrum can be identified, which is, however, less important for the following discussion. The acceleration process generally also follows some intrinsic dynamics, which are correlated e.g. to the temporal profile of the incident laser pulse and the cooling of the electron population. Numerical simulations show that the TNSA field actually takes some time to build up to its maximum field strength (see e.g. [162]) so that the ion source is affected by different field strengths throughout the whole interaction.

including the effects charge separation and the ion source geometry. This refined concept will eventually lead to the construction manual of micro-structured targets as a tool to generate monoenergetic ions from TNSA interaction.

### 2.3.2 Confinement of the proton source - the Esirkepov/Bulanov model

*A spatially confined interaction geometry was proposed for the generation of narrow-band proton beams, where all protons are initially located in the central homogeneous part of the TNSA field. If the proton source layer is thin and screening effects can be neglected, all protons are uniformly accelerated to the same energy.*

In agreement with the above reasoning, in 2002 Esirkepov et al. [30, 61] proposed an acceleration scheme with an advanced target geometry for the generation of monoenergetic proton beams. In this scheme, all protons are confined to a "dot" source located on a heavy ion carrier substrate (Fig. 2.4). The dot source is limited in transverse direction to the central field region of the TNSA field, and in longitudinal direction to a few nanometers thickness, sufficiently thin to avoid screening effects (see section 2.3.3 for an actual estimation of the penetration depth of the electric field). All protons hence experience the same potential and are accelerated to a monoenergetic distribution. In the next section (2.3.3) it will be shown that the limitation of the source layer thickness is actually not imperative: the longitudinal inhomogeneity of the electric field due to screening can be outweighed by charge separation effects, and the experimental restrictions on the source confinement are thus lessened significantly. However, before moving on to this more complex physical picture, it is instructive to review the purely geometrical acceleration scheme proposed by Esirkepov et al.

In their work, Esirkepov et al. [30, 61] provide an analytical model for the calculation of the resulting energy spectrum depending on the source geometry. The model sets out from an estimation of the field magnitude on the back of the positively charged target, using the average charge density  $\overline{Z}en_i$  of an ionized target slab:

$$\nabla \mathbb{E}_0 = \frac{1}{\varepsilon_0} \overline{Z}en_i. \quad (2.68)$$

Integration over the homogeneous slab gives

$$\mathbb{E}_0 = \frac{1}{\varepsilon_0} \overline{Z}en_i d, \quad (2.69)$$

where  $d$  is the target thickness. The electric field configuration is assumed to match a charged oblate ellipsoid of revolution, with its major semi-axis equal to the sheath radius  $\widehat{R}_\perp$  and the minor semi-axis given by  $d$ . The corresponding longitudinal and transverse field components can be found in [163]

$$\mathbb{E}_z = \frac{2}{3} \mathbb{E}_0 \widehat{R}_\perp^2 \frac{1}{R_\xi} \frac{\partial \xi}{\partial z} \quad (2.70)$$

$$\mathbb{E}_\rho = \frac{2}{3} \mathbb{E}_0 \widehat{R}_\perp^2 \frac{1}{R_\xi} \frac{\partial \xi}{\partial \rho}, \quad (2.71)$$

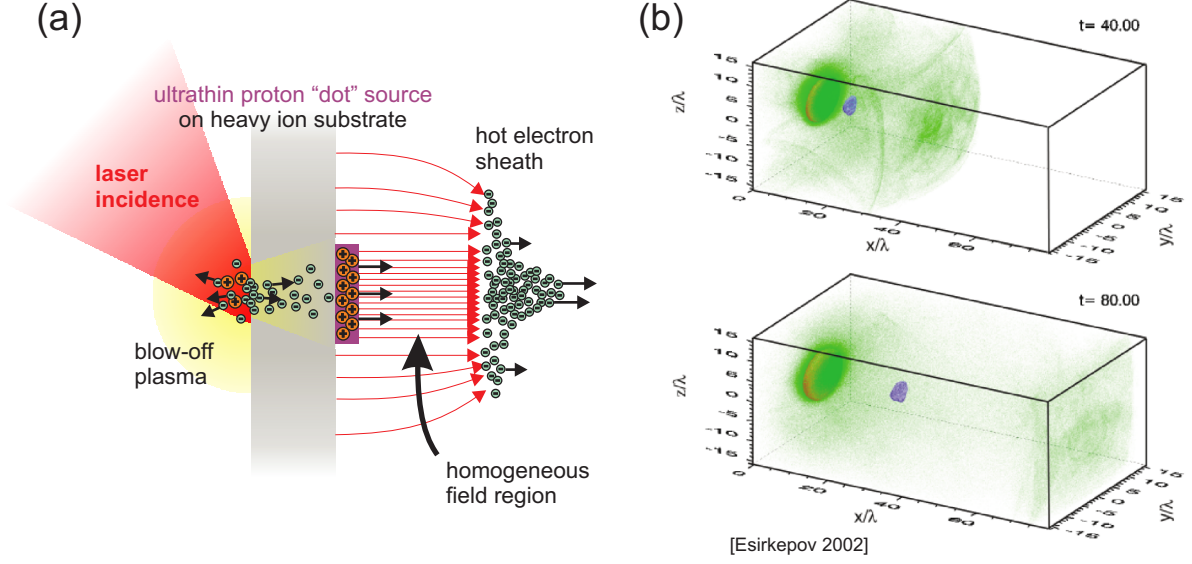


Figure 2.4: Proton acceleration from a geometrically confined, ultra-thin “dot” source (Esirkepov model). (a) An acceleration geometry for the generation of monoenergetic proton beams was proposed by Esirkepov et al. in 2002 [61, 164], which limits the proton source to the central homogeneous field region of the TNSA field at the rear side of a heavy ion substrate. If this dot source is sufficiently thin and screening effects are negligible, all protons will experience the same potential. Consequently, the dot will be detached as a whole and accelerated in a bunched, uniform manner, leading to high quality monoenergetic proton beams. Note that this model alone does not explain the monoenergetic spectra observed from the comparably thick dots at JETI, where additional charge separation effects must be taken into account. (b) Snapshots from a 3D-PIC simulation carried for the confined source geometry by Esirkepov et al. as presented in [61]. The proton dot (purple) is accelerated by the cloud of hot electrons (green), and departs from the heavy ion background (red disc) as a whole. The two graphs represent the times  $t = 40 \cdot 2\pi/\omega$  and  $t = 80 \cdot 2\pi/\omega$ , respectively.

with the abbreviations

$$\rho = \sqrt{x^2 + y^2} \quad (2.72)$$

$$\xi = \frac{1}{4} \left[ \sqrt{\left(\rho - \sqrt{\widehat{R}_\perp^2 - d^2}\right)^2 + z^2} + \sqrt{\left(\rho + \sqrt{\widehat{R}_\perp^2 - d^2}\right)^2 + z^2} \right]^2 - \widehat{R}_\perp^2 \quad (2.73)$$

$$R_\xi = \left(\xi + \widehat{R}_\perp^2\right) \left(\xi + d^2\right)^{1/2}, \quad (2.74)$$

$R_\perp$  being the transverse extent of the sheath field region, and  $x$  &  $y$  lying within the target plane. Note that close to the symmetry axis, the radial component  $E_\rho$  vanishes and the field vector points in target normal direction only. The longitudinal component then becomes

$$\mathbb{E}_z(z) \approx \frac{4}{3} \mathbb{E}_0 \widehat{R}_\perp^2 \cdot \frac{1}{\widehat{R}_\perp^2 - d + z^2}, \quad (2.75)$$

with the corresponding electrostatic potential

$$\Phi_{\text{el}}(z) = \frac{2\mathbb{E}_0\widehat{R}_\perp^2}{3\sqrt{\widehat{R}_\perp^2 - d^2}} \arctan \left\{ \frac{\sqrt{\widehat{R}_\perp^2 - d^2}}{z} \right\}. \quad (2.76)$$

This approximation holds true as long as no protons are located outside the transverse scale length of the field, i.e.  $\rho \ll \sqrt{\widehat{R}_\perp^2 - d^2}$ . In other words, if one intends to produce a monoenergetic proton beam from the central strong field region, the transverse extent of the sheath fields must be significantly larger than the proton source! Thus, the first condition for monoenergetic TNSA is a *radial confinement of the proton source*.

The spectrum of a proton population in this field can now be calculated assuming that their total charge is much smaller than the heavy ion background, i.e. they probe the field as test particles. With an initial distribution function  $f_0(z_0, v_0) = n_0(z_0) \delta(v_0)$ , i.e. a proton population at rest ( $\delta$  being here the Dirac delta function), and  $dn = f dz dv = f dE dt/m_p$ , the energy spectrum  $N(E) dE$  derives as follows

$$\begin{aligned} N(E) dE &= dE \int \frac{1}{m_p} f_0 dt \\ &= \frac{dE}{m_p} \int dt \delta(v_0) \\ &= \frac{n_0(z_0)}{m_p} \left| \frac{dt}{dv} \right|_{v=v_0} dE \end{aligned} \quad (2.77)$$

In the last step, the delta function has been eliminated by transcribing the time integration into a velocity integration using the Jacobian  $\left| \frac{dt}{dv} \right|_{v=v_0}$ . Acknowledging that the Jacobian corresponds to the reciprocal of the acceleration in the field,  $\left| \frac{dt}{dv} \right|_{v=v_0} = 1/|e\mathbb{E}_z/m_p|_{z=z_0}$ , and that the energy gain in the electric field is given by  $e\mathbb{E}_z = dE/dz$ , one obtains the particle spectrum

$$N(E)dE = \frac{n_0(z_0)}{\left| \frac{dE}{dz_0} \right|} dE, \quad (2.78)$$

where  $E$  is given by Eq. 2.75. This is a general expression for the dependency of the spectrum on the initial spatial particle distribution  $n_0(z_0)$ , showing that spectral spread of the protons accelerated in the locally uniform field close to the symmetry axis and the target surface is directly proportional to the decay of the electric field over the proton layer thickness  $dz_0$ ! The second condition for the generation of monoenergetic proton beams in this geometrical scheme is thus a *limitation of the source layer thickness*. Note that this second condition is not fulfilled for the comparably thick dots used at JETI. The Esirkepov model must hence be modified accordingly to account for our observations, which shall be done in the following.

### 2.3.3 Charge separation effects

*For thick dots, the formation of monoenergetic spectra is supported by charge separation effects between the fast protons and a slower heavy ion species. The sharp ion front represents a discontinuity, where charge neutrality is violated and a second sheath field is formed. Co-propagating protons are accelerated across the ion front and enter a zero-field region, where they form a stable monoenergetic bunch. Since the bunching is bound to the slower ion front, the spectral peak typically appears below the maximum proton energy.*

Following the acceleration geometry proposed by Esirkepov et al., experiments were carried out at JETI which demonstrated—for the first time—that monoenergetic proton beams can in fact be produced from laser plasmas (cf. section 4.1 for experimental data). However, the experiments showed that monoenergetic spectra can be obtained from much thicker dots than originally expected. Hence, the limitation of the source layer thickness required by the Esirkepov model is apparently not a necessary criterion, and a new theoretical basis needed to be found.<sup>8</sup>

A satisfactory explanation is found by including *charge separation effects* in the physical picture. Charge separation models of laser ion acceleration generally maintain that the formation of monoenergetic spectra involves at least two ion species, a heavy and a light one. For the polymer dots under discussion, this condition is satisfied by the proton and carbon contributions in the source layer. The potential of charge separation for the spectral modulation of laser-accelerated ion beams had been identified in earlier works already [62, 122]. In a detailed study regarding micro-dot acceleration, Robinson and Gibbon [54] presented numerical simulations which confirmed that monoenergetic spectra can in fact be produced from dots of up to micrometer thickness and may even vanish if the source layer is chosen too thin. Because of their central role for this work, the effects of charge separation shall be presented in detail in following.

Consider a confined ion source consisting of two ion species, say, protons and  $C^{4+}$ . Owing to their different  $q/m$ -ratios, the two ion species are accelerated differently according to  $\ddot{z} = q/m \cdot \mathbb{E}_z$ , and will hence separate at an early stage of the acceleration process. Consequently, two particle distributions with distinct particle fronts will propagate away from the target surface. This situation is shown in Fig. 2.5a: The fast proton front (red) and the slower carbon front (green) each terminate at a sharp  $z$ -position, whereas the carbon front overlaps with the low energy part of the proton distribution. Fig. 2.5a represents snapshot taken from a 1D-PIC simulation by Alex Robinson [55] for a  $1 \mu\text{m}$  thick target sitting at  $z = 100 \mu\text{m}$ , at

<sup>8</sup>In agreement with our observations, a simple estimation presented in [54] can be employed to see that typical dot thicknesses used in the JETI experiments indeed exceed the maximum thickness of a source layer that allows for monoenergetic acceleration according to the Esirkepov model. Assuming that the source layer is still thin and the hot electron population retains approximately a constant density in it, the damping of the electric field across the source layer can be described by integrating Poisson's equation  $\nabla_z \mathbb{E}_z = \rho/\epsilon_0$  to find  $\mathbb{E}_z = e(\tilde{n}_i - \tilde{n}_e) d_{\text{layer}}/\epsilon_0$ . If one takes the sheath electron density to be  $n_{e,0} = 2.0 \times 10^{20} \text{ cm}^{-3}$  as estimated in Eq. 2.62, and the ion density to be the proton density in the contamination layer,  $n_p = 2.24 \times 10^{23} \text{ cm}^{-3}$  (cf. section 3.1), then the field gradient amounts to  $\nabla \mathbb{E}_z \approx (4 \times 10^{12} \text{ V/m})/\text{nm}$ . This implies that for a maximum field strength of  $\mathbb{E}_{x=0} = 6.7 \times 10^{12} \text{ V/m}$  (cf. section 2.2.2), the field will be completely screened across a layer of 1.7 nm, i.e. roughly the contamination layer thickness. In other words, for any source layer of the order of the contamination layer or thicker, the spatial variation of the accelerating field will cause an energy spread large enough to prevent the proposed uniform acceleration of the whole dot.

Note that according to this simple estimation, the penetration depth of the electric field is proportional to  $1/n_i$ . Therefore, a stronger sheath field does not necessarily imply a greater ion yield; the high field may also lead to increased ionization and thus evoke stronger screening—a somewhat counter-intuitive relation.



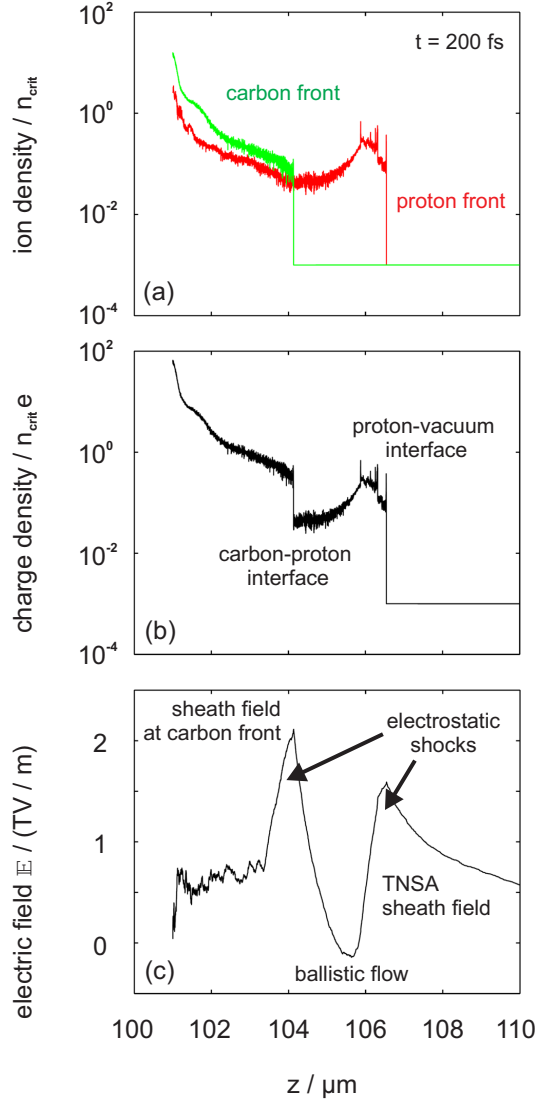


Figure 2.5: Charge separation effects supporting the generation of monoenergetic proton bunches. In TNSA, typically more than one ion species is involved in the acceleration process, which plays a central role for the generation of monoenergetic beams from a dot source. Due to their different  $q/m$ -ratios, the ion populations expand into the vacuum with different velocities, terminating to a distinct particle front for every single species. At JETI, the two leading ion species are protons and  $C^{4+}$ , represented by the red and the green line in Fig. (a). The sharp termination of the ion distributions causes two distinct discontinuities in the charge density, which is shown in Fig. (b). At these discontinuities, charge neutrality can not be retained, and the co-propagating hot electrons form sheath fields across the particle fronts boundaries, given by the two peaks in Fig. (c). At the proton front, the sheath field corresponds to the regular TNSA field driving that drives the proton acceleration; at the carbon front, however, the second sheath field effects that co-expanding light protons will be accelerated across the boundary, where they enter a region (of zero electric field screened from the first sheath field by charge-neutralized parts of the proton beam. In this zero-field region, protons are trapped in a state of quasi-ballistic flow and thus contribute to the monoenergetic bunch. All pictures are taken from a 1D-PIC simulation performed by Alex Robinson [55].

a laser intensity of  $I_{\text{FWHM}} = 10^{20} \text{ W/cm}^2$ .<sup>9</sup>

The total charge density is plotted in Fig. 2.5b. It displays two distinct discontinuities, one at the proton front ( $z \approx 106 \mu\text{m}$ ), and one at the carbon front ( $z \approx 104 \mu\text{m}$ ). Now, remember that TNSA is driven by charge separation at the solid-vacuum interface, where hot electrons are accelerated across the proton front and trapped to constitute the TNSA sheath field. Obviously, the same holds true for the charge discontinuity at the heavy ion front: The discontinuity represents a boundary where charge neutrality cannot be retained, and passing hot electrons will hence form a second sheath field across the carbon front.

This is illustrated in Fig. 2.5c, where the electric field behind the target is given. The two strong peaks correspond to two electrostatic shocks resulting from the sheath fields at the proton and heavy ion front, respectively. Between the peaks, there exists a zero-field region ( $z \approx 105 \mu\text{m}$ ), at which the proton front sheath field is already screened such that protons, accompanied by a colder electron population, may propagate undisturbed in quasi-neutrality. Evidently, this zero-field region is where *protons are accumulated to form a stable monoenergetic bunch*: Similar to the TNSA process at the proton front, the light protons from the low energy part of the spectrum are efficiently accelerated across the carbon boundary by the second sheath field, whereupon they immediately enter the zero-field region and remain in a state of motion of uniform ballistic flow.

This trapping of a part the proton population in a monoenergetic bunch located within the zero-field region is underlined by the evolution of the phase-space extracted from the same PIC simulation, shown in Fig. 2.6. The diagrams show that a quasi-monoenergetic proton distribution, represented by the wave-like structure in the plot, is formed with its center exactly in the zero-field region, e.g. around  $105 \mu\text{m}$  at  $t = 200 \text{ fs}$ , in agreement with Fig. 2.5.

The simulations by Robinson et al. [55] also confirm that the monoenergetic bunch does not disintegrate, but remains stable even for very long computing times. The peak energy thereby approaches a saturation value, reached typically after 200 fs as shown in Fig. 2.7a. The six spectra show the development of the (1D) proton spectrum over time, which witness a convergence of the peak position in the spectrum at about 10 MeV for the given simulation parameters. This stability and convergence is owed, on the one hand, to the quasi charge neutrality in the proton beam caused by co-propagating cold electrons, which preclude a substantial Coulomb explosion. On the other hand, the hot electron population will eventually cool down, preventing further acceleration and the related spectral broadening [55, 166]. This convergent behaviour is summarized in Fig. 2.7b, where the peak position is plotted for different simulation times. The two graphs represent two different proton-carbon mixtures in the dot material, whereas the ratio between the relative proton and carbon densities is  $n_{\text{p}} : n_{\text{C}^{4+}} = 1 : 1$  for the squares, and  $n_{\text{p}} : n_{\text{C}^{4+}} = 1 : 4$  for the circles. One can see

<sup>9</sup>The numerical code used in this simulation [55] is a 1D3P PIC code, which makes use of standard explicit PIC methods as discussed for example in [165]. Linear interpolation is used for particle and grid weighting, and the electric field obeys Gauss's law.

In the simulation, a grid of  $10^5$  spatial points was used with a cell size of 2 nm. The electron temperature was set to 20 keV. The heavy ion density was set to  $n_{\text{C}^{4+}} = 40 n_{\text{c}} = 4 \times 10^{22} \text{ cm}^{-3}$  and the proton density to  $n_{\text{p}} = 10 n_{\text{c}}$ , implying a relative proton density of 20% and an electron density of  $n_{\text{e}} = 170 n_{\text{c}} = 1.7 \times 10^{23} \text{ cm}^{-3}$ . The initial number of quasi-particles per cell was 4000, whereas  $2 \times 10^6$  quasi-particles were used for each species. The effects of reduced proton density will be discussed in detail in section 4.4.

The simulation was carried out at an intensity of  $I_{\text{FWHM}} = 10^{20} \text{ W/cm}^2$ , whereas the laser pulse was described by a  $\sin^2$  envelope with a pulse duration of  $\tau_{\text{laser}} = 80 \text{ fs}$  at a wavelength of  $1 \mu\text{m}$ . The snapshot was taken 200 fs after the interaction, which is justified by the fact that the particle spectrum has already attained its final form at that time (cf. Fig. 2.7).

that in both cases a final peak energy value is reached at about 200 fs (i.e. 6 MeV and 10 MeV, respectively) and maintained for the duration of the simulation. The significance of the different proton-carbon ratios in the dot material will be discussed in section 4.4.

Note also that the proton peak does not form at the maximum proton energy, but at an energy well below the cutoff, clearly visible in both the phase space plots of Fig. 2.6 and the spectra of Fig. 2.7a. Especially for late times, the spectrum can be seen to continue with an exponential high energy tail, resulting in a cutoff energy of about 20 MeV in contrast to a peak position of 10 MeV for the 300 fs-plot of Fig. 2.7a. This observation is in agreement with the fact that the peak formation is bound to the zero-field region behind the slower carbon front, and *not* to the perpetuating proton acceleration at the proton front. In particular, since the proton and the ion front are initially not well separated, the formation of an exponential high energy tail sets in at a later time (i.e. roughly after 200 fs) and continues to evolve while the peak position remains the same.

The charge separation mechanism thus implies that the central peak position is *necessarily* below the cutoff energy, which is well in accordance with experimental observations presented in the subsequent sections: Monoenergetic peaks regularly appear on top of an exponential background, and the peak positions are typically 30-50 % lower in energy than the maximum achievable cutoff energy for thermal proton spectra obtained with the JETI laser. The separation between peak position and cutoff energy thus underlines that the reduced bandwidth is not merely a simple geometrical effect, but involves fundamentally different physics, namely charge separation.

A few final remarks concerning charge separation shall be added. Besides the effects discussed here, two more mechanisms of charge separation were identified in a theoretical study by Brantov et al. [166], which could potentially lead to monoenergetic spectra. First, during the initial stage of the acceleration process, both ion species are still mixed in a quasi-homogeneous target slab. As the separation sets in, protons need to leave the mixed slab in order to become separated in the first place, passing thereby naturally the steep heavy ion front and forming a peak in the above-described fashion. This “initial charge separation mechanism” is closest to the ultra-thin source layer scenario proposed by Esirkepov et al. [61]. However, as mentioned above, for layer thickness of more than a few nm this monoenergetic bunch is typically not stable because the proton front itself is a non-charge-neutralized region, and Coulomb repulsion will soon dissolve the structure. Another mechanism is provided by “collisions” of the heavy ion and proton populations. In the region ahead of the heavy ion front, the positive ion charge may exert a push on the precursing protons, which may support or even give rise to monoenergetic bunching. Similar charge separation effects have also been involved in the explanation of the observed monoenergetic deuterons from droplet targets [166, 167], and spectral “dips” as seen in [168].

The general applicability of multi-ion species scenarios to laser acceleration experiments emphasizes that any mature model of TNSA should include charge separation effects in order to describe the acceleration conditions adequately. The presented model of “Confined TNSA”, comprehending a radial source confinement as well as charge separation effects, constitutes such an advanced theory, and also provides a roadmap for the experimentalist how to achieve monoenergetic proton beams from laser plasma interactions. This roadmap shall now be explored in the following.

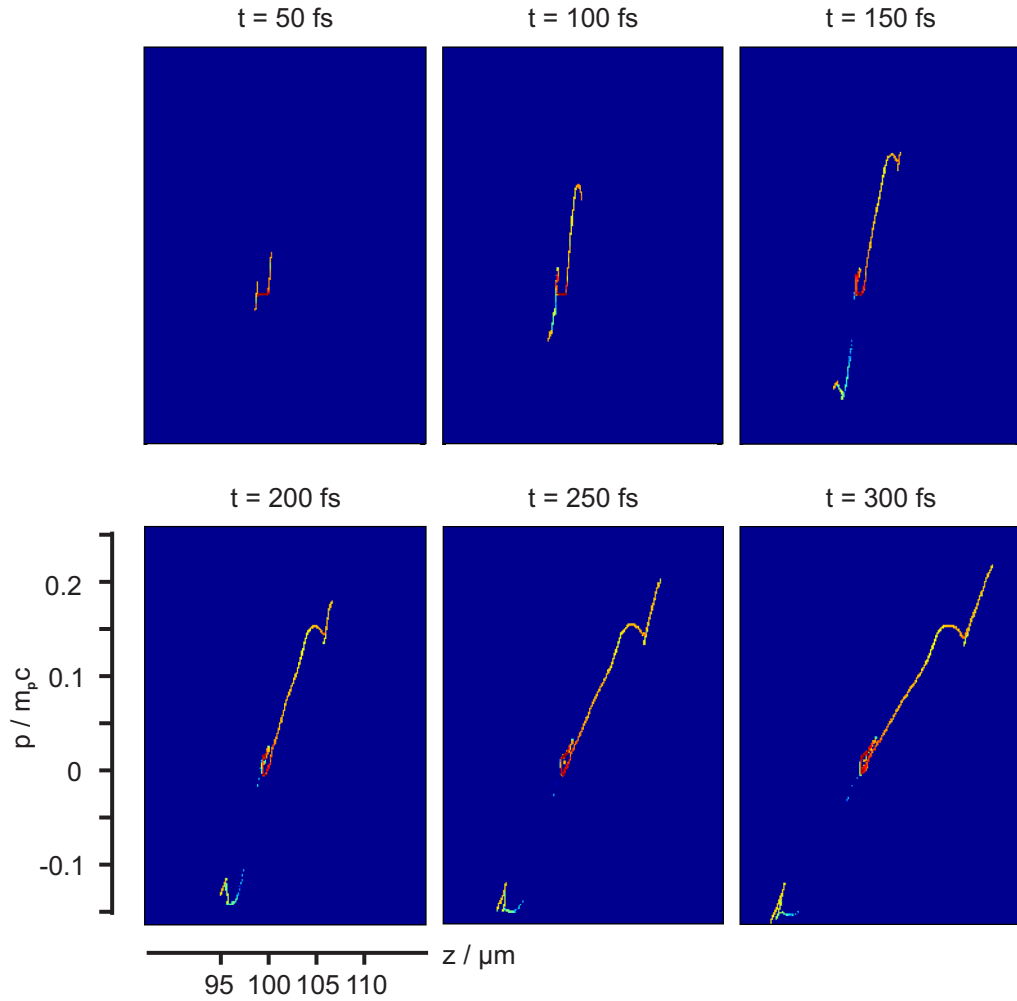
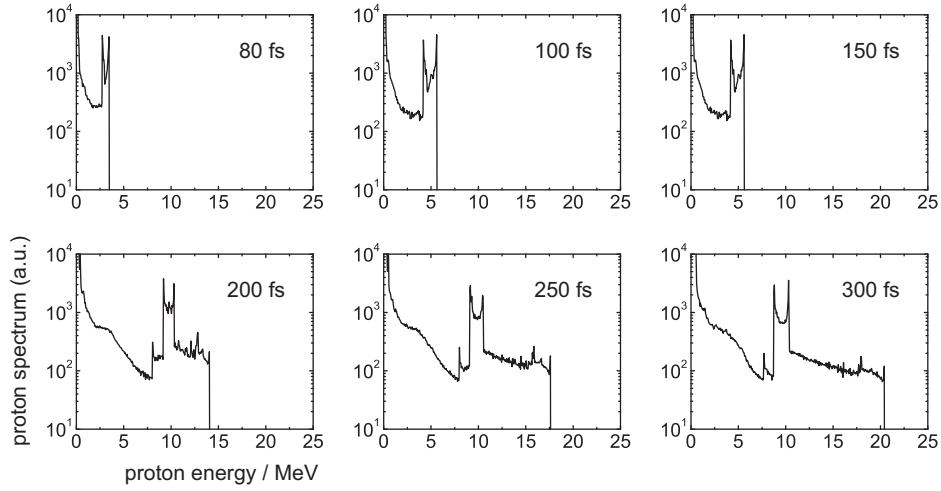
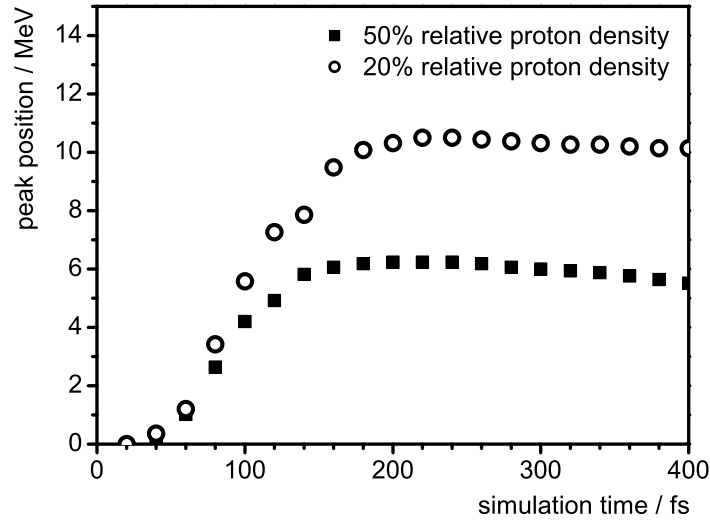


Figure 2.6: Proton phase-space during peak formation via charge separation as extracted from a PIC simulation by Alex Robinson [55] (see footnote 9 for simulation parameters). The  $z - p_z$  phase space of the expanding proton population is shown for different acceleration times. After an initial stage quasi-linear expansion, peak formation sets in at a time of about 100 fs, represented by a wave-like structure in the phase-space plot. This structure is located at a distance  $z = 105 \mu\text{m}$  at  $t = 200$  fs (target sits at  $100 \mu\text{m}$ ), which is exactly where the zero-field region is located in Fig. 2.5 for the same time. Furthermore, the peak can be seen to remain at the same  $p_z$ -position at times  $\geq 200$  fs, implying that the peak position in the spectrum converges towards a fixed value. In addition, the proton distribution expands beyond the peak structure for late times, resulting in an exponential high energy tail in excess of the peak energy, which can also be seen in Fig. 2.7.



(a)



(b)

Figure 2.7: Convergence of the peak position during the acceleration process as observed in PIC simulations [55]. (a) The evolution of the proton spectrum is plotted up to 300 fs after the initial interaction. The peak position can be seen to approach a value of 10 MeV for the given simulation parameters (see footnote 9 for simulation parameters), remaining stable for times  $\geq 200$  fs. On the contrary, the continuous part of the spectrum expands beyond the peak position as an exponential tail for late times. This localization of the peak position below the proton cutoff energy is in agreement with the theoretical model, which holds that the peak formation is bound to the slower heavy ion front, and not to the fast proton front which continues to be accelerated after the peak formation has finished. (b) The convergence of the peak position is plotted for two different dot compositions, featuring relative particle ratios between protons and carbons of 1 : 1 (squares) and 1 : 4 (circles). For the former, the peak position approaches 6 MeV, whereas the latter case yields a final peak position at 10 MeV. The different particle ratios in the material will play an important role discussing the PDR hypothesis below (cf. section 4.4).



## 3 Experimental considerations

### 3.1 Proton emission source size and source layer manipulation

*For typical laser acceleration experiments, protons are provided by adsorption layers on the foil surface. These source layers can be suppressed (e.g. using laser ablation), leading to an increased acceleration of ions from the foil bulk, or enhanced (e.g. using double layer targets). The transverse proton emission source size is of the order of 200  $\mu\text{m}$  and varies with energy.*

When considering Confined TNSA from an experimental point of view, it is pivotal to know about the actual dimensions of the sheath field region on the target back side and the consequent requirements on the target geometry—in other words: What is the maximum admissible size of the proton dot source to enable the generation of monoenergetic beams?

Several techniques have been developed to investigate the source size of the TNSA-accelerated ion beams, including mesh magnification experiments [17, 169], target structuring [170], and the controlled constriction of the proton beam path [171]. Other approaches rely on the direct imaging of the emission region, utilizing either plasma self-emission [108, 172], proton deflectionometry [161] or transverse all-optical plasma probing [117]. The literature agrees that the transverse extent of the ion source  $\hat{R}_\perp$  varies strongly for different proton energies, and should be at least 200 – 300  $\mu\text{m}$  in diameter for the parameters applied at JETI (e.g. 0.8 J, 5  $\mu\text{m}$  titanium foil,  $\sim 2$  MeV central peak energy) [169, 171].<sup>1</sup> Note that this value is significantly larger than the radius of electron emission  $R_\perp$  discussed for the Mora model in section 2.2.2 (Fig. 3.1). The derived proton source size suggests that a confined proton source should have a diameter of less than 20  $\mu\text{m}$ , i.e. 1/10 of the source size, in order to meet the requirements for Confined TNSA.<sup>2</sup>

In laser ion acceleration experiments, the ions are typically not provided by the foil bulk material but by *adsorption layers on the foil surface*, which are the result of the limited vacuum conditions. These contaminants, mostly water and oil vapours, represent the top layers exposed first to the ionizing TNSA field.<sup>3</sup> The composition of typical adsorption source layers was analyzed by Allen et al. [174] using x-ray photoemission spectroscopy. For a gold foil target of 15  $\mu\text{m}$  thickness and optical surface quality, the layer was determined to be 12  $\text{\AA}$  thick and consisted of 60.5% hydrocarbons, 12.2% water and 27% Gold. Thus, the predominant ion species to be accelerated in the sheath fields are indeed protons, favoured due to their largest  $q/m$ -ratio as mentioned above. The average layer density amounts to 5.94  $\text{g/cm}^3$ , and the corresponding particle density for hydrogen to  $n_p = 2.24 \times 10^{23} \text{ cm}^{-3}$ .

---

<sup>1</sup>The emission source size can be considerably smaller (of the the order of 20 – 50  $\mu\text{m}$ ) for the highest proton energies [17, 171]. However, as explained above, the highest proton energies do not constitute the proton peak in the monoenergetic spectra from Confined TNSA.

<sup>2</sup>There seems to be a general consensus in the literature that the formerly much cited smaller source size of a few microns diameter should rather be attributed to a virtual source located in front of the target [169]. This small virtual source size corresponds to the fact that protons are emitted with extremely high laminarity from the foil, resulting in excellent beam properties and the possibility to carry out sophisticated imaging experiments [17, 169] (Fig. 3.1).

<sup>3</sup>For the impact of surface purity on plasma expansion see e.g. [173].

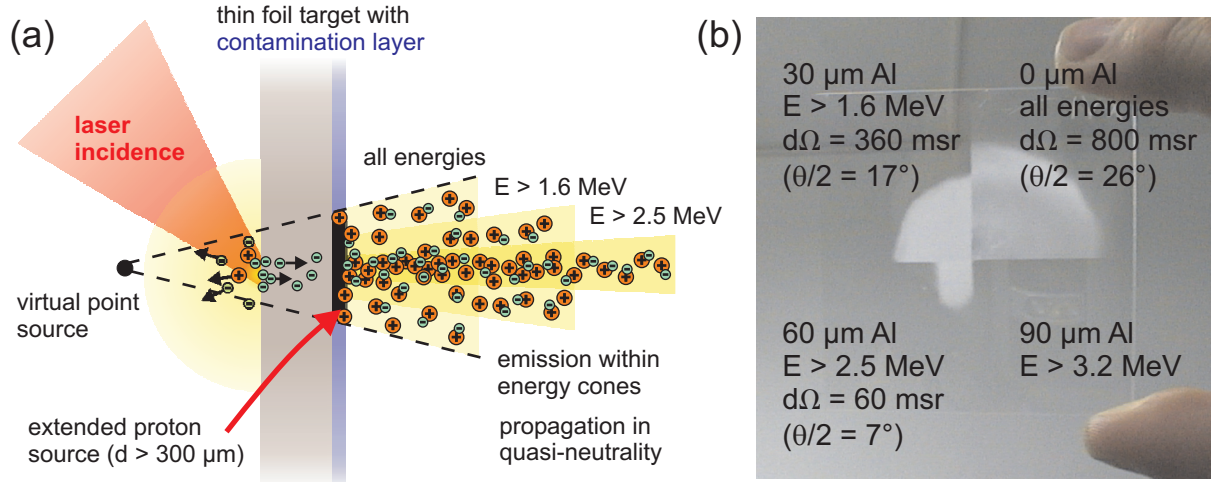


Figure 3.1: (a) Proton source size and emission within energy cones. The emission of TNSA-produced proton beams from a thin foil target happens in an extremely laminar fashion. The source size of the proton emission on the foil varies strongly with the proton energy and is typically of the order of  $200 - 300 \mu\text{m}$  for the parameters at JETI (e.g.  $0.8 \text{ J}$ ,  $5 \mu\text{m}$  titanium foil,  $\sim 2 \text{ MeV}$  central peak energy); however, the protons can also be allocated to a virtual point source located several hundred microns in front of the foil, which is constitutional for the excellent laminarity [17, 169, 171]. Furthermore, the proton emission happens in symmetrical cones, whereas the solid angle of emission again depends on the proton energy. (b) The emission cones can be measured for example with a piece of CR39 track detection plastic, which is covered with aluminium layers of different thicknesses and placed behind the foil target. Circular proton impact regions of different diameter are observed on the processed CR39 (white milky quarter-circles), corresponding to the solid angles of emission for different minimum energies transmitted by the aluminium layers. The corresponding half opening angles are given in parentheses.

Thus, in a source volume of  $V_{\text{source}} = \pi(100 \mu\text{m})^2 \cdot 12 \text{ \AA} = 38 \mu\text{m}^3$ , a total of  $N_p = 8.4 \times 10^{12}$  protons are available for acceleration. Other publications estimate the layer thickness to be  $\leq 100 \text{ \AA}$  and the hydrogen particle density to  $n_p \approx 10^{22} \text{ cm}^{-3}$  (cf. e.g. [156]), which yields similar total numbers for the same source size. Given this huge areal reservoir of protons, one has to establish means to dispose of this extended contaminant layer first if intending to provide a spatially confined proton source.

The *removal of the proton source layer* was first carried out as a direct proof of TNSA as opposed to other proposed acceleration mechanisms from the target front side. Manipulations of the rear surface showed an immediate impact on the proton yield, presenting a strong argument against the front side hypothesis. A reduction of the contamination layer was demonstrated with various techniques, including laser ablation [43, 53, 158, 175], resistive heating [6, 43, 176], and ion sputtering [43, 174]. All of these manipulation techniques are suitable to reduce the proton yield to almost zero. At the same time, a strong increase of the heavy ion yield from the bulk material is observed [6, 43, 176]. This indicates that as soon as the light protons are suppressed, the field energy is deposited onto ion species with next lower  $q/m$ -ratio, in agreement with the TNSA model.



On the other hand, one can also install additional ion source layers in order to enforce the acceleration of a certain ion species [51, 52, 61, 177, 178]. Such *double layer targets* ideally consist of a high-Z "carrier foil", which provides a sufficient number of electrons while ensuring a good 'contrast' for the acceleration of the light ions against the heavy ion background, and a thin hydrogen-rich "source layer" attached to the back side of the carrier foil. Organic materials (e.g. polymers) are rich in hydrocarbons and thus generally represent a good choice for the source layer. In [178], an increase in proton flux by a factor of 80 was reported using a double layer target made of copper and polyvenyl methylether (PVME). This large factor could not be reproduced at JETI; however, a reliable increase by a factor of 5 – 10 was observed for a combination of titanium and polymethyl methacrylate (PMMA) [175].

Given their effectiveness as proton sources, double layer targets in combination with rear surface cleaning represent powerful tools for the pursuit of Confined TNSA. The task is now to find a way to limit the source size to the central field region. This can be achieved by microstructuring the double layer targets, which shall be described in the following section.

## 3.2 Microstructured targets

*Proton source confinement was achieved using microstructured targets. Plain metal foils were first coated with a sub- $\mu\text{m}$  layer of PMMA and consequently structured using either femtosecond laser ablation or UV laser lithography. The resulting "dots" have a transverse extent of 10 – 20  $\mu\text{m}$ , much smaller than the transverse extent of the sheath field.*

The fabrication of adequate targets for Confined TNSA was realized in two steps. First, a layer of PMMA was applied on a thin carrier foil, typically titanium or tantalum with 2 – 5  $\mu\text{m}$  thickness. The polymer was evenly spread on the back side of the foil using a spin coating technique, which yielded well-defined layer thicknesses of 50 – 1000 nm. The spin coating process was carried out at the Institute of Applied Physics (IAP), Jena.

In a second step, the coated target surface was microstructured via laser ablation.<sup>4</sup> For this purpose, the target was mounted on a micrometer positioning system and irradiated on its PMMA-coated surface with a focussed Ti:Sapphire laser beam ( $E_{\text{pulse}} = 5 \mu\text{J}$ ,  $\tau_{\text{pulse}} = 60 \text{ fs}$ ) with kHz repetition rate. By translating the target mount within the target plane, square dots with a minimum size of  $10 \times 10 \mu\text{m}^2$  were carved out from the PMMA surface (Fig. 3.2).

The microstructuring process proved very sensitive to the applied laser parameters: Depending on target and layer thickness, strong focussing could lead to destabilization or disintegration of the foil; on the other hand, weak focussing resulted in highly "frayed" carving edges and thus to irregular dot structures or even spalling of the dots. For a typical PMMA layer of 200 nm thickness on a 5  $\mu\text{m}$  Titanium substrate, the applied single shot fluence was  $\Phi_{\text{fs}} \approx 0.1 \text{ J/cm}^2$ , which was accumulated over several shots at each focus position due to the relatively slow translation velocity of the target positioning system in comparison to the kHz repetition rate. The accumulated ablation fluence at each surface position on target thus amounted to  $\overline{\Phi_{\text{fs}}} \approx 3.2 \text{ J/cm}^2$ , producing clean and reproducible microstructures. The size and

<sup>4</sup>Note that the expression "laser ablation" is used in two different ways throughout this thesis, which should be easily distinguishable from their contexts. In sections 3.1 & 4.2, "laser ablation" refers to target cleaning, i.e. the removal of adsorbates from the target rear side, carried out with a pulsed Nd:YAG laser. In the current section, it refers to the microstructuring of the double layer targets as part of the target fabrication process. A detailed overview of the different types of laser ablation applied in this thesis is provided in Appendix A.

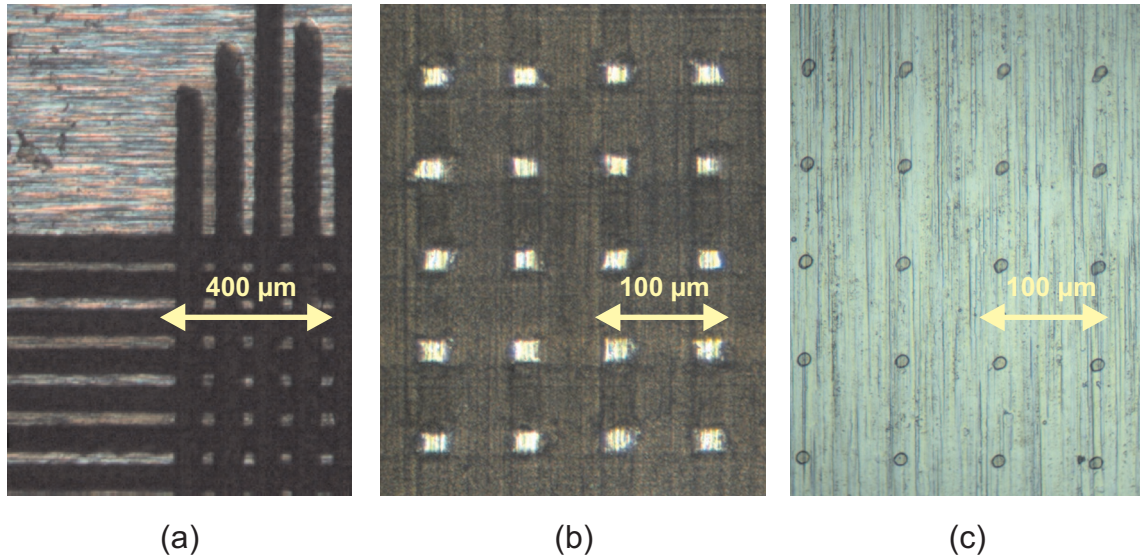


Figure 3.2: (a) + (b) Fabrication of microstructured targets via fs-laser ablation. For the fabrication of microstructured targets suitable for Confined TNSA, a layer of polymer (PMMA) with 50–1000 nm thickness was first applied to thin titanium foils via spin coating. From the polymer-covered surface, small square dots of 0.2 μm thickness,  $20 \times 20 \mu\text{m}^2$  extent and 80 μm separation were “carved out” with the help of a femtosecond laser system. Fig. (a) clearly shows the perpendicular carving traces ranging into the reddish polymer. In this particular case, the polymer contained some Rhodamine 6G contributions, which are the origin of the red colour. Note the well-defined carving edges typical for the multi-photon ablation processes occurring during fs-ablation. (c) Lithography targets. Round dots of 0.2 μm thickness and 10 μm diameter with 80 μm separation were generated on the PMMA-covered back side of the titanium foil via UV-lithography with a pulsed excimer laser through a custom-designed quartz glass mask. This alternative technique allows for a more flexible fabrication of micro-dots, which are, however, considerably more sensitive to laser ablation than those produced with the femtosecond system. For a detailed description of the ablation processed, see Appendix A.

the separation of the dots could be varied by defocussing the laser beam and compensating the pulse energy.

Alternatively, target microstructuring was also performed via photo-lithography. In this case, the PMMA surface was irradiated with a UV argon-fluoride excimer laser ( $\lambda = 193$  nm,  $E_{\text{pulse}} = 3$  mJ,  $\tau_{\text{pulse}} = 15$  ns) through a custom-designed chrome-layered quartz glass mask. The energy deposition per area necessary for the removal of the superfluous material depended again on the thickness of the PMMA layer. For a 200 nm layer on a 5  $\mu\text{m}$  titanium foil, typically 20 shots with an ablation fluence of  $\Phi_{\text{UV}} = 0.25$  J/cm<sup>2</sup> per shot were accumulated to excavate round dots of 5 – 20  $\mu\text{m}$  diameter from polymer (Fig. 3.2).

All microstructuring processes were carried out at IOQ facilities. For a more detailed description of the ablation physics and references, refer to Appendix A. The PMMA microstructures fulfill all the requirements put forth by the Confined TNSA model. That is, they provide a spatially limited proton source in the form of a compound with a heavier ion species (carbon) to be subject to the charge separation effects discussed above. Together with a robust target cleaning procedure described in section 4.2, they provide the means to pursue monoenergetic proton acceleration. In the following, the JETI laser system and the experimental implementation of the Confined TNSA scheme via microstructured targets shall be reviewed.

### 3.3 The Jena 10 TW Titanium:Sapphire laser system (JETI)

All experiments concerning the generation of monoenergetic ion beams via Confined TNSA were carried at IOQ with the *Jena 10 TW Titanium:Sapphire laser (JETI)*. In the following, the JETI laser shall be briefly introduced.

An overview of the JETI layout is given in Fig. 3.3. Like all high intensity laser systems, JETI is based on the chirped pulse amplification principle (CPA) [179–181]. The laser front end consists of a commercial Ti:Sapphire oscillator (“Tsunami”, Spectra Physics), which is pumped by a 5W cw-Neodym:YVO<sub>4</sub> laser (“Verdi”, Coherent) and delivers pulses of 10 nJ energy with 45 fs pulse duration (FWHM of laser intensity) at a central wavelength of  $\lambda = 795$  nm.

Before entering the first out of three amplifiers, the initial repetition rate of 80 MHz is reduced to a 10 Hz pulse train by a Pockels cell-based pulse picker. The pulses are then stretched by a double-pass grating stretcher, which introduces a positive chirp ( $d^2\phi/dt^2 = d\omega/dt > 0$ , where  $\phi$  is the spectral phase of the pulse and  $\omega$  is the laser angular frequency) to increase the pulse duration to 150 ps. In the first amplifier, a regenerative amplifier, the pulse energy is increased during 12 round trips to a saturation value of 2.5 mJ. The regenerative amplifier is followed by an additional ultra-fast Pockels cell to suppress pre-pulses and reduce contributions of amplified spontaneous emission (ASE) [182]. The Pockels cell has a compound switching time (including voltage supply) of about  $\tau_{\text{rise}}^{90/10} < 400$  ps which, together with an electronic jitter of about  $\pm 300$  ps, guarantees a pulse contrast of  $I_{\text{ASE}}/I_{\text{main}} \approx 10^{-9}$  at 0.7 ns before the main pulse arrives (cf. also below and Appendix B for more detailed contrast information) [182]. The remaining two amplification stages are both multipass amplifiers (a “4-pass butterfly” and “2-pass butterfly”) pumped by frequency-double Nd:YAG lasers (“Pow-erlite” and “Macholite” series, Continuum), where the pulse energy is raised to 320 mJ and a maximum of  $E_{\text{laser}} = 1.35$  J, respectively. Between the two multipasses, a spatial mode filter (pinhole) located at an intermediate focus serves to smooth the beam profile.

With a  $1/\tilde{e}^2$ -beam diameter of approximately 7 cm, the laser then enters the 4-grating vacuum compressor. Because of gain narrowing and nonlinear dispersion imposed during the

amplification process, the initial pulse duration cannot be recovered completely, and the final pulse duration amounts to  $\tau_{\text{laser}} = 80$  fs. The transmission efficiency of the compressor is limited to about 65%, which results in a total pulse power of  $P_{\text{pulse}} \approx 10$  TW available for experiments at JETI.

The final laser pulse parameters are characterized with several diagnostic tools, including a pulse front tilt measurement, and two third order auto-correlators (a 'home-built' one, and a "Sequoia" by Amplitude Technologies) for the determination of the pulse length and the ASE/pre-pulse profile. At JETI, a pulse contrast of  $I_{\text{ASE}}/I_{\text{main}} < 10^{-8}$  between ASE and main pulse is achieved up to 40 ps before the main pulse, followed by a single pre-pulse of the order of  $10^{-5}$  at 30 ps. After the pre-pulse, the ASE level decreases to  $< 10^{-8}$  again. A Sequoia autocorrelation trace is presented in Appendix B.

The proton acceleration experiments at JETI were carried out with  $45^\circ$  f/2 off-axis parabolic mirrors, where the quality of the laser focus and the focal spot size were determined by imaging the attenuated focus with a microscope objective onto a CCD camera. The achieved full-width half-maximum (FWHM) focal spot size is typically  $A_{\text{focus}} \approx 5 \mu\text{m}^2$ , which corresponds to an FWHM intensity of  $I_{\text{focus}} = 5 \times 10^{19} \text{ W/cm}^2$ . For an exhaustive description of the JETI laser system, please refer to [56, 57].

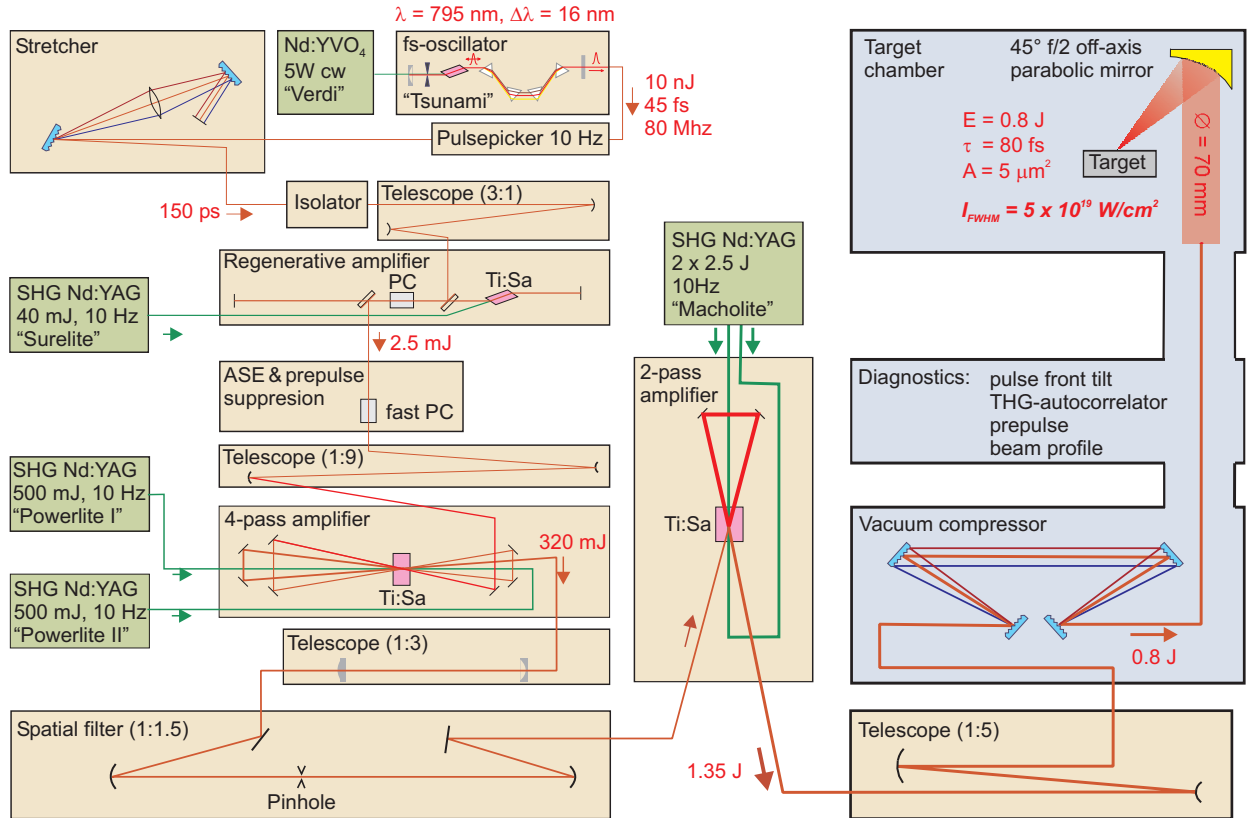


Figure 3.3: Schematic overview of the Jena 10 TW Titanium:Sapphire laser system (JETI) based on CPA technique.

### 3.4 Experimental setup for Confined TNSA

*The JETI pulses are focussed with an  $45^\circ$  off-axis parabolic mirror and hit the target exactly opposite to a microdot. The accelerated protons are dispersed in a Thomson spectrometer and detected either with a micro-channel plate (MCP) or CR39 plastics. The rear surface is cleaned from parasitic proton contributions using additional laser ablation.*

The experimental setup for the micro-dot experiments at JETI was as follows: The microstructured target was mounted on an  $xyz\Theta$ -translation and rotation stage, where  $\Theta$  lies in the  $xz$ -plane (parallel to the chamber base plate). A robust alignment procedure was employed to guarantee that the target surface was adjusted parallelly to the  $xy$ -translations axis with an accuracy of  $< 5 \mu\text{m}$  over the whole target width ( $50 \times 50 \text{mm}^2$ ) in order to prevent defocussing when translating the target to a new irradiation position.

The JETI laser pulses were focussed on the target front side at an angle of incidence of  $45^\circ$  with a gold coated  $f/2$  off-axis parabolic mirror, whereas the size and the quality of the focal spot were determined by imaging the attenuated focus with a microscope objective onto a CCD camera. By means of this imaging procedure, astigmatisms could be corrected by adjusting the horizontal and vertical tilt of the parabola.

The most critical part about microdot setup is owed to the fact that the JETI laser pulse must hit the thin foil target exactly opposite to the dot position (Fig. 3.4); that is, one needs to align the laser pulse impinging on the target front side with something that is visible only from the back side. For this purpose, the back side was observed with a long distance microscope with micrometer resolution. An attenuated JETI pulse was then used to create a small hole in the target ( $d \approx 10 \mu\text{m}$ ), whereupon the incidence position was marked on the observation screen such that the dots only needed to be translated to this reference position in order to achieve proper alignment. The overall accuracy of the alignment procedure proved to be better than  $5 \mu\text{m}$ .

In addition, the ablation laser hit the target back side under an angle of  $22.5^\circ$  co-centered with the JETI incidence position (Fig. 3.4). The laser was weakly focused on the surface with a diameter of typically  $d_{\text{foc}}(1/e) \approx 600 \mu\text{m}$  in order to cover the whole proton source area around the dot (cf. section 3.1), and could be attenuated with a variable set of neutral density filters to apply well-defined ablation fluences.

The generated proton and ion beams propagated towards the spectrometer chamber, where the beam diameter was reduced by a pinhole of variable size (0.3 mm, 1 mm or 3 mm). Subsequently, the limited beam was dispersed with a Thomson spectrometer, which applied an effective magnetic field of  $\mathbb{B} = 525 \text{mT}$  and a co-parallel electric field of  $\mathbb{E} = 2.7 \times 10^5 \text{V/m}$  perpendicular to the particle propagation direction and over a dispersion length of 10 cm [175]. The energy resolution of the spectrometer was defined by the pinhole diameter to e.g.  $\Delta E_{\text{res}} = 50 \text{keV}$  for 1 MeV protons using the 1 mm aperture. The particles were detected either with CR39 track detection plates, or with an online imaging system based on micro channel plates (MCP) in a chevron setup. The use of the MCP allowed for a very flexible experimentation and enabled the collection of large amounts of data, facilitating statistical analysis. The MCP was calibrated against both CR39 spectra and at the TCC-CV28 cyclotron of the Physikalisch-Technische Bundesanstalt (German National Metrology Institute) in Braunschweig, Germany [175].

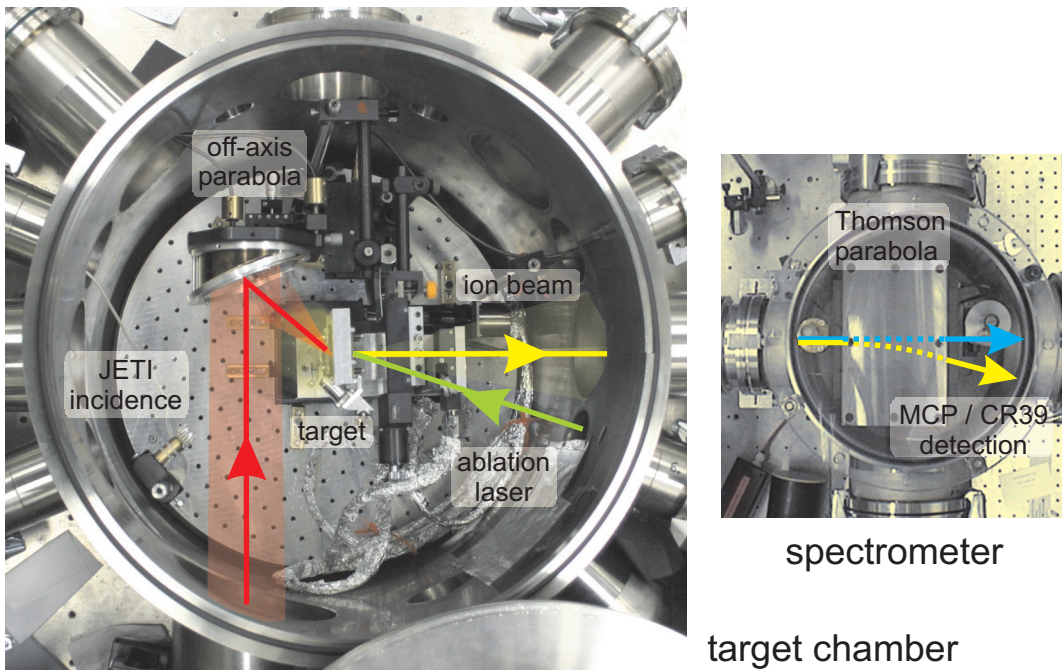
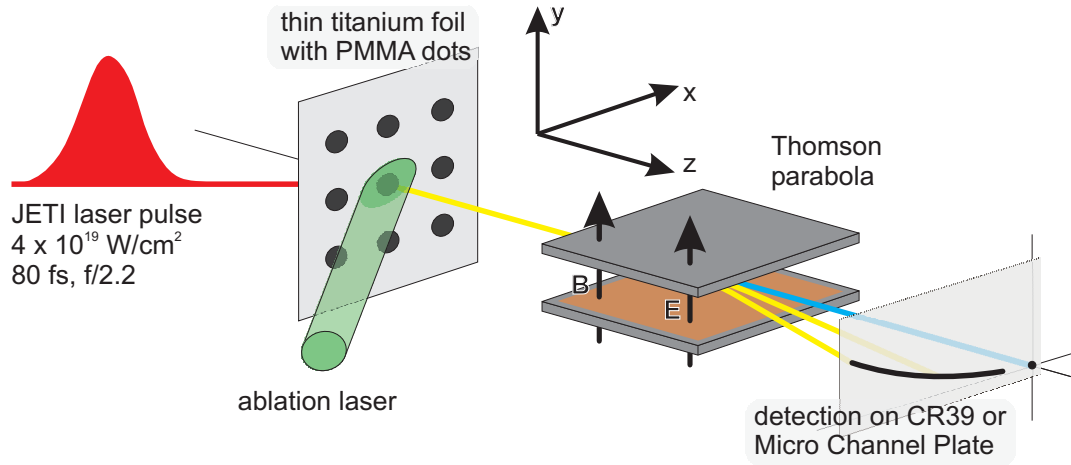


Figure 3.4: Experimental setup. The laser pulse hits the thin foil target at the front side exactly opposite to a micro-dot. Protons from the dot are accelerated within the central, homogeneous field region of the TNSA field and analyzed with a Thomson spectrometer. The ions can be detected either with CR39 track detection plastics or an online imaging system (MCP). A second laser, which hits the target on the back side concentrically with respect to the first, is used for the cleaning of the target from residual contamination layer protons. The bottom pictures represent top-view photographs of the target chamber and the detection chamber. The JETI pulse incidence is given in red, the ablation laser in green, and the accelerated proton beam in yellow.

## 4 Narrow-band proton and ion beams

In the previous chapters, the physics of relativistic laser plasma interaction has been introduced to the reader to provide the theoretical basis for particle acceleration based on high intensity lasers. In particular, the TNSA process has been identified as a potent mechanism for laser ion acceleration from thin foils. A modified version of the TNSA acceleration scheme called “Confined TNSA” has been presented, where the ion source on the rear side of the irradiated foil is confined to a small dot-like region in the homogeneous center of the TNSA field, and charge separation effects between multiple ion species in the beam lead to the formation of monoenergetic proton bunches at the slower heavy ion front. The potential of Confined TNSA for the generation of ion spectra with intrinsically narrow energy distribution has been discussed in detail, and a setup for the experimental implementation of this scheme has been provided, which uses microstructured double-layer targets.

In the following chapter, the results of a series of experiments with such microstructured targets shall be presented. All experiments were carried out at the JETI laser system. Under comparable conditions, various types of targets were irradiated including for example polymer dots on metal foils, deuterated polymers with low proton density, and carbon dots. This chapter will start out with a discussion of a small number of exemplary proton spectra recorded from polymer dot-targets, which will be compared in their properties to typical accelerator beams. Secondly, the reproducibility of the results will be examined, thereby emphasizing the importance of target surface cleaning. The high reproducibility and the overall large quantity of recorded spectra will allow, thirdly, to derive scaling laws between laser energy and the spectral parameters (i.e. the peak energy and width), which are well supported by numerical simulations. In the fourth section, the influence of the target composition on the acceleration process shall be discussed, resulting in a “proton density reduction scheme” (PDR) for the improvement of the produced spectra. Fifthly, the feasibility of Confined TNSA for the generation of heavy ion beams will be analyzed and demonstrated by the observation of monoenergetic carbon spectra from carbon-rich microdots. Finally, after a brief discussion of the observation of multiple modulations, alternative techniques for the generation of monoenergetic ion beams from laser plasmas shall be presented, before moving on to some application studies based on extrapolation of the current results.

### 4.1 Monoenergetic proton beams

#### 4.1.1 Exemplary proton spectra

*Narrow-band proton beams with peak energies  $\leq 3$  MeV and typically 10% – 20% energy spread are reproducibly observed from the irradiation of microstructured targets. The proton number per energy interval of the spectral peaks typically exceed the thermal spectra observed from the irradiation of plain foils by a factor of 4.*

In this section, two exemplary spectra taken from the thousands of recorded shots on microstructured targets shall be presented and analyzed in depth. Fig. 4.1 shows a compar-

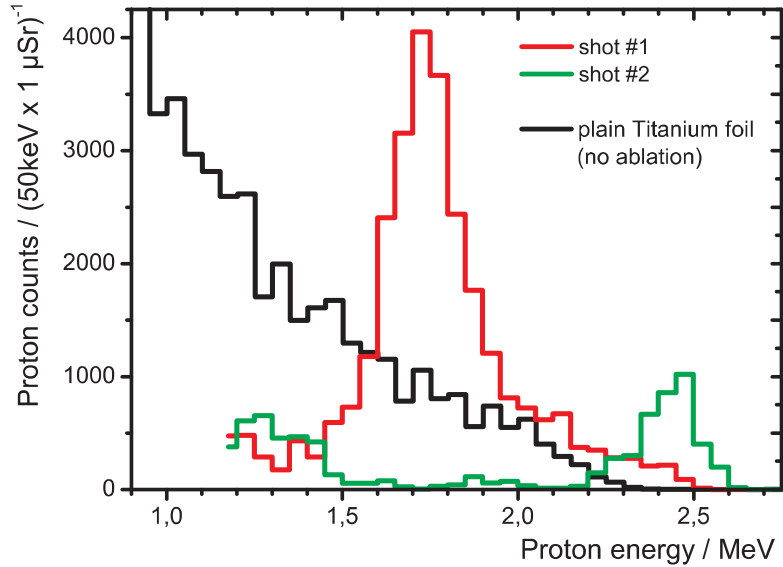


Figure 4.1: Spectra from the irradiation of PMMA micro-dots ( $20 \times 20 \times 0.2 \mu\text{m}^3$ ) after 10 consecutive laser ablation shots at the threshold fluence of  $\Phi_{\text{abl}} = 1.2 \text{ J/cm}^2$  (red and green lines) in comparison to plain, unstructured 5m Titanium foil (black line) [53]. The proton spectra from the polymer dots show distinct peaks at  $E_{\text{center}} = 1.7 \text{ MeV}$  with an energy width of  $\Delta E_{\text{FWHM}} = 0.25 \text{ MeV} = 15\%$  for Shot #1 and  $E_{\text{center}} = 2.5 \text{ MeV}$  with  $\Delta E_{\text{FWHM}} = 0.2 \text{ MeV} = 8\%$  for Shot #2. The ablation has suppressed the parasitic low-energy component of the spectrum and enables the acceleration of monoenergetic protons from the confined dot source. Narrow band features appear consistently once an ablation threshold fluence of  $\Phi_{\text{thr}} = 1.2 \text{ J/cm}^2$  at 532 nm is surpassed. In contrast, the irradiation of a plain Titanium foil (black line) yields the typical thermal distribution (average over 6 spectra).

ison between spectra obtained from shots on micro-dots of  $20 \times 20 \times 0.2 \mu\text{m}^3$  located on the rear side of a  $5 \mu\text{m}$  titanium foil (red and green line), and shots on a plain unstructured titanium of  $5 \mu\text{m}$  thickness (black line, average over 6 spectra).<sup>1</sup> The unstructured foils yield the typical smooth thermal distribution known from many TNSA experiments. On the contrary, the dot spectra display distinct peak features, located at  $E_{\text{center}} = 1.7 \text{ MeV}$  with  $\Delta E_{\text{FWHM}} = 0.25 \text{ MeV} \approx 15\%$  energy width for shot #1 (red line), and at  $E_{\text{center}} = 2.5 \text{ MeV}$  with  $\Delta E_{\text{FWHM}} = 0.2 \text{ MeV} \approx 8\%$  for shot #2 (green line). The two narrow band peak structures contain a total of about  $3 \times 10^4$  protons for shot #1 and  $4 \times 10^3$  protons for shot #2 (FWHM) within  $1 \mu\text{sr}$  solid angle of observation, whereas the peak maximum exceeds the exponential distribution by a factor of at least 4. The excess of the spectral peak is owed to the accumulation of protons in the zero-field region behind the ion front (cf. section 2.3.3), and is supported by the overall high hydrogen content in the dot material. Note, however, that the peak signal strength does typically not exceed the factor of 5-10 observed from targets with extended polymer-layers on the back (cf. section 3.1). The relative peak contrast between

<sup>1</sup>In addition, the rear surface of the microstructured target was cleaned from contamination layers using laser ablation, which will be discussed in detail in section 4.2. The averaging was carried out to account for small shot-to-shot fluctuations in the proton signal strength. Note that the production of thermal spectra from thin foils via TNSA is an extremely reliable process, leading to quasi-constant cutoff energies and proton temperatures over hundreds of shots.



the peak maximum and the low energy background is typically 10 within  $2 \cdot \Delta E_{\text{FWHM}}$  (i.e.  $\approx 4000/400$  for shot #1 and  $\approx 1000/100$  for shot #2).

For shot #1, it can be seen that the peak is located well below the cutoff energy of the proton spectrum, which continues with a quasi-exponential high energy tail. This behaviour is in agreement with the theoretical model of Confined TNSA as discussed in section 2.3.3. The model holds that the peak formation is caused by the charge separation between protons and carbons at the slower heavy ion front. In the JETI experiments, the observed peak positions are typically 30 – 50% lower than the maximum cutoff energy, and monoenergetic peaks regularly appear on top of an exponential background.<sup>2</sup>

The distinctly monoenergetic beams achieved with microstructured targets represent a significant improvement over the hitherto broad, quasi-thermal spectra obtained from laser acceleration: For the first time, ion beams with intrinsically narrow energy spread can be provided by a micrometer-scale accelerator [51, 53]. This demonstrates that spectral shaping of laser-accelerated particle beams may be achieved without subsequent beam shaping devices as known from conventional accelerators (e.g. combinations of magnets), and thus indicates that the small dimensions of laser accelerators can be retained when moving to narrow-band beams. The possibility of active spectral control via manipulation of the target geometry thus heralds a new quality in laser particle acceleration, paving the way for many applications.

#### 4.1.2 Beam properties

*Laser-generated proton beams possess a number of unique beam properties, including an ultra-short pulse duration and excellent emittance values, leading to an extremely high peak brilliance of  $\approx 10^{27} \text{ (eV s)}^{-1} \text{ (m}^2 \text{sr)}^{-1}$ . These qualities witness the singular physical regime accessed by laser accelerators.*

The number of protons contained in the spectra of Fig. 4.1 was limited by the solid angle of observation of the setup,  $1 \mu\text{sr}$ , which in turn was determined by a 1 mm pinhole in front of the ion spectrometer. Generally, this angle of observation could be varied from  $0.1 \mu\text{sr}$  to  $10 \mu\text{sr}$ , which corresponds to pinhole sizes of  $300 \mu\text{m}$  to 3 mm in the setup. In previous experiments, the divergence of thermal proton beams at JETI was measured to be much larger, amounting to 360 msr at a proton energy of 1.6 MeV, or 60 msr at 2.5 MeV (cf. Fig. 3.1), which implies that only a small fraction of the total number of protons is actually observed.<sup>3</sup>

Due to the given setup, it was not possible to obtain spectral data for monoenergetic spectra over the whole emission angle. However, simulation studies by Alex Robinson confirm that the narrow band feature in the spectrum is not limited to the small angle of observation, but appears equally over the whole emission range (cf. section 4.1.3) [55]. Another set of 2D-PIC simulations carried out by Timur Esirkepov indicates that the angle of emission for micro-dots is approximately 24 msr for a peak at 1.1 MeV and hence somewhat lower than the experimental values measured for plain targets [51]<sup>4</sup>. Using this solid angle of 24 msr as a conservative estimation for the total number of protons, one finds that shot #1 of Fig. 4.1

<sup>2</sup>In the case of shot #2, the signal strength of the exponential tail is too weak to be observed under the current conditions.

<sup>3</sup>Angular emission properties were studied at JETI with CR39 plates, which were covered with aluminium foil of different thicknesses and placed immediately behind the target foil. On these plates, concentric sectors of circles are observed, corresponding to well-defined solid angles of emission for protons with energies larger than the maximum stopping energy in the aluminium foil (cf. Fig. 3.1). The specific values were measured on  $5 \mu\text{m}$  titanium foils at  $I = 2 \times 10^{19} \text{ W/cm}^2$ .

<sup>4</sup>This could possibly be attributed to the confined source geometry.

contains about  $N_p \approx 4.1 \times 10^8$  in the FWHM peak. From integration over the narrow-band spectrum it follows that the *conversion efficiency* of laser energy (0.78 J on target) into kinetic energy of protons amounts to  $\eta_p = 1.4 \times 10^{-4}$  for the FWHM peak, which corresponds to a conversion efficiency from hot electrons into proton of 0.07% for the above assumed  $\eta_e = 20\%$ .

Building on this estimation, a number of beam parameters can be derived to put the present achievements in a broader context and rank laser-produced proton beams among conventional accelerator beams. In accelerator technology, two parameters of central importance are the longitudinal and the transverse emittance, which represent a measure for the geometrical confinement of the particle bunch and thus describe the propagation properties of the beam in comparison to an ideal ion trajectory [183, 184]. The *longitudinal emittance* is defined as the product of the pulse duration and the energy spread,  $\varepsilon_{\text{long}} = \Delta\tau_{\text{pulse}} \cdot \Delta E_{\text{kin}}$ , and gives a measure for the spatio-temporal broadening of the particle pulse in propagation direction (i.e. the “chirp”). Previous measurements carried out by Cowan et al. [17] revealed excellent emittance values of the order of  $\varepsilon_{\text{long}} < 10^{-4}$  eV s as a conservative estimation for laser proton acceleration from thin foils. Simulations indicate even lower values of the order of  $\varepsilon_{\text{long}} = 10^{-7}$  eV s. [ibid.] For the experiments under discussion, the FWHM energy spread of 0.25 MeV for shot #1 in Fig. 4.1 together with an initial pulse duration of 182 fs (corresponding to the effective acceleration time  $t$  introduced in section 2.2.2) yield a longitudinal emittance of  $\varepsilon_{\text{long}} = 4.6 \times 10^{-8}$  eV s for the narrow-band proton beams at JETI, which is an extremely low value. Even if the pulse duration is conservatively approximated by the lifetime of the TNSA sheath field of roughly 10 ps, one still finds a theoretical emittance of  $\varepsilon_{\text{long}} = 2.5 \times 10^{-6}$  eV s, which is many orders of magnitude below the values achieved by conventional accelerators (e.g.  $\varepsilon_{\text{long}} \approx 0.35$  eV s for CERN SPS [185]). This remarkable quality of laser accelerators is mostly owed to the ultra-short pulse duration, representing a physical regime not accessible to conventional accelerators.<sup>5</sup>

The *transverse emittance*, on the other hand, is given by the phase-space integral  $\varepsilon_{\text{trans}} = (1/\pi) \int n_i(x, p_x) dx dp_x/p_z$  and represents a measure for the transverse position-momentum uncertainty and thus for the laminarity of the beam. Here,  $x$  and  $dp_x/p_z$  are the radial particle position and normalized transverse momentum, respectively, and  $n_i$  is the initial ion density distribution. The transverse emittance determines the re-focussability of the beam and is hence important when considering future applications of laser-produced ion beams, for example as pre-acceleration stages for conventional accelerators. At the beam waist (i.e. immediately at the source or in a subsequent focus), the transverse emittance reduces to  $\varepsilon_{\text{trans}} \approx \beta\gamma \cdot \sigma_x \cdot \sigma_{x'}$ , where  $\beta$  and  $\gamma$  are the relativistic factors,  $\sigma_x$  is the beam diameter, and  $\sigma_{x'}$  is the divergence. For laser-plasma accelerators, emittance values of  $\varepsilon_{\text{trans}} < 4 \times 10^{-3}$  mm mrad have been measured using mesh magnification techniques [17]. At JETI, an estimation can be provided by taking into account the minimum solid angle of emission ( $24 \text{ msr} \simeq 155 \text{ mrad}$ ) and a proton source size determined by the diameter of the microdots ( $> 20 \mu\text{m}$ ), which yields a transverse emittance of  $\varepsilon_{\text{trans}} \geq 0.2$  mm mrad. This number still outmatches the emittances of conventional accelerators by more than one order of magnitude (e.g.  $\varepsilon_{\text{trans}} \approx 3$  mm mrad for the CERN SPS [185]), which clearly indicates the potential benefits of laser driven particle acceleration.

Finally, the beam *brilliance* is defined as particle flux  $dN/dt$  per area  $dA$ , bandwidth  $dE$

<sup>5</sup>Note that the proton pulse duration has not been explicitly measured yet. However, all current theoretical models suggest that the initial proton pulse duration should be of the order of the laser pulse duration.

	Shot #1	Shot #2
$E_{\text{center}}$	1.7 MeV	2.5 MeV
$\Delta E_{\text{FWHM}}$	0.25 MeV (15%)	0.2 MeV (8%)
$\Delta E_{1/e^2}$	0.7 MeV	0.4 MeV
peak contrast within $2 \cdot \Delta E_{\text{FWHM}}$	4000 : 400	1000 : 100
$N_{\text{p}}$	$4.1 \times 10^8$	$0.7 \times 10^8$
$\varepsilon_{\text{long}}$	$4.6 \times 10^{-8}$ eV s	$3.6 \times 10^{-8}$ eV s
$\varepsilon_{\text{trans}}$	0.2 mm mrad	0.2 mm mrad
$B$	$9.4 \times 10^{26} (\text{eV s})^{-1} (\text{m}^2 \text{sr})^{-1}$	$2.0 \times 10^{26} (\text{eV s})^{-1} (\text{m}^2 \text{sr})^{-1}$
$\eta_{\text{p}}$	$1.4 \times 10^{-4}$	$0.4 \times 10^{-4}$

Table 4.1: Beam properties of narrow-band proton spectra in Fig. 4.1.

and solid angle  $d\Omega$ ,

$$B = \frac{dN}{dt \cdot dE \cdot dA \cdot d\Omega} \approx \frac{N_{\text{p}}}{\pi \varepsilon_{\text{long}} (\varepsilon_{\text{trans}} / \beta\gamma)^2}, \quad (4.1)$$

which for the parameters of shot #1 add up to  $B = 9.4 \times 10^{26} (\text{eV s})^{-1} (\text{m}^2 \text{sr})^{-1}$ . In comparison, the peak brilliance of CERN SPS amounts to  $B_{\text{SPS}} = 5.3 \times 10^{24} (\text{eV s})^{-1} (\text{m}^2 \text{sr})^{-1}$  according to the parameters presented in [185]. Note, however, that a large acceleration facility like CERN SPS provides considerably more protons per pulse ( $\approx 10^{11}$ ) at a 5 orders of magnitude higher peak energy ( $\approx 450$  GeV) with a significantly smaller bandwidth! The beam properties of the laser-produced proton beams discussed in this section should hence be viewed as an illustration of the complementary and unique physical regime accessed by laser accelerators, rather than a competitive comparison between different machines aiming at the same parameters. All characteristics of the two exemplary JETI spectra presented in Fig. 4.1 are again summarized in table 4.1.

### 4.1.3 PIC simulations

*The experimental results are in excellent accordance with numerous Particle-In-Cell (PIC) simulations. PIC simulations help to understand the acceleration dynamics of Confined TNSA and demonstrate that the narrow-band peak appears over the full angle of proton emission.*

The observations at JETI are confirmed by numerous PIC simulations, which help to analyze and exploit the laser plasma dynamics of the acceleration process more efficiently. All simulations verify that the formation of narrow band spectra is an extremely robust mechanism: Monoenergetic peaks appear consistently for a wide range of simulation parameters (e.g. varying focal spot size, pulse energy, target composition, and simulation run time) if a micro-dot is irradiated.

Many of the simulations relevant for this thesis are owed to the dedicated work of Alex Robinson and Paul Gibbon [53–55]. The simulations were predominantly carried out at the Rutherford-Appleton Laboratories (UK) and the Forschungszentrum Jülich, and employed for example the 2D-PIC code OSIRIS [186] and the gridless tree code PEPC [187], the former of which shall be illuminated in some depth here for one particular set of simulations formerly presented in [53]. In the 2D-OSIRIS simulations, the target consists of a dot, represented by

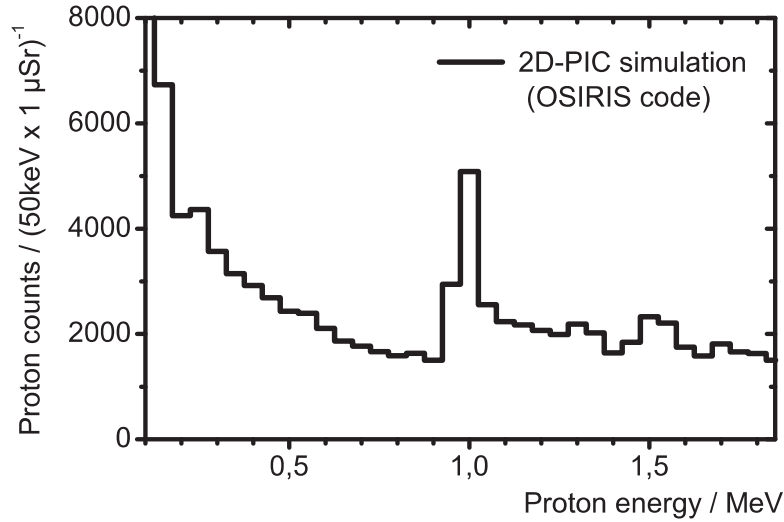


Figure 4.2: Results of the 2D-PIC simulation carried out by Alex Robinson with the OSIRIS code [53]. The interaction of a laser pulse with a  $1.2\ \mu\text{m}$  heavy ion foil carrying a micro-dot ( $0.2\ \mu\text{m}$  thickness,  $10\ \mu\text{m}$  diameter) was simulated for an intensity of  $I = 2.7 \times 10^{19}\ \text{W}/\text{cm}^2$  (corresponding to  $E_{\text{laser}} = 0.5\ \text{J}$  on target), whereas the dot consisted of 50 % protons and 50 %  $\text{C}^{6+}$ . In good agreement with the experimental results, the calculated spectrum yields a distinct peak at 1.0 MeV with 10 % bandwidth. The spectrum further possesses an exponential high energy tail, which indicates that the peak formation occurs at lower energy than the cutoff energy of corresponding thermal spectra. Similar simulations were carried out for different laser energies (cf. sections 4.3 & 5.1).

a  $0.2 \times 10\ \mu\text{m}$  mixed slab of protons at a density of  $40\ n_c$  ( $m_p/m_e = 1830$ ,  $q/m = 1 \cdot e/m_p$ ) and heavy ions at  $40\ n_c$  ( $m_p/m_e = 3660$ ,  $q/m = 1/2 \cdot e/m_p$ ), sitting on a  $1.2\ \mu\text{m}$  substrate (foil) slab consisting of ions only, with a density of  $80\ n_c$ . Note that the  $q/m$ -ratio of the heavy ions corresponds to  $\text{C}^{6+}$  or  $\text{D}^+$ . The assumption of a relative proton fraction of 50% is in good accordance with the applied dot material (PMMA [ $\text{C}_3\text{H}_5\text{COOCH}_3$ ] $_n$ ) where the hydrogen content is 53%. The laser pulse is normally incident at the center of the foil and has a triangular temporal profile with a FWHM duration of 80 fs. The simulation employed a simulation box of  $20 \times 20\ \mu\text{m}$  with cell sizes of  $\Delta x = \Delta y = 2.5\ \text{nm}$ . Initially, 64 particles per species were placed in each cell. The simulations were typically run up to 350fs.

Fig. 4.2 shows a typical spectrum obtained for a simulation at  $I = 2.7 \times 10^{19}\ \text{W}/\text{cm}^2$ . In the plot, a distinct peak is visible at 1.0 MeV with an FWHM bandwidth of 10%, which is in very good agreement with the experimental results. The total signal strength (i.e. 5000 protons per energy interval at the peak maximum) matches the experimental data very closely. The slightly lower peak position of 1.0 MeV compared to the 1.5 – 2.5 MeV observed in experiment can be attributed to the slightly different target geometry and composition in the simulation, which has an impact on the charge separation between different ion species and hence on the formation of monoenergetic peaks. In particular, the simulated dot contained only two ion species instead of multiple elements and ionization degrees, and the carrier substrate was assumed to be carbon instead of titanium, thus providing a smaller number of hot electrons. Furthermore, in this particular simulation, the ion charge state of the carbon contributions in the dot was chosen to  $\text{C}^{6+}$ , whereas the intensities available at JETI typically suffice to

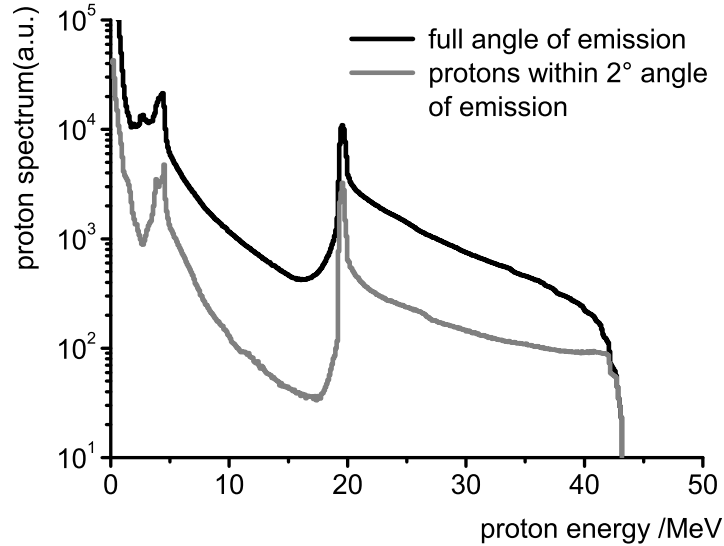


Figure 4.3: Angular emission properties of protons from a dot source [55]. The proton spectrum for different angles of emission was studied with the help of PIC simulations. The grey curve represents a spectrum of all protons emitted within an angle of  $\leq 2^\circ$ , whereas the black curve contains all protons emitted from the source. It can be seen that both spectra have a similar shape, displaying a sharp peak feature of the same width at the same energy. This proves that the monoenergetic proton bunch is not limited to a small angle of emission, but appears equally over the whole emission angle. Note, however, that the peak contrast is slightly higher in the low-angle case. A detailed discussion of the simulation parameters will be given in section 4.4. In particular, the black curve in this graph corresponds to the green curve of Fig. 4.11.

produce  $C^{4+}$  only. The choice of the background ion species has a noticeable impact on the peak formation, as will be discussed in section 4.4. Given these boundary conditions, the results of the simulation are in reasonable proximity to the experimental findings.

As mentioned above, PIC simulations also provide information about the angular beam spread. The simulations by Alex Robinson prove that the spectrum of all emitted protons differs from that of protons at very low divergence only by a constant factor. This congruence is shown in Fig. 4.3, where the grey line gives a spectrum for a proton angle of emission of  $< 2^\circ$ , and the black line represents a spectrum at full angle of emission, containing all protons accelerated from the dot.<sup>6</sup> A detailed experimental analysis was not feasible due to restrictions of the setup. It shall hence suffice to note that it can nonetheless be assumed that the monoenergetic bunching appear consistently over the full angle of emission, emphasizing that all protons emitted from the dot source can in principle be utilized for application.

<sup>6</sup>Note that in Fig. 4.3 the simulation parameters are different from those in 4.2, which explains the different peak energy and contrast. In the current context, the two graphs of Fig. 4.3 are only meant to highlight the angular emission properties; a detailed discussion of the exact simulation parameters will follow in section 4.4. In particular, the black curve of Fig. 4.3 corresponds to the green curve of Fig. 4.11.

## 4.2 Reproducibility studies and the inevitability of target cleaning

*Controlled removal of parasitic proton contributions resulting from adsorption layers around the microdot via pulsed laser ablations significantly improves the narrow-band proton acceleration. Above a well-defined threshold fluence of  $\Phi_{\text{thr}} = 1.2 \text{ J/cm}^2$ , reproducibility rates for the appearance of monoenergetic spectra exceeding 80% are observed.*

The removal of parasitic protons abundant in contamination layers around the microdot has been discussed in section 3.1 as a central prerequisite for Confined TNSA. In a series of experiments, the feasibility of laser ablation for the purpose of target cleaning was investigated at JETI.

First, the target cleaning procedure was tested on plain titanium foils by varying the ablation fluence of the frequency-doubled Nd:YAG ablation laser ( $\lambda = 532 \text{ nm}$ ,  $\tau_{\text{pulse}} \approx 5 \text{ ns}$ , 10 Hz repetition rate) from  $\Phi = 0.01$  to  $10 \text{ J/cm}^2$ . Above a distinct threshold fluence of  $\Phi_{\text{thr}} = (1.2 \pm 0.3) \text{ J/cm}^2$ , the proton signal was found to reduce to almost zero. The existence of threshold fluences is well known from pulsed laser ablation physics (cf. Appendix A), and the observed magnitude corresponds to typical values for the ablation of organic layers from surfaces at the given parameters (see e.g. [188–190]). Below the threshold fluence, no ablation of contamination layers is expected, and indeed no effect on the proton acceleration is observed.

In a second step, the effect of laser ablation was studied on microstructured targets. Below the threshold fluence, the observed proton beams correspond largely to those obtained from unstructured targets, regularly revealing peaks on a strong quasi-thermal background. However, once the ablation threshold  $\Phi_{\text{thr}}$  is surpassed, the continuous spectral components disappear and distinct, well-separated peak features are observed (Fig. 4.1). It can be concluded that all contaminants have been suppressed; only the PMMA dot has resisted the ablation and remained as a confined proton source on the surface.<sup>7</sup> Furthermore, in accordance with previous works on target cleaning [43], an increased acceleration of titanium ions ( $\text{Ti}^{1+} - \text{Ti}^{4+}$ ) from the foil bulk sets in when removing the contamination layer on the target back side. The observed ionization states agree well with the estimated TNSA field strength of a few  $10^{12} \text{ V/m}$ .

Having determined the ablation threshold, the reproducibility of Confined TNSA was then studied under single-shot ablation conditions. For this purpose, an additional shutter was introduced into the ablation beam path and connected to the JETI timer such that the main laser pulse arrives at the target approximately 5 ms after the last ablation shot. It was found that after one shot at the threshold fluence, almost all of the recorded spectra still display a predominantly exponential shape (Fig. 4.4). After two to four consecutive shots of ablation, the ratio between distinctly peaked and non-peaked spectra is evenly distributed, whereas for 6 or more shots the large majority of the spectra show a strongly reduced overall bandwidth. Irradiation with a higher fluence ( $\Phi = 1.7 \text{ J/cm}^2 > \Phi_{\text{thr}}$ ) reveals an even stronger dependency on the number of ablation shots. Already after two shots 70% of the spectra are peaked; after four shots almost all spectra show narrow-band features. This initial delay can be ascribed to

<sup>7</sup>If applied carefully, the micro-dots are generally sufficiently resistant to ablation. However, depending on the ablation parameters and the dot composition, it is certainly possible to ablate the dots gradually, or to “melt” them, so that after a certain number of ablation shots the dot structure has vanished. Another effect observed at JETI is the “spalling” of surrounding dots due to thermal stresses on the surface. Besides the below-mentioned incubation effects, it does therefore make a general difference whether the total required fluence to clean the target is applied within one or several ablation shots.

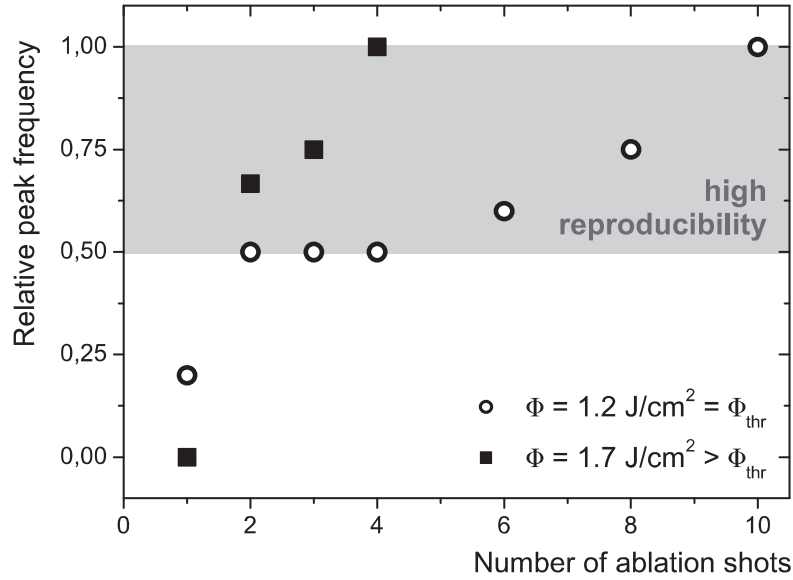


Figure 4.4: Relative frequency of peaked spectra as a function of the number of ablation shots [53]. The back surface of the microstructured  $5\ \mu\text{m}$  Titanium foil was ablated with a frequency-doubled pulsed Nd:YAG laser ( $\lambda = 532\ \text{nm}$ ,  $\tau_{\text{pulse}} = 5\ \text{ns}$ ) in single shot mode, whereas the desorption of the surface contaminants is subject to initial incubation effects. After 6 consecutive ablation shots at the threshold fluence  $\Phi_{\text{thr}} = 1.2\ \text{J}/\text{cm}^2$ , 60% of the produced proton beams showed narrow-band spectra (open circles), which impressively demonstrates the reliability of the aiming and ablation procedure. For an increased fluence of  $\Phi = 1.7\ \text{J}/\text{cm}^2 > \Phi_{\text{thr}}$ , an equally high reproducibility was reached after two shots already (black squares). In both cases, the relative frequency for the occurrence of peaked spectra approaches one when increasing the number of ablation shots. This means that narrow-band spectra are observed consistently, if a micro-dot is irradiated.

incubation effects: It is well known that sub-threshold fluences can significantly change the initial absorption behaviour by inducing photo-chemical modifications in layer composition (cf. Appendix A). The actual disposal of material may thus not start immediately, but only after a critical number of defects have been accumulated [188, 191–193].<sup>8</sup>

Building on these detailed ablation studies, a remarkable reproducibility of  $> 80\%$  for the appearance of monoenergetic proton spectra at JETI was achieved for hundreds of consecutive shots under optimum ablation conditions.

It is important to note that due to the vacuum conditions of the experiment, the ablated adsorption layers will start to recover immediately after the ablation has stopped. The time scale of such a recovery was studied by setting an additional delay between the last ablation shot and the JETI pulse. It was found that after a delay of  $\Delta t = 5\ \text{s}$  the spectrum had regained its exponential form completely, which is well above the  $100\ \text{ms}$  between two consecutive ablation shots and the  $5\ \text{ms}$  between the last ablation shot and the JETI incidence. The recovery time of adsorption layers can be estimated by the particle impact rate on the surface  $R = p / (3m k_B T)^{1/2}$  [194], following directly from kinetic gas theory. Here,  $m$  is the mass of the adsorbed molecule and  $T$  the temperature in the target chamber. Assuming conservatively

<sup>8</sup>This incubation behaviour can explain, for example, why some polymers may eventually be ablated at wavelengths at which they are originally transparent.

that the chamber pressure  $p = 10^{-5}$  mbar is determined by hydrocarbons only ( $m_{\text{CH}_4} \approx 2.7 \times 10^{-25}$  kg), the impact rate at  $T = 293$  K attains  $R = 6 \times 10^{15} \text{ cm}^{-2} \text{ s}^{-1}$ . A 12 Å contamination layer as put forth in [174] hence needs about 6 seconds to recover, which is in good agreement with the observations at JETI.

In summary, the target cleaning procedure shows a strong influence on the quality of the narrow-band spectra, their peak contrast as well as their reproducibility. With the help of controlled laser ablation, the generation of monoenergetic proton spectra from microstructured targets could be improved to a highly reliable mechanism, warranting reproducibility rates of  $> 80\%$  for the appearance of narrow-band features under optimum ablation conditions. In the following, the correlation between the spectral parameters of the peak and the laser energy shall now be analyzed.

## 4.3 Scaling laws for monoenergetic proton beams

### 4.3.1 Peak position scaling

*In the given parameter range, the average peak position in the spectrum scales linearly with laser energy. The observed scaling deviates from all hitherto scalings proposed for thermal proton spectra, and hence represents the first scaling law specifically for monoenergetic beams. The results are well confirmed by 2D-PIC simulations.*

A subject of great interest for the generation of monoenergetic proton beams is the scalability of the acceleration mechanism to higher laser powers. Having established the high degree of reproducibility discussed in the previous section, the peak parameters for many hundred monoenergetic spectra were evaluated as a function of the JETI pulse energy, keeping all other parameters (dot dimensions, focal spot size, laser pulse duration, prepulse conditions, ablation conditions etc.) fixed. It shall be emphasized that the use of an online detection system like an MCP clearly facilitates the collection of such large amounts of data.

Fig. 4.5 shows a subset of data where the JETI pulse energy was increased from 0.5 to 0.8 J on target (black squares). The four data points comprise a total of 140 spectra, all taken from 5 μm titanium foils carrying PMMA dots of 200 nm thickness after 10 consecutive shots of ablation at the threshold fluence  $\Phi_{\text{thr}} = (1.2 \pm 0.3) \text{ J/cm}^2$ . Statistical analysis yields that the average peak position increases from 1.42 to 1.63 MeV over this energy range. The error bars represent the standard deviation of the sub-sets and thus give a measure for the shot-to-shot fluctuation. Note that the energy range covered by the four data points was constrained by the available laser energy (upper boundary) and the detection range of the spectrometer (lower boundary).

The four data points strongly suggest a linear dependency between the peak position and the laser energy for the observed energy range. In order to support this evidence, we extended our 2D PIC simulation studies to the different laser energies applied in the statistical analysis (using the same simulation parameters as discussed in section 4.1.3). The results are shown in Fig. 4.5 as grey circles: Similar to the experimental data, the calculated peak position increases in a linear manner, rising from 1.17 to 1.35 MeV over the observed energy interval. An additional simulation was carried out by Alex Robinson for a pulse energy of 15 J in order to investigate whether this behaviour holds true also at higher laser energies [53]. This run yielded a monoenergetic peak at 9.3 MeV (cf. section 5.1, Fig. 5.1), in very good agreement



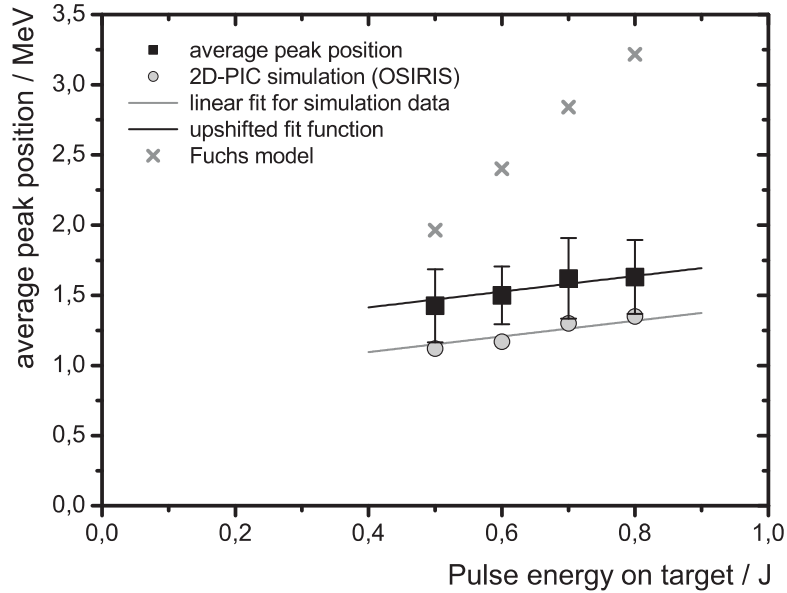


Figure 4.5: Energy dependency of monoenergetic proton peak position [53]. The laser pulse energy on target was varied from 0.5 to 0.8 J, which corresponds to intensities of  $2.9 - 4.7 \times 10^{19} \text{ W/cm}^2$ . Consequently, the average peak position rose from 1.42 to 1.63 MeV (black squares). All other parameters were kept fixed (identical micro-dots on a  $5 \mu\text{m}$  Titanium foil; constant ablation conditions of 10 consecutive shots at the threshold fluence). The four data points include a total of 140 monoenergetic spectra, which lends sufficient statistical significance to the results. The error bars represent the standard deviation of the statistical sample and thus delineate the shot-to-shot fluctuation. The observed proportionality is excellently reproduced by 2D-PIC simulations carried out by Alex Robinson for our experimental parameters (grey circles). The calculated peak positions lie slightly outside the standard deviation, but are well within statistical range of the sample sets. Together with an additional simulation for 15 J pulse energy (cf. Fig. 5.1), the calculated peak positions follow a linear function,  $E_{\text{peak}}^{\text{scale}}/\text{MeV} = 0.56 \times E_{\text{laser}}/\text{J} + 0.87$  (grey line), which represents the first scaling law particularly for monoenergetic spectra. All previous scaling laws refer to the cutoff energy of thermal spectra from plain foils and fail to account for our data. For example, the model by Fuchs et al. [7] predicts much higher energies and a steeper slope (grey crosses) for the current parameters.

with the linear extrapolation of the four calculated spectra between 0.5 and 0.8 J.<sup>9</sup> Together, the five simulation data points follow the linear function

$$E_{\text{peak}}^{\text{scale}}/\text{MeV} = 0.56 \times E_{\text{laser}}/\text{J} + 0.87, \quad (4.2)$$

represented by the grey line in Fig. 4.5.

Similar to the discussion of Fig. 4.1b, the numerical results appear systematically lower than the experimental values. However, it is striking how closely the slope of the simulation data matches that of the experimental data. The black line in Fig. 4.5 depicts the same linear fit function (4.2) upshifted only by 320 keV. This excellent accordance lends authority to the deduced linear scaling, which hence represents a scaling law for the generation of monoenergetic proton beams from microdot assisted laser proton acceleration.

The importance of this scaling law becomes evident when comparing it to other scalings proposed for laser proton acceleration. Various dependencies have been suggested to connect the proton energy to the laser power or intensity [7, 8, 110, 123], and it is known from previous measurements that for example the model by Fuchs et al. [7] successfully predicts the observed cutoff energies at JETI under certain assumptions. However, all of these scalings refer solely to the cutoff energy of thermal spectra from plain foils. Contrarily, it has been shown above that the peak position from Confined TNSA does *not* coincide with the cutoff energy of the corresponding thermal spectra, but is bound to the slower heavy ion front. It is therefore not ad hoc intelligible if or how the peak formation will scale with laser energy. Clearly, the thermal scaling laws cannot be expected to account for the peaks, and in fact a comparison of our data with the scaling law from [7] shows a strong discrepancy for the observed narrow parameter interval already. This deviation is illustrated by the grey crosses in Fig. 4.5, showing that the model by Fuchs et al. predicts much higher energy values and an approximately 8 times steeper slope.

Eq. 4.2 hence represents the first scaling law specifically for monoenergetic spectra, and verifies—for the first time—that techniques for the generation of intrinsically monoenergetic beams can be extrapolated to higher laser energies. Furthermore, it indicates that the peak energy scales slower than the thermal cutoff energies, and that thermal energy scalings might overestimate the potential of laser ion acceleration when it comes to monoenergetic beams, which are the prerequisite for most applications. Nonetheless, today’s capability of reliably generating  $\leq 10^9$  quasi-monoenergetic protons with less than 10 % bandwidth by means of a scalable technique marks an important step towards application.

### 4.3.2 Peak width scaling

*The average energy spread of the peak scales as the square root of the laser energy. For high laser energies, PIC simulations indicate that the peak approaches a saturation value of  $\approx 2.0$  MeV. Accordingly, the relative energy spread approaches zero at high energies.*

Similar to the peak position scaling, the dependency of the energy spread on the laser energy was investigated. For this purpose, it proved helpful to connect the peak width directly to peak position rather than the laser energy in order to gain immediate information about the relative energy spread. The interpretation of this peak width scaling to be discussed in this section proves to be a difficult task, and still poses some questions which could not be

<sup>9</sup>Note that this value of 15 J is clearly in the range of the upcoming generation of Ti:Sapphire lasers. See discussion in chapter 5.

completely resolved during the course of this thesis. Nonetheless, some tentative results and interpretation shall be presented in the following emphasizing, however, that more work needs to be done on this part.

Fig. 4.6 (black circles) shows the average peak width for the four data points already displayed in Fig. 4.5. Statistical analysis of the sample sets reveals that the average FWHM peak width increases from 0.21 to 0.41 MeV over the peak energy range of 1.42 – 1.63 MeV, which correspond to laser energies of 0.5 – 0.8 J. Like for the energy scaling, the four data points seem to suggest a linear proportionality. However, such a linear scaling would be somewhat surprising, given that the differential of the proton kinetic energy can be written as

$$dE = p dp/m. \quad (4.3)$$

Since the central momentum of the proton bunch  $p$  is furthermore related to the central peak energy as  $p_{\text{peak}} = \sqrt{2mE_{\text{peak}}}$ , one would rather expect a square root scaling  $\Delta E_{\text{peak}} \sim \sqrt{E_{\text{peak}}}$ . Applying thus a square root fit to the data, one finds that the peak width is in good agreement with the following function

$$\Delta E_{\text{peak}}/\text{MeV} = 0.71\sqrt{E_{\text{peak}}/\text{MeV} - 1.34} \quad (4.4)$$

(black dotted line). In comparison, it can be seen that the relative width (plotted in red) increases from 15% to 25% over the observed peak energy range.

However, this fit does still not live up to the complexity of the situation. Despite the apparently good agreement, there is strong reason to doubt that  $\Delta E$  scales uniformly as a square root of the peak position over a wider energy range. In the first place, a square root scaling would imply the absolute peak width to grow infinitely, which is in contradiction to all simulation studies, and also inconsistent with what one would expect from the charge separation model.

A more comprehensive picture can be obtained by taking into account simulation data points. This is shown in Fig. 4.6b. Again, the circles and dotted line represent the experimental data and square root fit, respectively. In addition, the absolute and relative peak widths obtained from various simulations have been inserted as crosses.<sup>10</sup> It can be seen that the simulation data matches the experimental data closely, showing good agreement with the square root fit for low peak energies. However, for high peak energies the peak width is found to run into saturation, leading to a strong deviation from the square root function (note the double-logarithmic scale of Fig. 5.1b). The absolute peak width thereby approaches a limit of  $dE_{\text{sat}} \approx 2.0$  MeV. Due to the steep initial slope of the peak width dependency, the relative peak width first increases to a maximum of 30%, and then decreases monotonously in the saturation region to  $< 1\%$ .

Although the encountering of a saturation behaviour for the peak width seems plausible, it is challenging to try to incorporate it into the above model. One possible explanation for the deviation of the actual data from the square root dependency allocated to the central momentum  $p_{\text{peak}} = \sqrt{2mE_{\text{peak}}}$  could be the fact that the energy spread  $dE$  of Eq. 4.3 does not only depend on the central momentum  $p$ , but also on some intrinsic beam energy spread  $dp$ . This intrinsic spread can be attributed to the initial acceleration dynamics and in particular

<sup>10</sup>The simulation data points include the 2D-PIC results of Figs. 4.2, 5.1 & 5.2, as well as the red and blue plots of the 1D-PIC results presented in Figs. 4.8a-c (i.e. the PDR runs for 50% and 30% proton density to be discussed below, warranting a sufficient comparability).

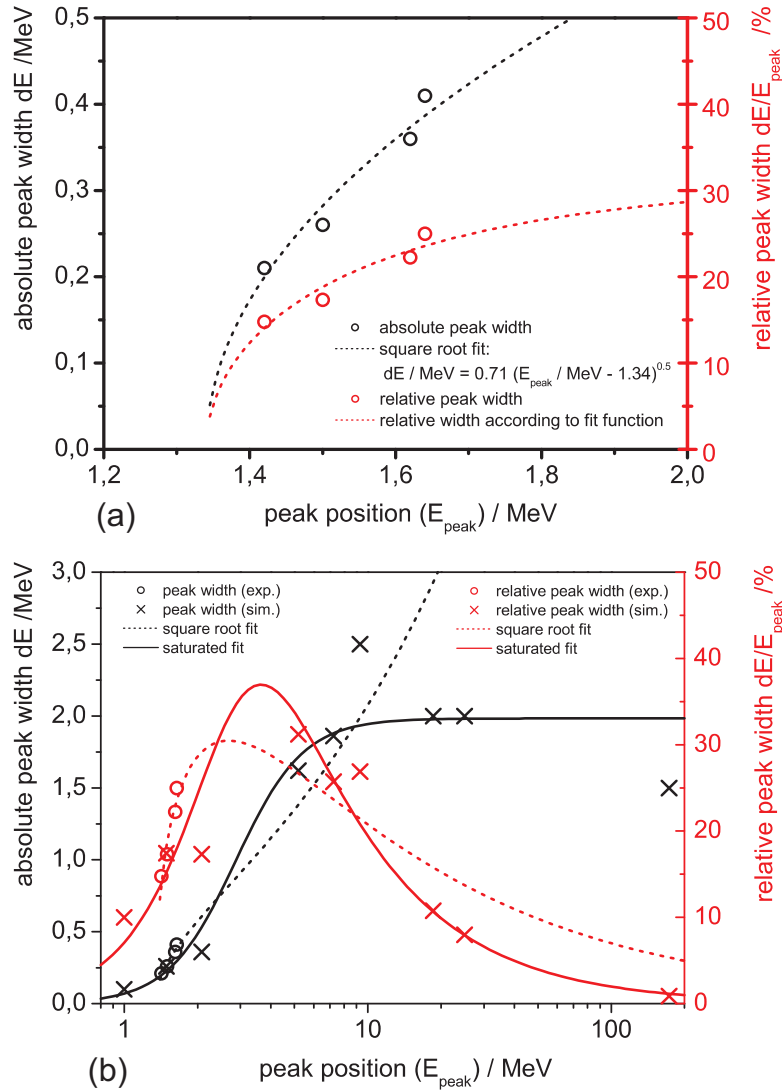


Figure 4.6: Peak width scaling. (a) The dependency of the average peak width on the peak position (black circles) is well fitted by a square root function,  $\Delta E_{\text{peak}}/\text{MeV} = 0.71 \sqrt{E_{\text{peak}}/\text{MeV} - 1.34}$  (black dotted line), which is well in agreement with the differential of the proton kinetic energy,  $dE = p dp/m \sim \sqrt{E}$ ,  $E$  being the central peak energy and  $p$  being the central momentum. This accordance also holds for the relative energy spread (red circles and dotted line). The four data point correspond to the four statistical peak position determined in Fig. 4.5. (b) For higher peak energies, PIC simulations indicate that the peak width runs into saturation at a maximum value of approximately 2.0 MeV, which is in contradiction to the square root fit. This deviation can be explained by the  $dp$ -contribution in the equation for  $dE$ , representing an intrinsic momentum spread. A saturation function has been added to the plot for illustration (black and red solid lines).

the charge separation process. Thus, the interplay of the two contributions  $p$  and  $dp$  may cause that the peak width  $dE$  does not scale uniformly over the whole energy range, but in fact allows for a saturation assuming that the  $dp$  component compensates for the  $p$  growth at high energies. However, this intrinsic spread  $dp$  is much harder to pinpoint analytically, and further experiments will be necessary to study the scaling behaviour over a larger range.

For the sake of illustration, the data points of Fig. 4.6b have been fitted with a standard saturation growth function (Hill function),

$$dE = \frac{(E_{\text{peak}}/\text{MeV})^n}{(E_{\text{peak}}/\text{MeV})^n + k^n} \times dE_{\text{sat}} \quad (4.5)$$

where the best agreement has been found for the parameters  $dE_{\text{sat}} = 2.0 \text{ MeV}$ ,  $k = 2.9$  and  $n = 3.1$ , matching the data closely for all peak positions. The saturation function is given as solid black line in the graph. In addition, the red line shows the relative peak width according to saturation function, i.e.  $dE/E_{\text{peak}}$ .

## 4.4 Target composition and the “Proton Density Reduction” scheme (PDR)

### 4.4.1 Impact of the heavy ion background on the proton spectrum

*The target composition determines the properties of the ion fronts involved in the charge separation during the acceleration process. PIC simulations indicate that a background of ions with large  $q/m$ -ratio (e.g. deuterium) facilitates the formation of narrow peaks at higher energy.*

Besides laser parameters, ablation characteristics, and target geometry, also the dot composition must be considered for the optimization of the acceleration process, which shall be the subject of the following sections. It has been elaborated above how the spectral peak is associated to the charge density gradient and the related electrostatic shock at the fastest heavy ion front. The magnitude and form of this crucial charge discontinuity is determined by the relative numbers of light and heavy ions in the beam, as well as by their specific ion charge state. Both parameters can be expected to influence the constitution of the sheath field, and hence to a great extent also the overall acceleration dynamics.

The impact of the heavy ion species on the proton peak was studied with 1D-PIC simulations carried out by Alex Robinson [55], using the same code as described in section 2.5. The results of this study can be seen in Fig. 4.7. Here, the black line gives the proton spectrum for a  $\text{C}^{4+}$  background, and the red line the spectrum for a  $\text{C}^{6+}$ -background. In both cases, the laser intensity was  $I = 1.0 \times 10^{19} \text{ W/cm}^2$ , and the initial particle densities were  $10 n_c$  and  $40 n_c$  for protons and carbon ions, respectively.<sup>11</sup> It can be seen that the choice of the background species influences the spectrum significantly: The proton peak for the  $\text{C}^{6+}$ -background displays a much smaller energy spread (0.1 MeV) and is also located at a higher energy (4.1 MeV) than for the  $\text{C}^{4+}$ -background, where the peak is found at 2.8 MeV with 0.4 MeV spread. This difference is plausible since an increased  $q/m$ -ratio corresponds to a higher expansion velocity of the heavy ion front, resulting in a proton trapping and ballistic flow at a higher kinetic energy.

<sup>11</sup>The reduced proton density is the reason behind the slightly increased peak energy in comparison to Fig. 4.2, which will become clear immediately.

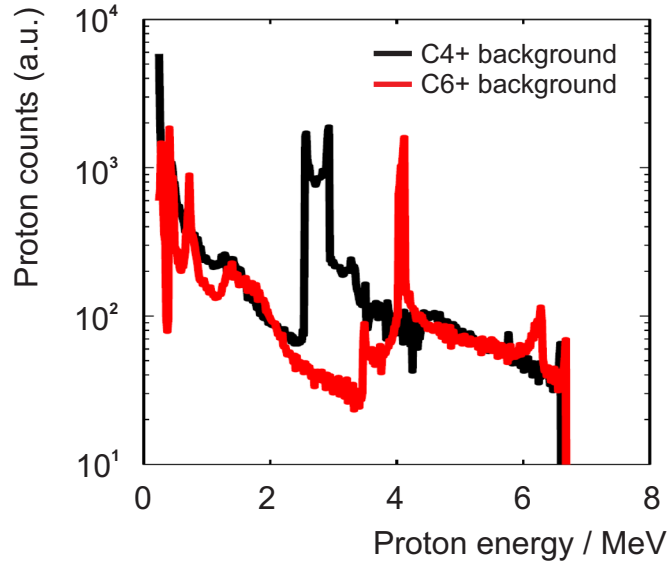


Figure 4.7: Impact of the heavy ion background species on the generation of monoenergetic spectra [55]. Proton acceleration from microdot targets was studied in 1D-PIC simulations for different heavy ion backgrounds. For a  $C^{4+}$ -background (black line), the proton peak is found located at  $\approx 2.8$  MeV with an energy spread of about 0.4 MeV, whereas for  $C^{6+}$  the peak is located at 4.1 MeV and has a width of 0.1 MeV. This difference demonstrates that the choice of the target composition has a considerable influence on the peak formation, indicating the advantageousness of a background ion species with high  $q/m$ -ratio, e.g. deuterium. The simulation results can be explained by the higher expansion velocity of  $C^{6+}$  in the electric field, resulting in a proton bunch formation at a higher kinetic energy.

Generally, the simulation results indicate that high charge states are preferable as background material. In the particular case of JETI, where the observed maximum ion charge state for carbon is typically  $C^{4+}$ , this suggests the use of proton-deuterium mixtures as target composites, as deuterium has the same  $q/m$ -ratio as  $C^{6+}$ . The  $q/m$ -ratio could thus be potentially improved from  $(q/m)_{C^{4+}} = 0.3$  to  $(q/m)_{D^+} = 0.5$ , thus enabling an enhanced narrow-band proton acceleration from the dot microstructures. In section 4.4.3, some experimental results will be presented which this approach.

#### 4.4.2 PDR theory & simulation studies

*PIC simulations indicate that the peak energy can be enhanced significantly by reducing the initial proton density in the dot. The rarefied protons behave like test-particles at the ion front, leading to a more pronounced peak formation at higher energies. This effect is predicted to saturate at proton density of a few percent.*

Let us now consider the impact of the relative particle densities at the heavy ion front. Again, it is instructive to recall that the monoenergetic peak is formed by those protons passing the heavy ion front and probing the subsequent ion sheath field. Evidently, the charge density gradient is steepest and hence the sheath field is strongest if the total positive charge ahead of the ion front attains a minimum, in which case the field is depleted the least. The theory holds that the mechanisms of proton trapping and ballistic proton flow work best if the trapped

Run (colour in Fig. 4.8)	$n_p/\text{cm}^{-3}$	$n_p/n_c$	relative density /%
black	$8 \times 10^{22}$	80	67
red	$4 \times 10^{22}$	40	50
<i>not displayed</i>	$2 \times 10^{22}$	20	33
green	$1 \times 10^{22}$	10	20
blue	$1 \times 10^{21}$	1	2.4
<i>not displayed</i>	$1 \times 10^{20}$	0.1	0.25

Table 4.2: Simulation parameters of the 1D-PIC simulation for the Proton Density Reduction (PDR) scheme.

Note that  $n_i = 40 n_c$  and the heavy ion species was chosen to  $\text{C}^{4+}$ , which matches the use of polymer dots at JETI.

proton bunch itself does not influence (i.e. deplete) the density gradient. This essentially requires the proton number to be small compared to the number of heavy ions, implying that the protons probe the sheath field in a test-particle like fashion. These above arguments have stimulated the idea of using targets with low initial proton density in the source layer in order enhance the monoenergetic beams obtained from Confined TNSA.

This “Proton Density Reduction” scheme (PDR) was explored in several theoretical works led by Robinson (see e.g. [55, 62]), which proved that the spectral peak position can indeed be shifted to significantly higher energies if the initial proton density in the target material is decreased below the regular hydrogen content of 53% in PMMA. The PDR hypothesis has led to a series of experiments at JETI using highly deuterated PMMA as the dot source material, which also comply with the above reasoning about the preferability of a deuterium background. These experiments will be introduced in section 4.4.3.

Prior to the experimental studies, however, the PDR scheme was thoroughly investigated with the help of simulations by Alex Robinson across a wide range of parameters and under specific consideration of JETI acceleration conditions, providing a roadmap for an experimental implementation. Moreover, extensive scaling studies in 1D, 2D and 3D were carried out for the three different intensity regimes  $10^{19} \text{ W/cm}^2$ ,  $10^{20} \text{ W/cm}^2$  and  $10^{21} \text{ W/cm}^2$  [55]. In the simulations, the targets are typically considered to have fixed heavy ion density of  $40 n_i$  with  $\text{C}^{4+}$  as the heavy ion species (if not indicated otherwise), and the proton density is varied between  $80 n_c$  and  $0.1 n_c$ . The simulations generally assume a laser wavelength of  $1 \mu\text{m}$ , and  $n_c$  is the critical density at this wavelength.

## 1D simulations

Three sets of six simulations each were carried out in 1D using the 1D3P electromagnetic PIC code with the specifications previously discussed in section 2.3.3. In each set, a systematic proton density scan was performed at a certain intensity, with proton densities ranging from  $n_p = 80 n_c$  to  $n_p = 0.1 n_c$  in front of a heavy ion background of  $\text{C}^{4+}$  at  $40 n_c$ , corresponding to a relative proton content of 67% to 0.25% in the target. The exact parameters are given in table 4.2.

The results of this 1D study are shown in Fig. 4.8. The top graph comprises the six runs at  $I = 10^{19} \text{ W/cm}^2$ , whereas the middle and bottom graphs display runs at  $10^{20} \text{ W/cm}^2$  and  $10^{21} \text{ W/cm}^2$ , respectively. A strong dependency of the peak position in the spectrum on the proton density is observed at all three intensities. The proton peak energy increases

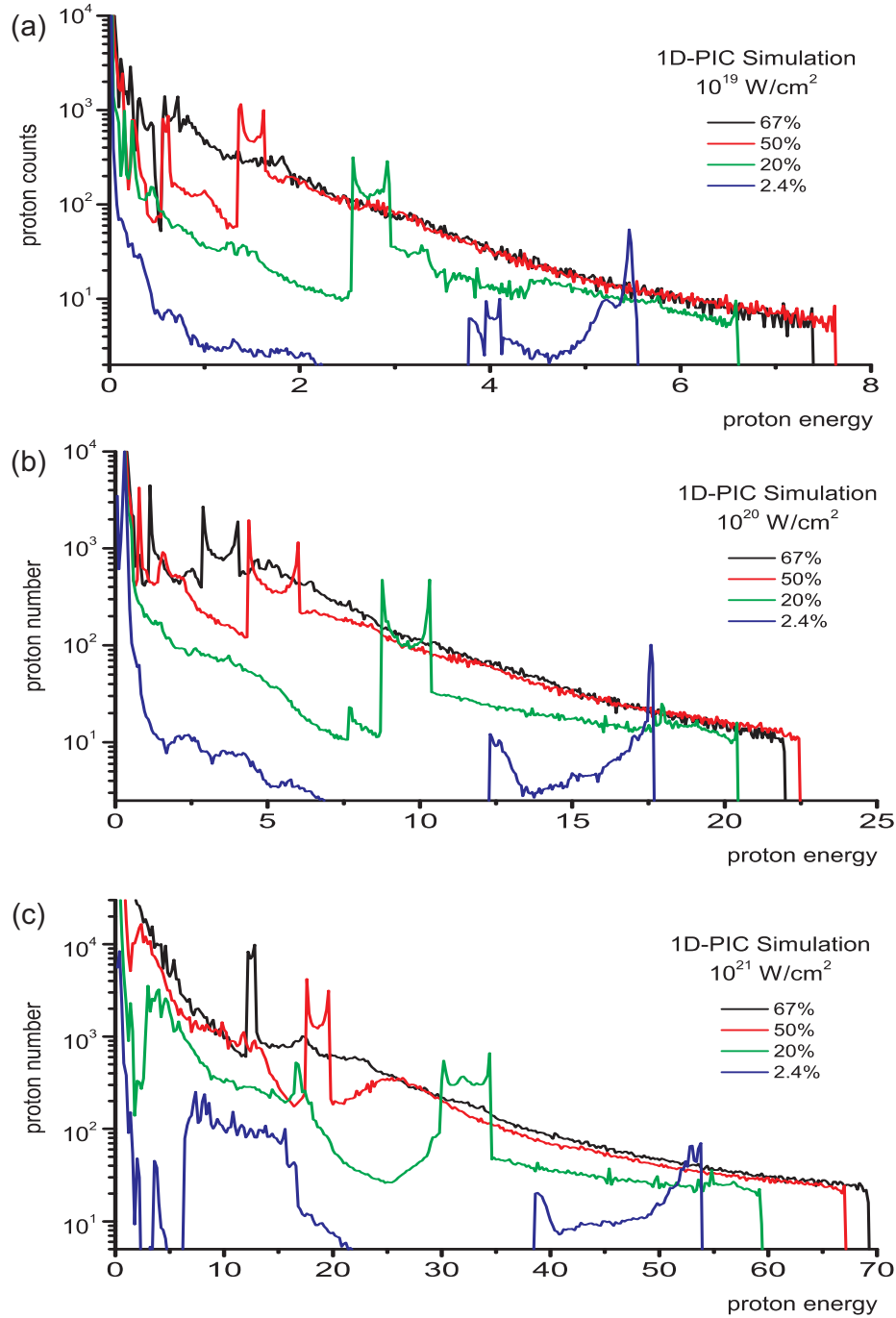


Figure 4.8: PDR studies with 1D-PIC simulation [? ]. Three series of 1D-PIC simulations were carried out by Alex Robinson for microdots with different initial proton densities (cf. figure legends) at different intensities ( $10^{19} \text{ W/cm}^2$ ,  $10^{20} \text{ W/cm}^2$ ,  $10^{21} \text{ W/cm}^2$ ). The spectral peak features, which take the form spiked towers in the 1D simulations, sit on top of the exponential background and can be seen to move to higher energies when decreasing the proton density. This increase in peak energy shows that the proton beams from microdot targets can be improved significantly when varying the target composition appropriately. For the lowest two density (2.4%), the peak intensity drops below the regular exponential high energy tails, which indicates a theoretical gain limit for the PDR scheme. The parameters used in the four simulations are summarized in table 4.2. Note that of the 6 density runs performed at each intensity, only 4 are displayed in the graph for the sake of clarity.



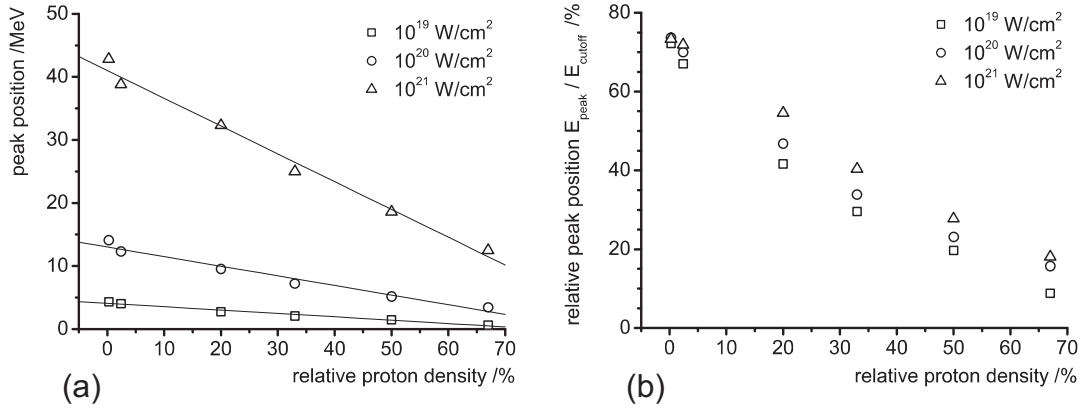


Figure 4.9: PDR peak energy scaling as a function of the initial proton density (1D-PIC).

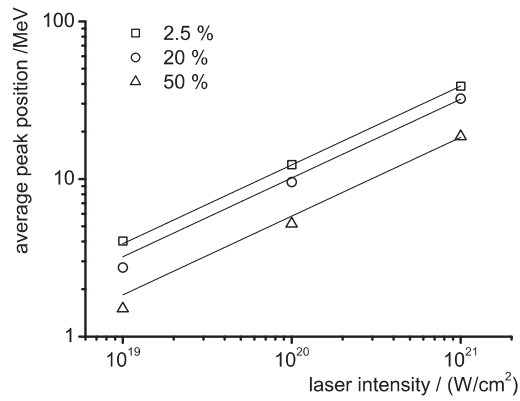


Figure 4.10: PDR peak energy scaling as a function of the laser intensity for different initial proton densities (1D-PIC).

continuously with decreasing proton density. The proton peak takes the form of a tower on top of an exponential background, flanked by two characteristic spikes. These spikes are known to be an 1D simulation artifact and disappear for the 2D and 3D runs (cf. below).<sup>12</sup> At the same time, the maximum proton energy of the thermal part of the spectrum can be seen to decrease systematically when reducing the proton density.

Note that for very low proton densities (2.4% and 0.25%), the proton peak drops below the exponential part of the high density spectra, which is in agreement with the fact that the total number of protons available for acceleration decreases as the proton density is reduced. Therefore, although the energy of the spectral peak continues to increase for these low density cases, there exists an optimum proton density below which the PDR scheme provides no further benefit, i.e. where the number of protons per energy interval in the peak will *necessarily* be smaller than the number accelerated from a conventional target. This specific density represents a “gain limit”, which for the current simulations can be identified to lie between the two runs at 2.5% and 20%. Furthermore, the spectrum attains a completely different shape in these low density runs. In the 2.4% run (cyan spectra), a second spectral peak located at the end of the spectrum can be seen to exceed the high density spectra, notwithstanding the fact that the spiked tower has disappeared almost completely. Note, however, that this peak contains only a negligible total number of protons.

The result of the simulations can be summarized in a set of peak energy scalings, which are plotted as a function of the proton concentration and the laser intensity in Figs. 4.9 and 4.10, respectively. It can be seen that for the density range under consideration, the peak position increases roughly linearly with decreasing proton density for all intensities (Fig. 4.9a). Similarly, the relative peak position  $E_{\text{peak}}/E_{\text{cutoff}}$  can be seen to increase roughly linearly for all three intensities up to a maximum of  $\approx 0.7 E_{\text{cutoff}}$  at very low proton densities (Fig. 4.9b). In Fig. 4.10, the scaling of the peak position with laser intensity is given for the three target compositions of 2.4%, 20% and 50% relative proton content, respectively. It turns out that for all compositions the data points are well fitted by an expression of the type  $E_{\text{peak}} \sim \sqrt{I_{19}}$ , where  $I_{19}$  is the laser intensity in units of  $10^{19} \text{ W/cm}^2$ . This proportionality is reasonable for a 1D calculation, as the velocity of the heavy ion front and hence the velocity of the monoenergetic proton bunch is proportional to the ion acoustic velocity, and the ion kinetic energy scales as  $E_{\text{peak}} \sim c_s^2 \sim T_e$  with  $T_e \sim \sqrt{I_{19}}$  (cf. Eq. 2.11).

## 2D simulations

A second series of numerical simulations regarding PDR was performed using the 2D3P OSIRIS code previously discussed in sec. 4.1. Here, the calculations were run on a spatial grid of  $8000 \times 8000$  cells of dimension  $(0.16 c\omega^{-1})^2 \approx (25 \text{ nm})^2$ . Like in the earlier sections, the target consisted of a slab of proton-free substrate material carrying a microdot on the rear surface. The slab of substrate material was  $10 \mu\text{m}$  wide and  $1 \mu\text{m}$  thick, and consisted of ions with a  $q/m$ -ratio of  $1/3660$  at a density of  $80 n_c$ , with equal electron density to obey charge neutrality. The microdot was  $4.8 \mu\text{m}$  wide and  $0.32 \mu\text{m}$  thick, and was located in the center of the substrate rear side. The dot consisted of a variable mixture of protons and ions with a  $q/m$ -ratio of  $1/2 \cdot e/m_p$ , corresponding to a deuterium background for the charge separation. The exact compositions in the various runs are given in table 4.3.

<sup>12</sup>As a matter of fact, the sharp peaks are associated with the turning points of sine-wave like structure in the proton phase space as discussed for Fig. 2.6.

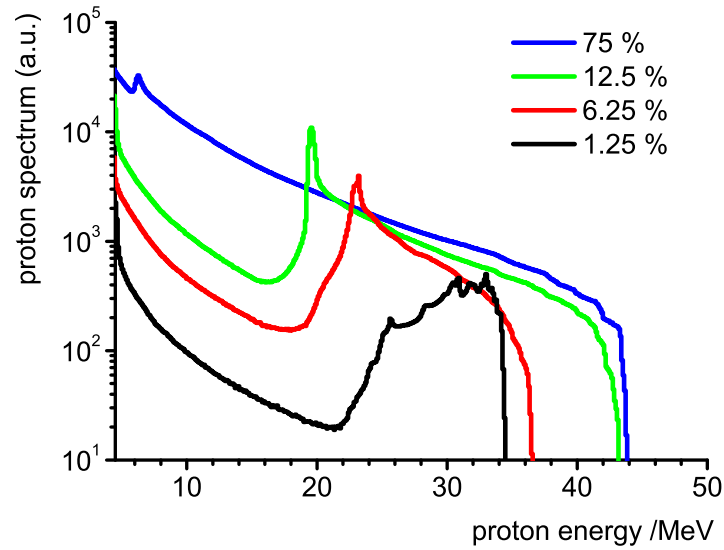


Figure 4.11: PDR studies with 2D-PIC simulations [55]. Four 2D runs for microdots with different initial proton densities were carried out with the OSIRIS code. Similar to the 1D simulations, the peak energy increases when decreasing the proton density in the dot source, and a gain limit is approached for very low densities. The parameters used in the four simulations are summarized in table 4.3.

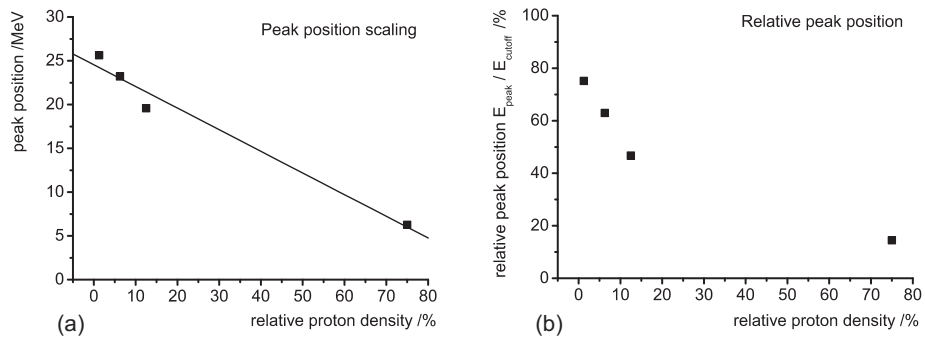


Figure 4.12: PDR peak energy scaling as a function of the initial proton density (2D-PIC).

Run (colour in Fig. 4.11)	$n_p/\text{cm}^{-3}$	$n_p/n_c$	relative density /%
Blue	$6 \times 10^{22}$	60	75
Green	$1 \times 10^{22}$	10	12.5
Red	$5 \times 10^{21}$	5	6.25
Black	$1 \times 10^{21}$	1	1.25

Table 4.3: Simulation parameters of the 2D-PIC simulation for the PDR scheme. For all runs, the intensity was  $I = 10^{21} \text{ W/cm}^2$ ,  $n_i = 80 n_c$ , and deuterium was chosen as the heavy ion species.

In the simulations, each cell contained 64 quasi-particles representing electrons, 64 representing protons, and 32 representing heavy ions. The laser pulse has a triangular temporal profile with a total pulse duration of 80fs, and impinges on the substrate front side under normal incidence. The FWHM intensities were set to  $10^{21} \text{ W/cm}^2$ , with a transverse  $1/e$ -width of the Gaussian laser pulse of  $40 c\omega^{-1} \approx 6.4 \mu\text{m}$ . All simulations were run up to 250 fs.

The results of the 2D-PIC studies for the PDR scheme are shown in Fig. 4.11. Similar to the 1D runs, the peak position in the spectrum increases when moving to lower proton densities, whereas the cutoff energy simultaneously decreases. In good accordance with the above results, a gain limit is observed at very low density. This time, the gain limit appears between  $n_i = 1n_c \dots 5n_c$ , which corresponds to a relative hydrogen concentration of 1.25% to 6.25% in the target, setting further constraints to the gain limit density range obtained from the 1D simulations. The results are again summarized in a density scaling plot for both the absolute and the relative peak position in the spectrum, where the central peak energy is once more found to increase in a roughly linear fashion with the proton density for the evaluated density range (cf. Fig. 4.12).

#### 4.4.3 PDR experiments

*Experimental PDR studies fully confirm the theoretical predictions: An increase of the average peak energy is observed when reducing the initial proton density, where for each density the peak position still scales with laser energy. No gain saturation is observed.*

A series of experiments was carried out at JETI to verify the predicted PDR effects on microdot acceleration. Acknowledging the specific results of the above PIC simulations, microstructured targets with strongly reduced proton concentration were designed, featuring deuterium as the leading heavy ion species. For this purpose, highly deuterated PMMA<sup>13</sup> which was diluted with different fractions of regular PMMA in order to obtain well-defined hydrogen concentrations in polymer microdots to be accelerated in front of a strong deuterium background. Similar to the conventional PMMA dot targets, the mixed polymer was applied on 2 – 5  $\mu\text{m}$  titanium foils via spin coating, resulting in homogeneous layers of 400 nm thickness. The layers were microstructured using the fs laser system as described in section 3.1.

In the course of the PDR experiments, several hundred shots on low-density microdots were carried out and evaluated statistically. The dot compositions applied in the experiment are given in table 4.4. As expected, a systematic increase of the central peak energy is

<sup>13</sup>Deuterated PMMA (dPMMA) resembles regular PMMA apart from the fact the hydrogen contributions in the polymer are substituted by the chemically equivalent deuterium. The purity of the dPMMA was  $n_{\text{dPMMA}} : n_{\text{PMMA}} > 99.5\%$ . The dPMMA samples were commercially obtained from Deutero GmbH, Kastellaun, Germany, and processed into a photo-resist suitable for spin coating by Allresist GmbH, Strausberg, Germany.

Colour Fig. 4.14b	$n_{\text{PMMA}} :$ $n_{\text{dPMMA}}$	total proton density /%	$E_{\text{peak}}/\text{MeV}$ at $E_{\text{laser}} = 0.6 \text{ J}$	$\sigma(E_{\text{peak}})/\text{MeV}$ at $E_{\text{laser}} = 0.6 \text{ J}$
Black	pure PMMA	53	1.50	0.28
Orange	10:1	45	1.63	0.26
Red	1:4	10	1.68	0.24
Blue	1:10	5	1.67	0.28
Green	1:50	1	1.75	0.55
Cyan	1:100	0.5	1.80	0.21

Table 4.4: Composition of deuterated polymer microdots used for the PDR study.

observed when the proton density is reduced. In Fig. 4.13, it can be seen that average peak position raises when the proton density is reduced, growing approximately linearly from  $E_{\text{peak}} = 1.5 \text{ MeV}$  at a hydrogen concentration of 53%, to  $E_{\text{peak}} = 1.8 \text{ MeV}$  at 0.5%.<sup>14</sup> All shots contained in Fig. 4.13 were taken at a laser energy of  $E_{\text{laser}} = 0.6 \text{ J}$  on target ( $\simeq 3.5 \times 10^{19} \text{ W/cm}^2$ ) under similar conditions. The error bars in the Fig. a represent the standard deviation of the statistical sample sets.

The observed energy increase from 1.50 MeV to 1.80 MeV when reducing the proton density from 53% to 0.5% equals a relative rise in peak energy of 20%. Although the gain is not as strong as predicted by the simulations, this proves that the generation of monoenergetic protons can be significantly enhanced with the PDR scheme.

An more detailed overview about PDR results for different laser energies is given in Fig. 4.14. In Fig. 4.14a it can be seen that independent of the laser energy, a reduction of the proton density causes a similar increase of the peak position. The green plot represents the same data as shown in Fig. 4.13. In particular, the detailed plots for 0.6 J and 0.7 J (green and red line) indicate that the initially moderate rise in peak energy is succeeded by a much steeper increase at very low proton densities, resulting in an average peak position as high as 2.13 MeV for a density of 0.5% at 0.7 J laser energy.

Fig. 4.14b shows the same data, rearranged to provide information about the energy scalings for the single densities under consideration. Here, the black curve corresponds to the systematic energy scan performed for regular PMMA dot as discussed for the scaling law in section 4.3. For all densities, the peak position is found to increase consistently with laser energy, very much in agreement with the previous findings. The results presented in Fig. 4.14 fully supports the PDR hypothesis, and underscores the feasibility of the PDR scheme for the improvement of the monoenergetic spectra obtained from Confined TNSA.

It shall be annotated that, contrary to the simulations, no explicit gain limit could be determined during the PDR experiments. Although the reproducibility for the 0.5% and 1.0% densities was comparably low, no actual depletion of the proton signal was observed.<sup>15</sup> A thorough investigation of the effects of gain limitation will be the subject of future experiments.

Let us briefly summarize the results of the target composition studies. A substantial increase

<sup>14</sup>Note the semi-logarithmic scaling in Fig. 4.13

<sup>15</sup>For example, the reproducibility rate at 1.0% was  $\approx 13\%$  as opposed to  $\approx 53\%$  at 10% proton density. Note that these comparably low overall rates are most likely due to difficulties encountered during the fabrication and alignment procedure of the deuterated targets rather than the PDR acceleration mechanism itself.

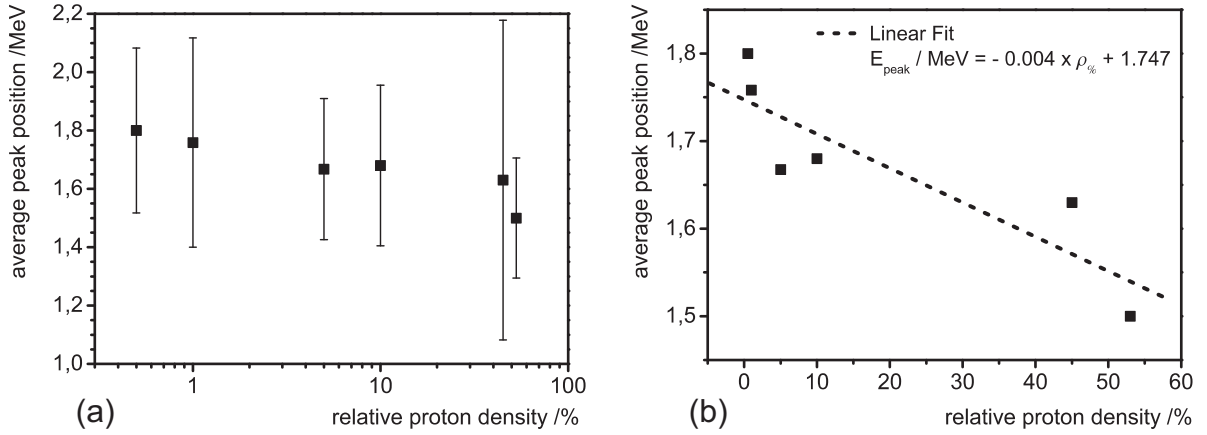


Figure 4.13: Scaling of the peak position as a function of the initial proton density at a laser energy of  $E_{\text{laser}} = 0.6 \text{ J}$  on target. As expected from the numerical studies, the peak position consistently increases when the proton density is reduced. For proton densities varying from 53% to 0.5%, the average peak position is found to rise from 1.5 MeV to 1.8 MeV. Figs. a and b represent the same data, plotted linearly and logarithmically with density, respectively. The error bars in Fig. (a) represent the standard deviation of the sub-sets. A linear fit has been added to the plot in Fig (b), where the error bars have been omitted for the sake of clear display, resulting in a dependency of  $E_{\text{peak}}/\text{MeV} = -0.004 \times \rho_{\%} + 1.747$ ,  $\rho_{\%}$  being the proton density in percent.

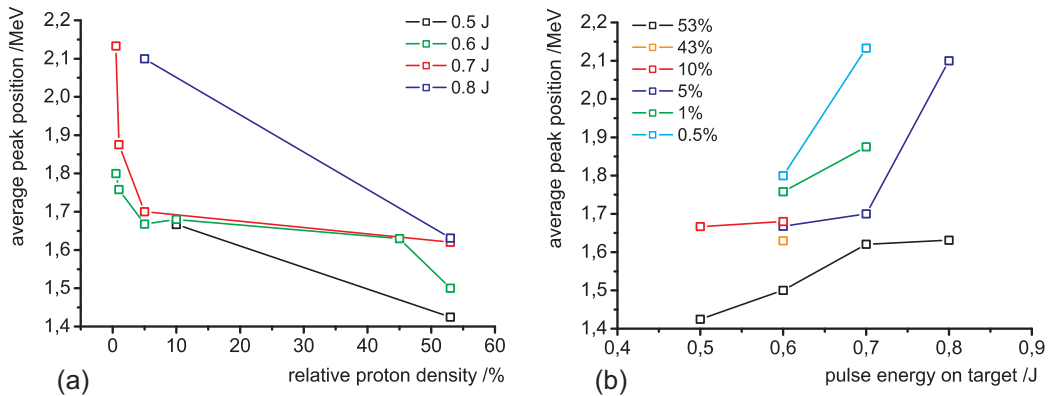


Figure 4.14: Scaling of the peak position with proton density and laser energy. (a) For all laser energies, the average peak position is found to increase when decreasing the proton density, which is well in accordance with the PDR theory. (b) The PDR data has been arranged to provide information about the peak position scaling with laser energy for each proton density. The observed proportionality is in agreement with the scaling law discussed in section 4.3, plotted here in black. The results of the PDR study demonstrate that the quality of the monoenergetic beams can be improved significantly by reducing the initial proton density in the microdot, which can be achieved for example by the replacing the hydrogen in the dot by deuterium.

of the peak energy is observed if the relative fraction of the leading ion species in the source layer (i.e. protons) is decreased to a few percent or less. This observation is supported by multidimensional PIC simulations, which predict the same (roughly) linear dependency of the peak energy as found in the experiments. Both experiment and simulation hold that the relative peak position can be improved to 3/4 of the thermal proton cutoff energy. A similar increase in peak energy is observed independent of the applied laser energy. At the same time, for each proton density the peak position scales with laser energy, which is excellent accordance with the previous scalability studies. The simulations indicate that PDR benefits can be expected at intensities up to  $10^{21}$  W/cm<sup>2</sup>, which underlines the importance of the current findings with respect to future laser systems (cf. section 5.1). Furthermore, simulations show that a heavy ion species with large  $q/m$ -ratio is beneficial for the acceleration process, both in terms of peak position and peak width. This suggests the use of deuterated target materials as implemented during the PDR experiments. The PDR findings point out a promising way to generate enhanced monoenergetic proton beams, achieving peak energies comparable to the cutoff energies of thermal spectra obtained from conventional TNSA while containing more protons per bandwidth interval.

## 4.5 Monoenergetic ion beams

*The microdot geometry can be transferred to other target material in a straightforward manner. Monoenergetic carbon beams with a typical peak energy of 3 MeV and 20% bandwidth are observed from the irradiation of tungsten carbide dots on a titanium foil.*

The successful implementation of PDR using deuterated targets indicates that the physical mechanisms of Confined TNSA should be generalizable to other target compositions. In particular, the question arises if Confined TNSA can be utilized to create narrow-band beams of other ion species. To answer this question, let us briefly reconsider the two central requirements for monoenergetic acceleration—radial source confinement and charge separation between multiple ion species. According to these requirements, one only needs to find a source material where the lightest ion species is not hydrogen, and furthermore ensure that this material can be provided in dot-like sources.

Both conditions should pose no insurmountable problem: Many inorganic materials such as metals, oxides or carbides can be easily applied to substrates in the form of ultra-thin layers for example using sputtering techniques, and are regularly processed to micro- or nanostructures. Nonetheless, the fabrication of such “heavy ion dots” on thin foils is far from being an easy task and requires subtle engineering.

Among all possible ion beams, carbon beams are of specific interest for application purposes (cf. discussion in chapter 5). Consequently, this thesis engaged in manufacturing targets with carbon as the lightest ion species. Such *carbon dot targets* were designed by sputtering a 200 nm layer of tungsten carbide (W<sub>4</sub>C) onto a 5 μm titanium foil. W<sub>4</sub>C represented the layer material of choice as it represents a standard sputtering material. The sputtering was performed at the Fraunhofer-Institut für Angewandte Optik und Feinmechanik (IOF) in Jena, and the obtained layer was microstructured similar to the PMMA-layered targets via femtosecond laser ablation, producing arrays of square dots with 10 – 25 μm base length.<sup>16</sup>

<sup>16</sup>Note that the use of compound materials such as W<sub>4</sub>C is not strictly necessary and was only chosen for pragmatic reasons. The required criterion of charge separation between two different ion fronts would in principle be fulfilled by the different degrees of ionization of one heavy element already (e.g. C<sup>3+</sup> vs. C<sup>4+</sup>).

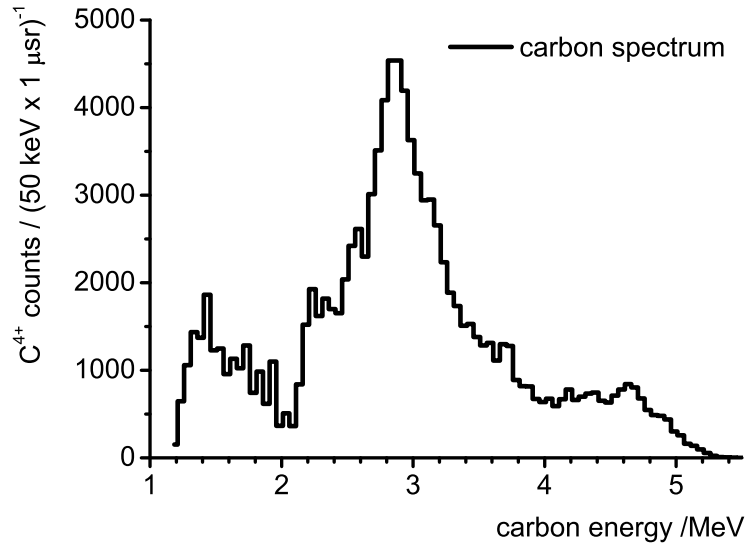


Figure 4.15: Monoenergetic carbon spectrum. The Confined TNSA scheme can be easily transferred to other dot materials. Narrow-band  $C^{4+}$  beams were observed from the irradiation of tungsten carbide ( $W_4C$ ). This demonstrates that in principle any type of monoenergetic ion beam can be produced by Confined TNSA if suitable targets are available, broadening significantly the scope of the present work.

The ion-dot targets were implemented and aligned in the JETI setup like a conventional polymer-dot target, and subjected to the same careful ablation testing procedures as described above. Good ablation results (i.e. a sufficient suppression of the parasitic proton contributions) were obtained for fluences  $\geq 4 \text{ J/cm}^2$ , which is slightly higher than for the polymer microdots.<sup>17</sup>

Fig. 4.15 shows an exemplary narrow-band spectrum of  $C^{4+}$  recorded for a JETI pulse intensity of  $I = 1.7 \times 10^{19} \text{ W/cm}^2$ , after 10 consecutive ablation shots at 10 Hz repetition rate with an ablation fluence of  $8.2 \text{ J/cm}^2$ . The spectrum displays a strong peak centered at an energy of  $E_{\text{peak}} = 2.9 \text{ MeV}$ , which corresponds to a kinetic energy per nucleon of about  $0.24 \text{ MeV/u}$ ,  $u$  being the atomic mass unit. The peak possesses an FWHM energy spread of  $0.6 \text{ MeV}$  ( $\cong 21\%$ ) and can be seen to continue with an exponential tail towards higher energies. Similar to the polymer dots, this tail is the result of the fastest  $C^{4+}$  ions ahead of a slower successor ion fronts. For the particular spectrum displayed in Fig. 4.15, the ion species with the next lower  $q/m$ -ration was determined from the MCP image to be  $C^{3+}$ . In other shots,  $Ti^{12+}$  was observed as the next lower species. Note that

The experimental results obtained from  $W_4C$ -dot on a titanium foil prove that the Confined TNSA scheme is straightforward transferable to other dot materials, and that hence any desired type of monoenergetic ion beam can in principle be produced from laser plasma interaction. Although the overall reproducibility for monoenergetic heavy ion beams was still rather low in comparison to the proton beams, this represents an important generalization of

<sup>17</sup>Despite the ablation, faint proton traces were regularly observed next to the carbon traces in the MCP images, which could be ascribed to hydrogen inclusions in the tungsten carbide. Note that in many cases, the accompanying proton traces were peaked as well.



the technique presented in this thesis and significantly broadens the scope of Confined TNSA for application. This fact is of particular importance since several applications for laser accelerators do in fact aim at ion beams rather than proton beams, which will be discussed for the case of medical ion beam therapy in section 5.3.2.

## 4.6 Multiple peak structures

*Multiple peak structures are occasionally observed in the proton spectra. These double and triple peaks can be attributed to the shock acceleration at multiple ion fronts (e.g. different carbon degrees of ionization).*

Besides the narrow-band spectra centered at one distinct peak energy in the spectrum, also proton spectra with multiple peak structures are observed in the micro-dot experiments. This observation is well in agreement with the acceleration model: The formation of monoenergetic proton bunches is related to the electrostatic shock resulting from the charge discontinuity at the successor ion species, i.e. typically  $C^{4+}$ . However, similar charge discontinuities exist at slower heavy ion fronts such as the carbon charge states  $\leq C^{3+}$ , or the titanium contributions from the foil bulk. Therefore, the charge separation mechanism responsible for the generation of monoenergetic peaks occurs also at lower proton kinetic energies, leading to multiple peaks in the spectrum.

Fig. 4.16 shows a typical spectrum with multiple modulations, recorded during the PDR experiments for a microdot with 0.5% initial proton density at a laser energy of 0.6 J on target.

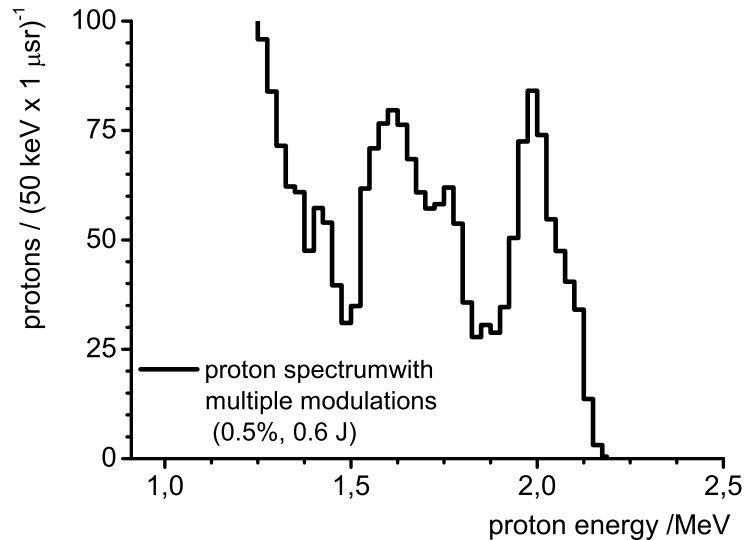


Figure 4.16: Proton spectrum with multiple peak structures. Occasionally, the formation of multiple peaks is observed in the proton spectra. The black curve represents a shot on a dot with 0.5% initial proton density at a laser energy of 0.6 J. Two pronounced peaks are visible at 2.0 MeV and 1.6 MeV, respectively, resulting from multiple charge separations at the different heavy ion fronts (e.g.  $C^{4+}$  and  $C^{3+}$ ).

Two distinct peak features are visible, centered at 2.0 MeV and 1.6 MeV, respectively. Multiple peak structures have been observed for all proton densities, but particularly frequently occur at low proton densities, which can be attributed to the more test particle-like acceleration, enabling pronounced peak formation over wide parts of the spectrum.

The phenomenon of multiple peak formation shall be touched upon only briefly here. More theoretical modelling regarding multi-species effects, as well as continuing experimental work, will be necessary to account for the physical processes at stake in a satisfactory manner.

## 4.7 Alternative approaches to narrow-band ion beams

*Several other techniques for the generation of monoenergetic ion beams have been discussed in the literature. These techniques can be categorized as either using charge separation effects [52, 167] or ultra-strong sheath fields to gate certain parts of the proton spectrum [195, 196].*

For the sake of comparability and completeness, a number of complementary techniques for the generation of monoenergetic ion beams from laser plasma interactions shall be presented. All these techniques have been developed specifically for laser accelerators and refrain from the magnetostatic beam shaping devices known from conventional accelerators. The techniques shall be discussed only shortly, pointing out differences and commonalities to the microdot setup where appropriate. For a more detailed review, please refer to the canonical references listed in the respective sections.

### Monoenergetic ion beams from ultra-thin carbon layers

In experiments carried out by Hegelich et al. [52] at the Trident Nd:glass laser (20 TW, 0.8 ps) at Los Alamos National Laboratory, the generation of monoenergetic  $C^{5+}$  and  $C^{6+}$  ions from an extended ultra-thin layer of graphitic carbon on a 20  $\mu\text{m}$  palladium foil was demonstrated. The carbon layers were created by catalytic decomposition of adsorbed hydrocarbon impurities, which arises after the target is resistively heated to a temperature of 1100 K, and were determined to be approximately  $\approx 10 \text{ \AA}$  thick. The resistive heating also warranted that parasitic proton contributions from the contamination layers were removed from the surface, similar to the effects of laser ablation in the JETI experiments

The recorded spectra showed monoenergetic features for the highest carbon charge state at a mean energy of typically 3 MeV per nucleon and 17% energy spread. The explanation for the observation of monoenergetic ions put forth by Hegelich et al. is somewhat related to the ultra-thin layer arguments presented in the Esirkepov/Bulanov model (section 2.3.2) and relies on “initial charge separation” between consecutive degrees of ionization as discussed by Brantov et al. [166] and in section 2.3.3. The  $C^{5+}$  or  $C^{6+}$  ion layer detaches from the substrate as a whole and propagates ahead of the slower ions as a directed bunch. For the ultra-thin carbon layer with high charge states and the heavy palladium background, the model predicts a clean separation between the expanding fronts.

The explanation provided by Hegelich et al. relies on a 1D model and does thus not explicitly account for the transverse inhomogeneity of the electric field. The observed monochromaticity can be assumed to be due to the high laminarity of the beam as discussed in [17] and in section 4.1.2, which causes that only ions from a certain initial position on the foil (and hence a well-defined kinetic energy) are observed through the pinhole.

On the other hand, a certain proximity between the results by Hegelich et al. and the Confined TNSA model becomes evident when considering the following 2D argument: In

a 2D case, the field strength decays in transverse direction. Therefore, the highest carbon charge state is only produced in a well-localized central region. The different degrees of field ionization associated with the inhomogeneous TNSA field create a natural limit of the carbon source size and hence automatically satisfy the geometrical prerequisites for Confined TNSA. This phenomenon is supported by the particularly large gap between the ionization energies of the  $C^{4+}$  and  $C^{5+}$  state, which are separated by more than a factor of 6 ( $E_{\text{ion}}(C^{4+}) = 64.5 \text{ eV}$ ;  $E_{\text{ion}}(C^{5+}) = 392.1 \text{ eV}$ ). Because of this difference, the  $C^{5+}$ -region will be sufficiently small and distinctly demarcated in order to warrant a dot like carbon source. The charge separation effects discussed in sections 2.3.3 and 4.5 hold true in this case, even for the thicker layers mentioned in [52].

### Monoenergetic deuterons from droplet targets

A paper by Ter-Avetisyan et al. [167] from the Max-Born-Institute in Berlin reported the emission of quasi-monoenergetic deuteron beams from heavy-water droplets. The theoretical model for the observed narrow-band acceleration equally refers to the “initial charge separation effects” for an homogeneously mixed composite target as presented by Brantov et al. [166] and discussed in section 2.3.3. At an early stage of the acceleration process, the light deuterons are accelerated across the plasma boundary. Due to the short acceleration time related to the laser pulse duration of 40 fs, the oxygen ions remain comparably immobile and constitute the necessary sharp potential jump. The limited transverse extent of the sphere allows front side electrons to access the rear side by passing around the target; the two electron currents inside and around the sphere may thus recombine at the rear side of the target, which can strongly enhance the electric field. Besides this initial charge separation, the peak formation is supported by the regular shock acceleration at later times, where the velocity of the oxygen ions defines the phase-space position of the monoenergetic deuteron bunch. The deuterons continue their acceleration in their own self-consistent electrostatic field created by the co-propagating hot electrons, which may lead to undesirable spectral broadening. For a more detailed discussion, see [166].

The irradiation of heavy water droplet targets delivered monoenergetic deuteron beams with typically 15% energy spread at a central peak energy of 2 MeV. Note that here, too, a certain analogy between the spherical mass-limited geometry and the microdot source confinement can be asserted: Since no ions are present outside the droplet sphere of  $20 \mu\text{m}$  diameter, all ions will naturally experience the central homogeneous TNSA field—very much like in Confined TNSA.

### Beam shaping with a laser driven micro-lens

An alternative to the *ab initio* narrow-band approaches from certain target geometries was presented by Toncian et al. [195, 197], who used a hollow laser-irradiated micro-cylinder as a focussing device to separate certain parts of temporally broadened proton beam and achieve spectral truncation with the help of a subsequent pinhole. In experiments carried out at the LULI laser facility, narrow-band features with approximately 3% bandwidth at 6 MeV were produced on top of a broad background.

The micro-lens setup requires two synchronized ultra-intense laser pulses, which were generated by introducing a beam splitter into the TW beam path. The first pulse creates a proton beam with broad energy distribution via TNSA on a thin foil target. The second pulse hits

the outer wall of a small cylinder located behind the foil and on the propagation axis of the proton beam, whereupon a relativistic electron population is generated and injected through the cylinder's wall. The electrons spread evenly on the inner wall surface of the cylinder and initiate the build-up of strong radial electric fields of the order of  $\leq 10^{10}$  V/m. These transient radial fields may be used to focus a narrow band component of the dispersed polyenergetic proton bunch, and hence enables the spatial selection of a monoenergetic peak feature by means of an additional aperture. Since the focussing fields are triggered by the second laser pulse, the focussed energy can be tuned by changing the timing of the two laser pulses.

The laser-driven micro-lens represents a handy device for active beam shaping on a femtosecond timescale. Due to its small dimensions, it seems highly preferable over the comparably large conventional magnetostatic ion optics when aiming at sustaining the favourably small dimensions of laser accelerators for applications (cf. discussion of section 5.3.2).

### Energy gating via multi-stage acceleration

In recent experiments at IOQ, multi-stage laser acceleration of ions was demonstrated for the first time. These results will be treated in detail elsewhere [198]; however, one aspect of the experimental setting fits well into the current discussion of alternative methods for the generation of monoenergetic proton beams and shall be introduced here briefly.

Similar to the laser-triggered micro-lens, the multi-stage acceleration setup makes use of two temporally correlated, ultra-intense laser pulses P1 and P2 impinging on two subsequent targets T1 and T2 (Fig. 4.17a). A proton beam with a quasi-exponential energy distribution is produced at the primary foil T1 via the TNSA mechanism. The proton beam expands towards the secondary foil T2 located a few millimeters behind the first one, and is temporally stretched

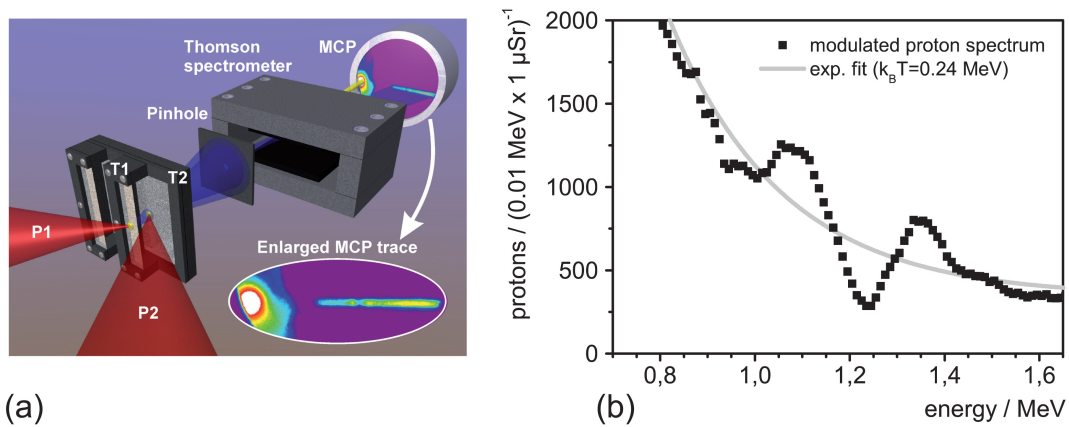


Figure 4.17: Energy modulation from multi-stage acceleration. (a) Double-stage setup at JETI. A proton beam with thermal energy spectrum is generated at the primary foil T1 via TNSA and expands towards the secondary foil T2. At T2, a second (synchronized) laser pulse creates a second TNSA field, strongly affecting the proton spectrum of the T1 beam. (b) Modulated spectrum from double-stage acceleration (black squares). The TNSA field at T2 causes an inhibition of certain energies in the T1 proton spectrum and an accumulation of these protons at higher and lower energies. A thermal fit ( $k_B T = 0.24$  MeV) has been added to the modulated spectrum (grey line), which is in good accordance with the typical thermal spectra observed when T1 is irradiated alone.

due to the different proton velocities. When the proton beam reaches the target T2, a second TNSA is created on T2, which strongly modulates the T1 proton spectrum around a certain energy determined by the distance between the two foil and the delay between the laser pulses (Fig. 4.17b): Those protons already behind T2 are boosted by the second TNSA field to higher energies, while their slower successors are decelerated at the target front side due to the positive Coulomb wall.

The spectral modulation achieved with the double-stage setup directly addresses the task of spectrally controlling laser-produced proton beams. The second plasma acts as a spectral filter, which works on the same femtosecond timescale as the proton source and utilizes the ultra-strong TNSA fields to gate and enforce certain proton energies while inhibiting others. In particular, the energy range to be affected can be selected by changing the delay between the two laser pulses—somewhat related to micro-lens setup. Beyond the great prospects of enabling successive energy gain, staged laser acceleration therewith proves feasible to custom-shape the spectrum of laser-produced proton beams.



## 5 Future prospects for laser-generated narrow-band proton beams

The previous chapters of this thesis have introduced a technique for the generation of monoenergetic ion beams based on the interaction of an ultra-intense laser pulse with microstructured thin foil targets. The technique was developed, tested and brought to maturity by a series of experiments carried out at the JETI laser facility, providing monoenergetic ion beams with  $\approx 10\%$  bandwidth in a reproducible and scalable fashion.

The quality of the currently achieved spectra in this work is mainly limited by two factors, the target design and the laser power, both of which determine the peak position, width and contrast. Several ways of improving the target design have been pointed in this work, including composite targets containing only a small contribution of the leading ion species (cf. section 4.4). An extensive research program has recently been brought on the way in cooperation with IAP Jena to develop standardized lithographic methods for a large-scale, quasi-commercial fabrication of microstructured targets, which would allow to transfer the micro-dot technique to other laser facilities. The replacement of individually crafted foils by standardized series of targets is pivotal when aiming at applications outside mere fundamental research. For sophisticated concepts like accelerator injectors or oncological radiation therapy, fluctuations of the beam quality resulting from an uncontrollable interaction geometry would be simply unacceptable. Target improvements continue to be a central subject of IOQ research and will be presented in separate works.

In the following, some improvements on the laser's side shall be discussed in detail, limiting, however, the discussion to two parameters, the pulse power and the pulse contrast. Finally, one promising application for laser-generated ion beams—laser-driven radiation oncology—shall be introduced to the reader, casting some light on the enormous impetus behind the rapid developments of the past years.

### 5.1 POLARIS Petawatt scaling

*The results of this thesis are extrapolated to higher laser energies using 2D-PIC simulations. For a pulse energy of 15 J, OSIRIS simulations by Alex Robinson yield a narrow-band peak at 9.3 MeV. For the Petawatt laser POLARIS (150 J, 150 fs), REMP-based simulations by Timur Esirkepov show monoenergetic peaks at 173 MeV with 1% bandwidth.*

At the time of the completion of this thesis, the physics community witnesses the advent of a new generation of high intensity lasers. Besides established Petawatt (PW) laser facilities of factory-like dimensions like VULCAN (Rutherford-Appleton Laboratories, UK [199]) and the JUPITER facility (Lawrence Livermore National Laboratories, USA [200]), a number of smaller PW lasers, much more suited to applications beyond laser plasma research, have recently started operation or will take up operation within the next months. This includes the ASTRA GEMINI laser at Rutherford-Appleton Laboratories [201], the Texas Petawatt at

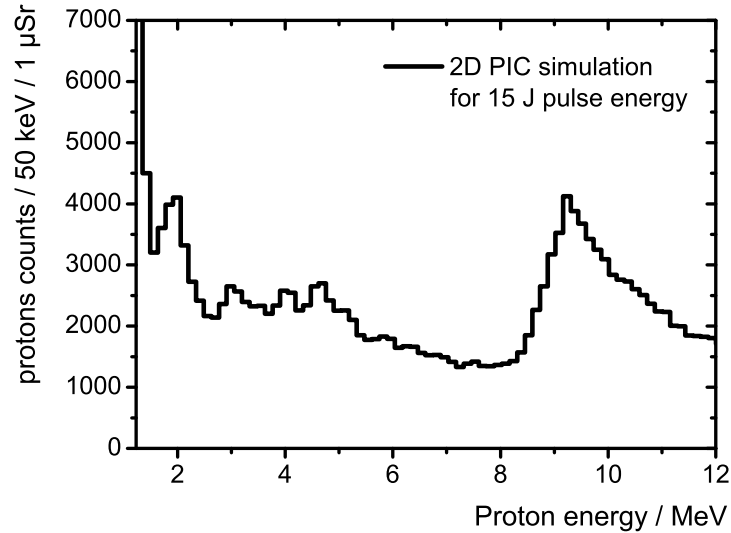


Figure 5.1: 2D-PIC simulation for 15 J pulse energy [53]. The irradiation of a microdots was simulated by Alex Robinson for a pulse energy of 15 J, resembling the fourth amplification stage of the POLARIS laser system. A narrow band peak at 9.3 MeV with approximately 2.5 MeV energy spread is observed. Apart from the laser energy, the simulation conditions correspond to those of Figs. 4.2 & 4.5.

the University of Texas at Austin [202], the HERCULES laser at the University of Michigan [203], and the POLARIS laser at IOQ [204].

POLARIS utilizes diode-pumped  $\text{Yb}^{3+}$ :glass to amplify pulses from a commercial Ti:Sapphire oscillator which has been detuned from its central wavelength to 1030 nm at a bandwidth of 19 nm to the PW level [205–209]. The enormous advantage of such a diode pumped solid state laser in comparison to the conventional flash lamp technique is the high conversion efficiency of pump light into laser radiation, preventing instability and damage problems related to thermal effects, and thus allowing for higher repetition rates. At POLARIS, presently four out of five amplification stages have been realized, achieving pulse energies of 15 J within 130 fs pulse duration at a repetition rate of up to 0.1 Hz. The final stage of POLARIS will provide 150 J pulse energy at an expected pulse duration of 150 fs.

Owed to the strong experimental links between the JETI and the POLARIS lasers, it is foreseeable that laser proton acceleration from microstructured targets will be among the first experiments carried out at POLARIS after its launching in 2008. In order to anticipate the experimental conditions to be encountered at POLARIS, we extrapolated our current results using the established PIC algorithms discussed in sections 4.1 & 4.3. In a first simulation, the laser parameters were fitted to the 4th POLARIS amplification stage of 15 J pulse energy. The calculations were performed by Alex Robinson using the OSIRIS code already used for the corroboration of the above-presented scaling laws. By keeping all other simulation parameters fixed (dot size, dot composition etc.), a direct comparability to the previous results can be warranted.

Fig. 5.1 shows the spectrum for the 15 J calculations. A distinct peak feature is visible



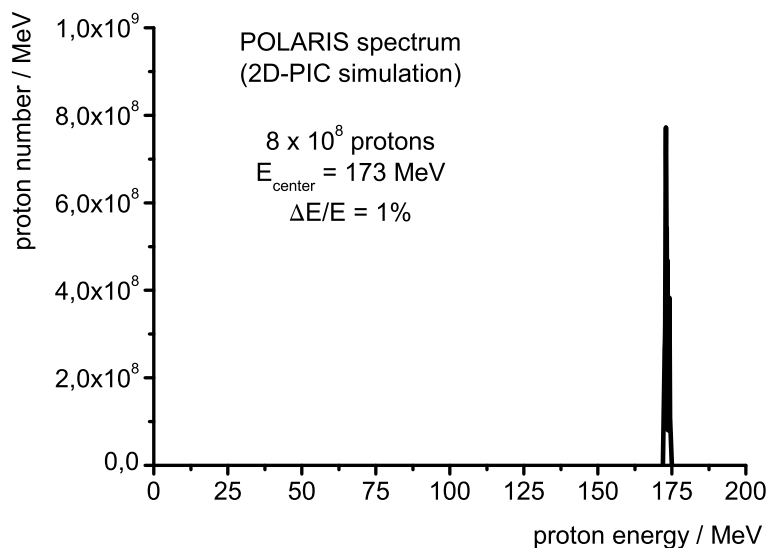


Figure 5.2: Scaling of the monoenergetic acceleration to the Petawatt regime [51]. The irradiation of a dot with  $2.5\ \mu\text{m}$  diameter and  $0.1\ \mu\text{m}$  by a  $150\ \text{J}$  &  $150\ \text{fs}$  laser pulse focussed to a spot of  $10\ \mu\text{m}$  diameter was simulated by Timur Esirkepov, which resembles the conditions for the Jena POLARIS laser system currently under construction. The resulting spectrum shows a distinct peak at  $173\ \text{MeV}$  with about  $0.9\ \%$  energy spread.

at  $E_{\text{center}} = 9.3\ \text{MeV}$  with an energy spread of about  $\Delta E_{\text{FWHM}} = 2.5\ \text{MeV} \simeq 27\%$ .<sup>1</sup> The comparably poor relative energy spread can be explained by the peak width scaling discussed in section 4.3, where it has been argued that the absolute peak width  $\Delta E_{\text{FWHM}} = 2.5\ \text{MeV}$  represents an asymptotic limit for high intensities. At this particular peak energy, the spread has just reached this limit, which leads to the somewhat unfavourable ratio  $\Delta E/E = 27\%$ .

A second simulation was performed by Timur Esirkepov to investigate the situation for the final POLARIS parameters. In the simulation, a laser pulse of  $E_{\text{POL}} = 150\ \text{J}$  and  $\tau_{\text{POL}} = 150\ \text{fs}$  is focussed to a spot of  $d_{\text{foc}} = 10\ \mu\text{m}$  diameter, leading to an intensity of  $I_{\text{POL}} = 1.2 \times 10^{21}\ \text{W}/\text{cm}^2$ . The target consists of a  $5\ \mu\text{m}$  Titanium foil with PMMA dots of  $d_{\text{dot}} = 2.5\ \mu\text{m}$  diameter and  $\Delta z_{\text{dot}} = 0.1\ \mu\text{m}$  thickness.<sup>2</sup>

The results of the simulation can be seen in Fig. 5.2. The calculation yields a distinctly peaked spectrum at  $E_{\text{center}} = 173\ \text{MeV}$  with an energy spread of about  $\Delta E_{\text{FWHM}} = 1.5\ \text{MeV}$  or  $0.9\ \%$ , which represents an improvement by a factor of  $\approx 70$  in terms of peak energy and  $\approx 10$  for the relative energy spread in comparison to the beams currently available at JETI. Note that for such ultra-high intensities, the conditions of ion acceleration are expected to change (cf. section 2.2.2), and indeed the spectrum deviates from the linear scaling law 4.2. Instead, one may refer to the Petawatt scaling law 2.67 provided by Esirkepov et al. in [126]. However,

<sup>1</sup>Note that the peak is used in the peak energy scaling law proposed in section 4.3.

<sup>2</sup>The simulation is based on the 2D Particle-in-Cell (PIC) code REMP (“relativistic electromagnetic particle-mesh”) and the hydrodynamic model of Matsukado et al. [156], as used already in ref. [61] for the prediction of the monoenergetic spectra. Here, the fully vectorized motion of  $8.2 \times 10^8$  particles was calculated at the NEC SX-5 computer at Osaka University, Japan.

on a closer look the Petawatt scaling also fails to account for the simulation, predicting a maximum proton energy of 228 MeV rather than 173 MeV. This deviation can be explained by the fact that Esirkepov’s scaling law holds true only for the optimum critical depth as mentioned in section 2.2.2, which is not fulfilled in the POLARIS simulation. Therefore, the Esirkepov model holds, but the optimum boundary conditions are not met.

For the Petawatt regime, the simulations also yield that the acceleration of protons from a dot source is no longer limited by the skin depth of the electric field. All protons are detached from the foil and accelerated in a bunched manner. The monoenergetic peak thus contains all  $8 \times 10^8$  protons abundant in the dot.

Note also that for Petawatt laser matter interaction the proton motion becomes relativistic. The relativistic factor amounts to

$$\gamma = \frac{E_{\text{kin}}}{m_p c^2} + 1 \approx \frac{173 \text{ MeV}}{1 \text{ GeV}} + 1 = 1.173, \quad (5.1)$$

which is no longer negligible and thus requires an advanced theoretical treatment. On the other hand, the laser-induced ion quiver motion still remains comparably small since the relativistic parameter  $a_0$  scales as  $\sim 1/m_i$ .

## 5.2 Contrast improvements

*Laser proton acceleration can be significantly enhanced by improving the pulse contrast to a level of  $\approx 10^{-10}$ . Such ultra-high contrasts can be achieved with plasma mirrors.*

The decisive role of the pulse contrast for laser acceleration experiments has already been pointed out in earlier sections (cf. 2.1.1, 2.1.4 & 2.2.3). A number of recent publications underscore this importance, demonstrating that the proton emission can be significantly enhanced when moving to ultra-high contrasts  $I_{\text{ASE}}/I_{\text{main}} < 10^{-10}$ . For example, proton energies  $> 5$  MeV from laser-foil interactions at an intensity of  $I \approx 5 \times 10^{18} \text{ W/cm}^2$  were reported by Cecotti et al. [210], which exceeds the maximum energies at JETI despite the significantly lower intensity. This extraordinary improvement is owed to the very efficient electron heating mechanisms, related to a shift of the predominant absorption mechanism from resonance absorption and  $\vec{j} \times \vec{B}$ -heating to Brunel absorption. In addition, with such clean pulses the irradiation of ultra-thin targets becomes possible, accessing target thicknesses of the order of tens of nanometers. For such thin foils, Neely et al. [211] showed that also the conversion efficiency of laser energy into hot protons as well as the temperature of the proton population are enhanced significantly in comparison to micrometer thick foils.

In both works, the ultra-high pulse contrast was achieved with the help of a plasma mirror. Plasma mirrors are a groundbreaking and elegant way to dispose of ASE and pre-pulse contributions in the laser pulse profile, exploiting the high reflectivity of an overcritical plasma by introducing an originally transparent medium into the weakly focussed laser beam (e.g. an anti-reflection coated glass substrate). While the ASE does not suffice to pass the medium’s ionization threshold, the rising edge of the main pulse will create a plasma slab with a very steep plasma gradient at the surface, which serves as a mirror to be “switched on” within an optical timescale [85–88]. The plasma mirror technique allows to improve the contrast ratio by several orders of magnitude, easily reaching values  $< 10^{-10}$ .

A plasma mirror setup is currently being installed at JETI. The setup will be hosted in an additional stretch of beamline right in front of the ion acceleration experiment. In this

configuration, switching between high contrast and low contrast pulses is immediately possible, which will allow to study the irradiation of microstructured targets in a comparative manner. The reader may also note that several advanced acceleration schemes (radiation pressure dominated regime, circular polarization etc.) have been discussed in section 2.2.2, which explicitly require the high pulse contrast made available by plasma mirrors. Finally, it shall be but mentioned here that the pulse contrast provided by plasma mirrors can be utilized to generate high harmonics from solid targets, which gives access to the exciting field of attosecond science [212–215].

### 5.3 Radiation oncology based on laser accelerators - an estimation

*Laser accelerators have the potential for a number of outstanding applications. In particular, medical physics would greatly benefit from the availability of compact particle beam sources, for example in the fields of PET isotope production and oncological ion beam therapy.*

In this concluding section, laser particle acceleration shall be discussed from a broader perspective, aiming at applications outside purely physical research. It is well known that over the past decades, particle beams have acquired an irreplaceable role in medical physics, and particularly in radiation oncology. Particle-based radiation oncology uses the controlled energy deposition from scattering processes to create local damage in cancerous tissue—preferably a double-strand breaking in the DNA of the cancer cells—thus inhibiting the reproduction of the cancerous cell (clonogenic death), or causing the cell's death directly (apoptotic death).

Like surgery, radiation therapy mainly addresses so-called “localized primary tumors” as opposed to already metastasized tumors. Primary tumors represent 58% of all medical cases and are treated with surgery and radiation therapy roughly one third each. For the remaining third ( $\approx 18\%$  of all medical cases), all current treatment methods fail. In order to give an idea of the total patient numbers involved, consider that there are about 436,500 new cancer cases every year in Germany, with an 5-year survival rate of approximately 56% (values dated 2004, [216]). This implies that 78,500 patients per year could potentially benefit from new treatment methods in Germany alone. Acknowledging that all OECD countries suffer from comparable cancer rates, this significant number represents an imperative to develop new radiological techniques, and to make current state-of-the-art techniques more widely accessible. The high demand has stimulated a debate about the potential of laser-based particle beam sources for oncological purposes, whereas two possible applications have aroused particular interest— isotope production for positron emission tomography (PET) and ion beam therapy (IBT) [27–32, 217–219].

In PET, short-lived radio-isotopes such as  $^{11}\text{C}$  ( $\tau_{1/2} = 20.4$  min) and  $^{18}\text{F}$  ( $\tau_{1/2} = 109.7$  min) are introduced as radiopharmaceutical markers into the blood circuit of the patient, where they circulate and eventually undergo  $\beta^+$  decay. The emitted positron is stopped in the body and annihilates with an electron to two 511 keV photons, which can be used for medical imaging of the blood circulation and tumors via coincidence detection. As of today, PET isotopes are mostly produced via  $(p, n)$  reaction from cyclotrons or Van-de-Graph accelerators, which due to their considerable costs, size and shielding requirements are prohibitive for most hospitals. Fritzler et al. [27] argued convincingly that laser-produced particle beams could provide an alternative for PET isotope source with favourably less shielding requirements and investment costs. In experiments carried out at the Laboratoire d'Optique Appliquée in Paliseau, France,

the feasibility of 10 MeV protons produced by a 10 Hz laser system for the induction of  $^{11}\text{B}(p, n)^{11}\text{C}$  reactions sufficient for PET isotope production was demonstrated, assuming that the laser operation could be enhanced to 1 kHz.

The second application, IBT, shall be treated in greater detail here, because it is often referred to as the most auspicious of the ambitious application plans for laser-generated ion beams. Starting from a brief overview about the physical principles of IBT, the alluring question shall be addressed if and how lasers can contribute to radiation therapy with ions.

### 5.3.1 Ion beam therapy vs. other radiation treatments - a physical overview

*Ion beams display a characteristic stopping behaviour in matter, leading to a well-localized energy deposition at the end of the penetration path. This “Bragg-peak” explains the superiority of ions over electrons and photons for the treatment of deep-seated tumors in a sensitive vicinity. With this respect, carbons are preferable over protons, but are much harder to provide.*

The crux of all radiation therapy is the achievement of a high target dose in contrast to a low integral dose, that is, the optimization of the energy deposition in a tumor with a minimum effect on the surrounding healthy tissue.<sup>3</sup> A typical therapeutic dose applied in radiation therapy is 60 Gy over a time of 30 days, where individual doses of  $\approx 2$  Gy are delivered during daily sessions of a few minutes. Note that in comparison the lethal whole-body dose for humans is only about 7 Gy.

The key advantage of ion beams in comparison to other types of radiation (photons, electrons) is the characteristic stopping behaviour of ions in matter [220–223]. The energy deposition of ions is described by the Bethe-Bloch formula [222, 224]

$$-\frac{dE_{\text{kin}}}{ds} = \frac{4\pi}{m_e} \left( \frac{e^2}{4\pi\epsilon_0^2} \right)^2 \cdot \frac{n_e Z^2}{v^2} \left\{ \ln \frac{2\gamma^2 m_e v^2}{E_{\text{ion}}} - \frac{v^2}{c^2} - \ln \left( 1 - \frac{v^2}{c^2} \right) \right\}, \quad (5.2)$$

which gives the differential loss of kinetic energy (i.e. the energy deposition) along the penetration path. Here,  $Z$  is the projectile charge,  $\gamma$  the relativistic factor, and  $E_{\text{ion}}$  is the ionization potential of the target atom.

The stopping interaction can be basically divided into two contributions, an electronic and a nuclear one, which correspond to two different regimes of energy loss [224]. In the regime of electronic interaction, the incident ion performs a relatively straight propagation with quasi-constant energy loss, thereby displacing, exciting or liberating hull electrons along its path. If the particle is already sufficiently slow, elastic scattering at the positive nuclei gains importance and supports the stopping process, so that the particle comes to rest very quickly. In addition, ions may also undergo and cause nuclear fragmentation, which generates additional ionization along the penetration path and alters the composition of the incident beam, thus changing its overall stopping behaviour [225].<sup>4</sup>

Fig. 5.3 shows the specific stopping powers of electrons, protons and carbon ions (solid lines, left vertical axis) and their projected ranges (dashed lines, right vertical axis) in water as a function of the particle energy [226]. In addition, the attenuation factor for photons in units of  $\text{cm}^{-1}$  (solid blue line, left axis) and the 1%-attenuation depth in water (dashed blue line,

<sup>3</sup>As a matter of fact, the irradiation of healthy tissue with ionizing radiation may itself potentially lead to cancer formation.

<sup>4</sup>A typical nuclear fragmentation for an incident  $^{12}\text{C}$  ion is  $^{12}\text{C} + ^{16}\text{O} \rightarrow ^{11}\text{C} + ^{11}\text{O} + 2\ ^1_0\text{n}$ , and subsequently  $^{11}\text{C} \rightarrow ^{11}\text{B} + e^+$  and  $^{15}\text{O} \rightarrow ^{15}\text{N} + e^+$ . Such reactions along the beam path are for example utilized for the so-called “in-beam PET” monitoring during radiation treatment sessions [225].

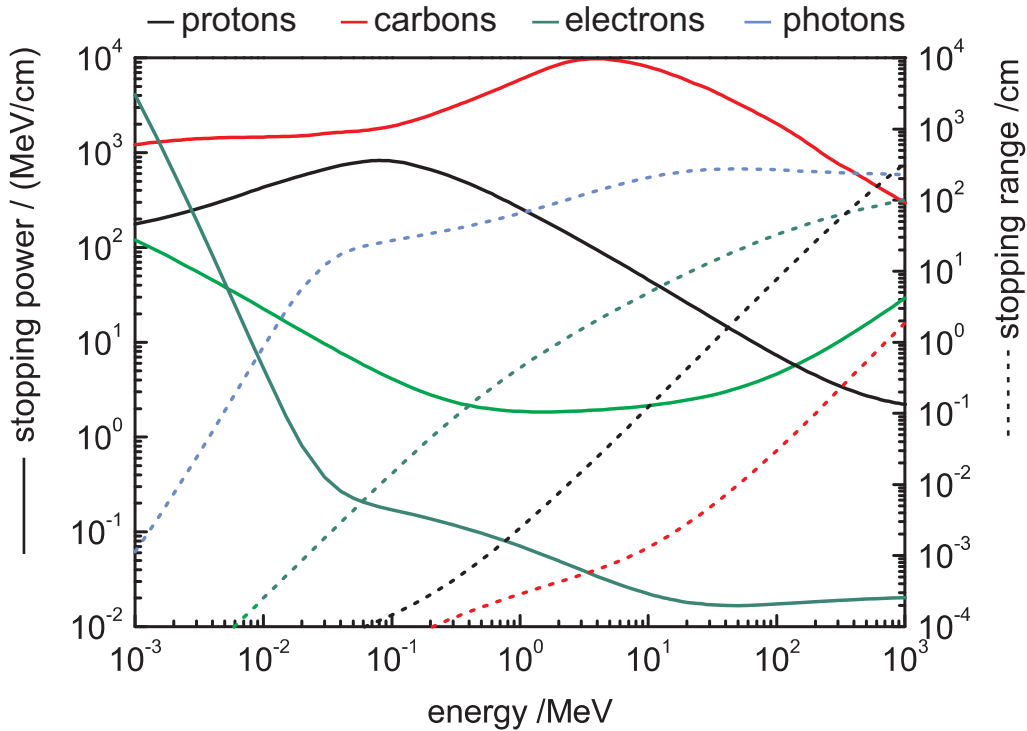


Figure 5.3: Comparison of the stopping power and range of electrons, protons and carbon ions in water. The solid plots show the energy loss in MeV/cm. Ions are superior to the electrons with respect to the maximum deposited energy, which is due to the confined absorption in the Bragg peak. This leads to a higher ionization rate and minimizes the effect on surrounding healthy tissues. The stopping range is given by the dashed lines.

right axis) are given. From this diagram it follows that, contrary to electrons and photons, ions lose their energy very rapidly once they have been slowed down to a kinetic energy of a few MeV per nucleon, which in conjunction with their overall high stopping power leads to a well-defined penetration depth and an maximum energy deposition at the end of the penetration path - the so-called Bragg peak. The resulting dose deposition patterns for the four different types of radiation are displayed in Fig. 5.4 for the irradiation of water. Here, the effective dose  $D = \eta_{\text{RBE}} \cdot \Delta E/m$  is given for 15 MeV photons (blue), 25 MeV electrons (green), 92 – 103 MeV protons (black) and 2 – 2.3 GeV carbon ions (red),  $\eta_{\text{RBE}}$  being the Relative Biological Effectiveness to be explained below. The spectra used for the calculation are displayed on the right hand side and are similar to those applied in actual radiation therapy.

The superiority of ion beams (including protons) over electrons and photons for targeted dose deposition becomes evident when considering for example a tumor of 1.5 cm diameter located at a depth of about 7 cm, as indicated by the grey rectangle in Fig. 5.4. Both electrons and photons display steady decrease in energy deposition, with the dose maximum located in the surface region, i.e. well before the tumor.<sup>5</sup> In contrast, for ions the major fraction of the beam energy is deposited in the tumor, minimizing the impact on surrounding tissue and

<sup>5</sup>The sudden drop in the dose curves close the surface is due to the initially non-equilibrated transport of secondary electrons into the tissue.

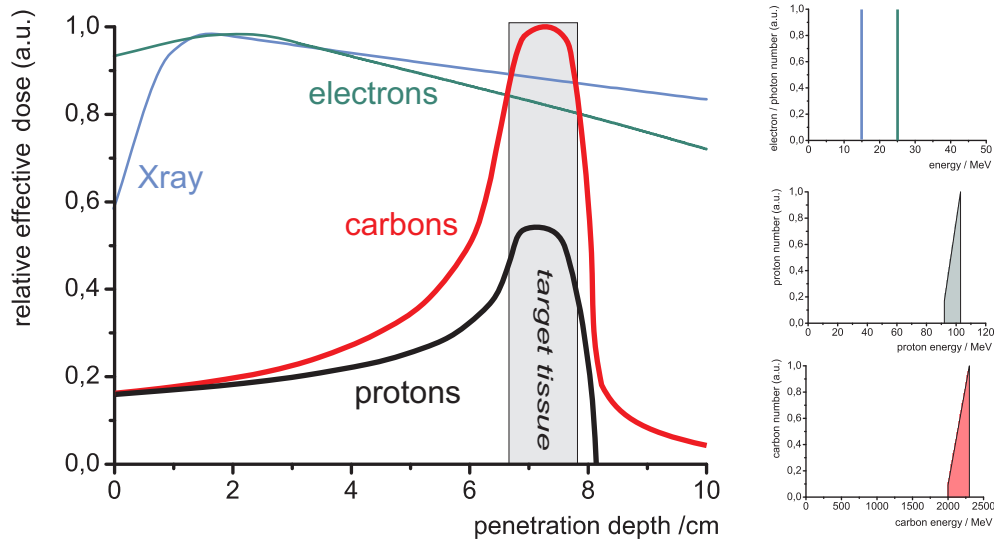


Figure 5.4: Dose deposition patterns for photons, electrons, protons and carbon ions. A comparison of the energy deposition in water for different particle species witnesses the superiority of ions for the treatment of deep sited tumors. For electrons and photons, the energy deposition maximum is located close to the surface (assuming typical particle energies as applied for therapeutic purposes here). In contrast, proton and ion beams deposit most of their energy at the end of the penetration path, well localized in the so-called Bragg-peak, which warrants an minimum effect on surround healthy tissue. The particle spectra which entered the dose calculations are displayed on the right hand side. Note that the dose plots for photons, electrons and carbons have been normalized to their maximum, whereas the proton plot has been normalized to the “carbon skin dose”.

leading to a least invasive treatment. This variability of the maximum dose position makes them the ideal candidates for the irradiation of deep-sited tumors in the vicinity of sensitive organs. Carbon beams prove to be even more efficient than protons but are, however, much harder to provide and also show a dose “tail” resulting from nuclear fragmentation that reaches beyond the Bragg peak into regions of possibly healthy tissues. In the viewgraph, the dose curves for photons, electrons and carbons have been normalized to their maximum, and the proton curve to the carbon “skin dose” (surface dose).

A few comments on the notion of “physical dose” shall be added for the sake of completeness. The physical dose represents only a rough measure for the effect of radiation on biological tissue. An empirical factor for the Relative Biological Effectiveness (RBE) is usually introduced into the calculations, which denotes the specific biological effect of the type of radiation in comparison to X-rays, measured for example with cell survival rates [222, 227, 228]. Protons are generally assumed to have a uniform RBE of 1.1, electrons of 1. For heavier ions, the RBE depends on several parameters such as the kinetic energy, the total dose, or the specific tissue composition, which makes the situation and adequate treatment plans significantly more complex. For carbon, the RBE can be as high as 6 in the Bragg peak, whereas for higher energies the RBE of ions approaches that of protons. RBE has been acknowledged in the calculations of Fig. 5.4.

Generally, one must also take into account the so-called Oxygen Enhancement Factor, which describes the specific effect of the presence of oxygen on the ionization power of the radiation

and is particularly important for tumors. The Oxygen Enhancement Factor has, however, not been included into our simple estimations for Fig. 5.4.

### 5.3.2 Laser-based ion beam therapy

*The rapid progress in the field of high power lasers and laser particle acceleration heralds the advent of a new generation of particle accelerators. Laser accelerators are compact and comparably cheap devices, which could in principle provide several types of radiation, while still fitting in a hospital laboratory. A number of serious engineering problems—including peak energy, spectral stability and beam shaping—need to be overcome before lasers may play a role in ion beam therapy.*

Now, how can laser-produced proton beams contribute to IBT? Let us approach this question by re-emphasizing first that IBT is indeed a most sophisticated technology, involving enormous operational, computational and material efforts. This fact is witnessed by the still very small number of treatment sites around the world; as of 2007, 27 IBT facilities are in operation [33]. The majority of the facilities (17) still belongs to physics laboratories, where the beam time is shared with “normal” accelerator research, thus limiting the available treatment capacities further. Altogether, approximately 50,000 patients have been treated with IBT since the first experiments in the 1950s, > 90% of which were treated with protons. These comparably small patient number indicate a demand for new IBT facilities—a demand which laser-based accelerators could help to answer.

In their 2007 study [33], Linz and Alonso asked the question “What will it take for laser driven proton accelerators to be applied in tumor therapy?” The authors presented a detailed though rather sceptic assessment of the technical hurdles that laser accelerators need to overcome before gaining any practical relevance for radiation oncology. In particular, they provided a list of key features of conventional accelerators that current laser accelerators do not meet, including beam energy, reliability, and dose conformation.

In the following, the pessimistic view of Linz and Alonso shall be encountered, arguing for a less static perspective on the issue and extrapolating the rapid development of high intensity laser technology of the past years into the close future. Central arguments concerning the potential of laser accelerators with respect to radiation shielding and overall costs shall be re-iterated, whereupon a roadmap for the future of laser-driven particle sources in the next years shall be drawn.

The first objective noted by Linz and Alonso is the low particle energy provided by laser accelerators. For IBT, particle sources are typically designed to enable a penetration depth of 30 cm in water, which corresponds to kinetic energies of 200 MeV for protons, and 5.3 GeV for carbon (cf. table 5.1). The authors contrast these numbers with the maximum proton energy hitherto achieved by laser accelerators, 58 MeV, which was reported at the large-scale high energy laser system at Lawrence Livermore National Laboratories [5]. In comparison, current table-top lasers typically provide proton energies of  $\leq 10$  MeV [27].

Leaving aside the fact that proton energies of  $\approx 60$  MeV is already sufficient for a number of specific IBT applications such as the treatment of eye cancer [229, 230], there is no doubt that the particle energies achieved with lasers will multiply within the next couple of years. Available laser powers have increased by almost 7 orders of magnitude over the past 20 years. At the moment, fully commercial table-top lasers of the 100 – 200 TW class are being installed in several laboratories around the world, replacing the current 10 – 20 TW systems. As discussed above, scalability studies indicate that the particle energy will increase with the square root of the laser power [7, 8], which puts proton energies of several tens of MeV clearly

Ion species	$E_{\text{kin}}$
$^1\text{H}$	220 MeV
$^4\text{He}$	870 MeV
$^{12}\text{C}$	5.3 GeV
$^{16}\text{O}$	8.5 GeV
$^{20}\text{Ne}$	12.2 GeV

Table 5.1: Kinetic ion energy required for the penetration 30 cm water.

in the scope of table-top lasers. In addition, contrast improvements and target engineering have the potential to increase particle powers by another order of magnitude (cf. section 5.2). Most notably, several Petawatt projects will be completed within the next couple of years, from which proton energies in excess of 100 MeV can be expected (Fig. 5.2). These machines clearly approach the energy requirements for IBT. Finally, it shall be emphasized that the possible benefit from cascaded acceleration schemes has not even been touched upon by laser accelerators: Similar to conventional accelerators, cascaded acceleration schemes would allow to increase the particle energy successively, thus overcoming the technological limitations of single-shot laser power, and multiplying the potential of laser accelerators.

A second central condition for IBT is a precise dose application. Following [33] here, this aim should better be divided into the sub-tasks of monochromaticity, energy variability, spatial dose localization, and beam intensity. Cyclotrons and synchrotrons typically achieve bandwidths of 0.1%, determined by the design of the accelerator and the beam transport. The well-defined penetration depth associated with this excellent bandwidth is for example exploited in the raster scanning technique [222, 231, 232], where the tumor is scanned with a focussed “pencil beam” as a series of volume pixels. However, the precision of the dose application is generally limited by lateral scattering and longitudinal straggling of the particle beam [222, 225]. For a penetration depth of 20 cm, the longitudinal or “energy straggling” amounts to about 0.2 cm for protons, and to about 0.1 cm for carbons. Furthermore, one must take into account the effects of fragmentation tails described above. The lateral scattering is even more significant, causing an average deviation of 0.9 cm for protons and 0.3 cm for carbon at 20 cm depth. Both types of deflection decrease for heavier ions, but are clearly a limiting element for IBT. In comparison, a longitudinal shift of a proton Bragg peak by 0.5 cm at 20 cm depth corresponds to an energy fluctuation of 2.5 MeV or 1.4%.

The monochromaticity of laser-produced ion beams is the central topic of this thesis. It has been shown that particle spectra of  $\approx 8\%$  can be obtained from microstructured targets in a reasonably reproducible manner, and similar values are reported for other target geometries (cf. section 4.7). Therefore, laser-driven particle beams might still suffer from a comparably large energy spread, but they are certainly not orders of magnitude off. It has been argued in section 4.3 that the peak width is likely to saturate for higher laser powers, resulting in an expected energy spread of  $\leq 1\%$  for the POLARIS parameters (cf. fig. 5.2). The bandwidth obtained from the POLARIS simulation will be comparable to the effects from straggling, and in conjunction with the high peak energy resemble the properties required for IBT closely.

It has been argued that the integral “spread-out Bragg peak” used in IBT dosimetry only requires bandwidths of a few percent, which is actually not that different from the proton spectra presented in this thesis [33, 233]. The reference to the “spread-out Bragg peak” parameters is a reasonable objection and indicates that laser accelerators may be able to



circumvent the prerequisite of a cyclotron-like bandwidth. This suggestion does, however, not solve the problem of energy stability and in fact puts more weight to it.

Regarding energy variability, at least for cyclotrons the energy selection is still a rather complicated process and connected to the generation of hazardous radiation caused by stopping foils or wedge filters. For laser accelerators, a sufficient energy variability is guaranteed by the dependency of the peak position on the laser power, and should thus in principle be only limited by the fluctuations of the pulse energy with an rms of typically  $< 2\%$ . Current monoenergetic beams are still subject to non-negligible fluctuations in terms of peak reproducibility, mostly determined by the quality of the target fabrication process and the alignment accuracy. The improvement of the energy stability to an IBT-relevant degree poses a substantial engineering challenge, but is not limited by any fundamental physical constraints and should therefore be manageable within the next years. <sup>6</sup>

Linz and Alonso continue arguing that the large emission angles and the broad energy spread of laser-produced beams prohibit an efficient beam shaping by means of conventional techniques. In the opinion of the author, this claim neglects the essential fact that the very parameters relevant for beam shaping, i.e. the longitudinal and transverse emittance, are one of the outstanding strengths of laser-produced beams, and compare already favourably with conventional accelerators. Thus, laser acceleration bears the potential for unprecedented beam shaping and most brilliant beams, given that appropriate technologies are developed. The rise of laser accelerators has been accompanied by the development of new beam shaping techniques acting on (sub-)picosecond timescales, including laser-driven lenses (cf. section 4.7) and numerous other proposals for other custom-designed beam shaping devices [219, 234–236]. Thus, the prospect of an all-optical particle accelerator with customized beam shaping devices remains an attractive and realistic promise, and does certainly not “only produce a technology that is a generation behind the scanning technique.”

In terms of beam intensity, approximately  $10^{10}$  protons per second are applied in a typical continuous IBT cyclotron beam over a time of several minutes, corresponding to currents of about 2 nA. Synchrotrons operate at a slightly lower average current ( $\leq 1$  nA). For laser accelerators, the generation of thermal spectra containing  $> 10^{13}$  protons with energy  $> 10$  MeV per shot were reported already in 2000 [5]. Current concepts for monoenergetic beams employ only a fraction of the totally available protons, leading to much smaller total number of e.g.  $7 \times 10^8$  per shot for the JETI experiments, or a projected  $8 \times 10^8$  for the POLARIS simulation (5.2). However, this only implies that the required dose needs to be delivered by accumulating over several shots. For example, consider a tissue volume of  $(2 \text{ cm})^3$  to be irradiated with an average dose of 2 Gy. The  $1/e$ -Bragg peak of the simulated POLARIS beam contains approximately 1.8 mJ within a localized penetration depth of 20.02 – 20.44 cm (Fig. 5.5). Averaging this Bragg peak energy over the designated volume, one obtains an average dose of 0.2 Gy per POLARIS shot. At a repetition rate of 0.1 Hz, a treatment session would hence take less than two minutes, which is comparable to IBT with conventional accelerators.

It shall be remarked that the particular biological effects of ultra-short particle pulses delivered by laser accelerators may well differ from those of conventional beams. It has been argued that the extreme peak currents associated with the femtosecond particle bunches could result in a higher RBE, which would multiply the benefits of laser accelerators and reduce treatment

<sup>6</sup>Note that the generation of thermal spectra with a well-defined cutoff energy and temperature via TNSA is already standard procedure at many lasers, reaching reproducibility rates of close to 100%.

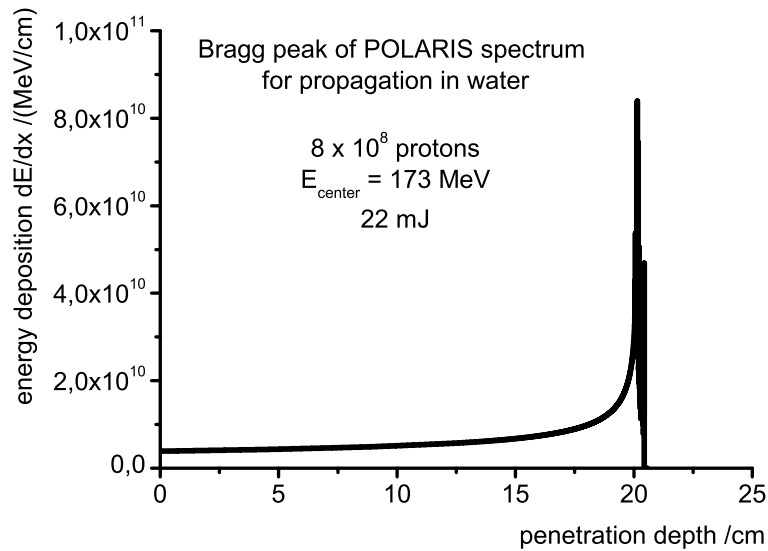


Figure 5.5: Bragg peak calculated for the POLARIS spectrum (Fig. 5.2) for propagation in water. Proton beams produced with the POLARIS laser will be capable of propagating 20 cm into water, which approaches the energy requirements for ion beam therapy (IBT). Several technological problems such as energy stability, energy selection and beam shaping must, however, be addressed before laser accelerators will be applicable for medical purposes, which sets the agenda for the development of laser particle sources in the next decade.

time further. At present, however, this is only a speculation, since experimental expertise is not available. Experiments concerning the dosimetry and biological effects of laser-produced electrons are underway at JETI, entering the regime of femtosecond radiology for the first time. Similar dosimetry experiments for protons are planned at POLARIS.

Finally, let us consider the costs for such a laser-based treatment facility. Current proton therapy centers typically employ cyclotrons or synchrotrons, which are well-established commercial devices with extremely high reliability. Nonetheless, such accelerators require extensive infrastructure, starting with the fact that IBT-suited cyclotrons (synchrotron) sources have a diameter of  $\geq 4$  m ( $\geq 10$  m). For carbon therapy, the requirements are even larger: No adequate cyclotron technology is currently available and one has to rely on synchrotrons of typically 20–25 m diameter, plus a similarly large injector line consisting of a linear accelerator and strippers. The accelerator is followed by large-scale beam shaping devices and a beamline to guide the particle beam into one or more fully rotational gantries with massive radiation shielding. For instance, the state-of-the-art proton and carbon therapy center in Heidelberg to be opened in 2008 [237] is located in a three-storey building with the base area of a soccer field, and features a 600 t gantry to be aligned in 3D around the patient with an accuracy of 0.5 mm. The whole treatment site is housed by 2 m thick concrete radiation shielding.

High intensity laser systems of the multi-100 TW class are not much smaller than a commercial cyclotron, and it will take several more years before PW lasers will shrink to that size. An application of laser accelerators as mere substitute front end particle sources while keeping all the conventional infrastructure seems therefore unintelligible. However, a second,

more auspicious implementation scheme was proposed by Bulanov and others [29, 32, 218], which locates the proton source (i.e. the comparably small thin foil target) as close as possible to the patient. Assuming for the time being that laser plasma sources can provide the desired proton beams *in situ*, e.g. with an appropriate combination of target engineering and customized all-optical beam shaping, the whole assembly of rotatable magneto-optics for beam transport and large parts of gantry system becomes superfluous—the only thing to be guided and rotated around the patient is laser light, which can be easily achieved with mirrors. In addition, hazardous radiation contributions from stripping or energy selection can be avoided; the amount of laser plasma-generated hot electron bremsstrahlung or laser-generated neutrons are certainly a manageable problem, given that the overall volume to be screened can be confined to the comparably small laser-plasma interaction volume.

Therefore, laser accelerators have the potential to greatly reduce the system of beam transportation and radiation protection, which can help to cut costs for an IBT facility significantly. Furthermore, the investments for the laser as the particle source can be expected to be much lower than that of commercial cyclotron or synchrotron sources, which typically cost  $> 10$  Mill. Euro. Present state-of-the-art 200 TW table-top lasers cost approximately 2 Mill. Euro. Given the furious development of laser technology, it is not too bold a prediction that Petawatt systems will become commercially available for the same amount within the next 5 years. By that time, many biophysical proof-of-principle experiments will have been carried out at many laboratories, and an adequate dosimetry for laser-produced particle beams will have been developed. Furthermore, target engineering and beam shaping will have significantly advanced according to the specific needs of laser accelerators, so that laser accelerators might enter a clinical test phase in 7-10 years from now.<sup>7</sup>

During this next decade, laser accelerators will not yet be a competitor to conventional accelerators with most respects. In fact, it is more appropriate to understand laser acceleration as a supplementary and—given the truly unique properties of pulse duration, emittance values and acceleration lengths—complementary technique, facilitating outstanding new applications in fundamental research, material science and biophysics. In the prospect of these promising experiments to come, today's capability of reliably generating several  $10^8$  quasi-monoenergetic protons with MeV energy and less than 10% bandwidth by means of a scalable technique marks an important step towards application and will contribute significantly to the future of laser particle acceleration.

---

<sup>7</sup>More visionary scenarios even propose that one laser plasma source could equally provide MeV ions, GeV electrons, and MeV X-rays simply by changing the target and the acceleration geometry. Such a flexible beam source would allow to switch between different types of radiation therapy while simultaneously enabling X-ray imaging and PET isotope production driven by the same source. Despite the very speculative character of this proposal, it is an exciting idea for such a versatile machine still to fit in a hospital lab.



## Appendix A: Laser ablation

The laser ablation of solids and in particular polymers continues to be a subject of great scientific interest. Over the past four decades, numerous theories have been proposed to describe the different effects that may lead to the removal of material layers, basically distinguishing between photochemical [188, 238–242] and photothermal models [188, 238, 243–246]. The ablation characteristics depend on various parameters including the laser wavelength, fluence, pulse duration and repetition rate. In the particular case of polymers such as PMMA, they also depend strongly on the specific composition of the material (e.g. impurities or dopation [193, 247, 248]). The wavelength dependency of the ablation process is correlated to the absorption spectrum of the polymer, which typically consists of broad band structures resulting from different absorption mechanism such as molecular vibrations (IR) and combinational vibrations (NIR-IR), electronic excitations (VIS-UV), and polaron excitations in carbon chains [188, 249–251]. Two complementary absorption spectra for PMMA from the literature are shown in Fig. 5.6.

The different types of laser ablation used in the thesis, i.e. surface cleaning with a pulsed Nd:YAG laser at 532 nm, and target microstructuring via UV-lithography or fs-ablation, belong to very different ablation regimes. It shall be remarked that the application of laser ablation to stretched foils of 2 – 5  $\mu\text{m}$  thickness is far from trivial and may easily lead to thermal deformation or damage of the foil if not carried out with great care and within a very narrow admissible parameter window.

The fs-structuring employed a Ti:Sapphire laser with a pulse duration of  $\tau_{\text{pulse}} = 60$  fs and typically  $E_{\text{pulse}} = 5 \mu\text{J}$  pulse energy at a repetition rate of 1 kHz. Together with a focal spot size of approximately 80  $\mu\text{m}$  diameter, the single shot fluence on target amounted to  $\Phi_{\text{fs}} \approx 0.1 \text{ J/cm}^2$ , yielding an accumulated fluence of  $\overline{\Phi}_{\text{fs}} \approx 3.2 \text{ J/cm}^2$  for the roughly 32 shots applied to each target position because of the comparably low target translation velocity

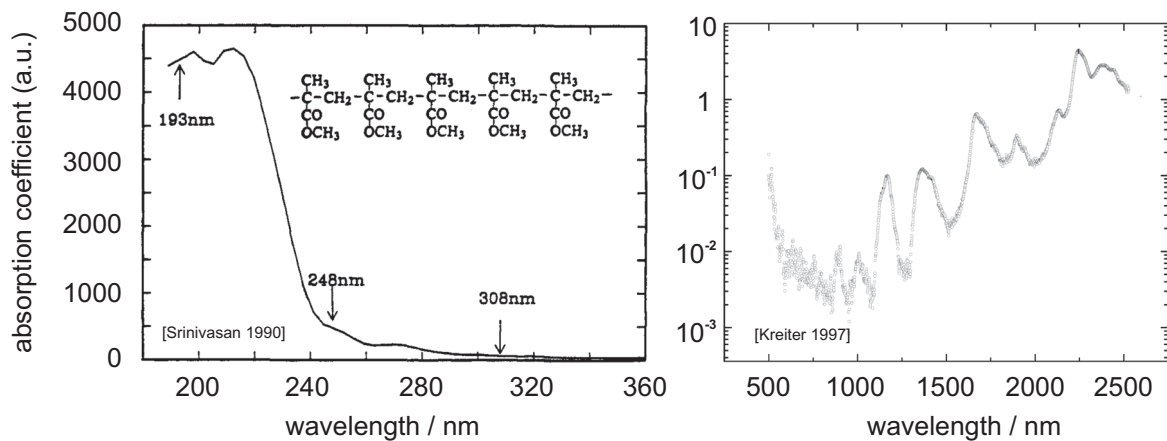


Figure 5.6: PMMA absorption spectra taken from [252] (LHS) and [253] (RHS), each given in arbitrary units.

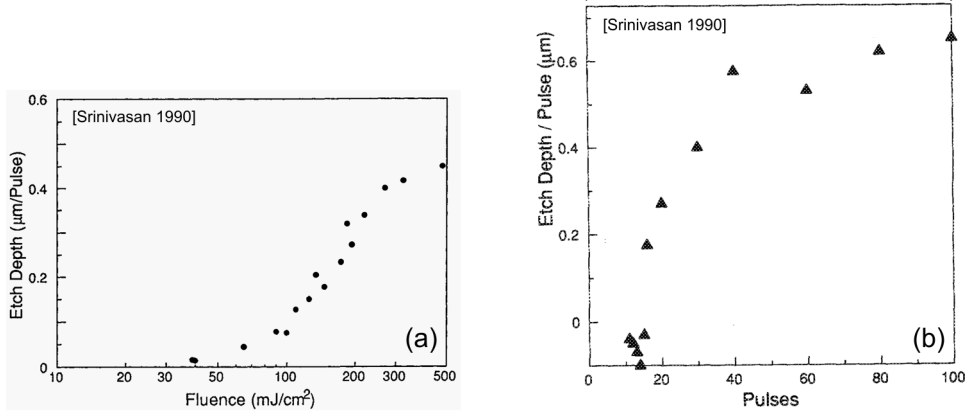


Figure 5.7: Etch rate and incubation effects for UV laser ablation of PMMA. (a) Plot of ablation (etch) depth vs. ablation fluence for 20 ns pulses at  $\lambda = 193$  nm as presented in [252]. The ablation sets in at a distinct threshold value of 40 mJ and enters a regime of linear fluence dependency between 100 and 400 mJ. (b) Average etch rate vs. applied ablation shot number for the irradiation of PMMA with  $\lambda = 248$  nm and 20 ns pulse duration at an ablation fluence of 900 mJ/cm<sup>2</sup>. The ablation curve clearly witnesses incubation effects; an initial number of  $\approx 15$  shots is necessary to start ablation. The graph was taken from [192] (b).

during the fabrication process. Despite this moderate fluence, the intensity in the ablation laser focus was  $I_{\text{foc}} \approx 1.7 \times 10^{12}$  W/cm<sup>2</sup> owed to the ultra-short pulse duration, which exceeds the threshold for multi-photon processes (cf. section 2.1.1). In this regime, multi-photon excitation and ionization lead to photochemical decomposition of the material caused by direct bond breaking, and a subsequent blow-off of fragments [68, 254–256]. Moreover, the ultrashort pulses do not allow for significant heat dissipation into the surrounding material because the phonon relaxation and heat conduction timescales exceed the laser pulse duration, resulting in very sharp ablation structures. However, in some cases, multi-photon effects may still lead to collisional heating and avalanche ionization via electron-phonon scattering, and therefore some thermal effects may play a role for the material decomposition [66, 68, 254]. The applied ablation fluences are in good agreement with literature values, where also the necessity of shot accumulation is described [255, 257, 258].

The mechanism of UV laser ablation of polymers is also known as “ablative photodecomposition” (APD) or “cold ablation” [239–242, 244, 259–262]. While with ns-UV pulses the threshold for multi-photon absorption is typically not reached, single-photon excitation becomes possible due to the shorter wavelengths. In the present case, the UV lithography was carried out with an argon-fluoride laser at  $\lambda_{\text{ArF}} = 193$  nm, that is, at a photon energy larger than the ionization energy ( $E_{\text{photon}} = 6.4$  eV  $>$   $E_{\text{ion}} = 3.5$  eV). PMMA has a strong absorption maximum at 180 – 220 nm resulting from electronic resonances in the chromophoric groups. Therefore, the ablation happens again mostly via direct (photochemical) bond breaking, supported by rapid heating due to energy transfer from excited electrons into rotational and vibrational states. The ablation process typically requires the accumulation of several laser shots in order to initiate ablation, known as “incubation effects”. Both the applied fluence of  $\Phi_{\text{uv}} = 0.25$  J/cm<sup>2</sup> per shot and the required accumulation of  $\approx 20$  shots are in very good agreement with the literature (cf. Fig. 5.7 and refs. [192, 193, 252]).

Contrary to the microstructuring process, the crucial aspect of surface cleaning via laser

ablation employed for Confined TNSA is to *not* damage or destabilize the PMMA structures. Instead, the process aims at removing adsorbed water and single hydrocarbon molecules—that is, a rather loosely structured contamination layer which may, nonetheless, adhere strongly to the surface [263]. The cleaning of surfaces from particles is a well-established application of laser ablation [189, 190]. Here, a frequency-doubled Nd:YAG laser at  $\lambda_{\text{Nd:YAG}} = 532 \text{ nm}$  was used for which the photon energy is below the single-photon absorption threshold, and the applied intensities of  $\approx 10^7 \text{ W/cm}^2$  are below the threshold for multi-photon processes. However, for pulse durations of several nanoseconds there is sufficient time to dissipate the photon energy as heat in the lattice during one pulse duration, which gives rise to photothermal decomposition effects [243–245]. In agreement with the literature, the ablation showed a distinct threshold fluence of  $\Phi_{\text{thr}} = (1.2 \pm 0.3) \text{ J/cm}^2$  for the removal of contaminants, accompanied by initial incubation effects [191, 255, 257, 264]. Note that the ablation threshold of PMMA is  $> 3 \text{ J/cm}^2$  at 308 nm [248, 262], and should be even higher at 532 nm, where PMMA is basically transparent. Still, the PMMA ablation threshold is certainly less than an order of magnitude away from the applied fluences and could easily be reached when increasing the pulse energy of the cleaning laser. However, unintentional damage of the PMMA dots could generally be avoided during the cleaning procedure.





## Appendix B: JETI THG-autocorrelation trace

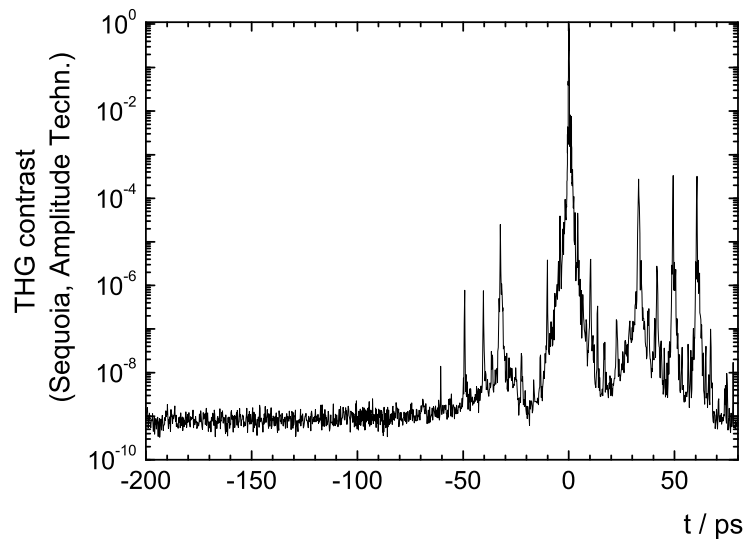


Figure 5.8: JETI THG-autocorrelation trace measured with a Sequoia (Amplitude Tech.). The temporal profile of the JETI laser pulse possesses a ASE contrast of  $I_{\text{ASE}}/I_{\text{main}} < 10^{-8}$  until 30 ps before the main pulse ( $t = 0$ ). Preceded by two correlation artifacts (“ghost pulses”) at  $t = -50$  ps and  $t = -40$  ps, the THG trace also reveals a pre-pulse at  $t = -30$  ps, where the contrast decreases to  $I_{\text{prepulse}}/I_{\text{main}} < 10^{-5}$ . After the pre-pulse, the contrast temporarily retrieves its original value ( $10^{-8}$  at  $t = -20$  ps), before the pedestal of the main pulse sets in.



# Bibliography

- [1] G. A. Mourou, T. Tajima, and S. V. Bulanov. Optics in the relativistic regime. *Reviews Of Modern Physics*, 78(2):309–371, 2006.
- [2] D. Umstadter. Review of physics and applications of relativistic plasmas driven by ultra-intense lasers. *Physics of Plasmas*, 8(5):1774–1785, 2001.
- [3] W. P. Leemans, B. Nagler, A. J. Gonsalves, C. Toth, K. Nakamura, C. G. R. Geddes, E. Esarey, C. B. Schroeder, and S. M. Hooker. Gev electron beams from a centimetre-scale accelerator. *Nature Physics*, 2(10):696–699, 2006.
- [4] S. Karsch, J. Osterhoff, A. Popp, T. P. Rowlands-Rees, Z. Major, M. Fuchs, B. Marx, R. Horlein, K. Schmid, L. Veisz, S. Becker, U. Schramm, B. Hidding, G. Pretzler, D. Habs, F. Gruner, F. Krausz, and S. M. Hooker. Gev-scale electron acceleration in a gas-filled capillary discharge waveguide. *New Journal Of Physics*, 9:415, 2007.
- [5] R. A. Snavely, M. H. Key, S. P. Hatchett, T. E. Cowan, M. Roth, T. W. Phillips, M. A. Stoyer, E. A. Henry, T. C. Sangster, M. S. Singh, S. C. Wilks, A. MacKinnon, A. Offenberger, D. M. Pennington, K. Yasuike, A. B. Langdon, B. F. Lasinski, J. Johnson, M. D. Perry, and E. M. Campbell. Intense high-energy proton beams from petawatt-laser irradiation of solids. *Physical Review Letters*, 85(14):2945–2948, 2000.
- [6] M. Roth, A. Blazevic, M. Geissel, T. Schlegel, T. E. Cowan, M. Allen, J. C. Gauthier, P. Audebert, J. Fuchs, J. Meyer-ter Vehn, M. Hegelich, S. Karsch, and A. Pukhov. Energetic ions generated by laser pulses: A detailed study on target properties. *Physical Review Special Topics - Accelerators and Beams*, 5(6):061301, 2002.
- [7] J. Fuchs, P. Antici, E. D’Humieres, E. Lefebvre, M. Borghesi, E. Brambrink, C. A. Cecchetti, M. Kaluza, V. Malka, M. Manclossi, S. Meyroneinc, P. Mora, J. Schreiber, T. Toncian, H. Pepin, and R. Audebert. Laser-driven proton scaling laws and new paths towards energy increase. *Nature Physics*, 2(1):48–54, 2006.
- [8] L. Robson, P. T. Simpson, R. J. Clarke, K. W. D. Ledingham, F. Lindau, O. Lundh, T. McCanny, P. Mora, D. Neely, C. G. Wahlström, M. Zepf, and P. McKenna. Scaling of proton acceleration driven by petawatt-laser-plasma interactions. *Nature Physics*, 3(1):58–62, 2007.
- [9] H. P. Schlenvoigt, K. Haupt, A. Debus, F. Budde, O. Jäckel, S. Pfotenhauer, H. Schworer, E. Rohwer, J. G. Gallacher, E. Brunetti, R. P. Shanks, S. M. Wiggins, and D. A. Jaroszynski. A compact synchrotron radiation source driven by a laser-plasma wakefield accelerator. *Nature Physics*, 4(2):130–133, 2008.
- [10] H. Schworer, B. Liesfeld, H. P. Schlenvoigt, K. U. Amthor, and R. Sauerbrey. Thomson-backscattered x rays from laser-accelerated electrons. *Physical Review Letters*, 96(1):014802, 2006.

- [11] K. T. Phuoc, S. Corde, R. Shah, F. Albert, R. Fitour, J. P. Rousseau, F. Burgy, B. Mercier, and A. Rousse. Imaging electron trajectories in a laser-wakefield cavity using betatron x-ray radiation. *Physical Review Letters*, 97(22):225002, 2006.
- [12] K. T. Phuoc, F. Burgy, J. P. Rousseau, V. Malka, A. Rousse, R. Shah, D. Umstadter, A. Pukhov, and S. Kiselev. Laser based synchrotron radiation. *Physics Of Plasmas*, 12(2):023101, 2005.
- [13] A. Rousse, K. T. Phuoc, R. Shah, A. Pukhov, E. Lefebvre, V. Malka, S. Kiselev, F. Burgy, J. P. Rousseau, D. Umstadter, and D. Hulin. Production of a kev x-ray beam from synchrotron radiation in relativistic laser-plasma interaction. *Physical Review Letters*, 93(13):135005, 2004.
- [14] H. Schwoerer, P. Gibbon, S. Düsterer, R. Behrens, C. Ziener, C. Reich, and R. Sauerbrey. Mev x rays and photoneutrons from femtosecond laser-produced plasmas. *Physical Review Letters*, 86(11):2317–2320, 2001.
- [15] T. Ditmire, T. Donnelly, R. W. Falcone, and M. D. Perry. Strong x-ray-emission from high-temperature plasmas produced by intense irradiation of clusters. *Physical Review Letters*, 75(17):3122–3125, 1995.
- [16] M.M. Murnane, H.C. Kapteyn, M.D. Rosen, and R.W. Falcone. Ultrafast x-ray pulses from laser-produced plasmas. *Science*, 251(4993):531–536, 1991.
- [17] T. E. Cowan, J. Fuchs, H. Ruhl, A. Kemp, P. Audebert, M. Roth, R. Stephens, I. Barton, A. Blazevic, E. Brambrink, J. Cobble, J. Fernandez, J. C. Gauthier, M. Geissel, M. Hegelich, J. Kaae, S. Karsch, G. P. Le Sage, S. Letzring, M. Manclossi, S. Meyroneinc, A. Newkirk, H. Pepin, and N. Renard-LeGalloudec. Ultralow emittance, multi-mev proton beams from a laser virtual-cathode plasma accelerator. *Physical Review Letters*, 92(20):204801, 2004.
- [18] M. G. Haines. Saturation mechanisms for the generated magnetic field in nonuniform laser-matter irradiation. *Physical Review Letters*, 78(2):254–257, January 1997.
- [19] M. Borghesi, A. J. Mackinnon, R. Gaillard, O. Willi, A. Pukhov, and J. Meyer-ter Vehn. Large quasistatic magnetic fields generated by a relativistically intense laser pulse propagating in a preionized plasma. *Physical Review Letters*, 80(23):5137–5140, June 1998.
- [20] M. Borghesi, A. J. MacKinnon, A. R. Bell, R. Gaillard, and O. Willi. Megagauss magnetic field generation and plasma jet formation on solid targets irradiated by an ultraintense picosecond laser pulse. *Physical Review Letters*, 81(1):112–115, July 1998.
- [21] M. Tatarakis, I. Watts, F. N. Beg, E. L. Clark, A. E. Dangor, A. Gopal, M. G. Haines, P. A. Norreys, U. Wagner, M. S. Wei, M. Zepf, and K. Krushelnick. Laser technology - measuring huge magnetic fields. *Nature*, 415(6869):280–280, January 2002.
- [22] V. Malka, J. Faure, Y. A. Gauduel, E. Lefebvre, A. Rousse, and K. T. Phuoc. Principles and applications of compact laser-plasma accelerators. *Nature Physics*, 4(6):447–453, 2008.

- 
- [23] K. Krushelnick, E. L. Clark, R. Allott, F. N. Beg, C. N. Danson, A. Machacek, V. Malka, Z. Najmudin, D. Neely, P. A. Norreys, M. R. Salvati, M. I. K. Santala, M. Tatarakis, I. Watts, M. Zepf, and A. E. Dangor. Ultrahigh-intensity laser-produced plasmas as a compact heavy ion injection source. *IEEE Transactions on Plasma Science*, 28(4):1184–1189, 2000.
- [24] M. Roth, T. E. Cowan, M. H. Key, S. P. Hatchett, C. Brown, W. Fountain, J. Johnson, D. M. Pennington, R. A. Snavely, S. C. Wilks, K. Yasuike, H. Ruhl, F. Pegoraro, S. V. Bulanov, E. M. Campbell, M. D. Perry, and H. Powell. Fast ignition by intense laser-accelerated proton beams. *Physical Review Letters*, 86(3):436–439, 2001.
- [25] J. Meyer-ter Vehn. Fast ignition of icf targets: an overview. *Plasma Physics and Controlled Fusion*, 43:A113–A125, 2001.
- [26] H. Hora, J. Badziak, M. N. Read, Y. T. Li, T. J. Liang, Y. Cang, H. Liu, Z. M. Sheng, J. Zhang, F. Osman, G. H. Miley, W. Y. Zhang, X. T. He, H. S. Peng, S. Glowacz, S. Jablonski, J. Wolowski, Z. Skladanowski, K. Jungwirth, K. Rohlena, and J. Ullschmied. Fast ignition by laser driven particle beams of very high intensity. *Physics Of Plasmas*, 14(7):072701, 2007.
- [27] S. Fritzler, V. Malka, G. Grillon, J. P. Rousseau, F. Burgy, E. Lefebvre, E. d’Humières, P. McKenna, and K. W. D. Ledingham. Proton beams generated with high-intensity lasers: Applications to medical isotope production. *Applied Physics Letters*, 83(15):3039–3041, 2003.
- [28] K. W. D. Ledingham, P. McKenna, and R. P. Singhal. Applications for nuclear phenomena generated by ultra-intense lasers. *Science*, 300(5622):1107–1111, 2003.
- [29] S. V. Bulanov, T. Z. Esirkepov, V. S. Khoroshkov, A. V. Kunetsov, and F. Pegoraro. Oncological hadrontherapy with laser ion accelerators. *Physics Letters A*, 299(2-3):240–247, 2002.
- [30] S. V. Bulanov and V. S. Khoroshkov. Feasibility of using laser ion accelerators in proton therapy. *Plasma Physics Reports*, 28(5):453–456, 2002.
- [31] E. Fourkal and C. Ma. Laser-accelerated carbon ion beams for radiation therapy. *Medical Physics*, 30(6):1448–1448, 2003.
- [32] V. Malka. Electrons and protons beams produced by compact lasers: a new tool for medicine. *Radiotherapy And Oncology*, 73:S10–S10, 2004.
- [33] Ute Linz and Jose Alonso. What will it take for laser driven proton accelerators to be applied to tumor therapy? *Physical Review Special Topics-Accelerators And Beams*, 10(9):094801, 2007.
- [34] M. Everett, A. Lal, D. Gordon, C.E. Clayton, K.A. Marsh, and C. Joshi. Trapped electron acceleration by a laser-driven relativistic plasma-wave. *Nature*, 368(6471):527–529, 1994.
- [35] A. Modena, Z. Najmudin, A. E. Dangor, C. E. Clayton, K. A. Marsh, C. Joshi, V. Malka, C. B. Darrow, C. Danson, D. Neely, and F. N. Walsh. Electron acceleration from the breaking of relativistic plasma-waves. *Nature*, 377(6550):606–608, 1995.

- [36] D. Umstadter, S.Y. Chen, A. Maksimchuk, G. Mourou, and R. Wagner. Nonlinear optics in relativistic plasmas and laser wake field acceleration of electrons. *Science*, 273(5274):472–475, 1996.
- [37] R. Wagner, S.Y. Chen, A. Maksimchuk, and D. Umstadter. Electron acceleration by a laser wakefield in a relativistically self-guided channel. *Physical Review Letters*, 78(16):3125–3128, 1997.
- [38] F. Amiranoff, S. Baton, D. Bernard, B. Cros, D. Descamps, F. Dorchies, F. Jacquet, V. Malka, J.R. Marques, G. Matthieussent, P. Mine, A. Modena, P. Mora, J. Morillo, and Z. Najmudin. Observation of laser wakefield acceleration of electrons. *Physical Review Letters*, 81(5):995–998, 1998.
- [39] C. Gahn, G.D. Tsakiris, A. Pukhov, J. Meyer-ter Vehn, G. Pretzler, P. Thirolf, D. Habs, and K.J. Witte. Multi-mev electron beam generation by direct laser acceleration in high-density plasma channels. *Physical Review Letters*, 83(23):4772–4775, 1999.
- [40] V. Malka, S. Fritzler, E. Lefebvre, M. M. Aeonard, F. Burgy, J. P. Chambaret, J. F. Chemin, K. Krushelnick, G. Malka, S. P. D. Mangles, Z. Najmudin, M. Pittman, J. P. Rousseau, J. N. Scheurer, B. Walton, and A. E. Dangor. Electron acceleration by a wake field forced by an intense ultrashort laser pulse. *Science*, 298(5598):1596–1600, 2002.
- [41] A. Maksimchuk, S. Gu, K. Flippo, D. Umstadter, and V. Y. Bychenkov. Forward ion acceleration in thin films driven by a high-intensity laser. *Physical Review Letters*, 84(18):4108–4111, 2000.
- [42] S. P. Hatchett, C. G. Brown, T. E. Cowan, E. A. Henry, J. S. Johnson, M. H. Key, J. A. Koch, A. B. Langdon, B. F. Lasinski, R. W. Lee, A. J. Mackinnon, D. M. Pennington, M. D. Perry, T. W. Phillips, M. Roth, T. C. Sangster, M. S. Singh, R. A. Snavely, M. A. Stoyer, S. C. Wilks, and K. Yasuike. Electron, photon, and ion beams from the relativistic interaction of petawatt laser pulses with solid targets. *Physics of Plasmas*, 7(5):2076–2082, 2000.
- [43] M. Hegelich, S. Karsch, G. Pretzler, D. Habs, K. Witte, W. Guenther, M. Allen, A. Blazevic, J. Fuchs, J. C. Gauthier, M. Geissel, P. Audebert, T. Cowan, and M. Roth. Mev ion jets from short-pulse-laser interaction with thin foils. *Physical Review Letters*, 89(8):085002, 2002.
- [44] M. Kaluza, J. Schreiber, M. I. K. Santala, G. D. Tsakiris, K. Eidmann, J. Meyer-ter Vehn, and K. J. Witte. Influence of the laser prepulse on proton acceleration in thin-foil experiments. *Physical Review Letters*, 93(4):045003, 2004.
- [45] J. Faure, Y. Glinec, A. Pukhov, S. Kiselev, S. Gordienko, E. Lefebvre, J. P. Rousseau, F. Burgy, and V. Malka. A laser-plasma accelerator producing monoenergetic electron beams. *Nature*, 431(7008):541–544, 2004.
- [46] C. G. R. Geddes, C. Toth, J. van Tilborg, E. Esarey, C. B. Schroeder, D. Bruhwiler, C. Nieter, J. Cary, and W. P. Leemans. High-quality electron beams from a laser wakefield accelerator using plasma-channel guiding. *Nature*, 431(7008):538–541, 2004.

- 
- [47] S. P. D. Mangles, C. D. Murphy, Z. Najmudin, A. G. R. Thomas, J. L. Collier, A. E. Dangor, E. J. Divall, P. S. Foster, J. G. Gallacher, C. J. Hooker, D. A. Jaroszynski, A. J. Langley, W. B. Mori, P. A. Norreys, F. S. Tsung, R. Viskup, B. R. Walton, and K. Krushelnick. Monoenergetic beams of relativistic electrons from intense laser-plasma interactions. *Nature*, 431(7008):535–538, 2004.
- [48] A. Pukhov and J. Meyer-ter Vehn. Laser wake field acceleration: the highly non-linear broken-wave regime. *Applied Physics B-Lasers And Optics*, 74(4-5):355–361, 2002.
- [49] B. Hidding, K. U. Amthor, B. Liesfeld, H. Schwöerer, S. Karsch, M. Geissler, L. Veisz, K. Schmid, J. G. Gallacher, S. P. Jamison, D. Jaroszynski, G. Pretzler, and R. Sauerbrey. Generation of quasimonoenergetic electron bunches with 80-fs laser pulses. *Physical Review Letters*, 96(10):105004, 2006.
- [50] M. Geissler, S. Rykovanov, J. Schreiber, J. Meyer-Ter-Vehn, and G. D. Tsakiris. 3d simulations of surface harmonic generation with few-cycle laser pulses. *New Journal Of Physics*, 9:218, 2007.
- [51] H. Schwöerer, S. Pfotenhauer, O. Jäckel, K. U. Amthor, B. Liesfeld, W. Ziegler, R. Sauerbrey, K. W. D. Ledingham, and T. Esirkepov. Laser-plasma acceleration of quasimonoenergetic protons from microstructured targets. *Nature*, 439(7075):445–448, 2006.
- [52] B. M. Hegelich, B. J. Albright, J. Cobble, K. Flippo, S. Letzring, M. Paffett, H. Ruhl, J. Schreiber, R. K. Schulze, and J. C. Fernandez. Laser acceleration of quasimonoenergetic mev ion beams. *Nature*, 439(7075):441–444, 2006.
- [53] S. M. Pfotenhauer, O. Jäckel, A. Sachtleben, J. Polz, W. Ziegler, H. P. Schlenvoigt, K. U. Amthor, M. C. Kaluza, K. W. D. Ledingham, R. Sauerbrey, P. Gibbon, A. P. L. Robinson, and H. Schwöerer. Spectral shaping of laser generated proton beams. *New Journal Of Physics*, 10:033034, 2008.
- [54] A. P. L. Robinson and P. Gibbon. Production of proton beams with narrow-band energy spectra from laser-irradiated ultrathin foils. *Physical Review E*, 75(1):015401, 2007.
- [55] A.P.L. Robinson, P. Gibbon, S. M. Pfotenhauer, O. Jäckel, and J. Polz. Scaling of the proton density reduction scheme for the laser acceleration of proton beams with a narrow energy spread. *Plasma Physics and Controlled Fusion Special Issues: Laser and Plasma Accelerators*. To appear in February 2009.
- [56] Christian Ziener. *Aufbau eines 12 Terawatt Titan:Saphir-Lasers zur effizienten Erzeugung charakteristischer Röntgenstrahlung*. PhD thesis, Friedrich-Schiller-Universität Jena, 2001.
- [57] F. Ewald. *Harte Röntgenstrahlung aus relativistischen Laserplasmen und laserinduzierte Kernreaktionen*. PhD thesis, Friedrich-Schiller-Universität Jena, Cambridge, 2004.
- [58] Paul Gibbon. *Short pulse laser interactions with matter*. Imperial Collge Press, 2005.
- [59] F. Amiranoff. Fast electron production in ultra-short high-intensity laser-plasma interaction and its consequences. *Measurement Science and Technology*, 12(11):1795–1800, 2001.

- [60] S. C. Wilks, A. B. Langdon, T. E. Cowan, M. Roth, M. Singh, S. Hatchett, M. H. Key, D. Pennington, A. MacKinnon, and R. A. Snavely. Energetic proton generation in ultra-intense laser-solid interactions. *Physics of Plasmas*, 8(2):542–549, 2001.
- [61] T. Z. Esirkepov, S. V. Bulanov, K. Nishihara, T. Tajima, F. Pegoraro, V. S. Khoroshkov, K. Mima, H. Daido, Y. Kato, Y. Kitagawa, K. Nagai, and S. Sakabe. Proposed double-layer target for the generation of high-quality laser-accelerated ion beams. *Physical Review Letters*, 89(17):175003, 2002.
- [62] A. P. L. Robinson, A. R. Bell, and R. J. Kingham. Effect of target composition on proton energy spectra in ultraintense laser-solid interactions. *Physical Review Letters*, 96(3):035005, 2006.
- [63] D. Umstadter. Relativistic laser-plasma interactions. *Journal of Physics D - Applied Physics*, 36(8):R151–R165, 2003.
- [64] P. Lambropoulos. Mechanisms for multiple ionization of atoms by strong pulsed lasers. *Physical Review Letters*, 55(20):2141–2144, 1985.
- [65] A.S. Epifanov. Theory of electron-avalanche ionization induced in solids by electromagnetic-waves. *IEEE Journal Of Quantum Electronics*, 17(10):2018–2022, 1981.
- [66] M. Sparks, D. L. Mills, R. Warren, T. Holstein, A. A. Maradudin, L. J. Sham, E. Loh, and D. F. King. Theory of electron-avalanche breakdown in solids. *Physical Review B*, 24(6):3519–3536, 1981.
- [67] P.P. Pronko, P.A. VanRompay, C. Horvath, F. Loesel, T. Juhasz, X. Liu, and G. Mourou. Avalanche ionization and dielectric breakdown in silicon with ultrafast laser pulses. *Physical Review B*, 58(5):2387–2390, 1998.
- [68] B. C. Stuart, M. D. Feit, S. Herman, A. M. Rubenchik, B. W. Shore, and M. D. Perry. Nanosecond-to-femtosecond laser-induced breakdown in dielectrics. *Physical Review B*, 53(4):1749–1761, January 1996.
- [69] I. Last and J. Jortner. Dynamics of the coulomb explosion of large clusters in a strong laser field. *Physical Review A*, 62(1):013201, 2000.
- [70] William L. Kruer. *The physics of laser plasma interactions*. Addison-Wesley, 1988.
- [71] W.L.L Kruer and K. Estabrook. Jxb heating by very intense laser-light. *Physics Of Fluids*, 28(1):430–432, 1985.
- [72] P. Bauer, D. And Mulser and W.H. Steeb. Relativistic ponderomotive force, uphill acceleration, and transition to chaos. *Physical Review Letters*, 75(25):4622–4625, 1995.
- [73] E.A Startsev and C.J. McKinstrie. Multiple scale derivation of the relativistic ponderomotive force. *Physical Review E*, 55(6, Part B):7527–7535, 1997.
- [74] B. Quesnel and P. Mora. Theory and simulation of the interaction of ultraintense laser pulses with electrons in vacuum. *Physical Review E*, 58(3):3719–3732, 1998.
- [75] S. C. Wilks, W. L. Kruer, M. Tabak, and A. B. Langdon. Absorption of ultra-intense laser-pulses. *Physical Review Letters*, 69(9):1383–1386, 1992.



- 
- [76] M. Schnürer, M. P. Kalashnikov, P. V. Nickles, T. Schlegel, W. Sandner, N. Demchenko, R. Nolte, and P. Ambrosi. Hard x-ray-emission from intense short-pulse laser plasmas. *Physics Of Plasmas*, 2(8):3106–3110, 1995.
- [77] G. Malka and J.L. Miquel. Experimental confirmation of ponderomotive-force electrons produced by an ultrarelativistic laser pulse on a solid target. *Physical Review Letters*, 77(1):75–78, 1996.
- [78] U. Teubner, I. Uschmann, P. Gibbon, D. Altenbernd, E. Forster, T. Feurer, W. Theobald, R. Sauerbrey, G. Hirst, M. H. Key, J. Lister, and D. Neely. Absorption and hot electron production by high intensity femtosecond uv-laser pulses in solid targets. *Physical Review E*, 54(4):4167–4177, 1996.
- [79] T. Feurer, W. Theobald, R. Sauerbrey, I. Uschmann, D. Altenbernd, U. Teubner, P. Gibbon, E. Forster, G. Malka, and J. L. Miquel. Onset of diffuse reflectivity and fast electron flux inhibition in 528-nm-laser solid interactions at ultrahigh intensity. *Physical Review E*, 56(4):4608–4614, 1997.
- [80] M. Schnürer, R. Nolte, T. Schlegel, M. P. Kalachnikov, P. V. Nickels, P. Ambrosi, and W. Sandner. On the distribution of hot electrons produced in short-pulse laser-plasma interaction. *Journal Of Physics B-Atomic Molecular And Optical Physics*, 30(20):4653–4661, 1997.
- [81] P. A. Norreys, M. Santala, E. Clark, M. Zepf, I. Watts, F. N. Beg, K. Krushelnick, M. Tatarakis, A. E. Dangor, X. Fang, P. Graham, T. McCanny, R. P. Singhal, K. W. D. Ledingham, A. Creswell, D. C. W. Sanderson, J. Magill, A. Machacek, J. S. Wark, R. Allott, B. Kennedy, and D. Neely. Observation of a highly directional gamma-ray beam from ultrashort, ultraintense laser pulse interactions with solids. *Physics Of Plasmas*, 6(5):2150–2156, 1999.
- [82] M. Schnürer, R. Nolte, A. Rousse, G. Grillon, G. Cheriaux, M. P. Kalachnikov, P. V. Nickles, and W. Sandner. Dosimetric measurements of electron and photon yields from solid targets irradiated with 30 fs pulses from a 14 tw laser. *Physical Review E*, 61(4):4394–4401, 2000.
- [83] Neil W. Ashcroft and N. David Mermin. *Solid state physics*. Saunders College Publishing, Philadelphia, 1976.
- [84] Peter W. Milonni and Joseph H. Eberly. *Lasers*. Wiley, New York, 1988.
- [85] H.C. Kapteyn, M.M. Murnane, A. Szoke, and R.W. Falcone. Prepulse energy suppression for high-energy ultrashort pulses using self-induced plasma shuttering. *Optics Letters*, 16(7):490–492, 1991.
- [86] C. Ziener, P.S. Foster, E.J. Divall, C.J. Hooker, M.H.R. Hutchinson, A.J. Langley, and D. Neely. Specular reflectivity of plasma mirrors as a function of intensity, pulse duration, and angle of incidence. *Journal Of Applied Physics*, 93(1):768–770, 2003.
- [87] B. Dromey, S. Kar, M. Zepf, and P. Foster. The plasma mirror - a subpicosecond optical switch for ultrahigh power lasers. *Review Of Scientific Instruments*, 75(3):645–649, 2004.

- [88] Anna Levy, Tiberio Ceccotti, Pascal D'Oliveira, Fabrice Reau, Michel Perdrix, Fabien Qurere, Pascal Monot, Michel Bougeard, Herve Lagadec, Philippe Martin, Jean-Paul Geindre, and Patrick Audebert. Double plasma mirror for ultrahigh temporal contrast ultraintense laser pulses. *Optics Letters*, 32(3):310–312, 2007.
- [89] K.G. Estabrook, E.J. Valeo, and Wl. Kruer. 2-dimensional relativistic simulations of resonance-absorption. *Physics Of Fluids*, 18(9):1151–1159, 1975.
- [90] D.W. Forslund, J.M. Kindel, K. Lee, E.L. Lindman, and R.L. Morse. Theory and simulation of resonant absorption in a hot plasma. *Physical Review A*, 11(2):679–683, 1975.
- [91] D.D. Meyerhofer, H. Chen, J.A. Delettrez, B. Soom, S. Uchida, and B. Yaakobi. Resonance-absorption in high-intensity contrast, picosecond laser-plasma interactions. *Physics Of Fluids B-Plasma Physics*, 5(7, Part 2):2584–2588, 1993.
- [92] S.C. Wilks and W.L. Kruer. Absorption of ultrashort, ultra-intense laser light by solids and overdense plasmas. *IEEE Journal Of Quantum Electronics*, 33(11):1954–1968, 1997.
- [93] P. Mulser, M. Kanopathipillai, and D. H. H. Hoffmann. Two very efficient nonlinear laser absorption mechanisms in clusters. *Physical Review Letters*, 95(10):103401, 2005.
- [94] F. Brunel. Not-so-resonant, resonant absorption. *Physical Review Letters*, 59:52, 1987.
- [95] G. Bonnaud, P. Gibbon, J. Kindel, and E. Williams. Laser interaction with a sharp-edged overdense plasma. *Laser And Particle Beams*, 9(2):339–354, 1991.
- [96] S. Kato, B. Bhattacharyya, A. Nishiguchi, and K. Mima. Wave breaking and absorption efficiency for short pulse p-polarized laser-light in a very steep density gradient. *Physics Of Fluids B-Plasma Physics*, 5(2):564–570, 1993.
- [97] P. Gibbon and A.R. Bell. Collisionless absorption in sharp-edged plasmas. *Physical Review Letters*, 68(10):1535–1538, 1992.
- [98] Paul Gibbon. Resistively enhanced proton acceleration in high intensity laser-foil interactions. *private copy*, -:-, 2004.
- [99] R. Dendy. *Plasma physics: an introductory course*. Cambridge University Press, 1993.
- [100] H. M. Milchberg and R. R. Freeman. Light absorption in ultrashort scale length plasmas. *J. Opt. Soc. Am. B*, 6(7):1351, 1989.
- [101] S. C. Rae and K. Burnett. Reflectivity of steep-gradient plasmas in intense subpicosecond laser-pulses. *Physical Review A*, 44(6):3835–3840, 1991.
- [102] J. C. Kieffer, P. Audebert, M. Chaker, J. P. Matte, H. Pepin, T. W. Johnston, P. Maine, D. Meyerhofer, J. Delettrez, D. Strickland, P. Bado, and G. Mourou. Short-pulse laser-absorption in very steep plasma-density gradients. *Physical Review Letters*, 62(7):760–763, 1989.

- 
- [103] J. C. Kieffer, J. P. Matte, S. Belair, M. Chaker, P. Audebert, H. Pepin, P. Maine, D. Strickland, P. Bado, and G. Mourou. Absorption of an ultrashort laser-pulse in very steep plasma-density gradients. *Ieee Journal Of Quantum Electronics*, 25(12):2640–2647, 1989.
- [104] E.G. Gamalii and V.T. Tikhonchuk. Effect of intense ultrashort light-pulses on a substance. *JETP Letters*, 48(8):453–455, 1988.
- [105] W. Rozmus and V.T. Tikhonchuk. Skin effect and interaction of short laser-pulses with dense-plasmas. *Physical Review A*, 42(12):7401–7412, 1990.
- [106] A.A. Andreev, E.G. Gamaly, V.N. Novikov, A.N. Semakhin, and V.T. Tikhonchuk. Heating of a dense-plasma with an ultrashort laser-pulse in the anomalous skin-effect regime. *Soviet JETP*, 101(6):1808–1826, 1992.
- [107] A. J. Mackinnon, Y. Sentoku, P. K. Patel, D. W. Price, S. Hatchett, M. H. Key, C. Andersen, R. Snavely, and R. R. Freeman. Enhancement of proton acceleration by hot-electron recirculation in thin foils irradiated by ultraintense laser pulses. *Physical Review Letters*, 88(21):215006, 2002.
- [108] M Roth, M Allen, P Audebert, A Blazevic, E Brambrink, TE Cowan, J Fuchs, JC Gauthier, M Geissel, M Hegelich, S Karsch, J Meyer-ter Vehn, H Ruhl, T Schlegel, and RB Stephens. The generation of high-quality, intense ion beams by ultra-intense lasers. *Plasma Physics And Controlled Fusion*, 44(Suppl. 12B):B99–B108, 2002.
- [109] Av Gurevich, Lv Pariiska, and Lp Pitaevsk. Self-similar motion of rarefied plasma. *Soviet JETP*, 22(2):449, 1966.
- [110] P. Mora. Plasma expansion into a vacuum. *Physical Review Letters*, 90(18):185002, 2003.
- [111] J. Fuchs, Y. Sentoku, E. d’Humieres, T. E. Cowan, J. Cobble, P. Audebert, A. Kemp, A. Nikroo, P. Antici, E. Brambrink, A. Blazevic, E. M. Campbell, J. C. Fernandez, J. C. Gauthier, M. Geissel, M. Hegelich, S. Karsch, H. Popescu, N. Renard-LeGalloudec, M. Roth, J. Schreiber, R. Stephens, and H. Pepin. Comparative spectra and efficiencies of ions laser-accelerated forward from the front and rear surfaces of thin solid foils. *Physics Of Plasmas*, 14(5):053105, 2007.
- [112] G. Pretzler, T. Schlegel, E. Fill, and D. Eder. Hot-electron generation in copper and photopumping of cobalt. *Physical Review E*, 62(4):5618–5623, 2000.
- [113] M. H. Key, M. D. Cable, T. E. Cowan, K. G. Estabrook, B. A. Hammel, S. P. Hatchett, E. A. Henry, D. E. Hinkel, J. D. Kilkenny, J. A. Koch, W. L. Kruer, A. B. Langdon, B. F. Lasinski, R. W. Lee, B. J. MacGowan, A. MacKinnon, J. D. Moody, M. J. Moran, A. A. Offenberger, D. M. Pennington, M. D. Perry, T. J. Phillips, T. C. Sangster, M. S. Singh, M. A. Stoyer, M. Tabak, G. L. Tietbohl, M. Tsukamoto, K. Wharton, and S. C. Wilks. Hot electron production and heating by hot electrons in fast ignitor research. *Physics Of Plasmas*, 5(5):1966–1972, 1998.
- [114] J. Yu, Z. Jiang, J.C. Kieffer, and A. Krol. Hard x-ray emission in high intensity femtosecond laser-target interaction. *Physics Of Plasmas*, 6(4):1318–1322, 1999.

- [115] R. B. Stephens, R. A. Snavely, Y. Aglitskiy, F. Amiranoff, C. Andersen, D. Batani, S. D. Baton, T. Cowan, R. R. Freeman, T. Hall, S. P. Hatchett, J. M. Hill, M. H. Key, J. A. King, J. A. Koch, M. Koenig, A. J. MacKinnon, K. L. Lancaster, E. Martinolli, P. Norreys, E. Perelli-Cippo, M. Rabec Le Gloahec, C. Rousseaux, J. J. Santos, and F. Scianitti. K<sub>α</sub> fluorescence measurement of relativistic electron transport in the context of fast ignition. *Physical Review E (Statistical, Nonlinear, and Soft Matter Physics)*, 69(6):066414, 2004.
- [116] K. L. Lancaster, J. S. Green, D. S. Hey, K. U. Akli, J. R. Davies, R. J. Clarke, R. R. Freeman, H. Habara, M. H. Key, R. Kodama, K. Krushelnick, C. D. Murphy, M. Nakatsutsumi, P. Simpson, R. Stephens, C. Stoeckl, T. Yabuuchi, M. Zepf, and P. A. Norreys. Measurements of energy transport patterns in solid density laser plasma interactions at intensities of  $5 \times 10^{20}$  W cm<sup>-2</sup>. *Physical Review Letters*, 98(12):125002, 2007.
- [117] Jens Polz. Zeitaufgelöste untersuchungen der ionenbeschleunigung bei relativistischen laser-plasma-wechselwirkungen an dünnen folien. Master's thesis, Department of Physics and Astronomy, Friedrich-Schiller-University Jena, 2008.
- [118] A. Pukhov. Three-dimensional simulations of ion acceleration from a foil irradiated by a short-pulse laser. *Physical Review Letters*, 86(16):3562–3565, 2001.
- [119] A. P. L. Robinson and M. Sherlock. Magnetic collimation of fast electrons produced by ultraintense laser irradiation by structuring the target composition. *Physics Of Plasmas*, 14(8):083105, 2007.
- [120] P. Mora. Thin-foil expansion into a vacuum. *Physical Review E*, 72(5, Part 2):056401, 2005.
- [121] M. Passoni, V.T. Tikhonchuk, M. Lontano, and V.Y. Bychenkov. Charge separation effects in solid targets and ion acceleration with a two-temperature electron distribution. *Physical Review E*, 69(2, Part 2):026411, 2004.
- [122] V.T. Tikhonchuk, A.A. Andreev, S.G. Bochkarev, and V.Y. Bychenkov. Ion acceleration in short-laser-pulse interaction with solid foils. *Plasma Physics And Controlled Fusion*, 47(Sp. Iss. SI Suppl. 12B):B869–B877, 2005.
- [123] J. Schreiber, F. Bell, F. Grüner, U. Schramm, M. Geissler, M. Schnürer, S. Ter-Avetisyan, B. M. Hegelich, J. Cobble, E. Brambrink, J. Fuchs, P. Audebert, and D. Habs. Analytical model for ion acceleration by high-intensity laser pulses. *Physical Review Letters*, 97(4):045005, 2006.
- [124] E. d'Humieres, E. Lefebvre, L. Gremillet, and V. Malka. Proton acceleration mechanisms in high-intensity laser interaction with thin foils. *Physics of Plasmas*, 12(6):062704, 2005.
- [125] T. Esirkepov, M. Borghesi, S.V. Bulanov, G. Mourou, and T. Tajima. Highly efficient relativistic-ion generation in the laser-piston regime. *Physical Review Letters*, 92(17):175003, 2004.
- [126] T. Z. Esirkepov, M. Yamagiwa, and T. Tajima. Laser ion acceleration scaling laws seen in multi-parametric pic simulations. *Physical Review Letters*, 96:105001, 2006.

- 
- [127] T. V. Liseikina and A. Macchi. Features of ion acceleration by circularly polarized laser pulses. *Applied physics letters*, 91(17):171502, 2007.
- [128] X. M. Zhang, B. F. Shen, X. M. Li, Z. Y. Jin, and F. C. Wang. Multistaged acceleration of ions by circularly polarized laser pulse: Monoenergetic ion beam generation. *Physics Of Plasmas*, 14(7):073101, 2007.
- [129] O. Klimo, J. Psikal, J. Limpouch, and V. T. Tikhonchuk. Monoenergetic ion beams from ultrathin foils irradiated by ultrahigh-contrast circularly polarized laser pulses. *Physical Review Special Topics-Accelerators And Beams*, 11(3):031301, 2008.
- [130] A. P. L. Robinson, M. Zepf, S. Kar, R. G. Evans, and C. Bellei. Radiation pressure acceleration of thin foils with circularly polarized laser pulses. *New Journal Of Physics*, 10:013021, 2008.
- [131] K. Krushelnick, E. L. Clark, M. Zepf, J. R. Davies, F. N. Beg, A. Machacek, M. I. K. Santala, M. Tatarakis, I. Watts, P. A. Norreys, and A. E. Dangor. Energetic proton production from relativistic laser interaction with high density plasmas. *Physics of Plasmas*, 7(5):2055–2061, 2000.
- [132] E. L. Clark, K. Krushelnick, M. Zepf, F. N. Beg, M. Tatarakis, A. Machacek, M. I. K. Santala, I. Watts, P. A. Norreys, and A. E. Dangor. Energetic heavy-ion and proton generation from ultraintense laser-plasma interactions with solids. *Physical Review Letters*, 85(8):1654–1657, 2000.
- [133] E. L. Clark, K. Krushelnick, J. R. Davies, M. Zepf, M. Tatarakis, F. N. Beg, A. Machacek, P. A. Norreys, M. I. K. Santala, I. Watts, and A. E. Dangor. Measurements of energetic proton transport through magnetized plasma from intense laser interactions with solids. *Physical Review Letters*, 84(4):670–673, 2000.
- [134] K. Nemoto, T. Kamei, H. Abe, D. Imanishi, H. Narui, and S. Hirata. Monolithic-integrated two-wavelength laser diodes for digital-versatile-disk/compact-disk playback. *Applied Physics Letters*, 78(16):2270–2272, 2001.
- [135] A. Maksimchuk, K. Flippo, H. Krause, G. Mourou, K. Nemoto, D. Shultz, D. Umstadter, R. Vane, V. Y. Bychenkov, G. I. Dudnikova, V. F. Kovalev, K. Mima, V. N. Novikov, Y. Sentoku, and S. V. Tolokonnikov. High-energy ion generation by short laser pulses. *Plasma Physics Reports*, 30(6):473–495, 2004.
- [136] M. Borghesi, D. H. Campbell, A. Schiavi, O. Willi, M. Galimberti, L. A. Gizzi, A. J. Mackinnon, R. D. Snavely, P. Patel, S. Hatchett, M. Key, and W. Nazarov. Propagation issues and energetic particle production in laser-plasma interactions at intensities exceeding  $10^{19}$  W/cm<sup>2</sup>. *Laser and Particle Beams*, 20(1):31–38, 2002.
- [137] Louise Willingale. *Ion Acceleration from High Intensity Laser Plasma Interactions: Measurements and Applications*. PhD thesis, University of London, 2007.
- [138] S. Karsch, S. Düsterer, H. Schwoerer, F. Ewald, D. Habs, M. Hegelich, G. Pretzler, A. Pukhov, K. Witte, and R. Sauerbrey. High-intensity laser induced ion acceleration from heavy-water droplets. *Physical Review Letters*, 91(1):015001, 2003.

- [139] M. Schnürer, S. Ter-Avetisyan, P. V. Nickles, and A. A. Andreev. Influence of target system on the charge state, number, and spectral shape of ion beams accelerated by femtosecond high-intensity laser pulses. *Physics of Plasmas*, 14(3):033101, 2007.
- [140] J. Jha, D. Mathur, and M. Krishnamurthy. Engineering clusters for table-top acceleration of ions. *Applied Physics Letters*, 88(4):041107, 2006.
- [141] L. Willingale, S. P. D. Mangles, P. M. Nilson, R. J. Clarke, A. E. Dangor, M. C. Kaluza, S. Karsch, K. L. Lancaster, W. B. Mori, Z. Najmudin, J. Schreiber, A. G. R. Thomas, M. S. Wei, and K. Krushelnick. Collimated multi-mev ion beams from high-intensity laser interactions with underdense plasma. *Physical Review Letters*, 96(24):245002, 2006.
- [142] A. R. Bell, J. R. Davies, S. Guerin, and H. Ruhl. Fast-electron transport in high-intensity short-pulse laser-solid experiments. *Plasma Physics And Controlled Fusion*, 39(5):653–659, May 1997.
- [143] F. Pisani, A. Bernardinello, D. Batani, A. Antonicci, E. Martinolli, M. Koenig, L. Gremillet, F. Amiranoff, S. Baton, J. Davies, T. Hall, D. Scott, P. Norreys, A. Djaoui, C. Rousseaux, P. Fews, H. Bandulet, and H. Pepin. Experimental evidence of electric inhibition in fast electron penetration and of electric-field-limited fast electron transport in dense matter. *Physical Review E*, 62(5):R5927–R5930, November 2000.
- [144] D. Batani, A. Antonicci, F. Pisani, T. A. Hall, D. Scott, F. Amiranoff, M. Koenig, L. Gremillet, S. Baton, E. Martinolli, C. Rousseaux, and W. Nazarov. Inhibition in the propagation of fast electrons in plastic foams by resistive electric fields. *Physical Review E*, 65(6):066409, June 2002.
- [145] E. Martinolli, D. Batani, E. Perelli-Cippo, F. Scianitti, M. Koenig, J. J. Santos, F. Amiranoff, S. D. Baton, T. Hall, M. Key, A. Mackinnon, R. Snavely, R. Freeman, C. Andersen, J. King, R. Stephens, M. R. Le Gloahec, C. Rousseaux, and T. E. Cowan. Fast electron transport and heating in solid-density matter. *Laser And Particle Beams*, 20(2):171–175, June 2002.
- [146] A. R. Bell and R. J. Kingham. Resistive collimation of electron beams in laser-produced plasmas. *Physical Review Letters*, 91(3):035003, July 2003.
- [147] F. Pegoraro, S. V. Bulanov, F. Califano, and M. Lontano. Nonlinear development of the weibel instability and magnetic field generation in collisionless plasmas. *Physica Scripta*, T63:262–265, 1996.
- [148] A. Pukhov and J. MeyerTerVehn. Laser hole boring into overdense plasma and relativistic electron currents for fast ignition of icf targets. *Physical Review Letters*, 79(14):2686–2689, 1997.
- [149] M. Honda, J. Meyer-ter Vehn, and A. Pukhov. Collective stopping and ion heating in relativistic-electron-beam transport for fast ignition. *Physical Review Letters*, 85(10):2128–2131, September 2000.
- [150] Y. Sentoku, K. Mima, P. Kaw, and K. Nishikawa. Anomalous resistivity resulting from mev-electron transport in overdense plasma. *Physical Review Letters*, 90(15):155001, April 2003.

- 
- [151] C. Reich, P. Gibbon, I. Uschmann, and E. Forster. Yield optimization and time structure of femtosecond laser plasma k alpha sources. *Physical Review Letters*, 84(21):4846–4849, May 2000.
- [152] F. Lindau, O. Lundh, A. Persson, P. McKenna, K. Osvay, D. Batani, and C.G. Wahlstrom. Laser-accelerated protons with energy-dependent beam direction. *Physical Review Letters*, 95(17):175002, 2005.
- [153] O. Lundh, F. Lindau, A. Persson, C.-G. Wahlstroem, P. McKenna, and D. Batani. Influence of shock waves on laser-driven proton acceleration. *Physical Review E*, 76(2, Part 2):026404, 2007.
- [154] I Spencer, KWD Ledingham, P McKenna, T McCanny, RP Singhal, PS Foster, D Neely, AJ Langley, EJ Divall, CJ Hooker, RJ Clarke, PA Norreys, EL Clark, K Krushelnick, and JR Davies. Experimental study of proton emission from 60-fs, 200-mj high-repetition-rate tabletop-laser pulses interacting with solid targets. *Physical Review E*, 67(4, Part 2):046402, 2003.
- [155] Y. Sentoku, T. E. Cowan, A. Kemp, and H. Ruhl. High energy proton acceleration in interaction of short laser pulse with dense plasma target. *Physics of Plasmas*, 10(5):2009–2015, 2003.
- [156] K. Matsukado, T. Esirkepov, K. Kinoshita, H. Daido, T. Utsumi, Z. Li, A. Fukumi, Y. Hayashi, S. Orimo, M. Nishiuchi, S. V. Bulanov, T. Tajima, A. Noda, Y. Iwashita, T. Shirai, T. Takeuchi, S. Nakamura, A. Yamazaki, M. Ikegami, T. Mihara, A. Morita, M. Uesaka, K. Yoshii, T. Watanabe, T. Hosokai, A. Zhidkov, A. Ogata, Y. Wada, and T. Kubota. Energetic protons from a few-micron metallic foil evaporated by an intense laser pulse. *Physical Review Letters*, 91(21):215001, 2003.
- [157] Malte Christoph Kaluza. *Characterisation of Laser-Accelerated Proton Beams*. PhD thesis, MPI für Quantenoptik, Garching, 2004.
- [158] A. J. Mackinnon, M. Borghesi, S. Hatchett, M. H. Key, P. K. Patel, H. Campbell, A. Schiavi, R. Snavely, S. C. Wilks, and O. Willi. Effect of plasma scale length on multi-mev proton production by intense laser pulses. *Physical Review Letters*, 86(9):1769–1772, 2001.
- [159] A. P. L. Robinson, D. Neely, P. McKenna, and R. G. Evans. Spectral control in proton acceleration with multiple laser pulses. *Plasma Physics And Controlled Fusion*, 49(4):373–384, 2007.
- [160] J. Fuchs, C. A. Cecchetti, M. Borghesi, T. Grismayer, E. d’Humieres, P. Antici, S. Atzeni, P. Mora, A. Pipahl, L. Romagnani, A. Schiavi, Y. Sentoku, T. Toncian, P. Audebert, and O. Willi. Laser-foil acceleration of high-energy protons in small-scale plasma gradients. *Physical Review Letters*, 99(1):015002, 2007.
- [161] L. Romagnani, J. Fuchs, M. Borghesi, P. Antici, P. Audebert, F. Ceccherini, T. Cowan, T. Grismayer, S. Kar, A. Macchi, P. Mora, G. Pretzler, A. Schiavi, T. Toncian, and O. Willi. Dynamics of electric fields driving the laser acceleration of multi-mev protons. *Physical Review Letters*, 95(19):195001, 2005.

- [162] I. Velchev, E. Fourkal, and C. M. Ma. Laser-induced coulomb mirror effect: Applications for proton acceleration. *Physics Of Plasmas*, 14(3):033106, 2007.
- [163] L. D. Landau and E. M. Lifschitz. *Elektrodynamik der Kontinua*. Akademie-Verlag Berlin, 1971.
- [164] S. V. Bulanov, T. Z. Esirkepov, F. F. Kamenets, Y. Kato, A. V. Kuznetsov, K. Nishihara, F. Pegoraro, T. Tajima, and V. S. Khoroshkov. Generation of high-quality charged particle beams during the acceleration of ions by high-power laser radiation. *Plasma Physics Reports*, 28(12):975–991, 2002.
- [165] C. K. Birdsall and A. B. Langdon. *Plasma Physics via Computer Simulation*. Adam Hilger, 1991.
- [166] A. V. Brantov, V. T. Tikhonchuk, O. Klimo, D. V. Romanov, S. Ter-Avetisyan, M. Schnürer, T. Sokollik, and P. V. Nickles. Quasi-mono-energetic ion acceleration from a homogeneous composite target by an intense laser pulse. *Physics Of Plasmas*, 13(12):122705, 2006.
- [167] S. Ter-Avetisyan, M. Schnürer, P. V. Nickles, M. Kalashnikov, E. Risse, T. Sokollik, W. Sandner, A. Andreev, and V. Tikhonchuk. Quasimonoenergetic deuteron bursts produced by ultraintense laser pulses. *Physical Review Letters*, 96(14):145006, 2006.
- [168] M. Allen, Y. Sentoku, P. Audebert, A. Blazevic, T. Cowan, J. Fuchs, J. C. Gauthier, M. Geissel, M. Hegelich, S. Karsch, E. Morse, P. K. Patel, and M. Roth. Proton spectra from ultraintense laser-plasma interaction with thin foils: Experiments, theory, and simulation. *Physics of Plasmas*, 10(8):3283–3289, 2003.
- [169] M. Borghesi, A. J. Mackinnon, D. H. Campbell, D. G. Hicks, S. Kar, P. K. Patel, D. Price, L. Romagnani, A. Schiavi, and O. Willi. Multi-mev proton source investigations in ultraintense laser-foil interactions. *Physical Review Letters*, 92(5):055003, 2004.
- [170] P. K. Patel, A. J. Mackinnon, M. H. Key, T. E. Cowan, M. E. Foord, M. Allen, D. F. Price, H. Ruhl, P. T. Springer, and R. Stephens. Isochoric heating of solid-density matter with an ultrafast proton beam. *Physical Review Letters*, 91(12):125004, 2003.
- [171] J. Schreiber, M. Kaluza, F. Grüner, U. Schramm, B. M. Hegelich, J. Cobble, M. Geissler, E. Brambrink, J. Fuchs, P. Audebert, D. Habs, and K. Witte. Source-size measurements and charge distributions of ions accelerated from thin foils irradiated by high-intensity laser pulses. *Applied Physics B - Lasers and Optics*, 79(8):1041–1045, 2004.
- [172] J.J. Santos, F. Amiranoff, S. D. Baton, L. Gremillet, M. Koenig, E. Martinolli, F. Pisani, M. Rabec Le Gloahec, C. Rousseaux, D. Batani, A. Bernardinello, and T. Greison, G. and Hall. Propagation d'électrons rapides dans l'interaction d'une impulsion laser ultra intense avec des cibles solides : diagnostic d'émission propre de la face arrière. in: Rapport d'activité luli 2000. Technical report, Ecole Polytechnique, Palaiseau, France, NTIS: PB2001-106320, 2000.
- [173] W. Ehler, F. Begay, T.H. Tan, J. Hayden, and J. Mcleod. Effect of target purity on laser-produced plasma expansion. *Journal Of Physics D-Applied Physics*, 13(2):L29–L32, 1980.



- 
- [174] M. Allen, P. K. Patel, A. Mackinnon, D. Price, S. Wilks, and E. Morse. Direct experimental evidence of back-surface ion acceleration from laser-irradiated gold foils. *Physical Review Letters*, 93(26):265004, 2004.
- [175] Oliver Jäckel. *Vermessung von Ionenspektren aus relativistischen laserproduzierten Plasmen*. Diplomarbeit. Physikalisch-Astronomische Fakultät, Friedrich-Schiller-Universität Jena, 2006.
- [176] P. McKenna, K. W. D. Ledingham, J. M. Yang, L. Robson, T. McCanny, S. Shimizu, R. J. Clarke, D. Neely, K. Spohr, R. Chapman, R. P. Singhal, K. Krushelnick, M. S. Wei, and P. A. Norreys. Characterization of proton and heavier ion acceleration in ultrahigh-intensity laser interactions with heated target foils. *Physical Review E*, 70(3):036405, 2004.
- [177] J. Badziak, E. Woryna, R. Parys, K. Y. Platonov, S. Jablonski, L. Rye, A. B. Vankov, and J. Wolowski. Fast proton generation from ultrashort laser pulse interaction with double-layer foil targets. *Physical Review Letters*, 8721(21):215001, 2001.
- [178] H. Kishimura, H. Morishita, Y. H. Okano, Y. Okano, Y. Hironaka, K. Kondo, K. G. Nakamura, Y. Oishi, and K. Nemoto. Enhanced generation of fast protons from a polymer-coated metal foil by a femtosecond intense laser field. *Applied Physics Letters*, 85(14):2736–2738, 2004.
- [179] D. Strickland and G. Mourou. Compression of amplified chirped optical pulses. *Optics Communications*, 56(3):219–221, 1985.
- [180] O. E. Martinez. Design of high-power ultrashort pulse amplifiers by expansion and compression. *IEEE Journal of Quantum Electronics*, 23:1385, 1988.
- [181] P. Maine, D. Strickland, P. Badot, M. Pessot, and G. Mourou. Generation of ultrahigh peak power pulses by chirped pulse amplification. *IEEE Journal of Quantum Electronics*, 24:389, 1988.
- [182] Daniel Albach. Aufbau einer apparatur zur vorpulsunterdrückung eines 15 terawatt-titan:saphir-lasers. Master's thesis, Department of Physics and Astronomy, Friedrich-Schiller-University Jena, 2005.
- [183] Frank Hinterberger. *Physik der Teilchenbeschleuniger und Ionenoptik*. Springer, Berlin, 1997.
- [184] Shyh-Yuan Lee. *Accelerator Physics*. World Scientific, Singapore, 1999.
- [185] Gianluigi Arduini, P Baudrenghien, T Bohl, Paul Collier, K Cornelis, Wolfgang Höfle, Trevor Paul R Linnecar, Elena Shaposhnikova, Joachim Tückmantel, and J Wenninger. The lhc proton beam in the cern sps. In *Proceedings of the 2003 Particle Accelerator Conference*, 2003.
- [186] S. Lee, T. Katsouleas, R. Hemker, and W. B. Mori. Simulations of a meter-long plasma wakefield accelerator. *Physical Review E*, 61(6):7014–7021, 2000.
- [187] Paul Gibbon. Resistively enhanced proton acceleration via high-intensity laser interactions with cold foil targets. *Physical Review E*, 72(2):026411, 2005.

- [188] Dieter Bäuerle. *Laser Processing and Chemistry*. Springer, 1996.
- [189] T. Fourrier, G. Schrems, T. Muhlberger, J. Heitz, N. Arnold, D. Bauerle, M. Mosbacher, J. Boneberg, and P. Leiderer. Laser cleaning of polymer surfaces. *Applied Physics A - Materials Science & Processing*, 72(1):1–6, 2001.
- [190] N. Arnold, G. Schrems, and D. Bauerle. Ablative thresholds in laser cleaning of substrates from particulates. *Applied Physics A - Materials Science & Processing*, 79(4-6):729–734, 2004.
- [191] D. Ashkenasi, M. Lorenz, R. Stoian, and A. Rosenfeld. Surface damage threshold and structuring of dielectrics using femtosecond laser pulses: the role of incubation. *Applied Surface Science*, 150(1-4):101–106, 1999.
- [192] R. Srinivasan, B. Braren, and K. G. Casey. Nature of incubation pulses in the ultraviolet-laser ablation of polymethyl methacrylate. *Journal Of Applied Physics*, 68(4):1842–1847, 1990.
- [193] Henning Schmidt. *Physikalisch-chemische Aspekte des excimerlaserinduzierten Ablationsprozesses an Polymeren*. PhD thesis, Georg-August-Universität Göttingen, 1994.
- [194] Andrew Zangwill. *Physics at Surfaces*. Cambridge University Press, 1988.
- [195] T. Toncian, M. Borghesi, J. Fuchs, E. d’Humieres, P. Antici, P. Audebert, E. Brambrink, C. A. Cecchetti, A. Pipahl, L. Romagnani, and O. Willi. Ultrafast laser-driven microlens to focus and energy-select mega-electron volt protons. *Science*, 312(5772):410–413, 2006.
- [196] S. M. Pfothenauer, O. Jäckel, J. Polz, S. Steinke, H.-P. Schlenvoigt, J. Heymann, A. P. L. Robinson, and M. C. Kaluza. Multi-stage laser proton acceleration. to be submitted.
- [197] O. Willi, T. Toncian, M. Borghesi, J. Fuchs, E. D’humieres, P. Antici, P. Audebert, E. Brambrink, C. Cecchetti, A. Pipahl, and L. Romagnani. Laser triggered micro-lens for focusing and energy selection of mev protons. *Laser And Particle Beams*, 25(1):71–77, 2007.
- [198] Oliver Jäckel. *Investigations of Ion Acceleration from Relativistic Laser-Plasmas*. PhD thesis, Friedrich-Schiller-Universität Jena, expected 2009.
- [199] Url <http://www.clf.rl.ac.uk/facilities/vulcan/index.htm>.
- [200] Url <http://jlf.llnl.gov/>.
- [201] Url <http://www.clf.rl.ac.uk/facilities/astraweb/astrageminhome.htm>.
- [202] <http://www.ph.utexas.edu/utlasers/>.
- [203] Url <http://www.engin.umich.edu/research/cuos/researchgroups/hfs>.
- [204] Url <http://www.physik.uni-jena.de/polaris/>.
- [205] J. Hein, M. C. Kaluza, R. Boedefeld, M. Siebold, S. Podleska, and R. Sauerbrey. *Lasers and Nuclei: Lecture Notes in Physics*, chapter POLARIS: An All Diode-Pumped Ultrahigh Peak Power Laser for High Repetition Rates, pages 47–66. Springer Berlin / Heidelberg, 2006.

- 
- [206] M. Siebold, J. Hein, M. Hornung, S. Podleska, M.C. Kaluza, S. Bock, and R. Sauerbrey. Diode-pumped lasers for ultra-high peak power. *Applied Physics B: Lasers and Optics*, 90(3):431–437, 2008.
- [207] Marco Hornung, Ragnar Bödefeld, Mathias Siebold, Matthias Schnepf, Joachim Hein, Roland Sauerbrey, and Malte C. Kaluza. Alignment of a tiled-grating compressor in a high-power chirped-pulse amplification laser system. *Appl. Opt.*, 46(30):7432–7435, 2007.
- [208] Matthias Siebold. *Hochrepetierende, diodengepumpte Festkörperlaserverstärker für den Ultrakurzbereich*. PhD thesis, Department of Physics and Astronomy, Friedrich-Schiller-University Jena, 2006.
- [209] J. Hein, S. Podleska, M. Siebold, M. Hellwing, R. Bodefeld, R. Sauerbrey, D. Ehrhart, and W. Wintzer. Diode-pumped chirped pulse amplification to the joule level. *Applied Physics B - Lasers and Optics*, 79(4):419–422, 2004.
- [210] T. Ceccotti, A. Levy, H. Popescu, F. Reau, P. D’Oliveira, P. Monot, J. P. Geindre, E. Lefebvre, and Ph. Martin. Proton acceleration with high-intensity ultrahigh-contrast laser pulses. *Physical Review Letters*, 99(18):185002, 2007.
- [211] D. Neely, P. Foster, A. Robinson, F. Lindau, O. Lundh, A. Persson, C. G. Wahlstrom, and P. McKenna. Enhanced proton beams from ultrathin targets driven by high contrast laser pulses. *Applied Physics Letters*, 89(2):021502, 2006.
- [212] F. Quere, C. Thaury, P. Monot, S. Dobosz, P. Martin, J. P. Geindre, and P. Audebert. Coherent wake emission of high-order harmonics from overdense plasmas. *Physical Review Letters*, 96(12):125004, March 2006.
- [213] C. Thaury, F. Quere, J.-P. Geindre, A. Levy, T. Ceccotti, P. Monot, M. Bougeard, F. Reau, P. D’Oliveira, P. Audebert, R. Marjoribanks, and P. H. Martin. Plasma mirrors for ultrahigh-intensity optics. *Nature Physics*, 3(6):424–429, 2007.
- [214] B. Dromey, S. Kar, C. Bellei, D. C. Carroll, R. J. Clarke, J. S. Green, S. Kneip, K. Markey, S. R. Nagel, P. T. Simpson, L. Willingale, P. McKenna, D. Neely, Z. Najmudin, K. Krushelnick, P. A. Norreys, and M. Zepf. Bright multi-keV harmonic generation from relativistically oscillating plasma surfaces. *Physical Review Letters*, 99(8):085001, 2007.
- [215] F. Quere, C. Thaury, H. George, J. P. Geindre, E. Lefebvre, G. Bonnaud, S. Huller, P. Monot, and P. Martin. Basic mechanisms of laser high-order harmonic generation from plasma mirrors. *Journal Of Modern Optics*, 55(16):2711–2721, 2008.
- [216] Wolf Ulrich Batzler, Klaus Giersiepen, Stefan Hentschel, Gabriele Husmann, Peter Kaatsch, Alexander Katalinic, Joachim Kieschke, Klaus Kraywinkel, Martin Meyer, Roland Stabenow, and Ute Wolf. *Krebs in Deutschland 2003-2004. Häufigkeiten und Trends*. Robert Koch-Institut Berlin & Gesellschaft der epidemiologischen Krebsregister in Deutschland e.V., 6. auflage edition, 2008.
- [217] E. Fourkal, J. S. Li, W. Xiong, A. Nahum, and C. M. Ma. Intensity modulated radiation therapy using laser-accelerated protons: a monte carlo dosimetric study. *Physics In Medicine And Biology*, 48(24):3977–4000, 2003.

- [218] V. Malka, S. Fritzler, E. Lefebvre, E. d’Humieres, R. Ferrand, G. Grillon, C. Albaret, S. Meyroneinc, J. P. Chambaret, A. Antonetti, and D. Hulin. Practicability of proton-therapy using compact laser systems. *Medical Physics*, 31(6):1587–1592, 2004.
- [219] C. Ma, E. Fourkal, J. Li, I. Veltchev, W. Luo, and A. Pollack. A laser-proton accelerator for radiation oncology: System design. *Medical Physics*, 31(6):1855–1855, 2004.
- [220] R. R. Wilson. Radiological use of fast protons. *Radiology*, 47(5):487–491, 1946.
- [221] E. B. Hug. Protons versus photons: A status assessment at the beginning of the 21(st) century. *Radiotherapy And Oncology*, 73:S35–S37, 2004.
- [222] G. Kraft. Tumor therapy with heavy charged particles. *Progress In Particle And Nuclear Physics*, Vol 45, Supplement 2, 45:S473–S544, 2000.
- [223] Gerhard Kraft. *Tumorthherapie mit schweren Ionen. Physikalische und Biologische Grundlagen, Technische Realisierung an der GSI, Klinische Ergebnisse*. Gesellschaft für Schwerionenforschung & Verein zur Förderung der Tumorthherapie mit schweren Ionen e.V., 2008.
- [224] Klaus Bethge, Gertrud Walter, and Bernhard Wiedemann. *Kernphysik*. Springer, 2001.
- [225] Fine Fiedler. *Anwendung des in-beam PET Therapiemonitorings auf Präzisionsbestrahlungen mit Helium-Ionen*. PhD thesis, Technische Universität Dresden, 2008.
- [226] National institute of standards and technology: Physical reference data.
- [227] W. K. Weyrather and G. Kraft. Rbe of carbon ions: Experimental data and the strategy of rbe calculation for treatment planning. *Radiotherapy And Oncology*, 73:S161–S169, 2004.
- [228] P. Scampoli. Biological effects of accelerated protons. *Radiotherapy And Oncology*, 73:S130–S133, 2004.
- [229] B. Damato, A. Kacperek, M. Chopra, M. A. Sheen, I. R. Campbell, and R. D. Errington. Proton beam radiotherapy of iris melanoma. *International Journal of Radiation Oncology Biology Physics*, 63(1):109–115, 2005.
- [230] B. Damato, A. Kacperek, M. Chopra, I. R. Campbell, and R. D. Errington. Proton beam radiotherapy of choroidal melanoma: The liverpool-clatterbridge experience. *International Journal of Radiation Oncology Biology Physics*, 62(5):1405–1411, 2005.
- [231] T. Haberer, W. Becher, D. Schardt, and G. Kraft. Magnetic scanning system for heavy-ion therapy. *Nuclear Instruments & Methods In Physics Research Section A-Accelerators Spectrometers Detectors And Associated Equipment*, 330(1-2):296–305, 1993.
- [232] G. Kraft. Tumorthherapie with ion beams. *Nuclear Instruments & Methods In Physics Research Section A-Accelerators Spectrometers Detectors And Associated Equipment*, 454(1):1–10, 2000.
- [233] E. Fourkal, I. Veltchev, J. Fan, J. Li, W. Luo, and C. Ma. Analytical calculation of spread-out-bragg-peak distributions for laser-accelerated proton beams. *Medical Physics*, 32(6):2027–2027, 2005.

- 
- [234] E. Fourkal, R. Price, C. Ma, and A. Pollack. Energy and intensity modulated radiation therapy using laser accelerated proton beams. *Medical Physics*, 31(6):1884–1884, 2004.
- [235] W. Luo, E. Fourkal, and C. Ma. A superconducting magnet design for a laser-accelerated proton therapy system. *Medical Physics*, 31(6):1859–1859, 2004.
- [236] W. Luo, E. Fourkal, J. S. Li, and C. M. Ma. Particle selection and beam collimation system for laser-accelerated proton beam therapy. *Medical Physics*, 32(3):794–806, 2005.
- [237] Universitätsklinikum Heidelberg. *HIT - Heidelberger Ionenstrahl-Therapiezentrum*. Medizinische Fakultät der Universität Heidelberg, 2008.
- [238] N. Bityurin, B. S. Luk'yanchuk, M. H. Hong, and T. C. Chong. Models for laser ablation of polymers. *Chemical Reviews*, 103(2):519–552, 2003.
- [239] E. Sutcliffe and R. Srinivasan. Dynamics of uv laser ablation of organic polymer surfaces. *Journal Of Applied Physics*, 60(9):3315–3322, 1986.
- [240] G. D. Mahan, H. S. Cole, Y. S. Liu, and H. R. Philipp. Theory of polymer ablation. *Applied Physics Letters*, 53(24):2377–2379, 1988.
- [241] R. Sauerbrey and G. H. Pettit. Theory for the etching of organic materials by ultraviolet-laser pulses. *Applied Physics Letters*, 55(5):421–423, 1989.
- [242] G. H. Pettit and R. Sauerbrey. Pulsed ultraviolet-laser ablation. *Applied Physics A - Materials Science & Processing*, 56(1):51–63, 1993.
- [243] N. Arnold and N. Bityurin. Model for laser-induced thermal degradation and ablation of polymers. *Applied Physics A - Materials Science & Processing*, 68(6):615–625, 1999.
- [244] G. C. D' Couto and S. V. Babu. Heat-transfer and material removal in pulsed excimer-laser-induced ablation - pulsewidth dependence. *Journal Of Applied Physics*, 76(5):3052–3058, 1994.
- [245] S. R. Cain, F. C. Burns, C. E. Otis, and B. Braren. Photothermal description of polymer ablation - absorption behavior and degradation time scales. *Journal Of Applied Physics*, 72(11):5172–5178, 1992.
- [246] J. E. Andrew, P. E. Dyer, D. Forster, and P. H. Key. Direct etching of polymeric materials using a xecl laser. *Applied Physics Letters*, 43(8):717–719, 1983.
- [247] C. Hahn, T. Lippert, and A. Wokaun. Comparison of the ablation behavior of polymer films in the ir and uv with nanosecond and picosecond pulses. *Journal Of Physical Chemistry B*, 103(8):1287–1294, 1999.
- [248] T. J. Chuang, H. Hiraoka, and A. Modl. Laser-photoetching characteristics of polymers with dopants. *Applied Physics A - Materials Science and Processing*, 45(4):277–288, 1988.
- [249] N. B. Colthoupe. *Introduction to infrared and Raman spectroscopy*. Academic Press, 1975.

- [250] N. J. Turro. *Modern molecular chemistry*. University Science Books, 1991.
- [251] K. Fesser, A. R. Bishop, and D. K. Campbell. Optical-absorption from polarons in a model of polyacetylene. *Physical Review B*, 27(8):4804–4825, 1983.
- [252] R. Srinivasan, B. Braren, and K. G. Casey. Ultraviolet-laser ablation and decomposition of organic materials. *Pure And Applied Chemistry*, 62(8):1581–1584, 1990.
- [253] Maximilian Kreiter. Photothermische strahlableitung zur charakterisierung von polymeren für die integrierte optik. Master's thesis, Department of Physics, Johannes-Gutenberg-University Mainz, 1997.
- [254] B. C. Stuart, M. D. Feit, S. Herman, A. M. Rubenchik, B. W. Shore, and M. D. Perry. Optical ablation by high-power short-pulse lasers. *Journal Of The Optical Society Of America B-Optical Physics*, 13(2):459–468, 1996.
- [255] W. Kautek, J. Kruger, M. Lenzner, S. Sartania, C. Spielmann, and F. Krausz. Laser ablation of dielectrics with pulse durations between 20 fs and 3 ps. *Applied Physics Letters*, 69(21):3146–3148, 1996.
- [256] M. D. Shirk and P. A. Molian. A review of ultrashort pulsed laser ablation of materials. *Journal Of Laser Applications*, 10(1):18–28, 1998.
- [257] S. Baudach, J. Bonse, J. Kruger, and W. Kautek. Ultrashort pulse laser ablation of polycarbonate and polymethylmethacrylate. *Applied Surface Science*, 154:555–560, 2000.
- [258] E. Spyratou, M. Makropoulou, and A. A. Serafetinides. Study of visible and mid-infrared laser ablation mechanism of pmma and intraocular lenses: experimental and theoretical results. *Lasers In Medical Science*, 23(2):179–188, 2008.
- [259] R. Srinivasan. Ablation of polymers and biological tissue by ultraviolet-lasers. *Science*, 234(4776):559–565, October 1986.
- [260] R. Srinivasan, B. Braren, and R. W. Dreyfus. Ultraviolet laser ablation of polyimide films. *Journal of Applied Physics*, 61(1):372–376, 1987.
- [261] S. R. Cain, F. C. Burns, and C. E. Otis. On single-photon ultraviolet ablation of polymeric materials. *Journal Of Applied Physics*, 71(9):4107–4117, 1992.
- [262] A. Costela, J. M. Figuera, F. Florido, I. Garciamoreno, E. P. Collar, and R. Sastre. Ablation of poly(methyl methacrylate) and poly(2-hydroxyethyl methacrylate) by 308-nm, 222-nm and 193-nm excimer-laser ablation. *Applied Physics A - Materials Science and Processing*, 60(3):261–270, 1995.
- [263] R. A. Bowling. *A theoretical review of particle adhesion*, pages 129–142. Plenum Press New York, 1988.
- [264] J. Kruger and W. Kautek. Femtosecond-pulse visible laser processing of transparent materials. *Applied Surface Science*, 96-8:430–438, 1996.

Geburtsdatum: 3.2.1980  
Nationalität: Deutsch

+ 1 617-955-1514  
pfotenh@mit.edu

## SCHULLAUFBAHN & ZIVILDIENTST

---

- 1998      ↗ Abitur, Albert-Schweitzer-Gymnasium Jena; Abschluss als Jahrgangsbester (Ø 1,0);  
Preisträger zahlreicher Wettbewerbe (Mathematik, Physik, Fremdsprachen und Sport)
- 1998-1999      ↗ Zivildienst in der Evangelisch-Lutherischen Kirchgemeinde Martin-Niemöller-Haus, Jena;  
Immigrationsarbeit mit Spätaussiedlern, Kinderbetreuung, Hausmeister Tätigkeit

## STUDIUM

---

- 1999-2006      ↗ Studium der Physik und Philosophie, Friedrich-Schiller-Universität Jena
- 2002-2006      ↗ Stipendiat des "Evangelischen Studienwerkes Villigst"
- 2002-2003      ↗ Auslandsstudium University of Toronto, Kanada;  
Stipendiat des „Transatlantic Science Students Exchange Programs“ (TASSEP),  
Mitarbeit in Arbeitsgruppe Laser-Onkologie, Ontario Cancer Research Network
- 2004      ↗ Visiting Student am „Center for Research on Cognition and Concepts“, Indiana University  
Bloomington (USA) bei Pulitzer-Preisträger Prof. Douglas Hofstadter (Autor von Gödel, Escher, Bach);  
Beschäftigung mit kognitiven Aspekten und Kreativität in wissenschaftlichem Denken
- 2006      ↗ Hochschulabschluss Physik-Diplom „mit Auszeichnung“:  
Diplomarbeit (Note: 1,0) am Institut für Optik und Quantenelektronik, Jena (Prof. Roland Sauerbrey)  
Teilnoten Diplomprüfungen: Theoretische Physik – 1,0      Laserplasmaphysik (Hauptfach) – 1,0  
Experimentalphysik – 1,0      Philosophie (Nebenfach) – 1,0

## PROMOTION

---

- 2006-2009      ↗ Promotion am Institut für Optik und Quantenelektronik, Friedrich-Schiller-Universität Jena, zum  
Thema Relativistischen Laser-Plasma-Wechselwirkung und Laser-Teilchenbeschleunigung;  
Wissenschaftlicher Mitarbeiter im SFB TR18 "Relativistische Laser-Plasma Dynamik"
- ↗ Zahlreiche Veröffentlichungen und Konferenzbeiträge
- ↗ Hochschullehre, inkl. Seminare zu „Fundamentals of Modern Optics“ und „Philosophische Probleme  
der Physik“
- ↗ Referee-Tätigkeit für internationale Physikjournale (Applied Physics B, New Journal of Physics)
- 2007      ↗ Interims-Vertretung der FSU Jena im „Laserlab Europe Participants Council“ (Integrated  
Infrastructure Initiative des FP6 EU-Rahmenprogrammes)
- 2009      ↗ Abschluss des Promotionsverfahrens „summa cum laude“:  
Dissertation „Generation of monoenergetic ion beams with a laser accelerator“ („summa cum laude“)
- ↗ Betreuer: Prof. Malte Kaluza; Gutachter: Prof. Roland Sauerbrey, Prof. Wolfgang Sandner
- ↗ Rigorosum („magna cum laude“): Laserplasmaphysik – 1,0  
                 Relativitätstheorie (Nebenfach) – 1,0  
                 Naturphilosophie (Nebenfach) – 1,0

## AUFBAUSTUDIUM & FORSCHUNG

---

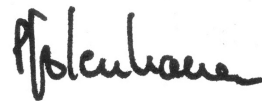
- 2008-2010      ↗ Postgraduales Studium "Technology and Policy" (S.M.), Massachusetts Institute of Technology,  
Cambridge, USA
- ↗ Vollstipendium des Bundesministeriums für Wirtschaft und Technologie und der Studienstiftung des  
deutschen Volkes (ERP-Programm)
- ↗ Wissenschaftlicher Assistent, MIT Portugal Program (Leitung Prof. Daniel Roos);  
Forschung zum Schwerpunkt „Transformation processes in research and higher education systems“

#### WEITERE INTERESSEN

---

- Musik
- Intensives Studium der Violine, zuletzt bei Prof. Georg Deutsch (Weimar)
  - Mitglied / Stimmführer / Konzertmeister zahlreicher Ensembles, inkl. stüba Philharmonie, Landesjugendsinfonieorchester Thüringen, Collegium Musicum Weimar, University of Toronto Hart House Symphony Orchestra und Chamber Strings
  - Organisation und Durchführung von Musik-Workshops und Konzerten
  - Als Mitglied der stüba Philharmonie Preisträger des Förderpreis des „Fonds Neue Länder“ der Kulturstiftung des Bundes für „herausragendes bürgerschaftliches Engagement für Kultur“ und des „Orchester-Selbstorganisationspreises“ der Jeunesses Musicales Deutschland
- Jugendarbeit
- Langjährige Mitarbeit in der evangelischen Jugendarbeit in Jena; Organisation und Betreuung von Seminaren und Freizeiten
  - 2000 – 2003 Mitglied des Kirchenrates Jena als Repräsentant für Jugendarbeit
- Fremdsprachen
- Englisch (fließend), Russisch (gut)

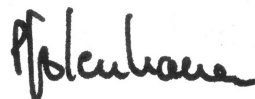
Cambridge, den 3. 2. 2008





- ▭ H. Schwoerer, S. M. Pfotenhauer, O. Jäckel, K.-U. Amthor, B. Liesfeld, W. Ziegler, R. Sauerbrey, K. W. D. Ledingham, and T. Esirkepov. Laser-plasma acceleration of quasi-monoenergetic protons from microstructured targets. *Nature* 439, 7075 (2006)
- ▭ S. M. Pfotenhauer, O. Jäckel, A. Sachtleben, J. Polz, W. Ziegler, H.-P. Schlenvoigt, K.-U. Amthor, M. C. Kaluza, K. W. D. Ledingham, R. Sauerbrey, P. Gibbon, A. P. L. Robinson, and H. Schwoerer. Spectral shaping of laser generated proton beams. *New Journal of Physics* 10, 033034 (2008)
- ▭ P. L. Robinson, P. Gibbon, S. M. Pfotenhauer, O. Jäckel and J. Polz. Scaling of the proton density reduction scheme for the laser acceleration of proton beams with a narrow energy spread. *Plasma Physics and Controlled Fusion* 51, 024001 (2009)
- ▭ H.-P. Schlenvoigt, K. Haupt, A. Debus, F. Budde, O. Jäckel, S. M. Pfotenhauer, H. Schwoerer, E. Rohwer, J. G. Gallacher, E. Brunetti, R. P. Shanks, S. M. Wiggins, and D. A. Jaronszynski. A compact synchrotron radiation source driven by a laser-plasma wakefield accelerator. *Nature Physics* 4, pp. 130-133 (2008)
- ▭ H.-P. Schlenvoigt, K. Haupt, A. Debus, F. Budde, O. Jäckel, S. M. Pfotenhauer, J. G. Gallacher, E. Brunetti, R. P. Shanks, S. M. Wiggins, D. A. Jaronszynski, E. Rohwer, and H. Schwoerer. Synchrotron Radiation from Laser-Accelerated Monoenergetic Electrons. *IEEE Transactions on Plasma Science* 36(4), pp. 1773-1881 (2008)
- ▭ S. M. Pfotenhauer.: “Telescopes” and “Physical Timescales”. In *Encyclopedia of Time*, ed. H. James Birx. To appear 2009
- ▭ S. M. Pfotenhauer, O. Jäckel, J. Polz, S. Steinke, H.-P. Schlenvoigt, J. Heymann, A. P. L. Robinson, and M. C. Kaluza. Multi-stage laser proton acceleration. To be submitted (2009)
- ▭ O. Jäckel, J. Polz, S. M. Pfotenhauer, H.-P. Schlenvoigt, M. C. Kaluza, H. Schwoerer. All-optical measurement of the electron sheath driving laser ion acceleration from thin foils. To be submitted (2008)
- ▭ S. M. Pfotenhauer, O. Jäckel, K.-U. Amthor, H. Schwoerer, B. Liesfeld, W. Ziegler, R. Sauerbrey, K. W. D. Ledingham, and T. Esirkepov. Monoenergetic Proton Beams from Laser Plasmas. *Conference on Lasers and Electro-Optics (CLEO)*, Long Beach, CA (2006)
- ▭ S. M. Pfotenhauer, O. Jäckel, J. Polz, H.-P. Schlenvoigt, K.-U. Amthor, W. Ziegler, H. Schwoerer, R. Sauerbrey, K. W. D. Ledingham, and T. Esirkepov. Spectral Control of laser accelerated proton beams. *DPG spring meeting*, Düsseldorf (2007)
- ▭ S. M. Pfotenhauer, O. Jäckel, J. Polz, H.-P. Schlenvoigt, M. C. Kaluza, H. Schwoerer, A. P. L. Robinson, P. Gibbon, R. Sauerbrey, and K. W. D. Ledingham. Scalings for Narrow-Band MeV Proton Beams from Laser Plasmas. *Conference on Lasers and Electro-Optics (CLEO)*, San Jose, CA (2008)
- ▭ S. M. Pfotenhauer, O. Jäckel, J. Polz (FSU Jena): Patentschrift Verfahren und Vorrichtung zur Beschleunigung von Ionen eines Ionenstrahls. DE 10 2008 044 781.1 (2008)

Cambridge, den 3. 2. 2008



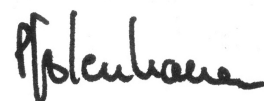


## Eidesstattliche Erklärung

Hiermit versichere ich, Sebastian Michael Pfothenhauer, geboren am 3. 2. 1980 in Jena, im Rahmen meines Promotionsverfahrens an der Physikalisch-Astronomischen Fakultät der Friedrich-Schiller-Universität Jena und an Eides statt, dass

1. mir die geltende Promotionsordnung (Stand 18.4.2000, Physikalisch-Astronomische Fakultät der FSU Jena) bekannt ist;
2. ich die Dissertation selbst angefertigt habe, keine Textabschnitte eines Dritten oder eigener Prüfungsarbeiten ohne Kennzeichnung übernommen habe und alle benutzten Hilfsmittel, persönlichen Mitteilungen und Quellen in seiner Arbeit angegeben habe;
3. außer mir keine weiteren Personen an Auswahl und Auswertung des Materials oder an der Herstellung des Manuskriptes beteiligt waren;
4. dass ich die Hilfe eines Promotionsberaters nicht in Anspruch genommen habe und dass Dritte weder unmittelbar noch mittelbar geldwerte Leistungen von mir für Arbeiten erhalten haben, die im Zusammenhang mit dem Inhalt der vorgelegten Dissertation stehen;
5. dass ich die Dissertation noch nicht als Prüfungsarbeit für eine staatliche oder andere wissenschaftliche Prüfung eingereicht habe;
6. dass ich weder die gleiche, noch eine in wesentlichen Teilen ähnliche, noch eine andere Abhandlung bei einer anderen Hochschule als Dissertation eingereicht habe.

Cambridge, den 17.11.2008





# Danksagung

Ich möchte all denjenigen ganz herzlich meinen Dank aussprechen, die mich auf dem Weg bis zur Fertigstellung dieser Arbeit begleitet und unterstützt haben.

Mein Dank gilt zuvorderst Prof. Malte Kaluza für die ausgezeichnete Betreuung meiner Dissertation. Sein unerschöpfliches Reservoir an Ideen sowie seine konstruktive und detaillierte Kritik haben mich stets ermuntert, Annahmen genauer zu hinterfragen und mehr aus mir (und den Daten) herauszuholen. Ich bin dankbar für die gelungene Kombination aus Professionalität und freundschaftlicher Nähe, die unsere gemeinsame Arbeit geprägt hat; für die mir gewährte Eigenständigkeit und für viele Gespräche jenseits der Physik.

Darüber hinaus richtet sich mein Dank an Prof. Heinrich Schwoerer (Stellenbosch, Südafrika), Prof. Roland Sauerbrey (Forschungszentrum Dresden-Rossendorf) und Prof. Ken Ledingham (Glasgow, UK). Prof. Schwoerer verdanke ich einen großen Teil meines Wissens über Laser und meiner experimentellen Fähigkeiten, sowie den Impetus, Experimente mit Zugkraft zum Abschluss zu führen. Prof. Sauerbrey danke ich für das große mir entgegengebrachte Vertrauen, weitreichende Unterstützung in allen Belangen und zahlreiche Ausschlag gebende Ideen. Ich danke Prof. Ledingham für die langjährige Unterstützung meiner Arbeit und vielfachen freundschaftlichen Rat in schwierigen Zeiten. Mein Dank und Respekt gilt darüber hinaus Prof. Gerhard Paulus, der in seiner Funktion als Institutsdirektor viele Energien freigesetzt und mich mit großem Zutrauen in meinem Tun bestärkt hat.

Ich danke allen Mitarbeitern des IOQ, die das Kunststück vollbracht haben, Forschung auf höchstem Niveau mit quasi-familiärer Atmosphäre beständig zu verbinden. Insbesondere bin ich meinem Freund und langjährigen Experimentierpartner Oliver Jäckel verbunden, mit und dank dem—eigentlich schon immer—alles geklappt hat. Ohne Oliver wäre die Mehrzahl der hier vorgestellten Ergebnisse nicht möglich gewesen. Ich danke ferner meinen Co-Doktoranden Hans-Peter Schlenvoigt und Jens Polz für die hervorragende gemeinsame Zeit und ihre unermüdliche experimentelle Tatkraft, sowie Jens Heymann, Sven Herzer, Maria Nicolai und Andreas Sachtleben für ihre Unterstützung und das freundschaftliche Arbeitsklima.

Kaum genug danken kann ich Burgard Beleites und Falk Ronneberger, deren weites Spektrum an Unterstützung sich von verlässlicher Konstanz im Ablauf des Laser-Alltags, über nächtliche Labor-Noteinsätze, bis hin zu wichtigen Worten der Kritik erstreckte. Das Gleiche gilt für Wolfgang Ziegler, dessen Kreativität beim Lösen von ingenieurstechnischen Problemen viele Experimente überhaupt erst möglich gemacht hat und ohne dessen Fertigkeiten weder Vakuumtechnik noch Patentanmeldung funktioniert hätten. Ferner richte ich meinen Dank an Dr. Kay-Uwe Amthor und Dr. Ben Liesfeld, die mich mit viel Geduld in die Materie eingeführt und vielen Experimenten den Weg bereitet haben. Ein weiterer Dank gebührt der Arbeitsgruppe Röntgenoptik um Prof. Eckhard Förster und Dr. Ingo Uschmann für die langjährige gute Zusammenarbeit und die vielfache Hilfe.

Ich danke ferner den Werkstätten der Physikalisch-Astronomischen Fakultät, ohne die der hohe technische und elektronische Aufwand nicht zu bewältigen gewesen wäre. Ihre (häufig kurzfristigen) Einsätze haben maßgeblich zum Erfolg der Projekte beigetragen. Ebenfalls danke ich herzlich den Sekretariaten des IOQ, deren dauerhafte Unterstützung die experi-

mentellen Abläufe enorm gestützt haben.

Eine Vielzahl von Personen außerhalb der Jenaer Physik verdienen meinen aufrichtigen Dank. An vorderster Stelle sei hier Dr. Alex Robinson (Rutherford-Appleton Laboratory, UK) genannt, der mit seinen physikalischen Modellen und numerischen Simulationen die vorliegende Arbeit in großem Maße bereichert hat. Viele der hier realisierten experimentellen Ideen fanden ihren Anfang in Gesprächen mit Alex. Gleichmaßen gilt mein Dank Dr. Paul Gibbon (Forschungszentrum Jülich) für seine Modellierung der Mikrodot-Experimente. In diesem Sinne seien auch die genutzten Computer-Ressourcen am Rutherford-Appleton Laboratory, der Science and Technology Facilities Council's e-science facility und dem Jülich Supercomputer Centre dankend erwähnt. Außerdem möchte ich mich bei Prof. Timur Esirkepov und Prof. Sergej Bulanov bedanken, die mit ihrer Arbeit den Anstoß zu meiner Arbeit gegeben haben.

Ich danke Waltraud Gräf, Dr. Hans-Jörg Fuchs und Dr. Ernst-Bernhard Kley sowie dem Institut für Angewandte Physik (IAP) Jena und dem Fraunhofer-Institut für Angewandte Optik und Feinmechanik (IOF) Jena für die andauernde Unterstützung bei der Targetherstellung. Ferner danke ich Ronald Lauck, Dr. Volker Dangendorf, Kai Tittelmeier und der Physikalisch-Technischen Bundesanstalt Braunschweig für die gute Zusammenarbeit und die Möglichkeit, das MCP am PTB-Zyklotron zu kalibrieren. Der Projektgruppe Laser-Teilchenbeschleunigung am Forschungszentrum Dresden-Rossendorf unter Dr. Ulrich Schramm bin ich für die gute Zusammenarbeit und die kurzfristige Aushilfe mit Geräten verbunden.

Ein Großteil meiner Arbeit wurde finanziert von der Deutschen Forschungsgemeinschaft (DFG) im Rahmen des SFB Transregio 18 "Relativistische Laser-Plasma Dynamik" und der Integrated Infrastructure Initiative (I3) "Laserlab Europe" des 6. Rahmenprogrammes der EU, wofür ich meine Dankbarkeit ausdrücken möchte. Beide Projekte boten hervorragende Rahmenbedingungen und die Gelegenheit, national und international mit Wissenschaftlern auf höchstem Niveau zusammenzuarbeiten.

Schließlich möchte ich all jenen danken, die meine Arbeit außerhalb des Physikalltags mitgetragen haben. Ich danke von ganzem Herzen meiner Mutter, ohne deren bedingungslosen Rückhalt ich diesen langen Weg, wie schon viele Wege zuvor, nicht hätte gehen können; ich danke ihr für das Vorbild, das sie mir war und ist, und für nächtliches Asyl in der Gillestraße, die nicht selten zum Schlusspunkt endloser Messzeiten wurde. Ich danke meiner Familie, die ihren Physiker immer mit offenen Armen empfangen und mit größtmöglicher Unterstützung bedacht hat. Ohne Euch wären die vergangenen Jahre nicht vorstellbar gewesen.

Ich bin dankbar für die Musik und die unentbehrlichen Freundschaften, die sie mir beschert hat—die STÜBA philharmonie und ihr Umfeld nehmen einen zentralen Teil meines Lebens ein. Ich danke Prof. Georg Deutsch (Weimar) für die Energie und die Momente der Klarheit, die ich aus den vielen gemeinsamen Stunden mitnehmen durfte. Ebenfalls danke ich dem Evangelischen Studienwerk Villigst und meinen Villigster Freunden für viel Inspiration, für prägende Einsichten in die eigene Verantwortung und zahllose Dinge jenseits des Tellerrandes.

Es bleibt, meiner Freundin Felicitas für ihr immerwährendes Verständnis zu danken; für die große Kraft in scheinbar endlosen Zeiten der Erschöpfung, die sie mir bedeutet; und für die Lebendigkeit und Freude, die ich aus unserer gemeinsamen Zeit zu schöpfen vermag.